CRANFIELD UNIVERSITY

M TRAPANI

DESIGN & MODELLING OF A COMPOSITE RUDDERLESS AEROELASTIC FIN STRUCTURE

SCHOOL OF ENGINEERING

PhD THESIS

Supervisor: S. Guo
November 2010

CRANFIELD UNIVERSITY

SCHOOL OF ENGINEERING

PhD THESIS

Academic Year 2010-2011

MATTEO TRAPANI

Design & modelling of a composite rudderless aeroelastic fin structure

Supervisor: Shijun Guo

November 2010

This thesis is submitted in partial fulfilment of the requirements for the degree of Doctor of Philosophy

Abstract

This thesis presents the study of a gapless and rudderless aeroelastic fin (GRAF) to enhance the directional stability and controllability of an aircraft. The GRAF concept was proposed and developed in the wake of previous research, targeted to improve flight performance and manoeuvrability, and to reduce fuel consumption and airframe weight. The study involved the subjects of aerodynamics, structural design and analysis, and flight mechanics.

The work includes conceptual design, structural modelling, aeroelastic analysis and flight performance evaluation of a GRAF variant designed for a small subsonic Unmanned Aerial Vehicle (UAV). The Eclipse UAV, a platform designed by part time students at the Department of Aerospace Engineering of Cranfield University, was chosen as a case study.

A new approach to design a more effective fin with an unconventional structural layout and novel techniques which have not been investigated in previous research is proposed. Despite the GRAF planform being similar to classical fin-hinged rudder configurations, it is provided with a flexible gapless control surface, kept as one continuous piece and integrated with the fin primary structure. With its fixed root and rudderless feature, the GRAF adopts an original method of operation. Its way of working relies upon an unconventional technique of combining morphing technology and aeroelastic effect. The morphable configuration is twisted to gain an aeroelastically beneficial effect to enhance the efficiency and manoeuvrability of the aircraft. This warping capability of the fin is the key role player enabling the GRAF surface to seamlessly generate the required aerodynamic forces.

Unlike the conventional structures designed to be as rigid as possible to withstand the external loads, the GRAF will exploit its structure's flexibility to use the aeroelastically induced twist deformations for a self-adaptive warping behaviour and improve flight dynamic response and performance.

In order to ensure the above features are achievable in practice, further study on the structural configuration was conducted. To achieve performance improvement, together with the original structural layout and aeroelastic effect exploitation, another three novel key components are investigated, proposed and introduced in the GRAF model. A structurally integrated actuation system, termed *L-shape stringers device (LSS)*, is designed to transform actuator axial forces in spanwise distributed bending moments, to create seamless deformations of the trailing edge (TE) section. An innovative trailing edge joint, namely the *swivel edge closure*, is specifically designed to enhance the mobility and degrees of freedom of the trailing edge box. It is a revolutionary concept which, by virtually interrupting the structural integrity of the closed TE section, allows relative translation and rotation of the TE panels. Finally, it is the novel concept of the *slot-connection* that, whilst appearing to clamp

the GRAF structure inside the slot, actually enables the design to increase the twist angle at the tip of the fin without overstressing the materials.

In order to enhance the GRAF efficiency, a tailored design of the fin structure was conducted. A novel internal structure configuration integrated with the key components has been designed to be connected to a flexible cladding skin, rotating ribs and a load-carrying tubular beam all of which constitute the primary parts of the GRAF model. With the ultimate goal of a lighter tail version, the entire design has been made by using composite, light frames, in an engineering trade-off of stiffness, elasticity, weight and cost of both glass and carbon fibre laminates.

The analysis via 2-D aerodynamic codes and FEA was conducted to assess and validate the GRAF model and the obtained performance. Static linear elastic analysis has been carried out to verify the structural layout of the novel design subject to strength and stiffness criteria in addition to the fin warping and cambering capabilities. Also an investigation of aeroelastic stability related to steady and unsteady aerodynamic conditions has been carried out during the model analysis phase. The study has shown that although the GRAF divergence and flutter margins are slightly smaller than those of the conventional fin, the design and performance requirements are satisfied within the very challenging objective of a lighter vertical tail structure.The dynamic analysis study has also demonstrated the beneficial effect obtained by damping yawing oscillations when such a self-adaptive structure, compared to a rigid one, can be operated under cross wind circumstances. The manufacturing feasibility and assembly of the GRAF structure has been explored with the construction of a 1:1 scale model of the fin prototype. The model has been used as concept demonstrator to assess the functionality of the introduced technical novelties, the ease of manufacturing and the structural weight of the final assembly.

Aknowledgments

I wish to express my gratitude to the Department of Aerospace Engineering, in particular to the Aircraft Design Group for sponsoring my PhD course.

I wish to thank especially my supervisor Dr. Shijun Guo who has guided me through this long and challenging path which I started as a student and have hopefully ended as a professional. His constructive criticism and technical support have been fundamental and essential aspects for the success of this research project.
I would also like to thank my co-supervisor, Dr. Giuliano Allegri. His remarkable technical competencies and expertise have been both important and helpful supports to initiate this research study. In addition, I would like to thank Dr. X. Zhang for the advice relating to my PhD study.

Special thanks go to all my friends who encouraged me during the last and most difficult years of the PhD experience: first of all, my friends Andrea and Valeria, who although thousands of miles away from me have daily and continuously supported me; secondly, my friends at Cranfield: Silvia, Linda, Pietro, and Parvathy; also, my friends and ex-office mates, Evandro and Michael, for their unique company and friendship shared during my Cranfield experience. Thanks are also due to my particular friend Lucija who demonstrated to me how exhausting, but eventually rewarding, it can be fighting for your own rights, ideas, and principles.

I would also wish to thank all my colleagues at the Aerospace Engineering Department in helping me through the final rush of the thesis submission - in particular my particular thanks go to my colleague Mr Ali Yarf-Abbasi for being extremely supportive and encouraging, especially in those moments when things seem to be going wrong, but above all for being a truly and precious friend.

Finally, I really wish my parents could read a little of this English so they can see how grateful I am to have had their support in sharing my difficulties, obstacles and doubts as well as the pleasant moments of my growing up, education, career and ongoing life in Aeronautical Engineering.

...to my parents,
and to myself.

List of contents

List of Figures

List of Tables

Notation

List of Acronyms:

AAW	Active Aeroelastic Wing
AC	Aerodynamic centre
AoA	Angle of attack
AR	Aspect ratio
BC	Boundary conditions
CAD	Computer aided program
CELAS2	Two-dimensional spring elements
CG	Centre of gravity
CP	Centre of pressure
Cp	Pressure coefficient
CTRIA3, CQUAD4	Triangular and quadrilateral mesh elements
DLM	Doublet Lattice Method
DOF	Degrees of freedom
EA	Elastic axis
ESDU	Engineering Sciences Data Unit
FEA	Finite Elements Analysis
FEM	Finite Elements Method
FLAVIIR	Flapless Air Vehicle Integrated Industrial Research
FRA	Frequency response analysis
GRAF	Gapless Rudderless Aeroelastic Fin
LE	Leading edge
LSS	L-shape stringers
MAW	Mission adaptive wing
MPC	Multi-points constraint
MRF	Magneto rheological fluids
MTOW	Maximum take-off weight
SPC	Single-point constraint
TE	Trailing edge
TRA	Transient response analysis

VLA	Very Light Aircraft
UAV	Unmanned Aerial Vehicle
WP	Waypoint

List of symbols

α^r	Initial angle of attack
α_{δ_R}	Angle of attack change for unit rudder deflection
b	Fin span
β	Side slip angle
c	Fin chord
$C(k)$	Theodorsen's function
C_D	Drag coefficient
C_{Di}	Induced drag coefficient
C_L	Lift coefficient
C_{mAC}	Pitching moment with respect to the AC
$C_{L\alpha V}$, $C_{L\alpha}$	Lift-curve slope coefficient
$C_{L\delta}$	Lift coefficient change for unit surface deflection
$C_{N\delta_R}$, C_{N_β}	Directional controllability and stability derivatives
C_X , C_Z	Aerodynamic resultant force vertical and horizontal components
$C^{\vartheta\vartheta}$	Flexibility influence coefficient
D_{ii} , D	Flexural stiffness
δ , δ_R	Command surface deflection
e	Oswald's number
E_i	Elastic Modulus of the i_{th} lamina
$E^a_{x_i}$	Effective elasticity of the i_{th} wall of the box
$(E\Gamma)_{BS}$	Warping rigidity

ϕ_x, ϕ_y	rotation about the *x* and *y* axes
F_H , F_V	Horizontal and vertical components of the actuator force
$\lfloor G_{kg} \rfloor$	Spline interpolation matrix
$G_{i,j}$	Shear Modulus of the i_{th} lamina
g	Gravity acceleration
$\Gamma(y)$	Flow circulation
γ_S	Shear deformation
$[\phi]$	Mode shapes function
$h,\ \alpha$	Heave and pitch variables
H	Gradient of the gust
k	Reduced frequency
I_t , J	Polar moment of inertia
$K_j(ik)$, $H_n^{(2)}(k)$	Bessel and Hankel functions
L_x , L_y	Plate dimensions
ΔL_V	Fin contribution to rolling moment
Λ	Sweep angle
M_t , T	Torsional moment, torque
N	Yawing moment
η_V	Fin-to-free stream air velocities ratio
n_1	Maximum design vertical load factor
$\nu_{i,j}$	Poisson's ratio of the i_{th} lamina
q_∞	Free stream dynamic pressure
Q_{ij}	Reduced stiffness
σ	Side wash angle
σ_i , ε_i	Direct stress and strain of the i_{th} lamina
σ_{xx}	Direct stress along x-direction
σ_Γ	Warping stress
$\psi(x,y)$	Warping function

P_z, p	Vertical component of the external force resultant
ρ	Air density
Q_h, Q_α	Aerodynamic external forces
$\boldsymbol{q}$	Generalised coordinates vector
S_V	Vertical tail surface area
S_b	Wing surface area
ϑ	Twist angle
τ	Shear stress
t	Plate thickness
u,v,w	Displacements in the x,y,z, reference system
U_d, V_d	Divergence speeds
U_r	Reversal speed
U_{ds}	Designed gust velocity
$\{u_g\}$	Structural grid points deflections
$\{u_k\}$	Aerodynamic grid points deflections
V_{NE}	Never exceed speed
V_f	Flutter speed
V_V	Air velocity on the vertical tail
V_∞	Free stream air velocity
x_V	Distance between vertical tail CP and aircraft CG
Y, F_Y	Side force
z_{V_S}	Distance between fin CP and aircraft longitudinal axis

“This page is intentionally left blank”.

Chapter 1 - Introduction

1.1 Performance Enhancement

Aerodynamic efficiency, flight performance, fuel saving designs, reduced manufacturing and maintenance costs are the main objectives of today's aviation technology.

Since the beginning of commercial aviation, designers have focused their attention on the development of longer range, faster and larger airplanes. Although for a vast diversity of sorties, up to now, over the past decades and for the foreseeable future, these objectives have not radically changed. Different design philosophies are approached in accordance with the diverse applications of all those projects, but with the common shared aim of enhancing aircraft performance.

Military applications are primarily targeting advanced flight manoeuvrability, multi-tasking and multi-configurable aircraft, enhanced flight performance and stealth capability. Conversely, civil and commercial projects, less interested in reducing aircraft radar visibility, are aiming to create lighter, more efficient and aerodynamically streamlined airplane versions. Lighter fuselage and wing structures are sought to increase the carrying payload capability and to extend the flight range and endurance of next generation aircraft. New designs aim also at reducing noise and CO_2 emissions and at lowering maintenance and manufacturing costs for the production of greener aircraft.

The global need for keeping an attentive eye on environmental issues renders efficiency and effectiveness as very important aspects of an environmentally friendly aviation industry that is projecting towards future generation aircraft. Hence, all facets of aircraft performance have become the primary objectives of current aeronautical research and technology.

Ultimately, the majority of these characteristics and requirements for novel and better performing configurations have merged into a new and unique discipline of

studying bio-mimetic design concepts. The aviation industry's trend has developed by trying to design airplanes in the same way as birds are 'designed' by nature. Since the original dreams of human flight, the characteristics of birds have been inspiring projects of past, present and future aviation. The main reason for studying different ways to copy and reproduce birds' features in airplane design is because of birds' ability to change and optimise their flight characteristics to any flight condition by simply adjusting the aerodynamics of their wing and body shapes. They are capable of maximising their level of performance at any flight altitude by easily adapting themselves to diverse situations with seamless skills. Modern technological attempts to replicate birds' features with bio-mimetic aircraft designs have been termed as *morphing technology.*

The ways in which birds can control flight attitudes and optimise both aerodynamics and "handling qualities" are today all inherent aspects integrated within the design of modern conforming and adaptive structure concepts. They represent the core of the actual morphing technology studies. The most remarkable and important characteristic of any morphable and adaptable structure is the capacity of potentially making the aircraft fly, with optimised performance, at any point of its flight envelope.

Recently, and particularly in the military sector, studies and projects on morphing technologies have increasingly sprung up due to the development of yet another branch of aviation technology, the Unmanned Aerial Vehicles (UAVs). Autonomous flying aircraft, such as the Eclipse UAV prototype [67, 68, 201] shown in Figure 1-1, have extended the possibility of using single airplanes for multiple purposes and with different capabilities. Furthermore, flying without crew members may reduce the risk of human personnel loss and can potentially extend flying hours to several days without landing.

The UAVs represent the perfect flying platforms to test morphing systems and new, unconventional vehicle layouts. It is certainly more costly and risky to conduct flight test campaigns and missions using larger and manned airplanes, rather than remotely controlled aircraft, especially when new and unconventional systems are being tested on board.

Technically speaking, the morphing technology can be metaphorically compared to a musical symphony, in which all the instruments are required to play together from the beginning of the project. The engineers are the musicians, and their instruments are the several disciplines and tools necessary for the completion of the final musical performance. Every instrument differs from the others, but all of them must play together to create a perfectly and harmoniously tuned symphony within a structure of multiple facets. Conceptual design, aerodynamics, materials, structures, actuation systems, and flight mechanics are the fundamental instruments that engineers have to use *in concerto* to realise a final morphable design with enhanced performance.
The author will attempt to be the director of his own little orchestra, used to play the "study, design and development of an aeroelastic morphing fin".

Figure 1-1 Eclipse UAV vehicle [67, 68, 201]

Surrounded by a similar conceptual attitude is one of the most successful examples of aircraft projects in which all those disciplines have come together to design a performance-improved vehicle – the Silent Aircraft project [90, 91]. The project was a study jointly started by MIT and Cambridge University [37] which embedded, in a unique research design, the recent trends and studies of the aviation industry for developing a greener and more aerodynamically efficient airplane for next generation aircraft. The Literature Review and Methodology Chapters will highlight the engineering reasons why 'morph-addicted' scientists still continue to study "birds' wings technology" for innovative bio-mimetic designs for future aviation.

1.2 Unconventional conceptual designs for performance enhancement

To date, there are hundreds of aeronautical studies and projects currently focusing on expanding aircraft versatility and improving airplanes' efficiency. As introduced in the first part of the chapter, most of these ideas and projects feature the application of morphing technology. However, despite the fact that morphing experiments and studies have exponentially grown during the last three decades, the original idea of this type of conceptual design can be traced back to the origins of modern aviation history. The first successfully flown morphing structure made its appearance over a century ago, when Wilbur and Orville Wright flew their Flyer III, on 17th December 1903 [197]. That pioneering attempt owed its success to the novel concept of a warping wing mechanism. (The details and characteristics of their invention are collected and described in detail in the US, under patent number 821,393.) This was the mechanical system that the Wright brothers adopted to handle the rolling and yaw motions of their flying machines at the very beginning of the 20th century [132]. It is also one of the most important concepts that inspired this research and many other projects in the history of aviation from that time to the present day. The Wright's patent claims to be the invention of a system for aerodynamic control that simply manipulates an aircraft's aerodynamic surface based upon helically twisting the outermost portions of the two half wings. The Wright brothers' patent describes the principle and first real application of the 'warping wings' concept, which finally provided an airplane with a three-axis-control system. Their invention represented the first milestone and the very beginning of morphing technology. It also represented the first time in history that a man, using a powered airplane, took off, flew and landed in a safe and, above all, controllable way. The Wright brothers wanted to replicate artificially on their biplanes' wings the innate ability of birds to bend and twist their wings to control in-flight manoeuvres. Despite the genius of their invention, suddenly, after those first soaring flights over Kill Devil Hills, that original way of controlling airplane flight attitudes was lost as more complex aircraft structures were built. The more severe flight speed regimes and stiffness requirements changed and imposed new structural layouts for wings and command

surfaces. They necessitated finding other ways for control systems, rather than twist-flexible structures. Therefore, new solutions such as smaller hinged aerodynamic surfaces for wings, and horizontal and vertical tailplanes, were born and developed. Innovations such as ailerons, flaps, slats, spoilers, elevators and rudders were then, and still are, designed with hinged connections and unsealed gaps separating them from the main wing and tailplane structures. Nevertheless, the ease of the design, maintainability, the rapid and easy manufacturing processes, and the reliability of those hinged surfaces, decreed their success for the vast majority of airplane designs, thus negating the need for further developments of warping and morphing models as options for integrated unconventional command surfaces. Morphing and warping designs are certainly more efficient and perform better than classical hinged and unsealed gap surfaces, but they are also more expensive and complicated in their manufacture and design. Paradoxically, the birth of morphing technology coincided with the demise of the Wright brothers' first manned, engine-powered aircraft. It was not until the late 1980s that new projects on morphing technology started to become again in vogue. It was also during this period that the contribution coming from the development of the new class of materials, *smart materials*, helped in the further development of these types of technology and innovations. Novel, compliant and "smart" structures enabled systems to increase their degrees of freedom and morphable capabilities in comparison to conventional mono-phase materials. Smart structures and research programmes such as the Mission Adaptive Wing (MAW) and the Active Aeroelastic Wing (AAW) projects of DARPA/NASA, gave a new drive to this research area. Designers spotted the opportunity to exploit variable and flexible configurations as the best instrument to make aircraft adaptable to any flight situations and any task by improving manoeuvrability and aerodynamic performance. As stated by Sanders *et al.* in their studies [153, 154], conventional aircraft are usually designed to optimise performances at only a few points of their flight envelope, flying the rest of them with compromises in efficiency, performance and fuel burning. The morphing philosophy, instead, envisions novel airplanes to continuously change their features and performances according to the different aspects and needs of the flight envelope points.

There are two main reasons which dictate the need to improve aircraft flight performance. On the one hand there are the aerodynamic aspects which aim to enhance the flight aerodynamic efficiency, increase endurance and flight range, and reduce fuel consumption. On the other hand, there are the flight handling quality aspects which characterise the aircraft stability and controllability of the vehicle on the three longitudinal, lateral/directional and vertical directions of the aircraft. The first group contains the set of performances, which is closely related to lighter structural designs, streamlined aerodynamic shapes and new generation engines. The second group pertains to longitudinal, lateral and directional stability and control characteristics of any aircraft design. Their study provides comfortable, stable, safe and controllable flight attitudes against any external disturbance, upsetting conditions or flight manoeuvres the aircraft may encounter in its life.

Therefore, engineers started focusing their attention on those areas in which development could contribute to novel technology and innovative designs in favour of better performing and efficient aircraft. The majority of the studies aimed at converting conventional wing structures into aerodynamically improved bio-mimetic designs. Lighter materials and aircraft structures were developed in conjunction with greener and lower fuel-consuming engines. During recent years, some attempts at proposing the same innovative conceptual designs for horizontal and vertical tailplanes as well, have not had the same success and performance impact as happened for the wing configurations. The tail design and application costs compared to the gained performance were not regarded as worthy of any further development. Generally speaking, the technical complexity and cost of morphing structures has always represented a challenging obstacle for the easy development of such technology on production series aircraft. Therefore, in order to guarantee performance and control, mechanically mounted and activated spoilers, slats, flaps, and command control surfaces such as ailerons, elevators and rudders were deployed. The efficiency and effectiveness of such control systems, operated by sliding and hinged devices, did not stop engineers and designers from thinking outside the box for revolutionary ways to control aircraft attitudes and enhance flight performance. The race towards bio-mimetic designs, with improved aerodynamics, structures and flight mechanics was not over yet. In the search for enhanced performance, the

mechanically hinged design was further engineered with the all-moving surface invention. The novel concept of all-moving surfaces used to control and manoeuvre aircraft in flight was specifically designed to augment the stability and control of certain classes of aircraft such as the supersonics. Mechanical leading and trailing edge flaps, and all-movable pivoted wings and tailplanes represented, for several decades of aviation history, the most successful devices, enabling vehicles to vary their flying performances by means of mechanically geared mobile parts. Only after the advent of smart materials did the designs enable wing layouts to seamlessly vary camber, geometry and the twist angle of wing structures. New techniques were also studied to beneficially exploit morphing and aerodynamically-induced deformations on flexible structures to enhance the flight performance of aircraft, such as the *aeroelastic effect*. The most popular expression of this concept in the modern era of jet fighters was the F/A-18 Active Aeroelastic Wing (AAW) vehicle, included in the AAW research programme presented by Voracek in [188] and published in [1-3]. The induced spanwise axial distortions were exploited to manoeuvre the vehicle in rolling by using the two opposite twisted half wings as active control surfaces rather than conventional ailerons. This aeroelastic rolling effect system was adopted to overcome and avoid reversal issues on the ailerons at transonic speeds, thus enhancing rolling manoeuvres at high speeds. In a similar way, this technique was also used in other projects to trim aircraft wings for wash-out effect for minimum induced drag generation at cruise speeds. The main advantage of having an adaptive aeroelastic twist for trimming purposes is that the surface can adapt itself to several differing speeds and attitudes by simply varying the rate of distortions across the wing structure. Morphing and aeroelastic effect-based technologies work by tailoring controlled deformations on wing and tailplane structures in order to shape and optimise their aerodynamic surfaces in the same way that birds do with their wings. The engineers' final objective is to create designs stiff enough to withstand all the external loads and, at the same time, be reliably flexible to change their configurations in a bio-mimetic fashion.

Structural continuity, aerodynamic smoothness and gapless configurations are also major aspects of wing and empennage designs which contribute to the enhancement of vehicle performances. The absence of any structural interruption helps to make

stiffer and lighter structures, while sealed gaps increase the aerodynamic efficiency, flight performance and in certain applications the aircraft stealth capability.

In order to improve the efficiency of aircraft, during recent decades, engineers came up with a novel version of old wing-body configurations whose original conception could be dated back to the 1940's. They are tailless, blended wing body (BWB) and flying-wing configurations. Those types of aircraft were designed to gain aerodynamic efficiency by exploiting the entire wing-body area as lifting surfaces. Engineers started to design flying-wings during World War II. At first there were the German Horten and Lippish prototypes, later followed by the American designs of Northrop and Grumman, up to the latest designs, amongst many others, of the modern Boeing Phantom Ray, the Cranfield University-BAE Systems Demon and Eclipse UAVs [66, 201], the Silent Aircraft, the Northrop B-2, and the Boeing X series with the X-45, X-46, X-47, and X-48 [109] test aircraft. All these variants appeared to be very aerodynamically efficient designs, but their tailless characteristic needed a sophisticated flight control system to handle the aircraft with stability and control. However, although difficult, good handling in longitudinal control was managed even without proper horizontal tailplanes. Instead, more severe problems due to a lack of vertical empennage were affecting and upsetting their directional stability and control attitudes. New forms of control systems and deployable devices were adopted on board those machines, such as split flaps, and spoilers were designed to enable heading and yaw control by generating asymmetric drag force on the two opposite half wings. Other expensive and complex architectures, such as thrust vectoring nozzles like the one designed for the Boeing X-45 UAV and the Demon vehicles have been also designed to stabilise and control the nose direction of these tailless aircraft. In those cases the engine exhaust nozzle orients the thrust towards the desired direction.

All these concepts can successfully orient the aircraft's nose in the required direction, thus substituting the tasks of vertical tails conventionally fixed on the rear of the fuselage. However, some penalties must be paid for their application because of their more complex configurations, in terms of cost, weight and design issues. The worst aspect of tailless designs is the short length of the moment arm between the centre of pressure of a potential fin and the aircraft's CG. That distance considerably affects

the aircraft yawing movement and the fin's directional effectiveness. Satisfactory directional effects might be obtained, even with shorter arms, by means of very large tail surfaces. But in that case, that will obviously translate into a loss of the aircraft's aerodynamic performance, due to the drag force such a large fin might generate. Other flying-wing designs, such as the solution adopted on the Northrop N-1M in Figure 1-2, relied upon tiltable adjustable wing tips or again on classical multiple small dorsal fins, as built on the Northrop B-35.

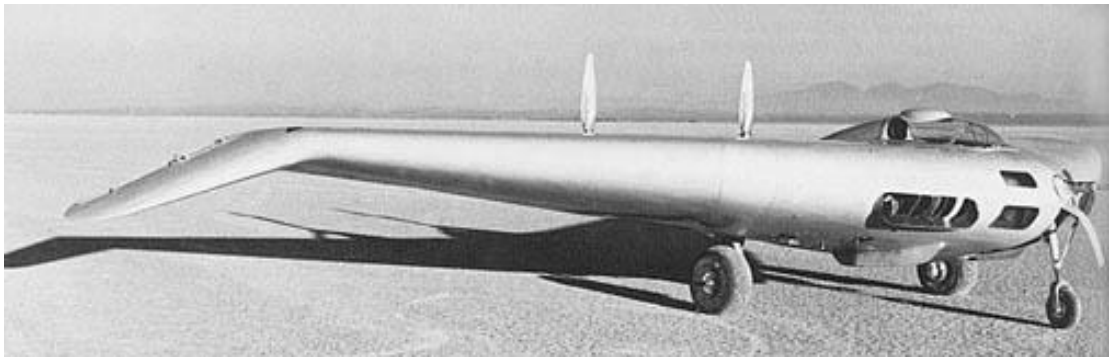

Figure 1-2 Northrop N-1M Tailless aircraft configuration [195].

Because of those complex directional controllability and stability issues, very few tailless prototypes went to a production series, and to date, none of them have commercial or civil applications. The only successful exception was the military Northrop-Grumman B-2 Spirit, based on a flying-wing concept without any vertical surface. It utilises split flaps to handle directional flight control and stability attitudes. Hence, due to technical complexity, maintenance and manufacturing costs, and structural weight of more sophisticated devices and novel technologies, the majority of conventional aircraft still rely upon classical vertical dorsal fins for control authority and stability purposes.

Either vertical control surfaces or adjustable devices are essential requirements to guarantee directional stability and control for any class of aircraft in every flight condition, in particular, to ensure directional authority during those critical phases of landing and take off when crosswind conditions may dangerously destabilise the aircraft flight attitude. During those phases all flying wings not provided with a vertical fin suffer from a lack of directional stabiliser, becoming practically unstable and difficult to control.

Therefore, in the wake of the continuous search for enhanced flight performance and aerodynamically efficient design concepts, stands this research study. The vertical empennage, as fundamental components of both fixed and rotary wings, cannot be eliminated from future designs unless substituted by other more precise and feasible technologies and control systems. As already mentioned in the first paragraph, a big help in developing novel and unconventional technologies, and by practically testing them before final application on board production aircraft, comes from the remotely piloted vehicle (RPV) and unmanned aerial vehicle (UAV) sectors. These two categories of aircraft have allowed engineers to assess and verify the outcomes of novel concepts and technologies before being tested on larger and manned scale versions. In most cases, RPVs and UAVs represent less risky and expensive flying platforms. Despite the recent exponential growth of the UAVs' production market, both their application and interest in them from aviation can be dated to an even earlier date than the Wright brothers' flight. Although already autonomous radioplanes were used to fly as target drones during World War II for military training in the 1940s, they started in practice to fly just at the end of the 19th century. It was almost a decade before the Wrights' first manned flight, when the first unmanned aerial vehicle was successfully flown in 1896 by S. P. Langley. It was a steam-powered ¼ model scale of a tandem wing configuration aircraft (Figure 1-3), representing the first stable and autonomous engine-powered, unmanned flying vehicle in aviation history.

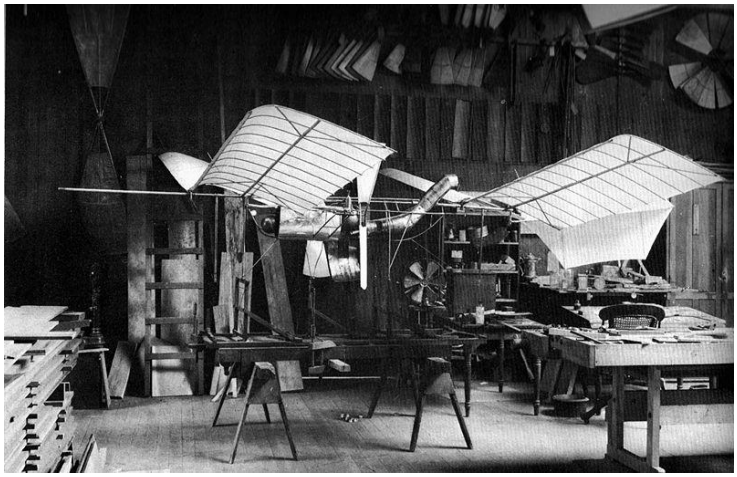

Figure 1-3 Langley's tandem wings steam powered unmanned aircraft [194]

Today, UAVs represent important flying platforms used either for multi-task missions or for testing new and unconventional technologies, systems and configurations. Mostly, they are used for military applications but are hoping to conquer a larger stake in the future civil airspace scenario.

1.3 Aim & Objectives of the Research Project

The research project's aim is:
" To design and validate a composite Gapless Rudderless Aeroelastic Fin (GRAF), for enhancing directional flight stability and control performance, within a novel unitised structural layout". Figure 1-4 shows the finalised model of the GRAF that will be presented with this study.

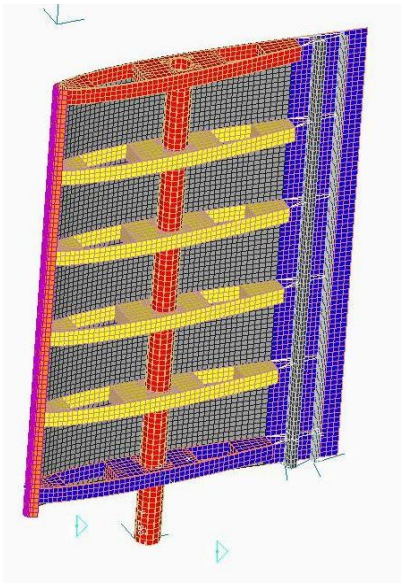

Figure 1-4 GRAF final assembly: internal components view

This study did not follow the configuration of classical vertical tails, provided with fin and hinged rudder or based on entirely moving surfaces, namely slab tails. Instead, a novel concept for vertical empennages has been developed, with the main features explored through the project objectives listed below. There are four main concerns which sum up and better identify the key features of the investigation.

They are:

- adaptability;
- efficiency;
- effectiveness;
- lightness.

These describe what is intended to be studied in detail with the research's objectives. The list of objectives can be identified as follows:

- To design an effective vertical empennage lacking a rudder element;
- To design a vertical empennage able to perform directional control and stability tasks by morphing and warping effects;
- To design a fin structure with a unitised layout and a structural configuration lighter than classical fin designs;
- To design a self adaptive fin able to enhance directional controllability and stability tasks by sensing wind direction and intensity;
- To design a warping structure concept devised to exploit aeroelastic effect induced deformations;
- To improve the aerodynamic efficiency of the empennage and, consequently, of the whole aircraft;
- To develop a design concept whose principle might also be adapted to other types of aerodynamic surfaces such as wings and horizontal tailplanes;
- To design an assembly able to satisfy the stiffness and strength requirements for both steady and unsteady aerodynamic loadings scenarios.

The primary novelty of this study, as introduced in the first objective of the list, is the elimination of a classical hinged command surface, the rudder. Directional control and stability tasks will be ensured by generating the required control forces by helically twisting and cambering the fin structure. The fin warping attitude will be produced by a combination of structural flexibility, compliant components layout and deformations caused by mechanical and aerodynamically-induced aeroelastic effects. The absence of the rudder component eliminates the hinge line gap between the two

parts. It also allows the use of internal mechanisms, as structurally integrated actuation systems, to seamlessly morph the camber of the fin profiles. The twist and camber actuation increases the fin aerodynamics and effectiveness during manoeuvres. Nonetheless, the sealed gap profiles reduce the total drag force generated in flight by the vertical tail. Moreover, when a more efficient tail is designed in comparison with the classic version, then its size might eventually be reduced, while still keeping a satisfactory level of performance. The reduction of the fin dimension may further decrease the drag generation effect and enhance the aerodynamic efficiency of the vehicle, which also contributes to a reduction in aircraft fuel consumption. The gapless and rudderless specifications imposed on the design are to be thought of as a one-piece configuration. The unitised structural layout is also aimed at designing a vertical tail version lighter than conventional fin-rudder variants. The weight saved might be used either to carry more fuel or payloads on board, or even to reduce the fuel burning due to a lighter structure. In both cases the range, endurance and aerodynamic efficiency of the aircraft will undoubtedly gain benefits from a lighter and more aerodynamically efficient empennage. In order to further increase the aerodynamic efficiency of the GRAF, all unsealed gaps between the fuselage and the fin body will be avoided. That translates into excluding the option of having a separated all-moving tail for the novel devoid-of-rudder configuration. Therefore by eliminating every hinge-movable option on the GRAF model, the only theoretical and technological options left to guarantee the operability of such a vertical tail reside in the application of morphing/aeroelastic concepts and techniques. The warping aeroelastic features of the empennage and the self-adaptive characteristics of the GRAF will try to improve the fin's *weather-cock effect*, exclusively applied for stability purposes, while the controllability of directional attitudes will be handled by the warping effect and profile cambering for enhancing the side force generation effectiveness. In order to obtain the required performances, five technical novelties have been introduced with the GRAF design to achieve the fin deflection and adaptive behaviour needed to accomplish the control and stability tasks. These novelties will be detailed and presented in Chapters 3 and 4. Amongst all, the most challenging aspect of the novel design was to convert the rudder function actively effective across the entire span of the fin surfaces into a

novel design with warping capability linearly distributed over a very low aspect ratio surface. The major difficulty was to obtain the same side force generation produced by a rigid deflected rudder by using only a twisted surface with fixed root. In order to better explain this concept, a parallel analogy is made with aeroelastic wings design. These are more sensitive, in terms of flight performance and structural deformations, than vertical tails. The reason is explained through the CAD drawing in Figure 1-6.

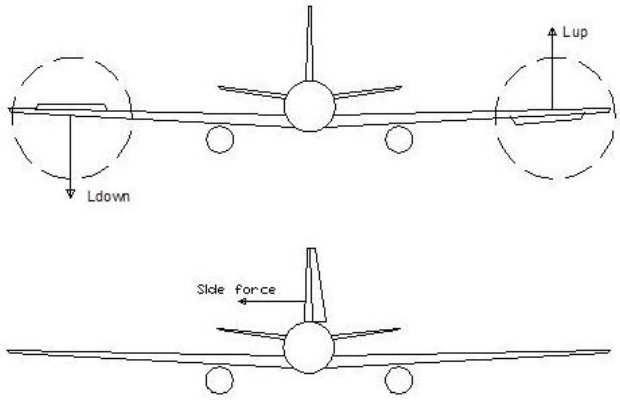

Figure 1-5 CAD illustrations: Ailerons/Rudder deflection and force generation

Let us take the example of substituting normal ailerons and rudder operations with aeroelastic effect designs. Figure 1-5 shows the aileron and rudder locations. The ailerons, differently from the rudder, occupy just a small portion of the aerodynamic surface. In particular, they are located at the outer wing section. Conversely, the rudder is span-wise distributed.

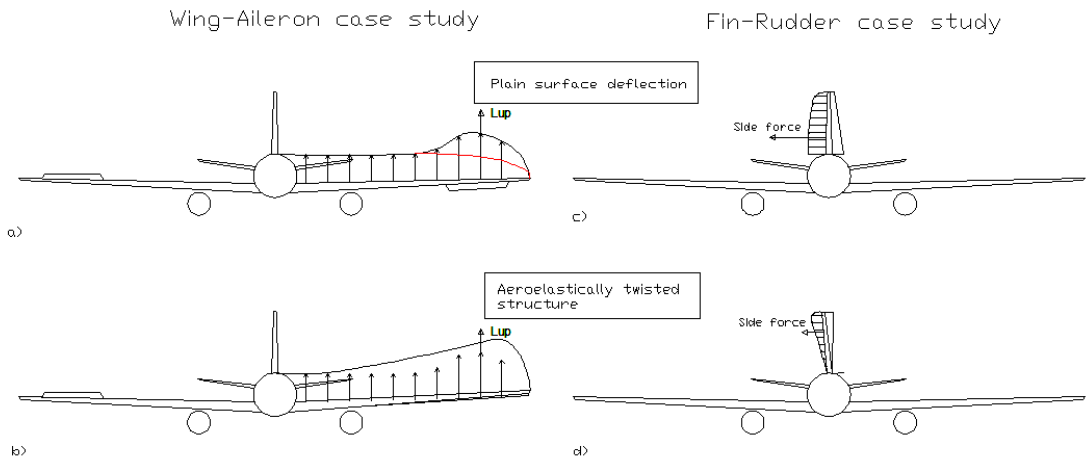

Figure 1-6 CAD illustration: force generated by twist deformation upon wing and fin surfaces

Looking at the aerodynamic loads distribution in Figure 1-6, it is possible to note the loading effect of the aerodynamically twisted shape for both the wing and the fin. The aileron deflection slightly alters the level flight load distribution of a wing. It increases the lift force only corresponding to its location. A similar effect can be obtained when a linear twist distortion is actuated along the wing structure. The airfoils at the wing tip will therefore be the most angled, generating the incremental lift necessary to equal that produced by the aileron rotation. The rudder deflection, instead, varies the loading distribution along the entire span of the fin. Therefore substituting the rudder deployment with a simply twisted empennage does not equal the conventional side force generation. The reason for this is that the twisted profiles near the fin root have angles of twist close to zero degrees, and thus do not generate great components of side force. Even a larger angle of twist will not ensure an adequate force, again because of the linear twist distribution along the fin and also because of approaching the profile's stall angles. Moreover, as will be explained in Chapter 3, the twist angle is directly proportional to the length of the structure. The wing aspect ratio is greater than that of the fin. The wing results in being more flexible than a squat structure such as the empennage. Therefore a more compliant fin structure had to be considered and designed to accomplish directional tasks as classic fin-rudder configurations do.

As already anticipated, the fin will be sized and designed for the small-medium class of subsonic unmanned aerial vehicles. In particular, the Eclipse UAV has been selected and taken as the reference baseline and case study [30, 77, 97] for this doctoral project. The Eclipse vehicle has been initially designed and built at the Aerospace Department of the School of Engineering at Cranfield University by part-time students and later integrated in the flapless research programme FLAVIIR [68]. The relevance of this research thesis to the aims of the FLAVIIR programme and the ready access to data and specifications available within the department group, made it a perfect case study for this project.

Each of the single objectives listed before represents a very challenging characteristic aspect of this project study. Most of these technological features have never been applied altogether on a vertical tail structure. A multidisciplinary integration of

different research areas of aeronautical engineering will eventually merge them into the unique model of the unconventional GRAF structure.

1.4 Research Criteria and Knowledge Contribution

The study and design process has gone through the evaluation of principles and disciplines of different areas of aeronautical engineering.
The author's technical background, together with the literature knowledge and a bit of personal intuition, have all contributed to the development of this novel configuration. The academic depth of the research will be primarily presented through the discussion and presentation of the second, third, fifth and sixth chapters of the thesis, but also through the sense of technical understanding and aeronautical knowledge transmitted by the author via a very conscious communication and presentation of the technical and challenging aspects of such an unconventional design. As already anticipated, there are five novel features purposely designed and introduced with the structure and mechanism of the GRAF concept. The group of five novelties, representing the personal contribution to the knowledge of this area, will be technically discussed in the following chapters. A brief description of the conceptual idea behind each of the novelties is summarised below:

- the 'L-shape stringer' device: used to activate the seamless deformation of the trailing edge panels by converting linear forces in applied bending moments;
- the trailing edge (TE) 'swivel closure' device: designed to keep the TE section sealed, but enabling it at the same time with relative motion of the parts;
- the tubular shaft and the rotating ribs: designed to constitute a compliant structure;
- the fin 'slot-connection': used to augment the fin twist degrees of freedom within a sealed gap configuration;
- the aeroelastic effect technique: the means exploited to allow self-adaptive behaviour of the GRAF tail for control and stability purposes.

This thesis aims to present clearly the technical details of this study and the development process conducted during the GRAF design research. The exploring and learning path followed by the author during the doctoral study is clearly outlined and reflected in the five phases listed below:

- Observe and describe;
- Predict;
- Explain;
- Bridging the gap (literally!);
- Constructive comments and criticism.

The first objective on the list – observe and describe – considers the background of the research area, the knowledge of the student and his capacity for finding out what is missing from other previous researches. The second point refers to the skills and intuition in understanding and completing the different stages of the research process. At this stage, the aim and objectives of the study are defined. The third phase – explain – aims to describe the methodology and theories used to approach the study and the resolution of the problems. Next is the analysis of the outcomes related to the applied solutions and innovations which, within an enhanced level of scientific consciousness, knowledge and technical experience, try to bridge the gap between the past and the future of the research. The final point emphasises the last phase of the study when the researcher must objectively claim and judge the benefits, advantages, flaws and drawbacks of his accomplished study. This philosophy has been followed by the author to guide his learning path during the past years of research, reflecting the more specific advice expressed by Phillips and Pugh [138] in their "how to get a PhD" treatise. They advise on how to manage a doctoral research from the perspective of both student and supervisor, giving some indications about what can be recognised as a scientific way of conducting the research and contributing to the knowledge in any particular research area. Listed below are the most remarkable points from their research criteria understanding, which have been purposefully selected and reported in this paragraph to outline the model upon which the project study and this dissertation have been based, conducted and built. The key points of the PhD research criteria are:

- Providing a single, original technique, observation or result in an otherwise unoriginal but competent piece of research;
- Using already known material but with a new interpretation;
- Trying out something in this country that has previously only been done in other countries;
- Taking a particular technique and applying it to a new area;
- Being cross-disciplinary and using different methodologies;
- Looking at areas that people in the discipline have not looked at before;
- Adding to knowledge in a way that has not previously been done before.

These guidelines tautly embody the characteristics of what has been enclosed in the core of this research study and presented in the next chapters of the thesis. All of those points are touched on by the content of this doctoral study. Some of them truly embrace the author's approach and philosophy to this research project. In particular, the fourth and sixth rules perfectly apply to the specific research study. Additionally, the fifth point describes what the foundation and skeleton of this research are. This research study has not only focused on one specific subject. It has been developed as a "symphony" of multi- and cross-disciplinary methodologies and analyses aimed at achieving the final design result which was eventually obtained throughout a long and rewarding scientific growth and learning experience of a PhD student.

1.5 Thesis Lay-out

This doctoral dissertation embodies eight chapters to describe the learning, studying and developing phases of the aeroelastic fin research project.
In detail, these introductory paragraphs, are part of the first chapter dedicated to the general overview of the thesis. **Chapter 1** encloses a brief history of aviation and the background of this particular research area. Before concluding with the thesis lay-out, it presents a preliminary description of the research with the aim and the

objectives of the project. **Chapter 2** opens with a section introducing the Literature Review. It will discuss several aspects of such a complex aeroelastic design and will present different concepts and applications for classical and unconventional fins. The chapter begins with an aerodynamic section dedicated to presenting the benefits and advantages of seamless and gapless designs. It will show different concepts applied on diverse aircraft used to vary the aerodynamic performance according to the flight circumstances. It will also discuss various structural solutions adopted in the design and assembly of aircraft fins, presenting the variety of unconventional designs based on morphing structures, smart materials, and smart actuation systems. The section will describe the specific sector of the morphing technology dedicated to describing the studies and projects related to the aeroelastic effect technique based on the warping theories also introduced at the end of the chapter.

Chapter 3 is the most theoretical and analytical part of the thesis where methodologies, theories and tools are applied and discussed for the design and modelling of the GRAF. It describes the process followed to conduct the study from the simple concept idea to the more complex finite element (FE) models and manufacturing of prototypes. This chapter will also present the technical novelties introduced with the novel empennage design.

All these principles and methods presented in **Chapter 3** will then be proven and demonstrated through the presentation of the results in **Chapters 5** and **6**. Within these two sections the final numerical results will be discussed.

Between the methodology and results Chapters (i.e Chapter **3**and **5** respectively), **Chapter 4** contains the part of the thesis entirely dedicated to the conceptual design characteristics of the aeroelastic warping fin. A brief description of the fin operating modes and the description of the selected case study will open the first paragraph. The chapter will continue and conclude with the technical description of the final version of the GRAF fin assembly and its components.

Chapter 5 will complete the technical description of the GRAF design by presenting the results of the loading action investigation and linear static finite element analysis (FEA). This section will also discuss the flight performance results of the novel configuration. The directional derivatives attained from the stability and controllability analysis will be presented at the end of the chapter and compared to

the baseline reference values of the chosen case study. In **Chapter 6** is listed another set of results, this time based on unsteady aerodynamics and aeroelastic dynamic analysis. The section is comprised of the static and aeroelastic studies of divergence and flutter analyses, and aeroelastic dynamic response analysis. A series of tables and diagrams will present the results attained to assess the structural safety of the GRAF design under dynamic conditions. As an adjunct to the aeroelastic instability investigation, the aeroelastic frequency and gust response analyses of the novel fin design will also be presented.

Chapter 7 will give a better view and clearer idea of what such designs should look like, by presenting a description and footage of the GRAF - MT4 fin prototyping. The ribs and skin manufacturing process, together with static deflection tests, and the fully assembled design will be presented. A brief description of the manufacturing and moulding techniques used to build the model will also be discussed.

Finally, the concluding part of the thesis is presented in **Chapter 8.** It will contain the final comments and general discussions which will conclude this thesis by presenting a list of achievements, missed objectives, limitations of the design and future developments of this research study.

Chapter 2 - Literature Review

2.1 Chapter Introduction

This chapter of the thesis introduces the several areas of aviation technology investigated for the study and design of the aeroelastic rudderless fin. This section is subdivided into four categories. The different research areas will review and consider the primary aspects of this research by discussing studies, theories and projects conducted during the past up and to the present time about:

- Flight mechanics and aerodynamics: in particular, directional stability and control;
- Fin structure designs and materials;
- Morphing technology application for enhanced flight performance;
- Warping systems: torsion theory and aeroelastic effect-based concept designs.

The literature review opens with the first section entirely dedicated to the flight performance and requirements description of the specific directional stability and control tasks demanded for vertical empennages. The first section also explores the aerodynamic benefits of seamless configurations with sealed gaps. The second part of the chapter presents diverse typologies of fin layouts and materials applied to the design and construction of vertical tailplanes either for classical or unconventional designs. Conventional composite and smart materials are listed. The third section discusses concepts and designs, whose characteristics rely on compliant structures and morphing technologies. This part of the literature review focuses on those concepts which potentially allow novel ways of enhancing flight performance and controlling aircraft flight attitudes without using classical hinged command surfaces. The chapter concludes with a description of torsion and warping theories and their

innovative exploitation and application through aeroelastic effect-based designs for more manoeuvrable and performing aircraft.

The reader will notice that the majority of the projects and models discussed in the following paragraphs are predominantly related to horizontal wing structures rather than vertical tails. A very small percentage of the studies refer to unconventional vertical tail projects. The main reason is that up to date**,** classical fin-rudder constructions are very cost-effective and reliable configurations when compared to novel unconventional fin designs. The currently used fin-rudder configurations have very simple designs, optimised under the perspectives of structural layout, weight, system complexity, actuation, manufacturing and maintenance costs. Heavier, novel and more complex empennage versions, also based on morphing technologies, made engineers realise that although enhancing the performance, the advantages of their application if compared to the costs and complexity of such unconventional designs, might not be worthy of any novel change. Hence, engineers and designers kept vertical tailplane designs almost unchanged for decades. They, instead, focussed their attention mainly on more applicable and exploitable smart wing structures rather than empennage design.

2.2 Aircraft Lateral/ Directional Stability

Manoeuvrability, comfort, navigation, and capability to stabilise flight attitudes against lateral gust and side wind circumstances, are all essential requirements demanded of vertical empennages on board any type of aircraft. Lateral/directional stability and control authority are fundamental requirements that must be guaranteed in any flight condition. In the history of military and commercial aviation only two types of vertical empennages went into a production series:

- fixed fins with hinged rudders;
- all-moving (slab) tails.

The CAD illustrations of Figure 2-1 show both concepts.

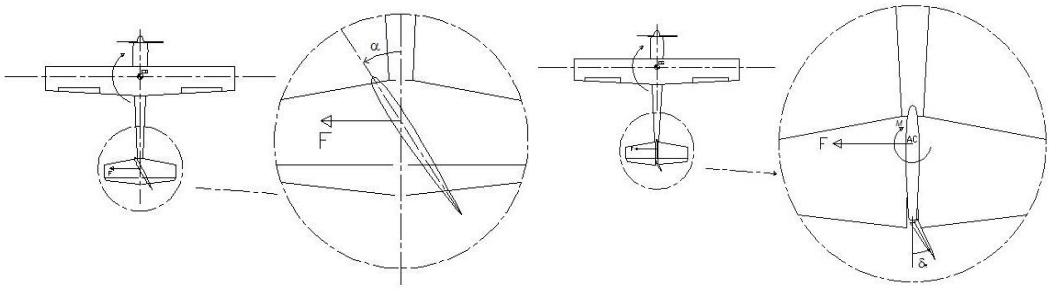

Figure 2-1 CAD illustration of all-moving tail and hinged rudder variant

The fixed fin and movable rudder are the two elements constituting the vast majority of vertical tailplanes used to date on either military or commercial aircraft. Their assembly works as a whole rigid, aerodynamic surface providing the aircraft with the required directional stability and authority in control via rudder deflection, when requested. The all movable fin, instead, wholly rotates around a pivoting boom to act in control and stabilise in-flight manoeuvres. All vertical tails have structural and aerodynamic characteristics identical to those of wings. The only exception with respect to lifting surfaces is that, when at zero angle of incidence, the empennage's symmetric profiles do not generate any lift unless an external factor changes their neutral angle of attack or their camber line. The lift generated by the fin airfoils lies on the horizontal x-y plane and is properly named after the vertical empennage's purpose as the *side force*. However, both definitions will be used in the thesis for the explanation of the aerodynamic and aeroleastic phenomena. When flying in straight level flight, the fin's symmetric sections produce only drag force. Only when in the presence of a cross wind component, or following a rudder deflection or whole tail rotation, does the fin start generating side force and the corresponding yawing moment.

The fin side force generates the yawing moment with respect to the aircraft centre of gravity (CG). It tends either to naturally restore the aircraft by heading into the relative wind direction or to orient the aircraft nose in the desired direction. The vertical tail represents the only element on board aircraft that can properly control and stabilise the directional attitude of the airplane. The most important directional stability effect performed by the whole fin is the *weathercock effect*.

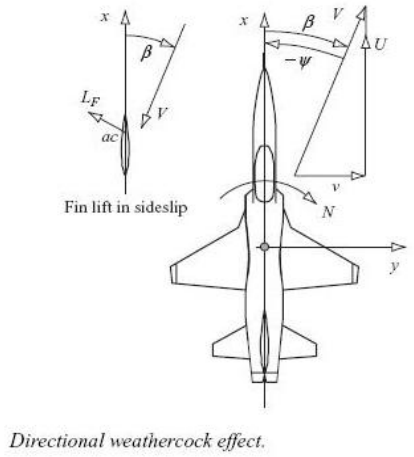

Figure 2-2 Stability weathercock effect description, Cook [48]

As described by Cook in his "Flight Dynamics Principles" [48], and illustrated in Figure 2-2, the weathercock effect is the natural tendency of the aircraft to generate a yawing action able to restore the original stable and level flight attitude which the vehicle had before a lateral disturbance occurred. Its effect can be substantially augmented if used in combination with rudder deflection, as is usually done for trimming conditions.

Vertical fins also affect the lateral controllability and stability of an aircraft. Fins play a key role in the rolling motion of the aircraft by either damping or exciting such out-of-the-wing plane manoeuvres. A few notes about this type of lateral-directional interaction will be discussed in the methodology chapter. However, for the purpose of the study only the directional effect will be taken into consideration in this research.

Since the very first stages of aircraft design, the size and position of the vertical tail play a key role in ensuring the lateral/directional stability and control of the vehicle. As discussed by Roskam in [150], and Stinton in [168], they are fundamental aspects which can sensibly affect the flight performance of an airplane. The horizontal and vertical tail configurations must be integrated with the structural and flight dynamic features of the vehicle at the early stages of the conceptual design.

The importance of the rear location of the vertical empennage on the aircraft is to make the stability and control actions more effective and responsive. The longer the distance between the fin and the aircraft CG, the longer the moment arm in between

the two points, i.e. the 'x_v' line indicated in Figure 2-3, and thus the more effective the yawing moment generated by the side force applied on the fin CP. That arm length is one of the components directly influencing the aircraft yaw either for stability or control circumstances.

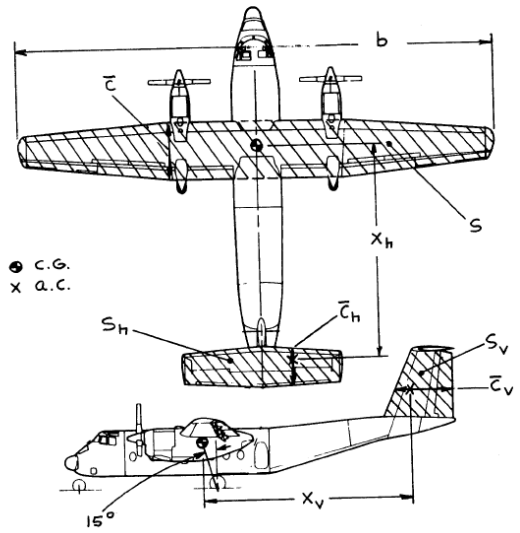

Figure 2-3 Generic aircraft parameters and dimensions, Roskam [150]

The 'x_v' parameter is usually taken into account in the preliminary design phase via the tail volume coefficient V_V definition, as follows:

$$V_V = x_V S_V / S_b \qquad (2.1)$$

where S_v and S_b are the fin and wing areas respectively. Once the tail volume coefficient has been determined, then the designer's attention can focus on other detailed aspects of the empennage design, such as the geometric shape and the profile of the airfoil sections. There are three key aerodynamic aspects which can be identified as mainly responsible for fin performance: camber line, aerodynamic centre (AC) and the angle of attack of the fin airfoil sections. Roskam [150] and Katz and Plotkin [103] in their textbooks help clarify their aerodynamic importance and definition within a more detailed and theoretical approach. The airfoil section's aerodynamic centre is that particular point about which the pitching moment coefficient remains invariant when the angle of attack changes. It totally differs from the centre of pressure, defined as the point at which the resultant of the aerodynamic forces acts on the airfoil. In the particular case of vertical empennages, built

exclusively with symmetrical sections, the two points are coincident. That means the lift or side force can be generated only by a change of speed and angle of attack, unless any control surfaces are deflected, by altering the profile camber. Conversely, non-symmetric profiles, instead, present two types of forces contributing to lift generation:

1. basic lift distribution: depending on camber;
2. additional lift distribution: depending on angle of attack.

All classes of fixed wing aircraft possess symmetrical fin shapes. Only one type of rotary wing machine, namely the helicopter, has asymmetric profiles built into their vertical tails. Their scope is just to generate asymmetric side force to counteract the torque effect of the main rotor in flight if the helicopter is not provided with coaxial or counter-rotating main rotors.

The aerodynamic centre location for conventional airfoils is located at the 0.25c point. It moves very little in subsonic regimes, while in transonic and supersonic conditions it tends to shift rearwards, even up to 0.5 chord point. That transition is positively exploited by means of the aeroelastic effects generation, by an all-moving tail to increase efficiency and stability at high flight speeds. Those configurations, by having the application point (i.e. the AC) of the aerodynamic forces located behind the pivoting boom, normally fixed at 0.3-0.4c, can control and reduce divergence and rotational instabilities phenomena when such tails are operated at high speeds. That is one of the main reasons that led certain types of supersonic jets, like the SR-71 and TSR2 (Figure 2-4), to adopt all-movable surfaces, either for horizontal or vertical tailplanes. The all-moving tails are more stable and effective to trim the rearward shift of the airfoil section aerodynamic centre that occurs at supersonic velocities. The rearward shifting of the centre of pressure, behind the fin pivot point, allows the aerodynamic forces to create a moment that tends to restore the neutral position of the tail when displaced. Conversely with the CP in front of the pivoting point, the effect of the side force will generate a diverging phenomenon. In this case, that condition will keep increasing the angle of rotation leading to potential structural failure.

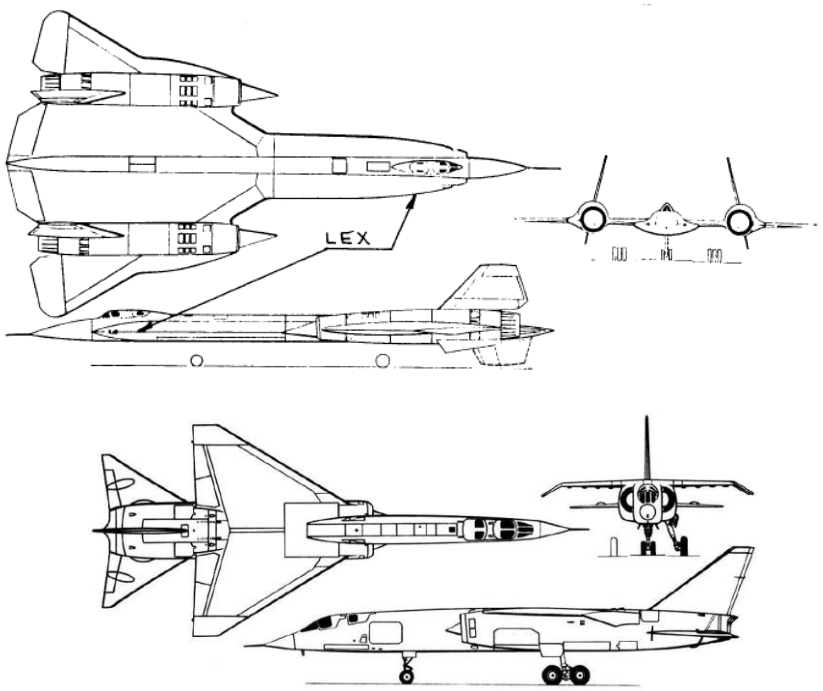

Figure 2-4 SR-71 and TSR2 aircraft with all moving fins [150]

Additionally, in conventional configurations, because of the high supersonic speeds, it was also discovered that the presence of rudders with hinges and gaps could cause severe local heating problems. Moreover, owing to their improved aerodynamics, all moving surfaces were generating less drag than larger fins with hinged rudders, therefore were applied on board sophisticated and high performing aircraft. However, at transonic speeds the AC can suddenly change locations. This occurs because of the aerodynamic interactions between shock waves and boundary layers. In the case of horizontal tailplanes, it can vary the pitching attitude of the aircraft and turn to a degenerating effect of unstable flight attitude if uncontrolled – and the same could happen with vertical tails. This phenomenon, generally called 'tuck' has been attempted to be avoided by modern fly-by-wire control systems.

Let us now introduce the phenomena and variables governing the aircraft flight mechanics for directional attitudes, but only for subsonic regimes. For the purpose of the study, the aerodynamic resultant will be retained to be applied to the aerodynamic centre of the airfoil sections. Generally speaking, the results can be decomposed into two component forces, lift 'L' and drag 'D', and one pitching moment 'M'. Each is respectively characterised by three non-dimensional coefficients: C_L, C_D, C_M. In particular, when discussing of vertical empennages

rather than horizontal wings, the nomenclature can differ slightly. The lift on a fin surface is conventionally referred to as *side force* 'Y' *or* 'F_Y', and the pitching moment as *yawing moment 'N'*, together with their respective non-dimensional coefficients C_Y and C_N. The drag force, instead, keeps the same definition for both applications. It is referred to as longitudinal drag, indistinctly generated on the same plane by all aircraft components. Although the different terminology used for forces and moments on vertical tails has been introduced, the principles and aerodynamics are practically identical.

The vertical tail tasks and *modus operandi* can be distinguished as follows:

1. Mode 1: Stability;
2. Mode 2: Controllability (Control Authority);

The first mode is inherent in the autonomous task and natural behaviour of the fin, whose geometry and aerodynamic shape are specifically designed for. The second mode, instead, refers to the artificially activated fin deflection operated by mechanical input sent from the pilot of the flight control system (FCS) in order to generate the side control effect needed to manoeuvre the aircraft in case of upsetting flight attitudes or when rapid or very effective heading corrections are needed. At that very moment when the asymmetric aerodynamic pressure distribution is created over the fin surface by a side wind circumstance or an FCS surface deflection, then the aircraft engages the yawing manoeuvre. Conventionally, there are two parameters used to estimate the effectiveness of the aircraft flight performance related to fin directional tasks. These two parameters are the *directional stability derivative* and the *directional control power derivative* of the airplane [54, 57], respectively expressed as:

$$C_{N_{\beta V}} = C_{L_{\alpha V}} \left(1 - \frac{d\sigma}{d\beta}\right) \eta_V \frac{S_V x_V}{Sb} \tag{2.2a}$$

$$C_{N\delta_R} = C_{L_{\alpha V}} \alpha_{\delta_R} \eta_V \frac{S_V x_V}{Sb} \tag{2.2b}$$

in which the quantity $\frac{S_V x_V}{Sb}$, as introduced at the beginning of the chapter, is the volume coefficient of the vertical tail, σ is the side wash coefficient, β the sideslip angle and $C_{L\alpha V}$ is the lift slope curve of the fin profile. Besides playing with the parameters of equations (2.2a - b) to increase fin stability effects, on subsonic aircraft it is more likely to find simple dorsal arrangements mounted on the fuselage body and integrated with vertical tail structures. They are normally installed in front of the fin leading edge as a forward extension of the root section of the empennage used to delay and avoid the fin stalling, caused by the aircraft's high angles of incidence or upsetting manoeuvres and to offer a larger lateral surface area to side wind circumstances.

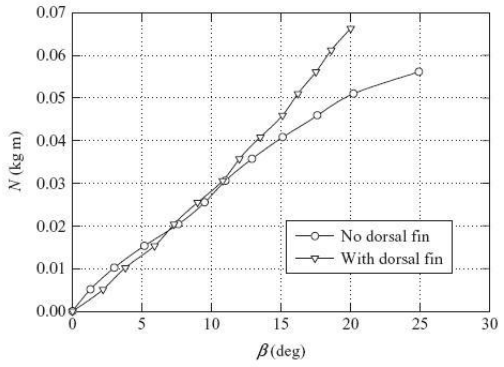

Figure 2-5 Flight dynamic effectiveness of dorsal elements, [48].

As shown in Figure 2-5 for the yaw moment plot by Cook, the dorsal fin element included on aircraft enhances the yaw effect in large sideslip angles. In this particular case, the diagram refers to a small wind tunnel test model aircraft subjected to different side slip attitudes.

2.3 Gapless layout for seamless command surfaces

This section introduces the second part of the literature review which starts uncovering the enhanced performances that gapless, morphing and novel

configurations might give to future aircraft designs. Recent trends in aviation and eco-sustainable researches have encouraged engineers to study new forms of more efficient and streamlined designs for next generation airplanes. As said before, the main objectives are to enhance flight performance, to increase the payloads and the number of passengers, and take into consideration greener targets such as noise reduction and fuel consumption. All projects are inspired by more demanding military needs and by greener next generation aircraft targeting more environmentally friendly scenarios, as discussed by Peeters in [135]. Engineers soon discovered the beneficial effect of the aerodynamics given by the sealed gap versions of wings and control surfaces. Sealing all the gaps between the wings' and tail's command surfaces would considerably enhance the aerodynamic efficiency of the whole aerodynamic section. Hence, engineers started concentrating their attention on designing structures with minimised gaps between components, and even with entirely closed ones. A singular treatise, collecting important information on how gaps can influence aerodynamics, and particularly the drag coefficient, is contained in the ESDU report No. 92039 [54, 55, 57, 58]. That study is the follower of several preceding reports published by the National Advisory Committee for Aeronautics (NACA) on theoretical studies and wind tunnel experiments conducted on different NACA series profiles to assess their aerodynamic characteristics with sealed and unsealed gaps. Those reports, collected in references [7, 32, 94, 164, 165], studied generic airfoil sections with and without hinged flaps combined with the use of tab sections. They investigated the consequences of having spanwise gaps separating the fixed section of the profile from the movable flap. The observed effect of those types of gaps, reported in both ESDU and NACA data collection, was seen as generating a loss of overall lift and an increase in the nose-up pitching moment of the tested profiles. Nonetheless the following remarkable effects were noted:

(a) an increase in drag,
(b) an increase in angle of attack at zero lift,
(c) an increase in pitching moment at zero lift,
(d) a slight decrease in lift-curve slope,
(e) a minor forward shift in aerodynamic centre position.

It transpires that there are several valuable reasons to “bridge” those gaps, especially from beneficial aerodynamic and flight mechanic perspectives. In the specific case of the GRAF research, the first and fourth points are the most important issues worth being improved with the novel features of the aeroelastic tail. Sealing the gaps is not only advantageous for reducing the drag force; other benefits include: the reduction of control-surfaces actuation force, hinge moment coefficients, increase of lift coefficient, enhancement of stealth capability, and benefits in military applications too. As Sears in [155, 156] examined in his work the effect of the flap nose shape and the relative gap distance of a test-wing. He found that blunt nosed shapes for flaps rather than sharp ones, as shown in Figure 2-6, were alleviating the pilot from excessive stick forces necessary to control and rotate the mobile parts in flight but, nonetheless, were improving its effectiveness. As the taper of the flap nose was increased, the profile drag coefficient increased. Moreover, closing the gap was found to be enhancing the control effectiveness and delaying flow separation over the flap, thus further reducing the overall drag.

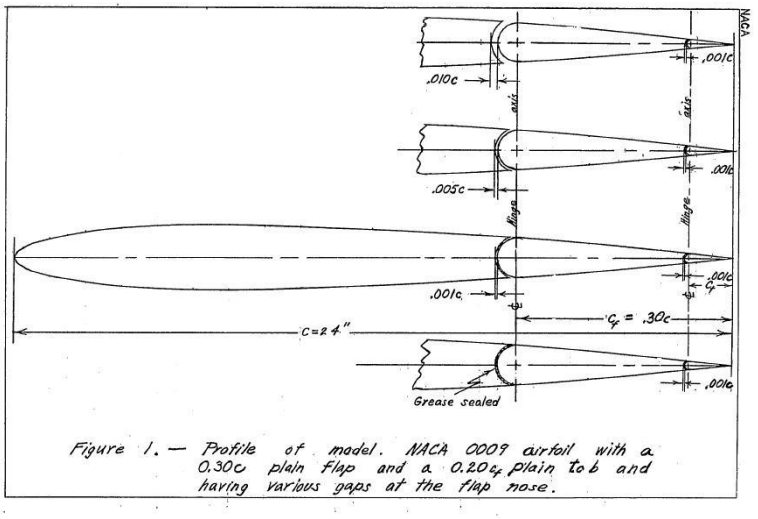

Figure 2-6 Sears’ test flap configuration [155].

Jones *et al.* in 1942 [102] and Hoggard *et al.* in 1944 [94] proved that surface continuity coupled with a sealed gap configuration alleviates the entire surface from excessive hinge moments during large flap deflection. That also contributes to distributing more uniformly the aerodynamic pressure over the wing surface. Those aerodynamic benefits were assisted by the combination of sealed joint layouts and

bevel shaped TE sections. In addition to those aerodynamic advantages, there are also structural benefits resulting from sealed configuration adoption. Lower and more uniformly distributed load pressure helps reduce the structural stress level at the hinge line connection. Thus the volume of material necessary to resist the loading actions can be reduced. Thereby, lighter structure versions may be designed. One of the most important NACA documents explaining the reasons for this challenging race towards sealed gap designs is enclosed in Spearman's work [164, 165]. He carried out a series of studies on a symmetric airfoil section, NACA 0009 with hinged 0.25c flap, for both sealed and unsealed gap configurations, and varying gap distances. He proved the benefits of the sealed variant which positively enhanced the $C_{L\delta}$, C_{La}, and a_{δ} coefficients of the aerodynamic surfaces. He also tested different combined versions of deflected flap and rotated tab surfaces, demonstrating how the tab deflection can further beneficially change the hinge moment effect. That consequently influences the control stick force necessary to move the command surface, helping the surface to displace rather than hinder the rotation. Figure 2-7 shows the airfoil section used for the tests. It was a profile divided into three segments: the leading section, the 25% chord flap, and the tab element. As can be noticed from the figure below, each of those parts was separately adjustable. That profile section, tested in the early 1960s, preceded futuristic cambering devices and conforming structures of modern morphing mechanisms. It was, in a simplistic way, a forerunner of bio-mimetic wing designs.

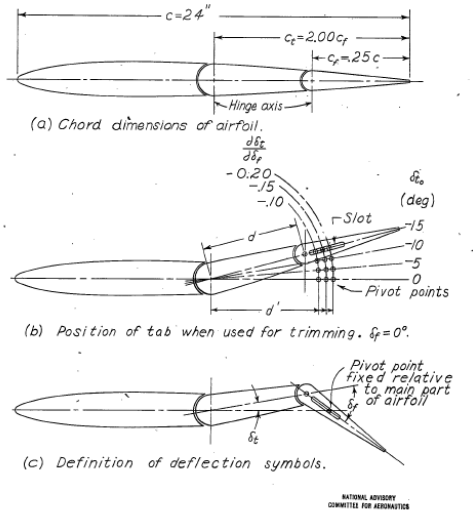

Figure 2-7 NACA wind tunnel variable camber profile [164].

Figure 2-8 shows Spearman's study results of the lift coefficient curves for sealed and open gaps with deflected flap. It can be seen how varying the gap thickness from 0.005c on the left side diagram, to complete sealed configuration on the right one, is raising the curves to coefficient values of 1.4, i.e. approximately 8% more than with an unsealed configuration.

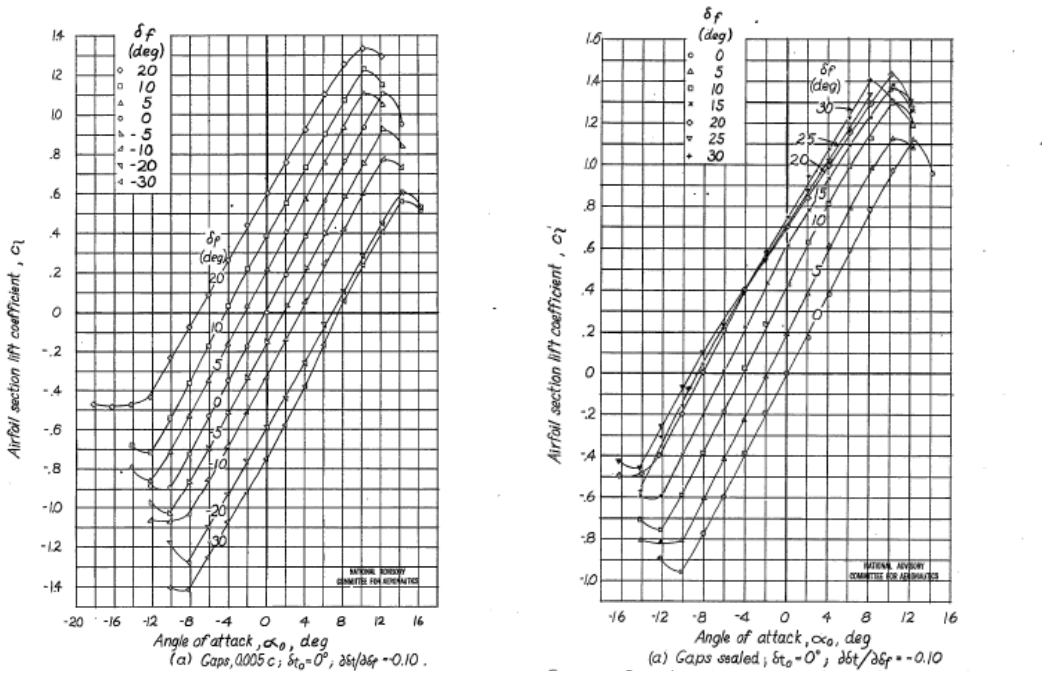

Figure 2-8 Lift coefficient curves for 0.005c unsealed and sealed gap flaps.

The importance of minimising the gaps between parts is also investigated in the work of Campbell *et al.* [42]. They studied the aerodynamic performances and characteristics of low aspect ratio (AR) wings (e.g. typical of fighter aircraft wings and tailplanes), provided with unsealed gaps. Their investigation showed that in order to keep the flow over the wing as smooth as possible and reduce the drag induction over the trailing edge section, the gap must be equal to or less than 0.5% of the overall wing chord. Another similar aerodynamic study conducted after Spearman's wind tunnel tests was that of Martins and Catalano [122] who demonstrated the theoretical efficiency and effect of sealed gaps on cambered profiles on aircraft wings. They studied a gapless variable camber wing configuration, illustrated in Figure 2-9, for a subsonic transport jet aircraft. They evaluated the potentiality of sealed gaps wings for extending flying capabilities such

as range and endurance. They tried to reduce the viscous drag over the wing surface by adopting deformable LE and TE sections, to optimally trim the vehicle for any flight speed. The aircraft's range value, applying only morphing TE, increased by 7%, and further up to 24% when combined with LE activation.

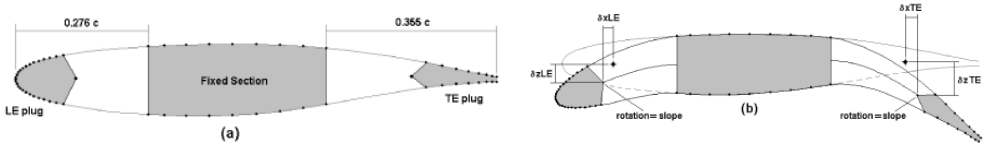

Figure 2-9 Martins and Catalano varying camber profile configuration [122].

They showed how a gapless configuration and a variable camber section can sensibly augment both the profile and aircraft performance. Highlighting the importance of the aerodynamic gaps reduction for enhanced performance and reduced drag is within the work proposed by Lai [107]. He studied how closing the gaps between train cars can reduce energy consumption caused by the consistent gap-generated drag force. He considered how the three effects of gap length, position-in-train, and yaw angle of wind were important factors affecting train aerodynamics and subsequently, fuel consumption. These were different areas of application but with the same shared characteristic parameters and targets of aeronautical research: efficiency. In the same wake, of attempting to enhance aerodynamics and improve flying qualities is the philosophy of bio-mimetic designs. Such configurations inspired by nature and by the ideas of engineers kept developing advanced concepts for more performing designs. Bio-mimetic design represented the foundation of morphing technology and of more efficient designs. The continuous search for optimised performances and more efficient aerodynamics is well synthesised with the Silent Aircraft project. It embraces all the most efficient characteristics and features with which an aircraft might be thought to be designed. Everything is integrated into the united shape of a blended wing body, as depicted in Figure 2-10. As already presented in the introduction chapter, it was developed as a joint project between MIT and Cambridge University, almost a decade ago.

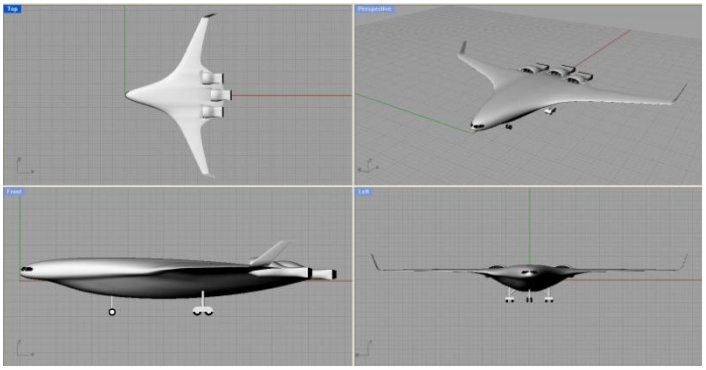

Figure 2-10 Silent Aircraft conceptual design [37].

During this research programme, Hileman *et al.*, evaluated and studied the potential benefits this tailless wing model might gain by adopting such a novel aerodynamic configuration with fewer noisy features. The project was aimed primarily at reducing fuel consumption and giving more comfort to passengers. Their work presented, see references [89-91], discussed the advantages such an all-lifting airframe can potentially give. One of best results showed a reduction of the fuel burn up to a margin of 25%. One of the keys elements enabling these optimistic results was a direct result of the smooth aerodynamic shaping of the central body of the aircraft and also the absence of a big, central, vertical tail. The silent aircraft configuration will also allow lower speeds, up to 28% lower, for the final approach and landing phases than similar sized aircraft, thus contributing to noise reduction when approaching airports, in civil airspace and populated areas.

2.4 Fin Structures

Raymer in his textbook [146] describes and shows several different tail shapes of past and modern aircraft designs, see Figure 2-11. Although some of them present very unconventional forms, they all share the same final scope by aiming merely at controlling the aircraft direction and stabilising its flight attitudes.

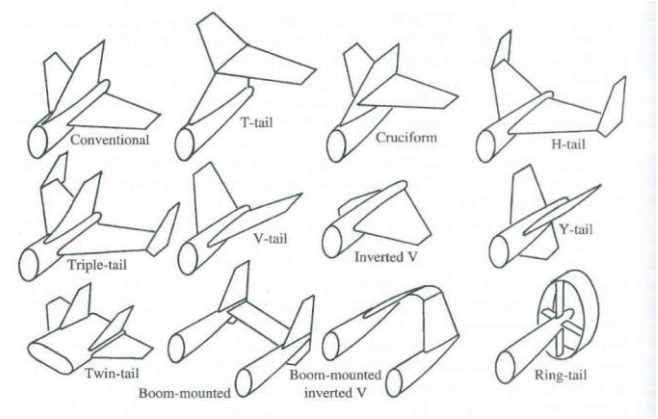

Figure 2-11 Horizontal and Vertical tailplanes configuration [146].

Vertical and horizontal tail structural layouts are similar to those of the wings. Classical fin structures consist of main spars, lightened ribs, stiffened skins and hinged command surfaces. Very few structural exceptions are designed with special configurations in order to better host all-moving gear mechanisms or morphing devices for smart fin variants. Both metallic and composite materials are used for their construction. Aluminium alloy tailplanes mostly rely upon a conventional riveted and stiffened thin skin, with ribs and multi-spar design, while composite versions are normally fabricated into mono-coque shells with a few internal ribs bonded to the skin and a main spar. The typology of their construction also depends on the size of the tail and the manufacturing facilities available to machine it. The majority of commercial airplanes have single mounted fins with hinged rudders. However, there are also cases of aircraft, both in the past of aviation history and in the present day, which have adopted multi-tail configurations. Multi-tail versions are usually associated with multi-engine configurations. The main reason for that is to guarantee satisfactory controllability and stability of the aircraft during critical flight conditions, especially, as may happen, when asymmetric thrust situations due to engine failure occur. The fin on the same side of the flamed-out engine can be properly trimmed to back up the lack of directional thrust and stability. The additional fin allows a more precise handling of the aircraft in an emergency situation. Enhanced authority on multi-fin vehicles is the same reason that justifies twin fins being placed right behind the wake of multi engine wings of the aviation aircraft of the past, as it was in the case of the British World War II bombers Lancaster and Handley Page, the German Junkers, Heinkel and Heishel, and the

American Mitchell B-25 and B-24 Liberator. Those vertical tails, spaced by horizontal tailplanes, were always merged in the engines' wakes. In this way they ensured the greater effectiveness of fins and rudders even at very low speeds, and a prompt response to sudden lateral manoeuvres of the aircraft. Twin fins also help to rapidly counteract, when needed, the massive inertia of large sized aircraft such as the Antonov An-225 Mryia, provided with two of the biggest fins ever built in aviation. There are also other reasons which explain the twin configurations as adopted on the American Grumman F-14 Tomcat and McDonnel\Douglas F/A-18, and on the Russian Sukhoi Su-27/30 and Mikoyan-Gurevich Mig-29 Fulcrum. They are the preferred and more practical designs for those classes of machine that are carried on board aircraft carriers. These are vessels where the height of the carried aircraft is a crucial component to be taken into account in order to allow the parking of the jets inside the below deck hangar, hence the reason for having two small fins rather than a single bigger one. Moreover, because almost all of them are pluri-engines aircraft, the two or multiple fins are very effective in control, in comparison to a single central one.

As already mentioned in the introduction paragraphs, aerodynamic performance reasons have brought engineers to install slab fins on board the Lockheed SR-71 Blackbird, the F-117 Nighthawk and the BAC TSR-2. The SR-71 adopted two canted fins on top of each engine nacelle. The F-117 fins are also canted outwards working as a V-tail. The TSR-2, however, was provided with only one dorsal all-movable fin. Despite the aerodynamic benefits gained from the rearwards shifting of the AC at supersonic speeds, the all-moving options, due to costs and technical complexity, were carefully discarded in favour of conventional fin-rudder versions.

In commercial applications, at present, none of the currently flying aircraft is provided with an all-moving vertical fin, with the exception of the CH-series aircraft produced by Zenith [203]. They are very light aircraft (VLA) for sport/leisure activities and DIY aviation with "all-flying rudders", as termed by their engineers, mounted and pivoted on the fuselage rear end. This all-moving fin, as shown in Figure 2-12, is made by a single main spar and spaced ribs connected together to the boom attachment at the rear section of the fuselage. The whole structure is covered by a very thin skin made of aluminium alloy.

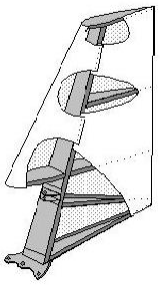

Figure 2-12 Zenith Aircraft all moving rudder design [203].

Figure 2-13 shows other examples of more complex all-moving tailplanes structures. The internal layout is purposely arranged to host the boom components, gears, bearings and spars necessary to form a solid connection with the fuselage attachment. The boom is also the only component used to transfer the withstanding loads of the entire control surface to the fuselage frame. The core structure of such tailplanes can be constituted either by honeycomb elements or by multi-spars and ribs. Foam core is only applied for very small aircraft within the VLA class and for UAVs.

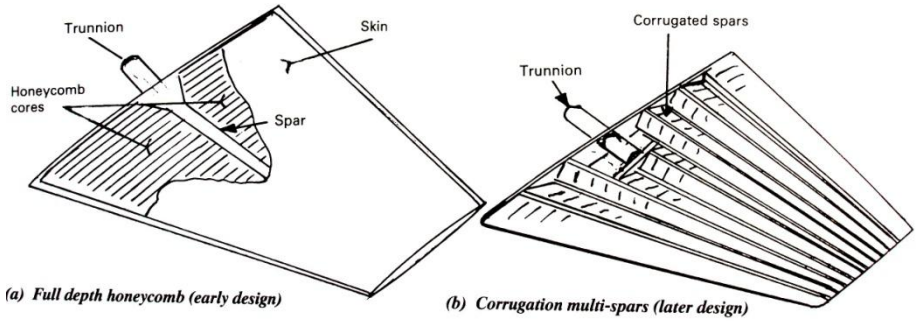

Figure 2-13 Honeycomb and multi-spars all moving tail structure [131].

Conventional empennages, in the majority of aircraft, are exclusively provided with fixed tailplanes and hinged command surfaces on their trailing edge section. They are elevators for horizontal tails and rudders for vertical ones. In both elements there are no extractable or deflectable leading edge (LE) devices such as slats and flaps for wings. Despite the potential gains in performance, the implementation of similar devices on normal tailplanes would not be worth the cost and complexity of designing and operating them on such surfaces.

The internal structure of the empennages, in most cases is based on two main spars. They have all the bending material concentrated in the spar caps and in the built-up

skin panels. Lightened ribs and leading and trailing edges help provide a further reinforcement to the structure. Moreover, they contribute to keeping the fin profile aerodynamic shape unchanged under the action of external aerodynamic loads. Close spaced ribs help stabilise the shape and provide strength to the external skin for torsional and bending loads, in particular to prevent aeroelastic instabilities. The classical layout with one or two main spars intersected by ribs and held together by the covering skin, is the simplest, most cost-effective and reliable empennage design. This layout represents the best compromise of weight, stiffness requirements, and performance. Figure 2-14 shows the vertical tail of a Lockheed L1011 Tristar, designed in the 1960s, with the two key elements, fin and rudder, joined together by hinges aligned across the fittings mounted on both parts.

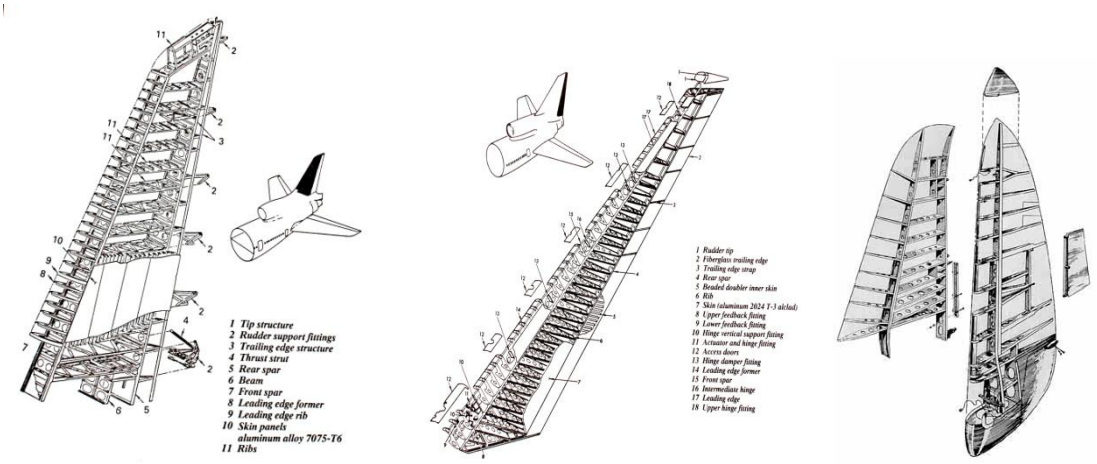

Figure 2-14 L-1011 Tristar (left) and Spitfire (right) fin and rudder components [131].

As can be noted from the figures above, looking also at the Spitfire (1936-1947) tail on the right hand side of Figure 2-14, the vertical tail designs have not essentially changed in decades of aviation history. Fin-rudder construction philosophy has not radically changed during past years; only a few structural modifications have been included to lighten the tail frames. Large use of cut-out elements for ribs and spars, together with the introduction of composite materials, has reduced the weight and manufacturing cost of tail parts. Moreover, beaded and dimpling skins are used to reinforce thinner fin panels and save weight on the tails of small-medium class vehicles. Nonetheless, in order to avoid excessive loads and consequent high stress levels on board large aircraft which will imply stiffer and heavier structures, the solution of using split rudder tails was adopted in most of the larger aircraft that went

into production series. This configuration was designed to prevent excessive loads on hinges at high speeds and avoid instability phenomena on the mobile control surface, such as reversal, flutter and buffeting. With this system the command surface is divided into two sections with a lower and upper rudder section. Both sections are conjunctly used at low speed, but only the lower part provides control authority at high speeds, while the top end is restrained. The reason for that is because the top section, when deflected, might result in being too effective by generating an unbearable loads case scenario for the entire fin structure and thus raising the risk of causing potential structural failures. Stiffness is also a critical issue when T-tail configurations are adopted. Examples of such configurations can be found in the general aviation aircraft Tomahawk, Figure 2-15, in most gliders, either in the modern McDonnel Douglas MD-80series or Learjet and Gulfstream executive jets, or also aboard the grounded and dismissed from service Lockheed F-104 Starfighter. All these configurations require the vertical structure to have adequate bending and torsional stiffness to counteract loads and flutter phenomena due to the interaction of vertical empennage and the tip horizontal surface on top of it. Mounting the horizontal tail and the elevator on top of the fin can significantly vary the torsional frequency of the vertical tail. That causes designers to increase the stiffness of the fin and hence the overall weight of the aircraft structure, resulting in a loss of performance.

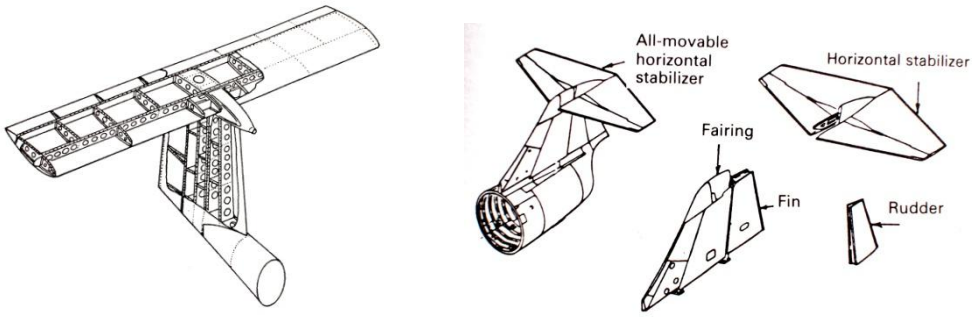

Figure 2-15 Tomahawk (left) [75] and Lockheed F-104 (right) [131] T-tail configuration.

That is the reason why, in such configurations, much thicker airfoil sections are used when those fin versions are designed. Thicker profiles will give higher bending and torsional stiffness qualities which are necessary for dynamic instabilities on these types of tail. One of the advantages of these tail variants surmounted by horizontal tailplanes is hidden in the fact that the fin efficiency is enhanced as a stabiliser.

Despite the added structural stiffness, the T-vertical tail performs much better than conventional tail arrangements. With this configuration, the fin works like an aerodynamic surface between two endplates, the horizontal tailplane and fuselage, reducing extremities drag and enhancing its aerodynamic effectiveness.

2.5 Conventional and unconventional materials

The first aircraft in aviation history were built using wooden frames, steel tubes and fabrics to make cladding suitable to generate lifting forces and withstand loads in flight. Evolution and progress in materials and structural design enabled engineers to modernise those configurations by adopting new aluminium and titanium alloys, and lighter composite material laminates. They also made use of hybrid combinations of composite layers and aluminum sheets as lately successfully applied in hybrid metallic-composite layouts embedded into the technological uniqueness of the GLARE [185, 187]. That is the benchmark hybrid material in modern aircraft production, well represented by the Airbus A-380 fuselage structure.

Going back to the origins of aviation history, and the need for several more and bigger airplanes, has pushed engineers to seek building methods and materials which would lend themselves better than wood and tubes to manufacture stiffer parts of airplanes, by means of relatively easy and quick tooling machines. Thus, configurations in aluminium alloys and other metals started to be created. At the beginning hybrid designs, with a combined usage of wooden and metallic parts were produced, such as those seen on the Hawker Hurricane, the Boeing series of the B-24 and B-17, and the British Avro-Lancaster. It was mainly the advent of jet engines that prompted engineers to design full metallic airframes for more solid structures. Materials and design philosophy have evolved up to the present day, when the large use of composite materials seems to be the latest challenge for modern aircraft projects. The major benefits of composite materials are addressed by the best combination of lightness and mechanical characteristics. This feature has enabled

designers to reduce the Maximum Take-Off Weight (MTOW) of aircraft while increasing their payloads and performances [130].

2.5.1 Composite Materials for Aircraft Structures

Although aluminium- and titanium-based metallic alloys represent very effective materials for aircraft structural applications, their role is going to be overtaken by the exponentially growing market of composite materials. As anticipated, the success of composites is decreed by the low weight-to-stiffness ratio compared to conventional metallic ones. Figure 2-16, from reference [177], shows an example of the growth of composite materials usage in the aviation industry. In this particular case the figure represents the composites evolution in the design philosophy of Boeing over the last four decades. As it can be noted, only 1% of composite materials were used on the B-747 in the 1970s, whereas the same percentage increases up to 50% on board the modern B-787s.

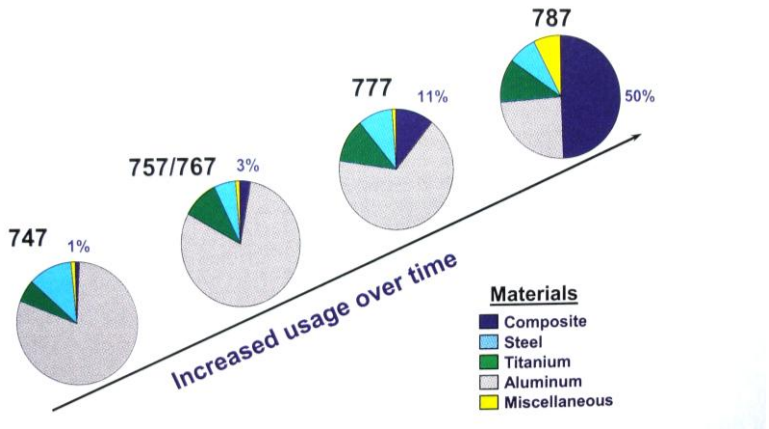

Figure 2-16 Use of composites in aviation [177].

Another illustration, Figure 2-17, shows the last version of the McDonnel Douglas F/E-18 Hornet. Shaded in dark grey are the parts made in composites. They cover almost 50% of the whole aircraft surface. The most used composite compounds are based on carbon, graphite, kevlar, boron, and glass fibres. Amongst them, the most versatile and widely used of those reinforcements in aviation industry is the carbon

fibre. Despite the cheaper and modest mechanical properties of glass fibres, which are largely used for interiors of fuselages, radome cones, and both nose and tail fairings, the carbon fibres, although more expensive, exhibit more efficient and effective properties for structural parts.

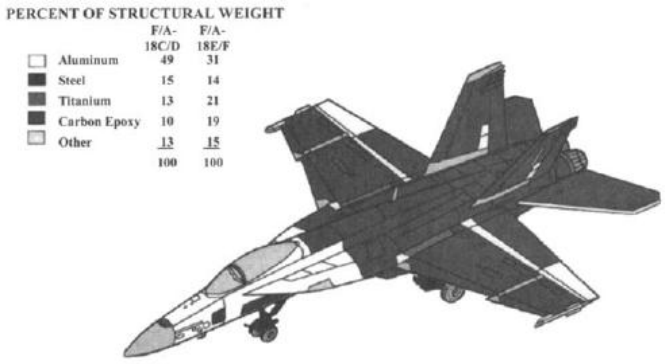

Figure 2-17 Use of composites on Boeing F/A-18E Hornet [13]

Collimated, yarn, and pre-impregnated tapes and cloths are available for any type of production. In order to be completely effective and properly performing, fibres must be integrated within the matrix. Resins, plastic materials, metals and ceramics-based matrices are used to interconnect the fibres together into a firm compound. Among them, the most used matrices in aviation are within the thermoset category of the epoxy resins. Thermosetting polymers will also be the class of matrices considered for this project. Thermoset matrices undergo a chemical reaction by the action of heat. They develop a well-bonded three-dimensional structure upon curing. As described by Baker in [13] the matrices help the fibres form the shape of the final component, provide additional stiffness and transfer the loads. They also separate the fibres from each other to avoid fibre failure propagation. The most used and effective matrices are based on:

- Epoxy resin: good mechanical properties and chemical resistance with excellent adhesion to fibres;
- Polyester resin: it offers a lower cost option than epoxy, modest mechanical properties;
- Polyamides resins: good mechanical properties and stability at very high temperatures;

- Phenolic resin: mechanically not as excellent as epoxy, it offers good moisture and chemical resistance;
- Thermoplastic matrix: they can be easily reprocessed or reconsolidated during the manufacturing phase; lower elastic modulus, usage suitable for non-structural part applications.

Matrices also preserve and protect the fibres from the external environment. Matrix-dominated properties are related to temperature and environment resistance, and also give longitudinal compression, transverse and even shear strengths. But at the same time, the matrix can be brittle and weak for tensile stresses, whereas the fibres, being able to carry out the job in a tensile stress direction, enable the material to resist bending and traction solicitations. The fibres, primarily responsible for strength and stiffness of composite structures, are generally produced in a circular cross-sectional shape, and grouped in filament, yarns, tows and fabrics. Yarns, fibres and filaments can be interlaced together to constitute fabrics of different thickness and density. The variety of fibres available for aeronautical application is listed as follows:

- Fibreglass: low cost, medium-light weight and high strength properties. The E-glass type has high strength-to-weight ratio and good resistance to fatigue; the S-glass version has improved compressed strength and up to 40% higher tensile strength;
- Kevlar fibre: very high toughness, stiffness and high tensile strength properties, good capacity of energy absorption under impact;
- Carbon (or Graphite) fibers: they differ exclusively for the percentage of pure carbon particles in each fiber. It is 93%-95% for the carbon ones, and above 95% for the graphite fibers. They have high strength-to-weight and stiffness-to-weight ratios;
- Boron fibers: despite the higher tensile strength and final lightweight product output, they have high costs and larger fibre diameters.

Generally speaking, indistinctly from the matrix and fibre types, all composites design processes should follow the basic design practices suggested by Beckwith in [20] and listed in Table 1.

Table 1 - Beckwith's rules for composite design [20]

Composite Practice	*Reason Applied*
• Try to employ "Balance" and "Symmetry" whenever possible	• Minimizes value of "B-matrix", avoiding bending, coupling, warping and twisting effects
• Avoid stacking too many plies all at one angle	• Delamination and residual stresses more likely if not avoided
• Add fabric ply to inner or outer layer	• Fabric ply can absorb more impact damage as well as minimize drilling "breakout" for holes
• Add ±45° plies with at least one pair on laminate extremes (except for specific designs where bending loads require 0° or 90° outer plies (moments)	• Increases buckling for thin laminates as well as better damage tolerance
• Use larger fraction of +/- plies in shear regions	• Shear loads are best handled with additional +/- plies in a structure
• 0°/90°/±45° laminate with minimum of one layer in each direction	• 0° layers for longitudinal loads • 90° layers for transverse loads • ±45° layers for shear loads • Makes it "quasi-isotropic" as well
• A +45° and -45° ply are in contact with each other	• Minimizes interlaminar shear
• 45° layers are added in pairs (±45°)	• In-plane shear is carried in tension and compression in the 45° layers
• Minimize stress concentrations	• Composites are essentially elastic to failure
• Maintain a homogeneous stacking sequence by banding several plies of the same orientation together	• Increased strength achieved
• Minimize fiber orientation angle between adjacent plies	• Reduces free-edge stresses (delaminations) • Avoids microcracking – particularly for cryogenic or wide temperature excursion applications

A classification of diverse structural theories is expected when the study and analysis of composite laminates is approached in a research project. As Reddy presents in his textbook [148] diverse methodology can be listed, as:

- Equivalent single layer (ESL) theory:
    - Classical laminated plate theory;
    - Shear deformation laminated plate theory;
- Three-dimensional elasticity theory:
    - Traditional 3-D elasticity formulations;
    - Layerwise theories;
- Multiple model methods.

The theory most often applied for composite laminate is the ESL. It is derived from the 3-D elasticity theories by simply adapting the assumptions concerning the stress state and the kinematics of deformation through the thickness of the laminate, to composite materials, thus allowing the reduction of the problem from a 3-D to a 2-D problem. In this way it will be dealing with simple 2-D plates rather then modelling

each layer as a 3-D solid. The ESL theory, presented in the next chapter and also applied to this research study, is based on the assumption that the field of stresses or displacements can be expressed by a linear combination of unknown functions such as:

$$\varphi_i(x,y,z,t) = \sum_{j=0}^{N} (z)^j \varphi_i^j(x,y,t) \tag{2.3}$$

where φ_i represents the ith component of stress or displacement in the plate coordinates, with φ_i^j functions to be determined according to the considered field.

The simplest ESL theory is the classical laminated plate theory which, by extending the assumptions of the *Kirchoff's* classical plate theory [75] to composite plates, can express the displacement field as :

$$\begin{aligned} u(x,y,z,t) &= u_0(x,y,t) - z\frac{\partial w_0}{\partial x} \\ v(x,y,z,t) &= v_0(x,y,t) - z\frac{\partial w_0}{\partial y} \\ w(x,y,z,t) &= w_0(x,y,t) \end{aligned} \tag{2.4}$$

while the first-order shear deformation theory is based on the displacement field

$$\begin{aligned} u(x,y,z,t) &= u_0(x,y,t) + z\phi_x(x,y,t) \\ v(x,y,z,t) &= v_0(x,y,t) + z\phi_y(x,y,t) \\ w(x,y,z,t) &= w_0(x,y,t) \end{aligned} \tag{2.5}$$

where ϕ_x and ϕ_y represent the rotation about the *x* and *y* axes. The main difference with the previous theory is in the assumption that includes a transverse shear deformation in its kinematics, while the first model theory neglected any transverse shear effects. That is the theoretical model applied to this study.

Composites can be classified as anisotropic, monoclinic, orthotropic, transversely isotropic and isotropic.

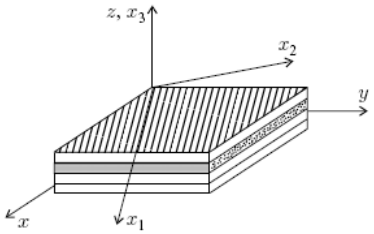

Figure 2-18 Lamina global (x,y,z) and local (x1, x2, x3) coordinate systems [104].

From the general expressions of the stiffness and compliance matrices of an anisotropic composite, it is possible to extrapolate the characteristics and definitions of the other system configurations, as listed before. Monoclinic materials are defined when the fibres are aligned to a symmetry plane; whilst orthotropic materials are normally defined as such when there exist three mutually perpendicular symmetry planes with respect to the directions of the fibres. For the sake of brevity, more details about the stiffness matrix in the case of both monoclinic and orthotropic materials are included in Appendix A of the thesis and by Kollar in [104]**.**

The compliance matrix for an orthotropic material presents few elements with zero values. The reason of those zero elements is embedded in the symmetric properties of an orthotropic lamina. They are also the terms responsible for uncoupling certain stresses and strains of the ply. This characteristic type of matrix implies that the application of normal stress σ_i on planes of symmetry causes all the out of plane strains, γ_{ij}, to be equal to zero, thus decoupling deformation effects. Particularly interesting is the case of transversely orthotropic materials which have the same characteristic coefficients as the stiffness and compliance matrices for the simple orthotropic material. The only difference between them is that some of the coefficients change because the transversely orthotropic configuration has the third symmetry plane featuring isotropic properties, i.e. $E_2 \equiv E_3$. In this case only the two basic longitudinal and transverse elastic moduli characterise the material with their respective Poisson's coefficients.

Laminates or plies are stacked up in specifically ordered sequence to orient the plies' fibres in predetermined fixed directions when constituting the laminate. The stacking sequence defines the balanced, symmetrical, cross-ply and angle-ply laminates as described in the following list:

- *Symmetrical laminate:* **w**hen the laminate is symmetrical, in terms of number of plies and fibres orientation, with respect to the midplane;
- *Balanced laminate:* when, for every ply in the $+\theta$ direction there is an identical ply in the $-\theta$ direction;
- *Cross-ply laminates*: in cross-ply laminates fibres are only in the 0- and 90-degree directions; cross-ply laminates may be symmetrical or unsymmetrical;
- *Angle-ply laminate:* they consist of plies in the $+\theta$ and $-\theta$ directions; they can be symmetrical or unsymmetrical, balanced or unbalanced;
- *π/4 laminate:* they represent laminates in which the plies' fibres are in the 0-, 45-, 90-, and −45-degree directions. The number of plies in each direction is the same (balanced laminate).

In most composite applications, the laminate inter-laminar dimension compared to the laminate sizes is very small. That is one of the reasons why laminates are mostly studied with the in-stress plane theory approach. Hence, in the specific case of plane stress $(\sigma_3 = \tau_{23} = \tau_{13} = 0)$, the constitutive equations can be written as:

$$\{\varepsilon\} = [S]\{\sigma\} \tag{2.6}$$

or $\varepsilon_{ij} = S_{ij}\sigma_{ij}$ with $i, j = 1,2,6$

and, by inverting the compliance matrix $[S]$, the system, in terms of stiffness, can be expressed as:

$$\begin{Bmatrix} \sigma_1 \\ \sigma_2 \\ \tau_{12} \end{Bmatrix} = \begin{bmatrix} Q_{11} & Q_{12} & 0 \\ Q_{12} & Q_{22} & 0 \\ 0 & 0 & Q_{66} \end{bmatrix} \begin{Bmatrix} \varepsilon_1 \\ \varepsilon_2 \\ \gamma_{12} \end{Bmatrix} \Rightarrow \{\sigma\} = [Q]\{\varepsilon\} \tag{2.7}$$

or $\sigma_{ij} = Q_{ij}\varepsilon_{ij}$ with $i, j = 1,2,6$

where the Q's are the reduced stiffnesses: $Q_{ij} = \dfrac{C_{ij} - C_{i3}C_{j3}}{C_{33}}$, they depend on the stiffness influence coefficients. More details about the composite design theories and methods are presented in Chapter 3.

2.5.2 Smart Materials

In this section, the principles and basic features of smart materials will be discussed. As will be shown in the next part of the chapter, via projects and concept designs, this class of materials has considerably helped the development of morphing technology during recent years. However, despite their technological advantages, smart materials have not been considered for a practice use on the GRAF aeroelastic tail. Weight and power supply issues are the main motivations for this choice. Smart materials technologies have the ability to sense change and enhance their functionality according to different and numerous circumstances. As Worden *et al.* discuss in [199], smart materials enable the design to exploit these benefits in performance, efficiency and costs. Addington and Schodek [4] in their textbook try to conceptualise a good technical definition of smart materials independently from their application area. They refer to both NASA and the Encyclopedia of Chemical Technology as baseline definitions. The former states smart materials to be: 'materials that remember configurations and can conform to them when given a specific stimulus'; the latter defines them as: 'smart materials and structures are those objects that sense environmental events, process that sensory information, and then act on the environment'. NASA refers to them as substances, alloys or compounds strictly defined by their molecular structures, whereas the Encyclopedia of Chemical Technology defines them more as a series of actions and configurations. The reason for these interchangeable definitions is mainly due to the extreme versatility these systems offer in several fields of scientific research. The following part focuses briefly on describing the properties of shape memory alloys, magneto-rheological fluids, and piezoelectric materials used in designing morphing concepts and compliant structures for the new generation of bio-mimetic aircraft concepts.

Shape Memory Alloys (SMAs)

SMAs have the characteristic to modify, by thermal energy, their internal crystal structure. They are in the two solid phases of martensite and austenite. The latter is the parent phase that can be recovered once the material is heated up. The former, instead, is the final crystal configuration into which the SMA can be forced by

stretching its internal structure. ‘One-way’ SMAs are alloys that can be stretched to deform in one desired shape and subsequently retrieve their original configuration once energised. The ‘two-way’ SMAs instead feature the characteristic of having memorised a predefined shape also in the parent phase, thus working between two memorised deformed and undeformed configurations when thermally activated and cooled down. When stressed, the SMA atoms move to achieve the martenistic phase generated by deforming the austenite crystal structure. Then, when heated up, they can remember and recover their original positions set into the origin parent phase as illustrated in Figure 2-19.

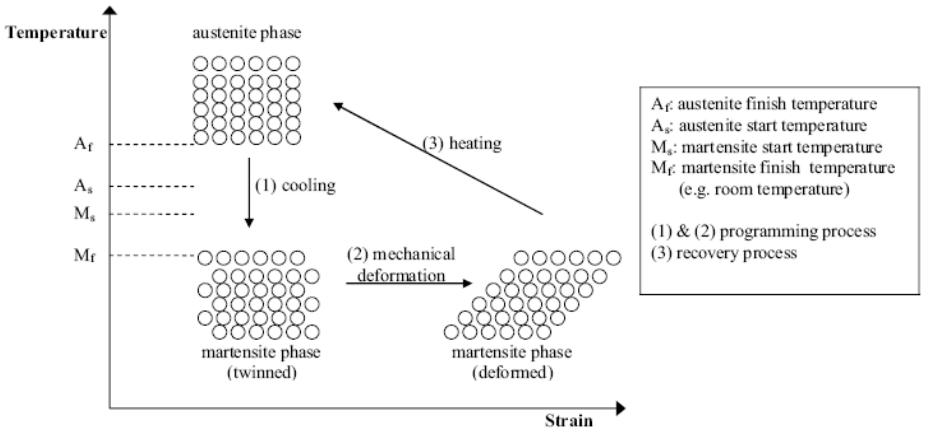

Figure 2-19 Temperature-strain diagram of one-way SMA material [170].

The most common and exploited SMAs are copper-based and NiTi-based alloys. They offer the best compromise between mechanical properties, costs and corrosion resistance. The first class of alloys presents high activation temperatures (>200 deg Celsius) and recoverable strains from approximately 3%, whilst NiTi alloys have lower operating temperatures (-200 to 100 deg Celsius) and larger scalable recoveries from 3% to 7%. However, the percentage of strain recovery ranges according to the number of cycles they will be designed and used for. The more strain recovery is requested the fewer number of life cycles the material can sustain.

Piezoelectric Materials

Piezoelectricity is commonly a characteristic found in some crystals which lack a centre of dielectric symmetry. They have an internal ‘dipole’ configuration caused by

the non coincidence of the centre of ‘gravity’ of the positive and negative charges. Thus, when mechanical stresses are applied, altering the polarisation and the alignment of the dipole inside the crystal, electrical charges are brought to appear on the surface of the crystal itself. This phenomenon is defined as the “direct piezoelectric effect”. Conversely, the application of an external electric field will deform the dipole which will induce distortion into the crystal, termed as the “inverse piezoelectric effect”.

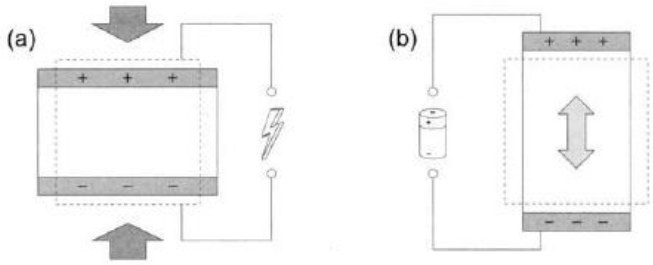

Figure 2-20 Direct (a) and converse (b) exemplification of piezoelectric effect [4].

According to the first or second mode of activation, piezoelectric devices can be used as sensors and actuator systems. On the one hand, due to their high resonant frequency, piezoelectric materials have short response times that make them perfect to measure or activate, with extreme precision, rapid varying forces. On the other hand, they require considerably powerful energy suppliers in order to work. That translates into being a heavy component for certain types of aeronautical applications in which weight is always one of the most important issues. Table 5 considers a comparison of three smart materials potentially applicable on smart structures or actuation mechanisms. In particular, this table summarises the case study conducted for a smart helicopter rotor blade flap design, as presented by Straub and Merkley in their study in reference [169].

Table 2 - Rotor blade flap actuation system variants

Material	Force	Motion	Frequency	Power
Piezoelectric	Med	Low	High	Small
Magnetostrictive	Low	Med	High	Small
Shape memory alloy	High	High	Low	Med

They tried to design a well performing rotor blade-embedded actuator to be fast, reliable and powerful enough for the entire helicopter manoeuvres envelope. The actual result was that the heavier weight of the mechanism imposed a restricted flight envelope on the specified helicopter used for the tests.

Magnetostrictive Systems

The final materials to conclude this short overview of smart systems are the magneto-rheological compounds. They are based on changing the physical dimensions inside a magnetic material, as the magnetic state changes. Two diverse types of effect can be distinguished: linear magnetostriction and volume magnetostriction. This material can be effectively used as an actuation system. It varies dimensions by changing the magnetic field. However, despite the modest amount of electrical energy needed to activate the magnetic field, the density of the material itself can, in some aeronautical applications, exceed reasonable weight requirements. Similar characteristics are exhibited by *magnetorheological* fluids. They are field-response and controllable fluids, normally in the state of gel or semisoft solids, which suddenly solidify when a magnetic field is applied to them, thus, increasingly changing their stiffness and mechanical properties.

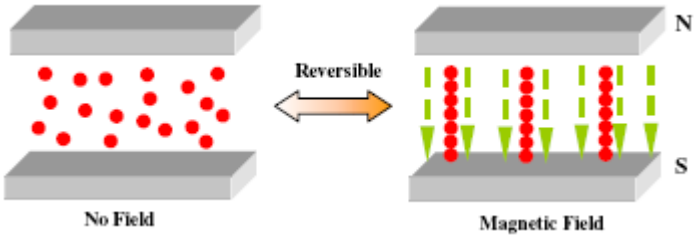

Figure 2-21 Magnetic field activation on magnetostrictive particles [163].

Their features collocate them more in a range of stiffening and reinforcing devices than actuation mechanisms, as also demonstrated in the concept idea of Song and Zeng [163] which used the MRF to lock the external ring of an adaptive fan nozzle. The interesting properties of this type of smart material also suggested a concept idea for the design of the rudderless aeroelastic fin. The concept was based on distributing a series of tiny tubes internally bonded to the fin skin and filled with MRF. By changing the magnetic field around the MRF, the fluid would change its status, thus

releasing the fin flexibly when fluid and holding the whole structure rigidly when solidified. The high density of the MRF meant this concept option was discarded in the preliminary stage of the design.

2.5.3 Composites' stiffness and strength criteria

There are several different factors which may cause failure of fibre-reinforced composites. The most common are fibre breakage, micro-buckling or kinking of fibres, delamination and matrix cracking, or even a combination of two or more of them.

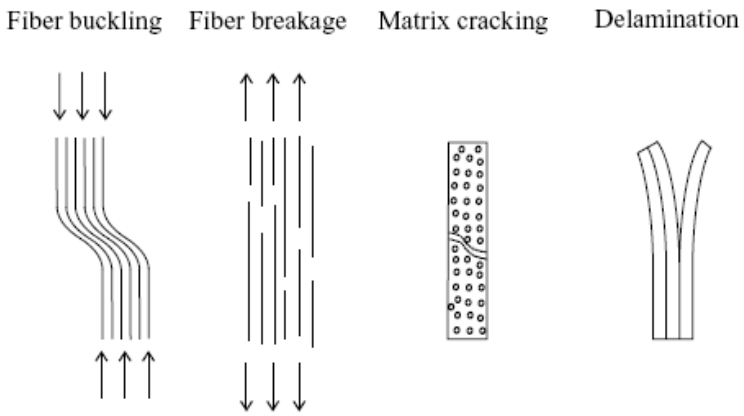

Figure 2-22 Fibres failure mechanisms [104].

Fibre breakage reduces the strength of the fibre in carrying tensile loads. Although the matrix can transfer the load and bridge the gap created by broken fibres to continue working, fibre integrity is essential to guarantee ultimate loads on composite structures. The fibre buckling instability, instead, reduces the compressive stiffness and strength of composite laminates. Compressive loads can also cause cracking failure in the matrix and consequently induce further damage to the whole composite by weakening the entire laminates. Finally, delamination is a failure which may be introduced even during manufacturing or because of certain types of

load application. It fundamentally reduces bending stiffness and strength, and also the capacity of the laminate to withstand compressive loads.

Therefore failure criteria are needed either for designing composite structures or improving properties of new materials. The most applied failure criteria are:

- the maximum stress criterion;
- the maximum strain criterion;
- the quadratic criterion.

Before starting to define the principles on which the three listed criteria are based, let us introduce another aid design parameter used to determine failure in laminates, i.e. the strength-to-stress ratio '*R*'. It is the ratio between the maximum, ultimate or allowable strength and the applied stresses. It is defined as:

$$R = \frac{\sigma_i^{\max}}{\sigma_i^{applied}} \tag{2.8}$$

The strength-to-stress ratio establishes when $R \le 1$ failure occurs. While, when $R > 1$ the laminate is safe and failure does not occur until the applied stress reaches the value factor of $\sigma_i^{applied} = \sigma_{\max} / R$'.

The criteria description will use the same notation adopted by Tsai in [175] and by Baker and Kollar in [13, 104]. As expressed by Baker, the maximum stress-based criterion establishes that the first ply failure in a generic laminate will not occur if:

$$\max\left(\frac{\sigma_1}{X_T}, \left|\frac{\sigma_1}{X_C}\right|, \frac{\sigma_2}{Y_T}, \left|\frac{\sigma_2}{Y_C}\right|, \left|\frac{s_{12}}{S_{12}}\right| \right) < 1 \tag{2.9}$$

Similarly, the maximum strain-based criterion formulation can be expressed as:

$$\max\left(\frac{\varepsilon_1}{\varepsilon_{1T}}, \left|\frac{\varepsilon_1}{\varepsilon_{1C}}\right|, \frac{\varepsilon_2}{\varepsilon_{2T}}, \left|\frac{\varepsilon_2}{\varepsilon_{2C}}\right|, \left|\frac{\varepsilon_{12}}{\gamma_{12}}\right| \right) = 1 \tag{2.10}$$

where for both theories the subscripts T and C, refer to critical stresses and strains for tension, compression and shear. The two preceding expressions can take into account even bi-axial (multiaxial) loads. The quadratic criterion can be presented

with three, slightly different, variant perspectives of the Tsai-Wu, Hill and Hoffman model theories. The basic equation common to the three theories defines that failure occurs if:

$$F_{ij}\sigma_i\sigma_j + F_i\sigma_i = 1 \qquad i, j = 1,2,3,4,5,6 \qquad (2.11)$$

where $\sigma_{i,j}$ are the stress components due to the applied loads, while F_{ij} are the strength parameters depending on the materials.

The last parameter introduced in this section is the failure index '*k*' used for the FEA defined according to Tsai's formulation as:

$$k = \left[G_{ij}\varepsilon_i\varepsilon_j\right]\left[\frac{1}{k}\right]^2 + \left[G_i\varepsilon_i\right]\left[\frac{1}{k}\right] = a\left[\frac{1}{k}\right]^2 + b\left[\frac{1}{k}\right] = 1 \qquad (2.12)$$

The indexes R and k are reciprocal.

2.6 Definition of morphing technology

The Merriam Webster dictionary defines to "morph" as undergoing transformation to change the form or character of something. Similarly, the NATO Research Technology Organization, and Applied Vehicle Technology (AVT) Technical Team on Morphing Vehicles (AVT-168) define morphing as a "real-time adaptation to enable multi-point optimized performance".

Both definitions describe the essence of the works and concepts presented in the next paragraphs. This section of the literature review will be dedicated to discussing the morphing concepts and techniques used to design novel wing and tailplane compliant structures in order to enhance aircraft flight performance and accomplish advanced and adaptive tasks demanded by such unconventional configurations.

In particular, the last section of the chapter will be dedicated to two specific branches of morphing systems: warping concepts and aeroelastic effect techniques' application.

2.6.1 Mechanisms and designs for variable geometry wing structures

Morphing technology is born from the intent of making airplanes more efficient, manoeuvrable and capable of multi-tasking missions. The first concept applied to morph the flight characteristics of an aircraft was based on a mechanism to vary the wing geometry. It was a mechanical system that, for the first time in aviation history, enabled an aircraft to change its aerodynamic wing characteristics in flight, such as the aspect ratio (AR). The wing AR could be optimised for diverse flight speeds, phases and missions. It was the year 1931 when the first flying variable geometry wing made its appearance, with the Westland-Hill Pterodactyl IV. Its variable wing geometry had an angular motion of 4.75° in the wing plane. It was designed for handling quality purposes and to help the pilot trim the aircraft in flight by varying the wing position. That also changed the CG location and the handling quality of the vehicle. The Pterodactyl IV was the precursor of modern variable sweep wing aircraft.

The second attempt at this type of concept technology happened in 1944, when another variable-geometry wing prototype was built by the German company Messerschmitt. It was the Me P.1101 that unluckily never left the ground. It was soon after the German prototype that another variable wing aircraft took to the air in the United States. It was the American project of Bell Inc., the X-5, which successfully flew in 1951, later followed by the Grumman F10F Jaguar. The latter was stopped earlier because of poor flying qualities and inefficiency of the sweep mechanism. Then the Tactical Fighter Experimental programme gave birth to the General Dynamics F-111, as the first production series aircraft with variable sweep wing. Then, soon after the F-111 design, new studies and engineering researches inspired the development of the American Grumman F-14 Tomcat, the Rockwell B-1A/B, and the Russian projects started in the 1970's with the Sukhoi Su-17, the Mikoyan-Gurevich MiG-23 and Tupolev Tu-22. Furthermore, European countries in 1975 pioneered this technical innovation on board the new Multi Role Combat Aircraft (i.e. the MRCA75), by starting production of the Panavia Tornado.

Figure 2-23 Variable incidence wing on F-8 Crusader [195].

Morphing sweep angled wings have been only one of the several methods adopted to control speed and performances on aircraft. Owing to the increase of aircraft weight and wing-loading specifications, take-off and landing speed requirements started to change. Therefore, it was necessary for certain classes of vehicle to be fitted with very effective devices able to broaden the handling qualities of airplanes at different speeds and flight phases. Fighter and larger jet aircraft specifically needed to have wings designed for high speeds for cruising and low speeds for the take off and landing phases. High lift devices were purposely invented to increase wing efficiency and guarantee high wing loaded aircraft shorter distances for take off and landing. Thereby, new devices on LE and TE were developed to be used in those delicate phases to camber the profile and vary the speed performances. But those were not the only ways an aircraft wing could vary its low-speeds performance. On the Vought F8 Crusader, for example, the engineers, in addition to conventional high lift devices, designed another smart system to increase the wing performance. The Crusader, as shown in Figure 2-23, was provided with a fully variable incidence wing that could be mechanically tilted up. That system was used to offset a positive incidence on the entire wing section, thus varying the aircraft attitude and lowering the flight speeds necessary to take off and land.

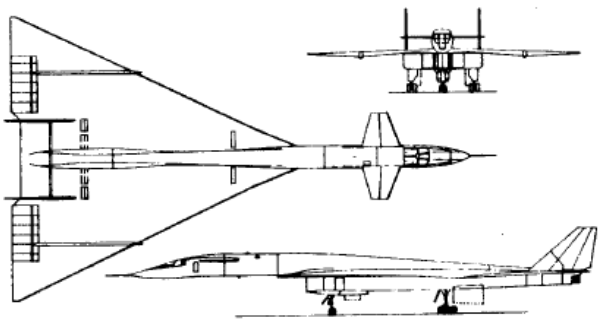

Figure 2-24 XB-70 Valkyrie with variable wing tips [150].

Sliding and rotating wing mechanisms were not the only ways used to morph vehicles' shapes and change aircraft characteristics. Original conceptual designs can be found in the past, some more than fifty years ago. One of these examples is the XB-70 Valkyrie, Figure 2-24. It was provided with movable outer wing sections, namely "folding wing tips", which could be canted according to the required flight speeds. That system was used to increase the aircraft's directional stability at supersonic speeds and furthermore to trap the shock wave underneath the aircraft in order to generate the compression lift phenomenon. The trapped shock waves were able to raise the lift of the entire aircraft by 5%. That conceptual design of more than forty years ago, has been recently updated into a modern similarly designed version of the tiltable wing tips concept studied by Bourdin *et al*. [29]. Their work shows how the outer wing sections can work as normal wing tips when horizontally deployed and as vertical winglets with a controlled surfaces function when tilted upwards by 90 degrees, as shown in Figure 2-25.

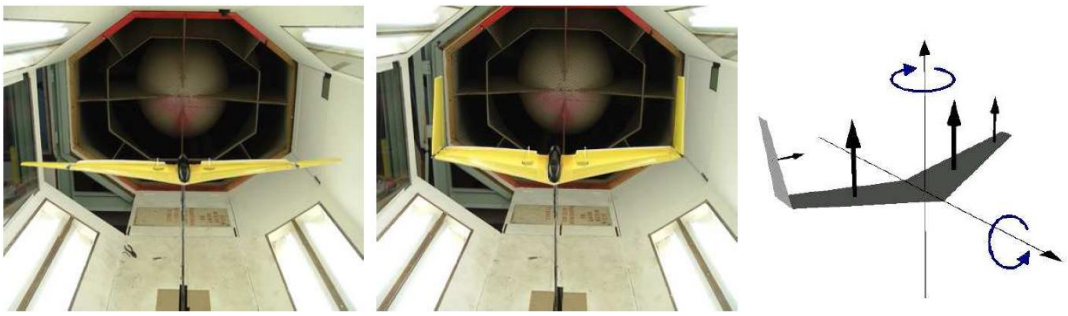

Figure 2-25 Tiltable wing tip design [28].

Another morphable wing tip concept is the one proposed by Ursache *et al.* in reference [182, 183]. It is a morphing winglet device, named "morphlet", based on a lightweight design able to perform as classic tip winglets do. At the same time, the design embeds a compliant structure that allows the winglet to cant and twist according to diverse flight circumstances. In this way the morphlet can be deformed to trim the aircraft wing for directional control tasks or to optimise the wing efficiency accordingly to diverse flight attitudes.

Figure 2-26 Morphlet prototype structure [182, 183].

A differing bird-like wing tip design is proposed by Smith and Cero´n-Mun˜oz *et al.* in their multi-winglets concept [161, 44]. It consists of a set of small winglets mounted at the outermost section of a wing tip and canted at different angles. They resemble birds' feathers designed to reduce aerodynamic drag and increase lift performance and wing efficiency, by reducing the tip vortexes.

Manned commercial and military aircraft are not the only machines tested to fly with novel unconventional and more performing technologies. Novel morphing concepts are also developed for the less risky and less expensive unmanned flying platforms. New designs were, in parallel, studied and applied to UAV projects, such as the polymorph variable and foldable wing designs of NASA and Lockheed Martin. Love *et al.* [119] tested the foldable wing shape of the Lockheed Martin UAV project through wind tunnel experiments, demonstrating the feasibility and operability of this unusual morphing model which is able to change its wingspan while flying, thus its flight speeds and types of mission.

Different techniques and concepts have been used instead to design telescopic mechanisms to enable UAV wings to extend their wingspan in flight.

The wing discussed by Neal *et al.* in [129, 130] and shown in Figure 2-27, can actively modify its aerodynamic characteristics, efficiency and consequently the entire vehicle flight performances for different types of applications. This concept wing was also provided with an internal twist mechanism which was aimed at varying the pitch attitude of the outer wing section for control and stability purposes.

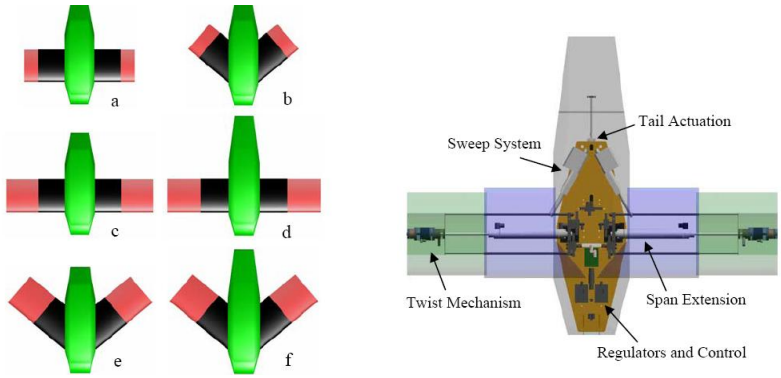

Figure 2-27 Telescopic UAV wing design with variable geometry variant [129].

A similar idea of another extendable system is the device designed by Blondeau [25] and shown in Figure 2-28. In origin his morphing design was thought to have a cladding made of a very flexible and stiff skin. But the researcher could not find a suitable or considerably elastic enough material for his model to satisfy both mechanical and elastic conditions. The main obstacle was to find a material that could stretch over twice its original length while continuing to support an aerodynamic load. Hence, a telescopic skin interrupted by gaps was the most feasible solution adopted in the design. That allowed several rigid sections to support the aerodynamic loads while in any configuration.

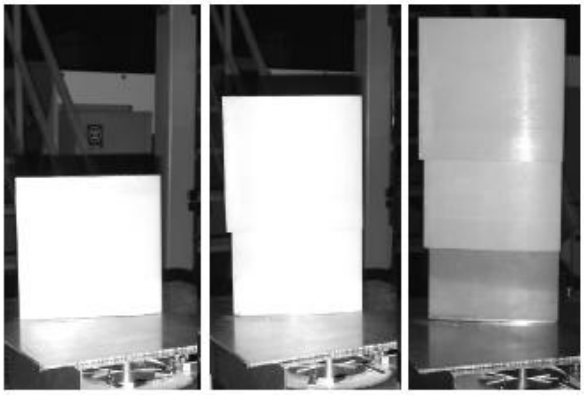

Figure 2-28 Retractable telescopic wing design [25].

The key element of this wing consisted of a pressurised telescopic spar that could undergo large-scale spanwise changes to vary the wing geometry. It is an effective device to vary the aerodynamic performance of a wing from a low aspect ratio model to a high aspect ratio variant, with enhanced efficiency. Also Leite *et al.* in their recent study of morphing wing concepts, published in 2009, in reference [110] designed a telescopic wing with morphing airfoil sections. The wing is made of

carbon fibre materials and can morph its airfoil section only in two predefined configurations for high and low speed wing profiles. The former is an NACA 0012 and the latter an Eppler 434. The telescopic spanwise and the mechanical chordwise variations allowed the wing to successfully vary its aerodynamic characteristic for diverse flight speeds according to the flight phases. However, a few design problems still have to be solved before starting the flight test campaign, such as the increased weight of the wing components and the open gap created on the LE and TE of the inner wing. That gap was needed to allow more space for the LE and TE sections of the outer wing portion which works as external coverings for the inner one. Despite the recent projects and concept technologies developed for extendable wing configurations, their origins can be traced back even to the early 1930's. It was then that Ivan Makhonine and his MAK10 project showed one of the first telescopic morphing wing designs. That mechanism was used to vary the wing AR to fly at different flight speeds. The MAK10 design saw a finally optimised version of the MAK123, shown in Figure 2-29, and flown in 1941. A similar principle was used on the LIG-7 by Bakaev, where extendable additional airfoil-like cladding could be hidden inside the fuselage. This additional wing covering was extracted during slow landing and take off speeds. As shown in the figure below it changed the whole wing area to allow it to fly at slower speeds without stalling.

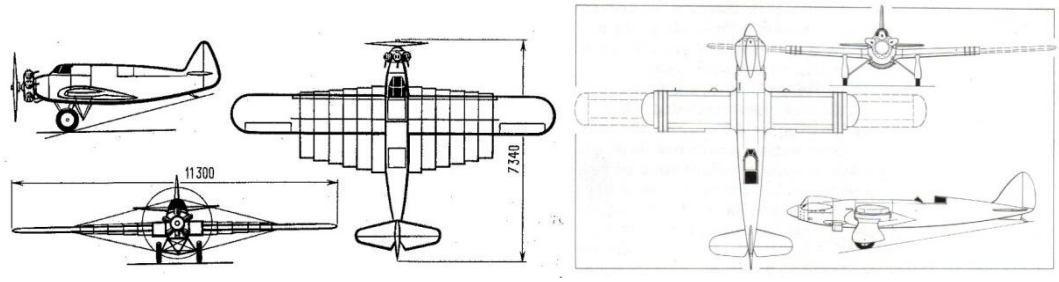

Figure 2-29 Application of telescopic wing concept on aircraft prototype.

The aim of all these varying platform wing designs was to allow the aircraft to increase the AR when it needed to fly slower, and be able to retract, fold, or sweep the wing into a low AR configuration in order to accelerate to faster flight speeds. A similar technique of extendable wings is the one developed by Cadogan in works [35, 36]. It is based on the design of an inflatable wing structure. Due to its extreme

flexibility, the wing was tightly packable, rapidly deployable and easily morphable to be actuated by either SMA wires or conventional servo-actuators. Another way suggested by Cadogan to control the wing profile's camber was based on differentially inflating the upper and lower panel skin. The flexible covering skin was formed by several micro tubes, spanwise aligned, which constituted a sort of inflatable grid embedded into the wing skin. By differentially expanding or contracting these capillary tubes on the two sides he could vary the curvature of the whole wing section. The same concept is applied by Jacob to induce warping onto an inflatable wing structure [99].

2.6.2 Adaptive camber designs

This section of the chapter introduces the structural configurations, the materials and the actuation mechanisms which enable wings and tailplanes structures' morphing capabilities. Project studies increased the interest in unconventional and bio-mimetic designs only a few decades ago. That was mainly because of the strong need for improved performance and reduced costs. However, concept developments of morphing wings to enhance flight performance by cambering airfoil sections started to appear with the first flying models born after the Wright's Flyer III.

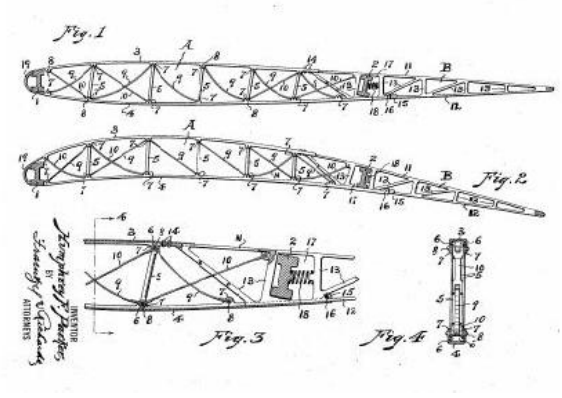

Figure 2-30 Parker design for variable camber wing [133, 134].

Mechanical devices designed to modify chordwise wing shapes were already born in the early 1920s, when one of the first patented adaptive wing concepts was developed by Parker [133, 134]. His design was able to autonomously change the profile camber shape from a clean streamlined configuration, straight for level cruise speed, to a cambered one for those slower speeds flown during take-off and landing phases. His patent, approved in 1920, was exploiting the wing loading variations between high and low speed conditions. As shown in Figure 2-30, there is a truss-like mechanism inside the wing structure made of thin steel strips. These metallic strips work as elastic bands or springs by forcing the profile to assume a curved shape, thus the camber, when a low wing loading condition applies. At high speeds, when the suction effect generated by the wing loading actions becomes dominant against the elastic action of the internal springs, the wing starts changing the cambered profile into a straight one. The latter performs more at high flight speeds than the former. Despite its technical manufacturing complexity, the tested mechanism was very effective during low speed phases, by considerably increasing the wing C_L and C_D coefficients. Burnelli's design in 1930 [34] adopted another innovative concept to camber wing sections.

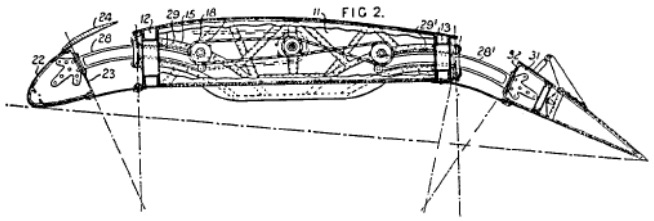

Figure 2-31 Burnelli's camber wing mechanism design [34].

His design used mechanical slides and guides on mechanically extendable leading and trailing edge parts to move the front and rear sections of the profile along a curved rail track path, as shown in Figure 2-31. Only a few years later, Hannah [85] came up with another device based on similar mechanical linear slides. His system was capable of uplifting, when needed, a limited portion of the wing upper skin. In this way the system increased the profile curvature and consequently its aerodynamic coefficients. The technical models of Lyon proposed in [121] offered another internal morphing mechanism made of a combination of pneumatic and mechanical pistons,

leverages, pushing and sliding rods to camber the flexible shape of LE and TE structures.

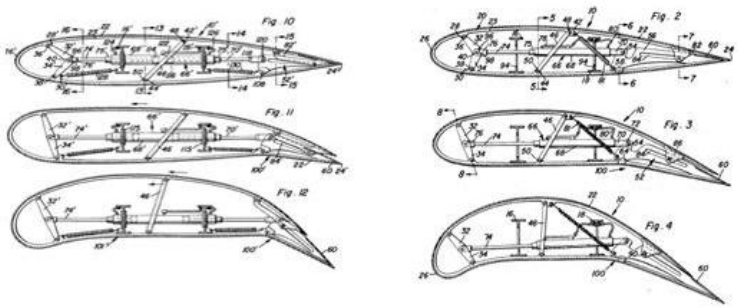

Figure 2-32 Lyon mechanism model for camber variation [121].

Large deformations were obtained with this model due also to the structural interruption of the cladding skin along the TE panels. In order to overcome the lack of flexibility for a rigid wing profile, Lyon, like many other designers, had to include gaps and he separated sliding edges to create a discontinuity on the external shell to increase the degrees of freedom (DOF) of the whole structure. That solution, still adopted in current morphing wing designs, allows structures with modest compliant capability to expand their DOF, whereas a restraining skin will hinder the motion and deformation of the whole profile. The LE and TE areas of wings are the two most effective regions of an airfoil section that under deflection or camber can considerably affect the performances of the entire aerodynamic surface. Therefore, several projects in order to enhance the aerodynamic performance of wing, and rarely tailplane, structures focussed on developing novel morphing LE and TE parts. In 1973, for the first time, the Boeing Company and the Naval Research Institute cast a eye over this revolutionary morphing-shape technology. The Advanced Technology Variable Camber Wing (ATVCW) research programme of Boeing and the Naval Research Department, summarised in the work of Ishimitsu in reference [98], showed another LE device used to seamlessly camber the nose area of a wing structure. The LE mechanism, shown in Figure 2-33, featured flexible skin panels attached to the nose beam, while the aft edges were tied to the front spar cap. The cambering deformation is activated by the extension of the actuator arm. This, in

turn, rotates the actuator crank and actuator link causing the main support arm to rotate down, thus moving the beam downwards and dragging in the upper skin following the deflection. The kinematics of this linkage allows the beam to rotate while curving the flexible upper surface of the wing and deflecting the LE downwards.

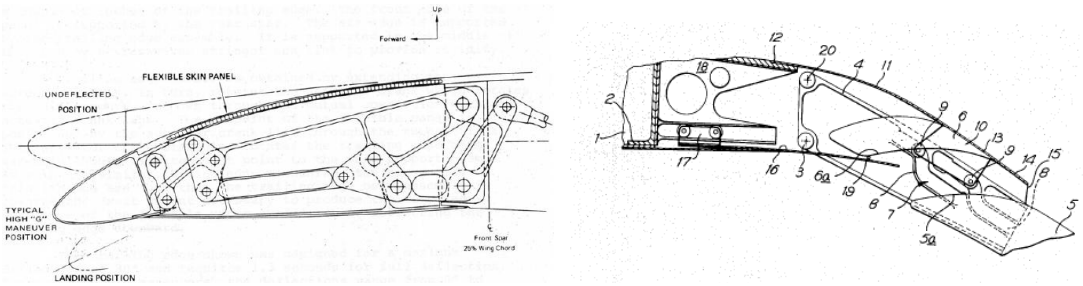

Figure 2-33 Ischimitsu LE concept (left) and Sharrock camber wing mechanism [98].

By exploiting a similar concept, Sharrock designed a camber wing mechanism in 1980 [157] to be fitted into the trailing edge sections of a wing in order to work as an aileron or slotted flap. A tiltable chordwise arm extends the flap section of the wing portion via trackways and roller slides. A flexible, but unextendable, skin can slide over the flap creating a continuous deformation for small and medium angles of deflection. An unsealed gap space is noted between the TE part and the central section of the flap when large deformations of the part are requested. The gap was necessary in order to achieve large displacements of the parts. Similar is the mechanism designed by Cole presented in [47]. The mechanical core of the design encompasses a series of rollers and a pinion gear device. They help the mechanism follow a curved cam track to downwardly deflect the LE nose of the airfoil section which is connected to a flexible upper skin in order to maintain the structural and aerodynamic continuity of the surface. Following the same principle of trying to keep the structural continuity between parts in motion, Berry [22] presented his option for a novel cambering device. He designed a variable curvature flap by means of several smaller, segmented flaps. Through a rail guide inside the mobile part of the TE, the actuating mechanisms push and retract the angularly variable segments by displacing

the actuation push-rod. The system replicates, in an artificial way, what a human finger articulation does.

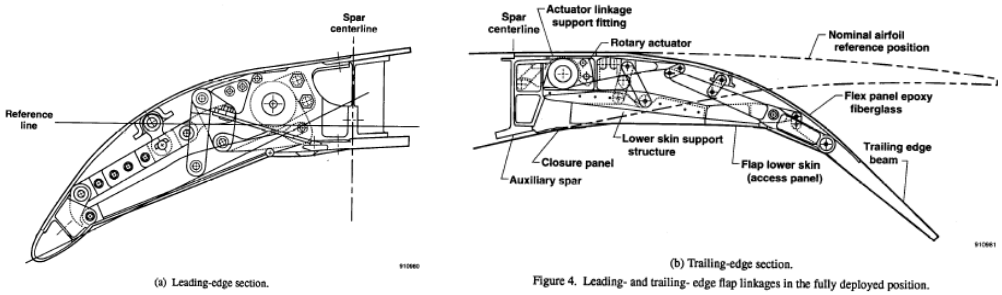

Figure 2-34 Mission Adaptive Wing LE and TE design [166].

It was only in 1982 with the patent claimed for a variable cambering edge mechanism by Statkus [166] that a large campaign of test flights was conducted on such a type of technology. He proposed a mechanical morphing device to deform either leading or trailing edges of wings. This mechanical system, based on sliding and flexible skin panels moved by hinged pushing-rods, was further developed and built by Boeing to be applied and tested on board the AFTI/F-111 MAW fighter aircraft within the NASA Mission Adaptive Wing (MAW) research programme [162]. The flying test vehicle was provided with variable LE and TE sections internally geared and linked to Statkus' device. The geared system task was to force deformations of the upper and lower skins of the flexible glass fibre panels. The cambering of the wing was controlled to handle and optimise each point of the flight envelope for several different flight attitudes. The project proved, in flight, the beneficial effects of adopting smart wings on aircraft, although a few penalties for the heavy mechanism and mechanical complexity of the devices had to be paid off. Also Fielding and Macci in [65] developed internal rotating and sliding mechanisms to activate LE and TE parts of variable camber wings in order to enhance the flight performance and efficiency for diverse points of the flight envelope. Monner *et al.* [124] within the high-lift device research programme at DLR, developed a chained mechanism to camber the trailing edge section of a Fowler flap for use on civil aviation wings, Figure 2-35 shows the concept design. They created an efficient kinematic mechanism to make ribs artificially flexible for a smooth deformation of an enhanced TE flap. That design can operate the command surface either as a conventional flap or an aileron. The system is based on a multi-sections trailing edge

rib which are attached to each other by revolute joints and a flexible skin connected to the ribs by a linear slide. The TE section is kept attached by another linear slide.

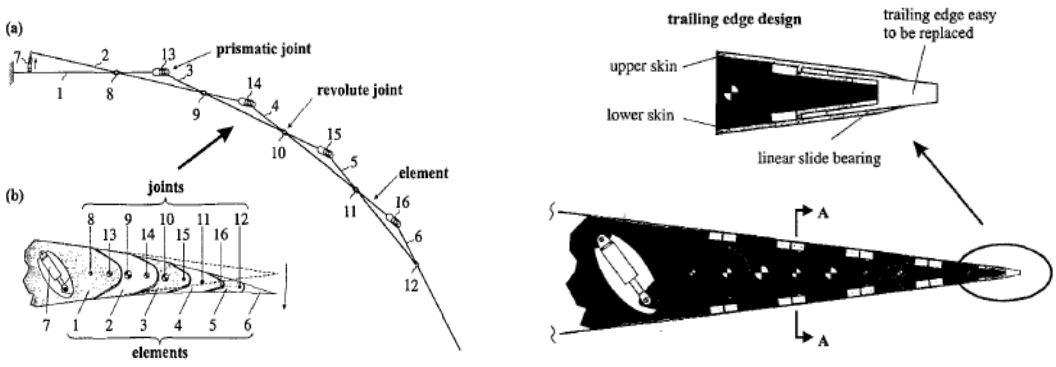

Figure 2-35 DLR high lift device camber mechanism [124].

The sliding TE closure will avoid the restraining problems that a rigid edge connection might cause. A different approach to flexibility is the concept idea developed by Good in his work [79]. He proposed a compliant design made of elastomeric materials rather then metallic joints, to allow smooth deformation of a TE wing section. The actuation forces will activate the solid-state hinge nodes on the truss-cells structure in order to rotate each node of the structural cluster. It will bend downwards and upwards the TE profile along the entire section, according to the input force direction. The achieved TE deflections were $\pm 4.27°$, which is not enough for a control surface task. Bartlye-Cho *et al.* in 2004 [18] presented, within the DARPA/AFRL/NASA Smart Wing programme, a study of a trailing edge mechanism designed to camber and twist the TE section of a wing in a seamless way. The final version of their research saw the optimisation of a design, already started in 1970 by Vought Aircraft, called an "eccentuator", and shown in Figure 2-36. A curved beam with one free end inserted into the TE section and the other one linked to the actuator is mounted inside the portion of the wing that needs to be deformed. The servomotor rotates the curved beam from 0 to 90 degrees. The rotation will drag the skin in deforming its panels according to the beam shape and orientation. In this way the covering skin is forced to deform and assume the same profile shape of the eccentuator beam at any angled position. The rotating beam works like a spine or a skeleton, imposing the covering to follow its curved shape and flexibly adapt the external panels to any single degree of rotation.

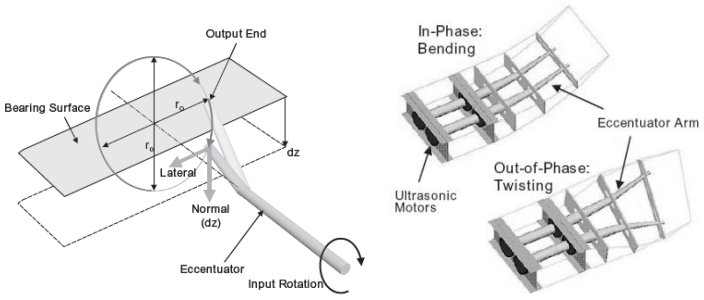

Figure 2-36 Eccentuator actuation mechanism [18].

The same mechanism was adopted by Perera and Guo [136] in the design of a seamless command surface for an aeroelastic wing structure. The main advantages of such device, when used in pairs or in multiple elements, are in the possibilities of coupling either the in-phase or out-of-phase bending inside the wing profile. The differential coupling can allow the system to work for different seamless purposes, such as ailerons, flaps or trimming tasks. The coupled action can be used for flap or aileron use. Conversely, the differential activation can induce a twist distribution along the edge for trimming or warping aeroelastic purposes. Kota and Hetrick in 2007 designed and patented [69] a morphing concept based on overlapping two compliant skin layers, internally supported by a flexible skeleton and connected to a set of linear actuators. They forced the TE deflection by simply pushing or pulling the internal supports linked to the compliant skins. In 2006, Ursache with his work [181], proposed another type of internal structure able to morph the external contour of the airfoil section. The concept was based on a spinal-rib configuration cambering the wing profile, via SMA wires, to improve its flying efficiency. With different features but with a similar concept idea, is the model of Campanile and Sachau, named the ‘belt-ribs’ concept [39], and shown in Figure 2-37.

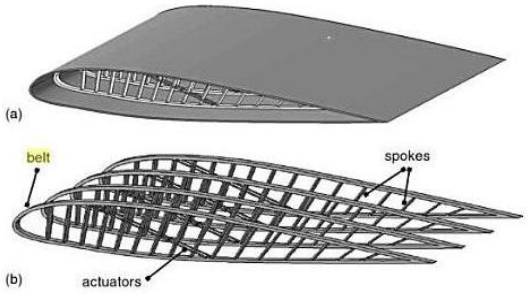

Figure 2-37 Belt-ribs concept structure [39].

The structure is based on a mono-coque composite belt internally supported by rigid elements, called spokes, which provide chordwise stiffness and also allow the required deformations. When mechanically activated by either conventional or smart actuators, the spoke's connection, acting as a solid-state hinge, allows the belt to 'slide' over the spokes themselves. However, the hinge's rigidity does not allow a completely free motion of the parts. Hence, the belt-ribs concept generates a simple elastic sliding of the elements to accomplish small displacements and camber the shape.

Campanile and Anders further developed the belt-ribs model for aeroelastic application on aircraft flaps to assess and validate the original design [40]. These researchers exploited the effect of the external aerodynamic pressure upon the wing to further force and obtain the required deformations for the solid-state hinge-belt design. They assessed that such a configuration, in order to perform efficiently, needs necessarily to work in conjunction with the aerodynamic loads to facilitate the actuation force needed to induce the overall deformations. Otherwise, the amount of energy necessary to activate the morphing capability of a belt-rib wing might not be worth this design adoption. Campanile in his work achieved deflections between 0.1mm and 3.0mm (5% flap chord) for a trailing edge section 60 mm long, with a total wing chord of 400 mm. The reasons for the modest results were attributed to the small size of the wing model and the difficulties of implementing a more efficient mechanism inside the small structure.

A different variant of the belt-ribs concept, proposed by Allegri *et al.* [6], is the one implementing the use of shape memory alloy wires to actuate the belt-ribs structure designed for an aeroelastic vertical tail. Their work proposes using SMA wires internally linked to the spokes and the belt in order, when energised, to force the semi-rigid supports to camber the shape of a vertical fin for enhancing control authority and stability of the aircraft. The system works in combination with an adaptive stiffness support which is able to release the fin for the exploitation of the aeroelastic effect deformations which in combination with the camber activation enhance the control and stability performance.

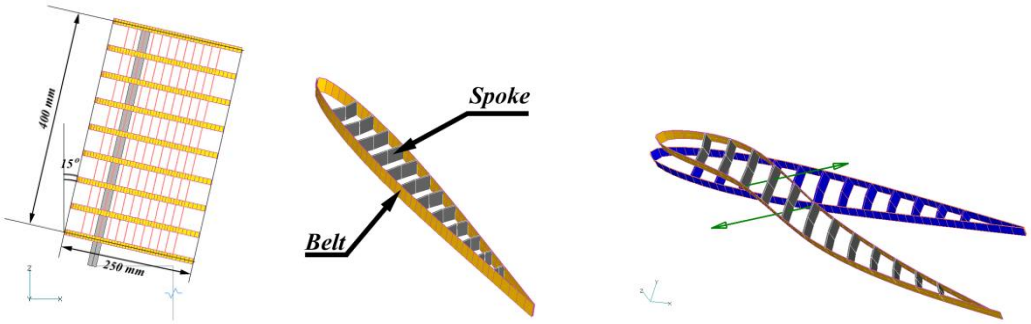

Figure 2-38 Aero-servo-elastic fin with belt-ribs structure [6].

Resembling Campanile's design concept which is based on designing a compliant core structure able to deform the conforming skin, it is also the engineering layout of the chiral structure concept studied by Bornengo *et al* [27]. This novel design encompasses a hexagonal chiral honeycomb configuration, designed to be the internal truss-like core of an airfoil section. The chiral cells work to accomplish two tasks. On the one hand they provide the internal stiffness to the airfoil structure in order to keep the aerodynamic shape and withstand the loads. On the other hand, the internal cells work together to induce reciprocal deformations on each other when activated. They morph the structure by contracting or extending the mechanical tendons between the cells. In this way, the core contraction will deform the internal volume and drag the external skin, bonded to the cells, to follow the deformation into the deflected shape.

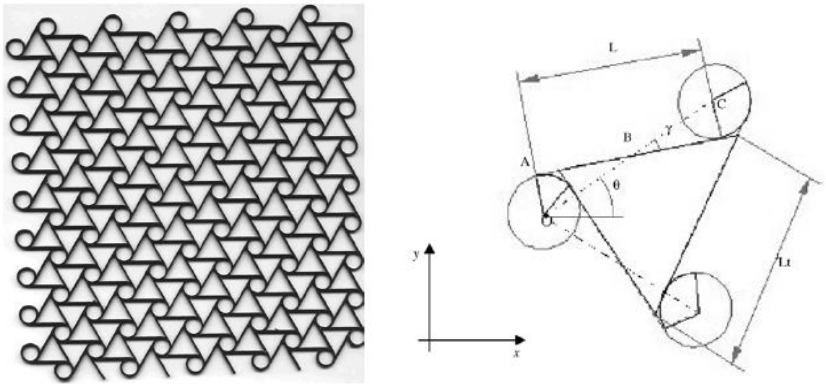

Figure 2-39 Chiral structure design: cells cluster (left), single cell (right) [27].

Good performances and deformations have been attained by this design application from preliminary bench tests. However, designers claimed potential difficulties in

realising large 3-D configurations with this model. The spanwise manufacturing complexity of each cluster of these hexagonal cells is one of the drawbacks that engineers are trying to solve for the practical application of the concept. The round circle in Figure 2-39 represents a single cell linked to the next one by flexible tendons. A similar concept based on a truss-like system realised by Ramrakhyani *et al.* is the one presented in [145]. That is a truss mechanism that can morph a wing structure for twisting and bending deformation purposes. The truss system layout works under the action of tendon elements which are released and tensioned on opposite sides of the framework in order to allow distortions of the truss structure. Another internal truss-like architecture is studied by Gandhi, in his design [72]. He proposed a concept structure embedding piezoelectric actuators to activate the contraction of the internal elements to deform the compliant flexible skin. A different way of activating a flexible skin was used by Strelec *et al.* in [170]. Their test model had a compliant cladding made of ABS material with metallic spars acting as the primary internal skeleton. The metallic elements support the skin and firmly clamp the base of the actuation system device. The actuation mechanism, made of SMA wires, is used to bend the entire profile shape when the smart wires are energised for contraction. The results have shown the gain in lifting performances at 0° of angle of attack, when comparing the streamlined and cambered shapes, was as much as equal to 6%. Another concept idea to enhance the lift force by camber is contained in the "*variform*" wing concept proposed by Gano in reference [73]. His design embeds a novel technique used to induce an autonomous reshaping of the external profile of a compliant structure. His original work includes a morphable bladder-based fuel tank internally fixed to the wing skin. Consequently the in-flight fuel consumption empties the bladder tank. Thereby the contents of the fuel tank are reduced in volume, and therefore the room occupied under the skin. When the volume reduction begins, it automatically drags the external cladding of the wing to follow the tank's change of shape. The purpose of the concept is to vary the section from an initially fully loaded thick profile contour into a final thin cambered airfoil section, which is more efficient than the initial one. A different solution of flexibility is that adopted by Poonsong. In this particular case, the elasticity is not demanded by a bladder fuel tank-like structure, but by the external compliant character of the wing skin described

in his work [143]. In his dissertation he proposes a hybrid layout realised by combining the use of latex sheets and polyester fabrics to form the cladding skin of a cambering wing section. The design alternates strips of stiff polyester material with strips of flexible latex in order to provide more flexibility to the skin. They are joined along their edges in the spanwise direction to favour chordwise bending deformations.

The system is internally activated by rotating steel push-rods. In an alternative idea, a different choice of materials and layout are evaluated by Sippola *et al.* in their morphing concept. Their work is based on a hybrid configuration of a quasi-isotropic glass fibre lay-up with embedded SMA wires [160]. Two prototypes of this smart wires adaptation have been tested. One version encloses the wires into mechanical sleeves bonded onto the composite layers and the other variant instead integrates the smart actuators in between the glass fibre plies. In both cases the actuation wires acted similarly to micro muscles embedded into the external skin which enabled the airfoil shape to be cambered once it was thermo-activated. The two versions demonstrated successful results in generating the required displacements. However, the first type was simpler to install and activate, while the second one was more difficult to manufacture and also represented a critical configuration for the composite plies. The SMA wires when heated up might deteriorate the interlaminar bond and cause serious problems of delamination. Furthermore, other modifications are necessary to include wires with larger diameters to exert forces that are sufficient to cope with the aerodynamic loads. Dong *et al.* in 2007 based their design on an articulated system of SMA spring actuators placed in the central section of a compliant wing structure [53]. The mean chord of the sections is provided with a rigid mounting plate, acting as support for the entire design, but above all, to support the set of SMA springs. These springs, with one end rigidly fixed to the rigid plate and the other end connected to the skin, are gradually energised with an uneven force distribution to bend the wing profile. The system demonstrated successfully the objective of the study but the heavy structure of the internal support and the energy required to activate the deformation did not suggest any further development of that concept. Instead, Giurgiutiu *et al.* in their work [76] exploited in different way the properties of smart materials. They created a hybrid laminate made of composite

layers and integrated SMA wires. With this technique they built up a TE device used for a rotor-blade tracking tab section, as shown in Figure 2-40.

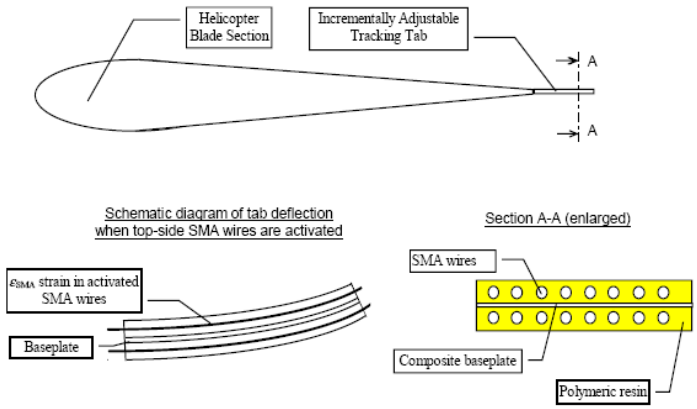

Figure 2-40 Piezoelectric system for rotor blade tracking tab application [76].

Two sets of SMA wires work independently, contracting and extending out of phase the two layers of the device to induce a bending curvature on the TE tab. The device helped to reduce, by a factor of ten, the normal tracking time for the tested class of helicopters, and also lowered the level of vibrations generated per revolution. Rediniotis [147] proposed another articulated mechanical arrangement of SMA wires for a bio-mimetic configuration of a morphing hydrofoil section. The design encompasses a multi-cell skeletal internal structure, as illustrated in Figure 2-42. Inside the profile, the SMA actuators, like muscles, rotate and bend each section according to the energised segments of the SMA wires. Each single smart wire works in between two adjacent vertebrae segments, inducing the relative movement of one with respect to the other. Their activation and movements occur by heating and cooling provision to the wires in order to activate and control several bi-directional rotations to vary the camber shape.

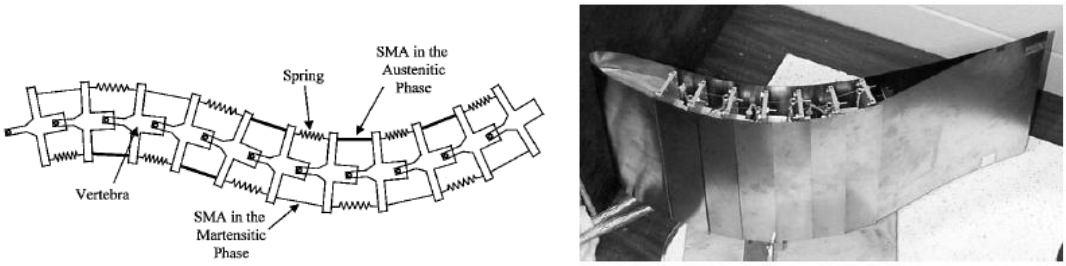

Figure 2-41 Bio-mimetic SMA hydrofoil configuration [147].

The system is very effective, but the complexity of the mechanism and the required power to activate the wires under external load conditions can affect its reliability and feasibility. Also, gaps are present in between the covering skin panels. A similar use of chained SMA wires linked together to activate diverse segments of the same airfoil section is the technique used by Barbarino *et al.* [14] in their design of the multi-body morphing TE section. The concept is provided with different segments assembled together in order to form the TE section of a wing profile. They are connected by elastic hinges and smart wires. The smart wires contract each segment of the TE section. Once their effect ceases, the elastic solid state hinges act like springs, restoring the un-deformed shape of the profile. Good deflection results are obtained. However, a more accurate study for a suitable covering skin has yet to be accomplished. A different concept design and material choice are the ones described by Vos in the conceptual idea presented in reference [189]. He applied piezoelectric materials to excite buckling deformations on wing structures, Figure 2-42. The device function was to generate and control camber deformations via piezoelectric plates, and used to work under conditions of post-buckling behaviour. The piezoelectric plate is integrated chordwise into the wing structures, mounted horizontally and pre-compressed between the wing main spar and the trailing edge. Once the piezoelectric laminates are activated, the plate releases the compression by buckling and curving its shape. This deformation consequently bends the TE according to the buckling curvature undertaken by the laminate and that drags the external shell to follow the deformation. It finally resulted in a cambering device, likely to be applicable to partially enhance the lift of a wing, but not with enough deflection to generate the same aerodynamic forces produced by a large deflection of conventional command surfaces.

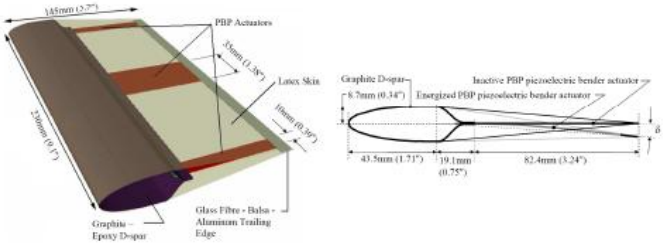

Figure 2-42 Piezoelectric plate for camber variation [189].

Also Bernhard in his concept design [21] and Centolanza in [43] apply piezoelectric materials to morphing devices for helicopter rotor blades. The former describes how to design a rotating actuator beam to control active rotor blade tips for reducing vibration on helicopters rotors. The latter designed a smart trailing edge device to trim the rotor blades and improve both aerodynamics and vibrations. However, piezo-actuators are useful for high bandwidth applications and small displacements. Bender devices are usually needed to be added to them in order to amplify the typical small displacements of piezoelectric materials. The extent of the maximum deflection achieved by Bernhard with his mechanism was equal to 2°. That was a successful result attained to control and trim blades' aerodynamics and vibrations, but these types of small displacements do not apply to designs such as the GRAF where large deflections are expected to generate great aerodynamic forces to guarantee satisfactory control and stability performance. A different typology of actuation system is the one Hinshaw demonstrated in his thesis [92]. He developed fibre reinforced flexible tubes filled up with fluid. He devised a design with semi-flexible composite tubes embedded in the core of a wing structure. The amount of fluid inside them will vary the tube stiffness to either allow deformations or to hold the whole structure rigidly. This mechanism was inspired and originally studied by Philen *et al.* in their works [137] with the scope of creating an embedded compliant structure for adaptive wing configurations. An identical design philosophy is that of Kothera and Yerkes who, in their respective works [105, 202], used pneumatic muscles to actuate trailing edge deflections of morphing wings, see Figure 2-43. The muscle extensions and contractions act as a conventional linear actuator by pulling and pushing the command surface. One of the main advantages of these fluid-dynamic muscles is the possibility to be shaped and bent into any form. They can be used to camber, extend or retract portions of wing structures for high lifting devices or control surfaces applications.

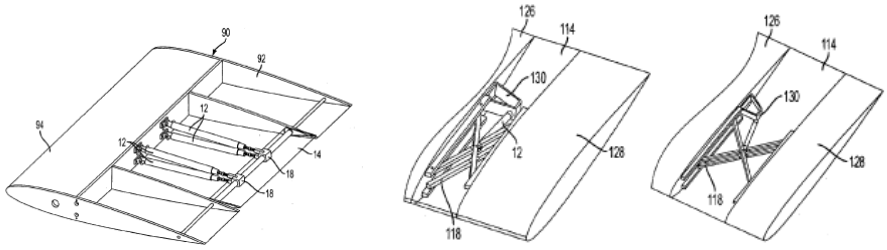

Figure 2-43 Various configuration for pneumatic muscles actuation [105].

As a conclusion of this section dedicated to the cambering/morphing designs, the project studied by Wildscheck *et al.* in [196] is discussed here. The concept idea of their work is shown in Figure 2-44. Their design, published in 2009, as will be noted later in the thesis, closely resembles the design of the L-shape stringers (LSS) device developed for the GRAF project and presented in the next chapter. They developed the same idea described in this thesis to use, as with the LSS system, rigid elements to convert the linear forces from the actuation system into applied bending moments for the skin panels of the TE section.

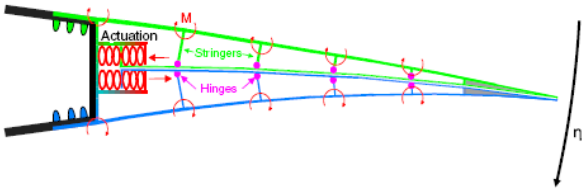

Figure 2-44 Internally actuated morphing split flap [196].

One difference with the concept developed for the GRAF design is that the TE device, show in the figure above, can morph and work as a unitised classical command surface but can also operate as a split flap by independently deflecting the two halves of the TE in opposite directions. The reason for that is to let the surface work as drag inducer, for yaw control, and airbrakes for installation on board blended wing bodies and tailless aircraft.

2.7 Warping theory and twist deformations

This section gives an overview of the principles and theories applied to those concepts and designs, whose performances and morphing capabilities rely upon twisting wing and tail structures. Warping-based layouts are obtained by inducing

twist distribution onto the aircraft components by means of mechanical forces and aeroelastic effect exploitation.

As already described in Chapter 1, one of the first seamless concept designs applied to change the shape of a wing structure for attitudes control, was the "warping-mechanism" designed by the Wright brothers and built into their Flyer III in 1903. A series of tautened cables connecting the biplane wings of the Flyer III were able to twist the structure under the controlled movement of the stick-bar. That system enabled the change in the outermost wing sections' incidence. In this way it was varying the lift on both sides of the wing and generating an asymmetric lift distribution necessary to roll the aircraft. That concept was created in 1903, at the beginning of the 20th century, but it is still, to date, a real benchmark for types of morphing devices. Engineers, soon after the Wright's flying experiments, abandoned the idea of adopting deformable structures to be used to handle airplanes' flight attitudes. They directed their attention towards simpler, classical hinged surfaces. It was in the late 1980's that a new flying project adopted again the Wright warping-wing principle to control aircraft flight attitudes. That was the F/A-18 Active Aeroelastic Wing (AAW) developed by NASA and DARPA [26, 51], and based on the exploitation of aeroelastic effect deformation upon flexible wing structures. The concept model will be explained in detail in the next Section. The twisted wing and tail shapes are the final outcome of the application of torsion and warping theories and principles to rigid structures. The study of torsion started in the 18th century with the experiments conducted by Coulomb [50] on simple symmetrical cylindrical bars. Later developments of his studies followed when Navier, as reported by Saint-Venant in his treatise on applied mechanics [16], started applying those theories to noncircular cross-sectional bars. However, both of them made the initial assumptions that during twist, the cross sections remain plane without any out-of-plane distortion. Their approach to torsion analysis brought them to erroneous conclusions which did not take into account any warping distortion. For example, the inaccuracy of the theory brought Navier to assess that maximum shearing stress occurs at the farthest point from the centroid of the element cross section. He assumed that at any point of the section the shear stress acts in the direction perpendicular to the radius linking the point A to the centroid O, as shown in Figure 2-45.

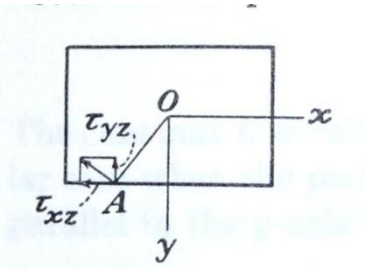

Figure 2-45 Torsional shear stress on generic cross section [175].

Therefore his explanation must include the presence of a shear stress component perpendicular to the contour of the bar. That is a contradiction of one of Navier's assumptions that the lateral surface is free from any external forces, hence it showed the erroneous result. The correct solution of the torsion problem of prismatical bars subjected to couples applied at their ends is then given by Saint-Venant, as discussed by Timoshenko in reference [175]. Saint-Venant assumed not only the presence of in-plane distortion of the cross section, but he also included an analytical description of the warping deformation occurring to a prismatical bar under twisting. The rotation of the cross section can be written by the following displacements expressions:

$$u = -\vartheta zy, \qquad v = \vartheta zx \tag{2.13}$$

where ϑ is the twist angle and z is the vertical coordinate of the bar. While the vertical displacement of the section can be described by the warping function $\psi(x, y)$ introduced as follows:

$$w = \vartheta\psi(x, y) \tag{2.14}$$

By skipping the passages corresponding to the components of strain calculation, and discussed in detail in reference [175], it is then possible to write the components of stress as a function of $\psi(x, y)$ as:

$$\begin{cases} \sigma_x = \sigma_y = \sigma_z = \tau_{xy} = 0 \\ \tau_{xz} = G\vartheta\left(\dfrac{\partial\psi}{\partial x} - y\right) \\ \tau_{yz} = G\vartheta\left(\dfrac{\partial\psi}{\partial y} - x\right) \end{cases} \tag{2.15}$$

From the equations of system (2.15) it can be seen that normal stresses acting on the longitudinal fibres of the bars or at any of its cross sections are zero. In order to solve the problem it is necessary to determine the correct warping function to satisfy the equilibrium of equation (2.16):

$$\frac{\partial^2 \psi}{\partial x^2} + \frac{\partial^2 \psi}{\partial y^2} = 0 \tag{2.16}$$

Instead of directly solving this problem, that according to the boundary conditions of various shapes might complicate the analysis, Saint-Venant proposed an alternative procedure to find out the final deformation, by introducing Prandtl's stress function $\phi(x, y)$. By considering the classical differential equation of equilibrium and substituting the stress function, it yields:

$$\frac{\partial^2 \phi}{\partial x^2} + \frac{\partial^2 \phi}{\partial y^2} = F \tag{2.17}$$

where $F = -2G\vartheta$, and

$$\begin{aligned} \frac{\partial \phi}{\partial y} &= G\vartheta\left(\frac{\partial \psi}{\partial x} - y\right) \\ -\frac{\partial \phi}{\partial x} &= G\vartheta\left(\frac{\partial \psi}{\partial y} + x\right) \end{aligned} \tag{2.18}$$

The stress function $\phi(x, y)$ is properly defined for each single case according to the specific cross section of the bar. Once the Prandtl's function is defined, the shear stresses and angle of twist for the single studied case can be calculated. Therefore by substituting the stresses and twist angle in the equations (2.15) and integrating them, the warping displacements $w(x, y)$ can be found as written in Eq. (2.14). The stress function is already determined for different singly and multiply connected bars, but in many other cases with much more complicated shapes, it must be analytically determined. In order to simplify the problem of working with differential equations to determine the stress function, Ritz introduced the method based on the strain energy computation of the twisted bar [33, 75]. Let us express the deformation energy as:

$$U = \iint \left\{ \frac{1}{2}\left[\left(\frac{\partial \phi}{\partial x}\right)^2 + \left(\frac{\partial \phi}{\partial y}\right)^2 \right] - 2G\vartheta\phi \right\} dxdy \tag{2.19}$$

The stress function is the kind of function which makes zero the variation of the integral of equation (2.19). The same expression may be attained by applying the principle of virtual works and the Prandtl's membrane analogy. Detailed discussions of both theories may be found in reference [75]. It was in 1940 that Vlasov [186] developed a new theory called *warping torsion* or *non-uniform torsion* which includes restrained warping, into the classical torsion theory of Saint-Venant. The first assumption stated with Vlasov's new theory was that the angle of warping ϑ is not constant along the longitudinal axis of the bar. He proposed a new differential equation to evaluate the rotation of the bar cross sections, which is written as follows:

$$EC_W \frac{d^4\varphi}{dx^4} - GI_t \frac{d^2\varphi}{dx^2} = m_x \qquad (2.20)$$

where GI_t and EC_W represent the torsion and warping stiffness respectively, while m_x is a distributed torsion moment along the bar. The warping constant C_W can be expressed as:

$$C_W = \int_A \psi^2 dA \qquad (2.21)$$

Vlasov also introduced the bi-moment term as a function of the axial stresses acting on the longitudinal fibres of the bar element, and defined as:

$$B = -\int_A \sigma_{xx} \psi \, dA \qquad (2.22)$$

The bi-moment is the consequence of the restraint applied to a warping section. It may be explained as the distribution of axial stresses needed to reduce the warping tendency of the section itself. It can also be expressed as a function of the warping constant as:

$$B = -EC_W \frac{d^2\varphi}{dx^2} \qquad (2.23)$$

thus leading to the following expression of the equilibrium between the torsion moment loading and the elastic reaction of the bar, as:

$$M_t = GI_t \frac{d\varphi}{dx} + \frac{dB}{dx} \qquad (2.24)$$

The Vlasov theory can be connected to the Saint-Venant expression when the warping stiffness and the moment distribution are zero, and if the section is free to warp. Hence, the final expression of the axial stress, under warping circumstances, can be written as:

$$\sigma_{xx} = \frac{N}{A} + \frac{M_y}{I_y} z - \frac{M_z}{I_z} y + \frac{B}{C_W} \psi \tag{2.25}$$

where the first term on the right hand side of the equation is related to the axial loads acting on the bar, while the second and third terms refer to bending moment loadings on the cross section's plane, and the last term represents the warping contribution to the overall stress of the beam. High order warping functions are taken into consideration by Fatmi in his work [64] to investigate the effect of non uniform warping of beams, especially when devoid of cross-sectional symmetry. He proposed the following expression for the out-of-plane displacements of the cross sections:

$$w(x,\boldsymbol{X}) = \eta_x(x)\psi^x(\boldsymbol{X}) + \eta_y(x)\psi^y(\boldsymbol{X}) + \eta^z(x)\psi_z(\boldsymbol{X}) \tag{2.26}$$

where η_x, η_y and η_z are the three warping parameters associated to the three warping functions ψ^x, ψ^y and ψ^z defined to study the non uniform distortion and derived from the classical Saint-Venant torsion theory. A high order deformation theory, is also applied by Hassis [87]. His theoretical approach used the deformation normal modes to take into account the effects of transverse shear deformation and a non-linear displacements distribution through the thickness of plates. Banarjee *et al.* in [12] studied an eight order equation to evaluate the effect of warping stiffness on the natural frequencies of an open section beam. Their analytical investigation proved the inaccuracy of the natural modes when warping stiffness is not taken into account. Errors in the natural frequency of the investigated beam showed results differing by up to 25% with respect to the natural frequencies ignoring warping.

With regard to results accuracy, the Vlasov and Saint-Venant torsion models have been further developed to study beam and bars within the perspective of a finite element method formulation by Lee and Kim in [108]. With the displacements assumption being based on small deflections, they superimposed the warping effect, in terms of stress and deformations, over the deformed beam cross sections. The

discretization of the beam in multiple elements helped simplify the calculation of the several cross sections constituting the profile of the twisted shape. Furthermore, another finite element modelling of a beam under a distortion and warping effect, was presented by Musat and Epureanu in [127]. They developed an FEM analytical model to increase the accuracy of the classical torsion theory for thin-walled beams, by proposing the discretization of the beam model in a number of "*s-plate*" elements, corresponding to strips of the beam itself and representing the macro-elements constituting the finite element model. They expressed the global stiffness matrix composed by the single matrices of each *s-plate* of the isotropic wall of the beam as:

$$\sum_{k-1}^{n} K_h = K = \frac{E}{\lambda^3}\left(I_{\omega_k} L' + \frac{I_d \lambda^2}{2(1+\nu)} L'' \right) \qquad (2.27)$$

where the first term on the right-hand side represents the contribution due to tensile and bending loads, while the second term is related to the angular displacement of the beam subjected to torsion loads. L' and L'' are the coefficient matrices for both types of distortion. The I_d term is the polar moment of inertia of the whole section and λ is the beam length. Musat and Epureanu proved the better accuracy of their model compared to the classical theory application when small displacement assumptions are made for closed, thin-walled sections.

The formulation of both torsion theories developed by Vlasov and Saint-Venant and these FEM discretized models apply only to isotropic material bars and thin-walled sections. Few corrections are introduced to also take into account the anisotropy of composite materials.

A number of investigators have focussed their attention on converting the isotropic torsion theory to composites-based models. Examples are Barrau *et al.* [15], who applied the finite difference method to study composite beams with free ends undergoing torsion, while Bicos and Springer in [23] and Bauchau in [19] give a detailed description of the analytical method applied to build and analyse a composite single cell beam with the classical torsion theory. Following the same philosophy and approach, Stemple *et al.* [167] extended the small displacements formulation of the finite element method to also take into account the warping deformations of composite beams. While Loughlan and Ata in [115-118] evaluated, in detail, the torsional and warping behaviour of composite beams when subjected to

restrained torsion, either for open or closed sections. The theoretical approach of their works was based on the following warping displacements expression:

$$w = -\omega(s)\frac{d\theta}{dz} \tag{2.28}$$

where the so-defined sectorial coordinate $\omega(s)$ was related to the primary and secondary warping distortions described through the integrals

$$\omega(s) = \int_0^s p_R ds \qquad (2.29a) \quad \text{and} \quad \omega^*(s) = \int_0^n n_R dn \qquad (2.29b)$$

where the p_R and n_R parameters identify the perpendicular and parallel distances respectively between the shear centre of the section and the tangent of the local profile of the section defined by the *s*-coordinate. Primary and secondary warping functions are determined according to the single or multiple symmetry of the subjected cross sections. In the specific case of a thin-walled closed section, the outcome of their analysis brought the final warping displacement and stress formulation for composite boxes as:

$$w = \frac{\omega_{eff}(s)T}{(GJ)_{BS}}\left[1 - \frac{\cosh[\mu_s(L-Z)]}{\cosh(\mu_s L)}\right] \tag{2.30}$$

$$\sigma_\Gamma = -\frac{\omega_{eff}(s)T}{\mu_s(E\Gamma)_{BS}}\left[\frac{\sinh[\mu_s(L-Z)]}{\cosh(\mu_s L)}\right]E^a_{x_i} \tag{2.31}$$

where $\mu_s^2 = \frac{(GJ)_{BS}}{(E\Gamma)_{BS}}$, with the warping rigidity $(E\Gamma)_{BS}$ determined from:

$$(E\Gamma)_{BS} = \frac{1}{\lambda_{eff}}\int_s \omega^2_{eff}(s)E^a_{x_i}t_{eff}ds \tag{2.32}$$

The analytical results produced good agreement with the experimental tests conducted by the same Loughlan and Ata.

Thin-walled boxes, to date, constitute the primary structures of several different constructions. Aircraft wings, bridges, wind turbine rotor blades amongst many others, adopt this layout based on light-frame construction and stiffness in torsion and bending. Especially for aircraft structures, composite technology has helped the development of very light thin-walled sections for wing and tailplanes applications. FangFang *et al.* in [63] studied the effects and implications of stiffening ribs inside the wing main box under torsion. Due to restrained torsion, the warping stress might affect the integrity of the thin skin structure for a thin-walled box. Therefore, they determined both the number and the spaced intervals between the internal structural reinforcements represented by rigid ribs. They eventually defined the average distance of two adjacent ribs as equal to 0.2 times of the beam length. Those spaced stiffening ribs were greatly reducing the warping stress in the middle part of the beam. The lower level of stress in the central part of the structural box also decreases the volume of material used to withstand loads in that area of the structure, and consequently its weight and cost. However, a small increase in the stresses was added to the fixed end. Another study to investigate ribs-based reinforcements was conducted by Gosowski in [80]. Within his study and experimental tests, he has proved the effectiveness of closed ribs stiffening flanges equally spaced and attached to an I-section beam subjected to torsion loading. The tests showed the poor effectiveness of battens joining simply the upper and lower flanges of the member, while the most effective results were obtained when the battens were also attached to the web of the same beam. The reinforcements worked like ribs intersecting the spars of a wing or tail construction. Hence, current aircraft wing and empennage structures are normally based on light, thin-walled primary boxes with internally spaced stiffening ribs. Stringers and stiffening battens or flanges are attached to panel skins and ribs respectively, to keep the design light and stiffer.

2.7.1 Warping- and twist- based concept designs

All the concept designs and actuation devices introduced in the previous parts of the chapter have presented morphing systems exclusively adopted to vary the camber

and planform geometry of wing structures. Slightly diverse is the content of this section that introduces those conceptual designs which are targeted to change the aerodynamic characteristics of a profile section by twisting and rotating the entire aerodynamic surface. One of the first examples of this type of project is the concept proposed by Jardine *et al.* in references [100]. They designed a torsion bar, built for an active wing, entirely made of SMA materials. The round shaped beam, made in TiNi, provided both stiffness and morphing capability at the same time. It was designed to generate enough torque to twist the structure of a $1/6^{th}$ scale model of an F/A-18 wing. The smart, hollow, round shaped beam successfully achieved the required 5° of twist to guarantee satisfactory flight control authority of the model. The adoption of this warping mechanism, rather than conventionally hinged ailerons, enhanced the wing aerodynamic performance by 8-12%. Garcia *et al.* [74] and Lind *et al.* [113] developed a similar warping-like actuation mechanism to be embedded into the composite wings of micro air vehicles. Simple twisting rods and tendon-cables have been used to morph the aerodynamic structure of small unmanned air vehicles. The very thin wing profiles considerably helped the mechanism during torsion. The absence of a thick torsion box inside the wing reduced the torsional stiffness of such structures. Successful flight tests demonstrated the effectiveness of the embedded warping mechanism for flight control authority. Phillips [139, 141, 142], instead of twisting the entire wing structure, concentrated his studies on the effects that a geometric and aerodynamic twist settled on the TE part of a wing may have along the whole span of a rectangular straight wing. He designed two flexible command surfaces, namely *twisterons*, that could be deflected and/or twisted in order to manoeuvre the aircraft or trigger a washout effect over the wing. When deflected, the two elements were working as conventional ailerons, but when twisted, they worked to aerodynamically trim the wing in order to optimise the airflow distribution over the wing surface. The scope of the twisted shape was to reduce the induced drag at each point of the flight envelope. By varying the twist deformation, the twisterons could change the wash-out effect responsible for the induced drag on wings. The concept worked and the scaled version used for flight tests showed a drag reduction of up to 20% more than with a straight wing.

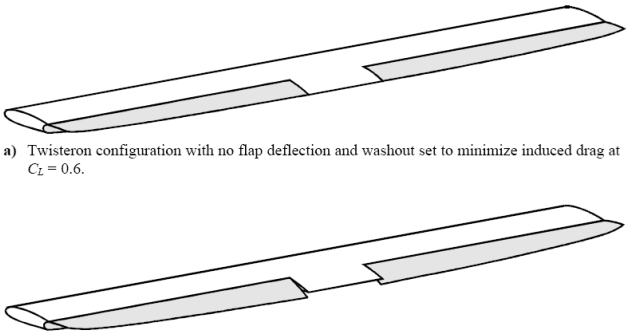

a) Twisteron configuration with no flap deflection and washout set to minimize induced drag at $C_L = 0.6$.

b) Twisteron configuration with 15° flap deflection and washout set to minimize induced drag at $C_L = 1.4$.

Figure 2-46 Twisterons concept exemplification [139].

A totally different concept design based more on control effectiveness than aerodynamic drag savings is the one presented next, where directionally attached piezoelectric fibres are used by Barrett in the fin prototype of reference [17]. The piezo-fibres constitute the elements of a hybrid plate made of composite materials and piezoelectric laminates designed to rotate a missile fin. The concept was designed by Barret. The piezoelectric laminates activate and warp the torsion spar installed inside the missile fin structure to control the surface rotation in flight.

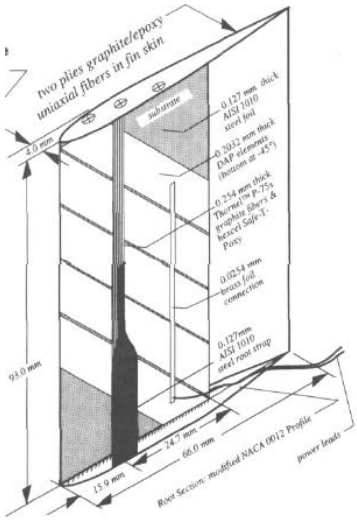

Figure 2-47 Piezoelectric actuated missile's fin [17].

As soon as the current is activated, the asymmetrically oriented distribution of piezo-fibres start bending and twisting the fin graphite spar. That leads the external structure to follow the spar deformation and initiate an axial rotation. The twist of the piezoelectric spar allows the vertical fin to achieve a maximum static pitch deflection of up to 5°. A penalty in the heavier configuration due to the use of directionally

attached piezo-fibres with respect to other options of conventionally attached piezo-electric materials has been faced by the designer during the fin prototyping. Despite that disadvantage, the heaviest option was chosen because it allowed the design to reach deflection performances as high as 32% more than the other conventional lay-out. The very quick response of the mechanism excludes any potential application for larger aircraft fins, unless a more powerful and different actuation system can be designed. The choice of piezoelectric actuators has been purposely made for that type of application. Missiles' flight speed and flight control response perfectly match piezoelectric characteristics.

A different mechanism for a twisting concept is the design adopted by Neal. It has already been introduced in the previous section with reference [129]. It is a mechanical system integrated within the main spar of the telescopic wing design. The internal telescopic shaft, running across the wing, can also rotate. That allows the wing tip sections to change the incidence and so vary the force generation. It twists the wing for control and high lifting purposes. A different philosophy, more closely related to the GRAF novel design, is the mechanism developed by Vos *et al.* in 2008 and presented in reference [190]. The main objective of their design is to actively induce warping deformations on a novel wing structure in order to gain beneficial aerodynamic effects without affecting the wing's structural stiffness. It is known that inducing wing torsion on closed structures may require powerful actuation and torque. They are needed to generate forces and moment enabling the mechanism to overcome the natural stiffness of the whole wing assembly in order to achieve the requested twist angle. However, Vos and his colleagues worked out a solution practically identical to the one that the author of this thesis has applied to the GRAF empennage, but designed one year earlier than Vos' concept design. They reduced the actuation power needed for warping actions by mechanically disconnecting the singly connected cell formed by the airfoil section contour subjected to torsion. They developed an airfoil section with a slit on the TE, as it is similarly done on the GRAF concept by means of the 'swivel-edge closure' device, into which they installed a threaded rod alternatively connected to both sides of the skin. They exploited the mechanically connected trailing edge only to increase the degrees of freedom of the cladding shell while warping. Whereas the GRAF design utilises the swivel TE

connection not only to reduce the torsional stiffnes of the whole structure, but also to enhance the TE deflection induced by the 'LSS' device for cambering purposes. The principle of the warping mechanism, the singly connected region with the gap/slit discontinuity, and the prototype model are shown in Figure 2-48.

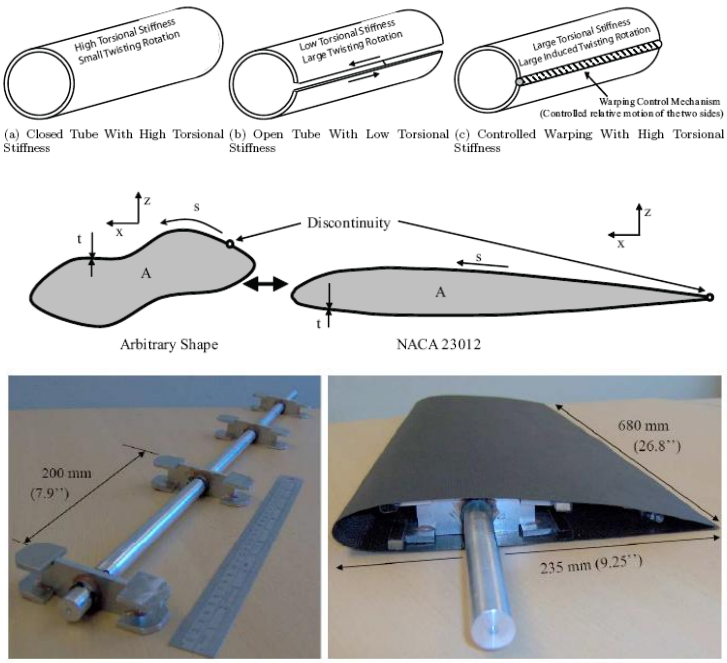

Figure 2-48 Principle of warping mechanism (top), wing section modelling (middle), warping wing mechanism and assembly (bottom) [190].

The rotation of the threaded rod placed near the TE closure, whose elements are connected to the profile skin, make the two separate trailing edges slide in opposite directions, thus inducing a differential motion of the sides of the section. Those differential displacements, by causing warping distortion on the wing cross sections, also induce torsion displacements on the entire structure. They verified that the ratio between the twist angle of the open and closed sections may be expressed as:

$$k = \frac{\vartheta_{open}}{\vartheta_{closed}} = 12\left(\frac{A}{t\oint_s ds}\right)^2 \qquad (2.33)$$

which is interpreted as the ratio between the area enclosed by the external profile and the area of the open section thin wall. The ratio is normally much larger than 1. By relating this expression to the polar moment of inertia of the cross sections and the torque expression, it gives an index of the section torsional stiffness. The positive

value of the ratio indicates saving actuation power when the same torque is applied to an open section. The development of this mechanism allowed the researchers to obtain 27° of peak-to-peak twist deformation with the added capability of twisting the wing section for wash-out or wash-in effect, varying the total lift coefficient up to a value of 0.7. The objective of the warping wing was to tailor the twisted shape for reducing the induced aerodynamic drag. These types of warping/morphing wing technologies allow designers to trim the profile sections to perform differently at any point of the flight envelope.

2.8 Aeroelasticity of aerodynamic surfaces

Finally, the conclusion of this chapter is dedicated to presenting the aeroelastic phenomena which characterise both wing and tailplane structures and how they are tried to be avoided or exploited by engineers to make structures either safer or better performing.

Aeroelastic phenomena are the most hazardous issues that can occur on aircraft wings and tails. Normally, designers tend to avoid aeroelastic deformation on aerodynamic surfaces to keep the flying structure in the safest part of the flight envelope without risking any structural failure or loss of control. Aeroelastic instabilities do not only affect the integrity of the structural parts, they also represent a disturbance for the flight comfort of crews and passengers but above all, they may cause upsetting flying attitudes for the aircraft. One characteristic aspect of these phenomena is that, before causing any structural failure, a sudden loss of control in handling qualities of the vehicle is perceived, as is very evident when phenomena such as buffeting and reversal of command surfaces occur.

However, the new trends in modern aviation technology see novel wing and empennage designs provided with torsion and warping mechanisms which seek to increase flight performance and efficiency of modern aircraft by exploiting those aeroelastic instabilities. They force flexible structures to follow out-of-plane

deformations for achieving more agile and bio-mimetic configurations. In practice, playing with the torsion effect on flexible structures might result in very unstable and dangerous situations with the aerodynamic surfaces likely to be susceptible to static and dynamic aeroelastic instabilities. Conventionally, as also discussed by Bisplinghoff in [24], aeroelastic phenomena, primarily said to be divergence, reversal, flutter and buffeting, tend to be avoided by designing adequate stiff and robust structures. These types of instabilities initially cause upsetting flight attitudes with the consequent failure of parts and collapse of the structures. For the sake of brevity and scope of the project, only the phenomena related to the warping fin issues will be discussed in this section.

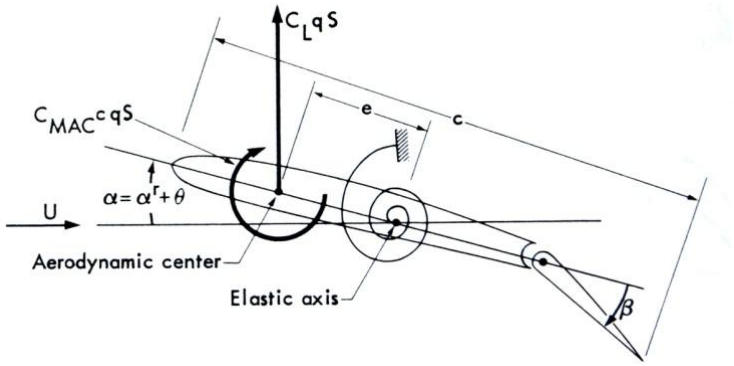

Figure 2-49 Aeroelastic phenomena on generic airfoil section [24].

The generic airfoil section, represented in Figure 2-49, hangs on by a torsional spring attached at its elastic axis (EA) and is used by Bisplinghoff to describe the phenomena involved with aeroelastic instabilities. Let us consider the aerodynamic forces resultant, produced by the positive angle of attack and the positive flap deflection, applied to the aerodynamic centre of the section. The vertical force generation produces a nose-pitching-up moment which tends to clockwise rotate the profile around its EA. This effect is further increased when the flap is deflected down. The amount of twist produced on the airfoil section is directly proportional to the stiffness of the structure which is, in this specific case, represented by the spring model of Figure 2-49, while in the specific case of this the fin model study, the spring represents the cross-sectional stiffness and the restraining boundary conditions.

The *torsional divergence* instability is a condition which if not properly addressed may limit the flight speed of aircraft structures to prevent loss of control and structural failures. Linear divergence theory normally applies to wing structure when small deflections and instabilities occur. Such assumptions must be changed when large twist deformations are taken into account for those aerodynamic surfaces, as is likely to happen in the GRAF design. Campanile and Thwapiah in [41] extended the non-linear theory of torsional divergence studied by Trahair in [178]. They applied the following formulation to describe the relationship between the twist angle and the torsional moment:

$$M_t(y) = GJ\frac{d\vartheta}{dx} + \frac{1}{2}EI_n\left(\frac{d\vartheta}{dx}\right)^3 \tag{2.36}$$

where I_n is the Wagner's function and varying according to the geometry of the considered section. The solution of the problem consists of solving the non-linear differential equation:

$$GJ\frac{d^2\vartheta}{dx^2} + \frac{3}{2}EI_n\left(\frac{d\vartheta}{dx}\right)^2\frac{d^2\vartheta}{dx^2} + m(x) = 0 \tag{2.37}$$

The main advantage of this approach is in the possibility of studying large deformations and also the post-critical static aeroelastic response of aerodynamic structures whose effect under linear theory consideration cannot be analysed. Moreover, Campanile and Thwapiah analytically demonstrated the increased structural sub-critical aeroelastic response of the model which, in the case of large twist angles, assumes more accurate and smaller deformation than the results attainable with the linear theory. As anticipated, the uncontrolled divergence is not the only instability affecting the static equilibrium of airplane wings and tailplanes. Another phenomenon which, historically, has tried to be avoided on aerodynamic structures is the loss of effectiveness on the controls due to the unexpected reversal of command surfaces. The reversal problem is generally caused by the dominant induced twist produced by the pitching moment generated by a deflected command surface. That pitching moment is more effective than the effect produced by the

control surface-generated lift. Therefore, with the two effects acting in opposite directions, if there is not an effective torsion box built to withstand those loading actions, the structure will end up by twisting the whole aerodynamic surface with the opposite effect expected by the manoeuvre motivator. When a control surface is deflected by an angle δ, the lift coefficient value corresponding to the command surface rotation is given by:

$$C_L = \frac{\left(\frac{\partial C_L}{\partial \delta} \frac{1}{(\partial C_L / \partial \alpha) C^{\vartheta\vartheta} qSe} + \frac{c}{e} \frac{\partial C_{mAC}}{\partial \delta} \right) \delta}{\frac{1}{(\partial C_L / \partial \alpha) C^{\vartheta\vartheta} qSe} - 1} \qquad (2.38)$$

The reversal point is that condition occurring when the command surface deflection is utterly ineffective, thus producing C_L=0. That translates in the numerator of the equation (2.38) as equal to zero, from which the reversal speed can be calculated. The next section will explain how the reversal and divergence instabilities are exploited by engineers to enhance aircraft performance.

The flutter problem is the last of the aeroelastic instabilities which will be discussed in this section for the purpose of the project. Historically, the first flutter solution was based on the models proposed by Theodorsen in 1935 and by Küssner and Schwarz in 1940. Their studies started with the unsteady theoretical aerodynamic problems obtained in two dimensions**.** They approached the solutions for flutter analyses by assuming that the loads, upon each spanwise station of a wing, depend only on the motion of that station. This strip-like approach, namely “strip theory”, was further developed and used in an early method of flutter analysis, later presented by Smilg and Wasserman (1942). Their refined study technique divided the wing into a number of strips, and calculated the aerodynamic loads on each strip on the basis of two-dimensional coefficients evaluated at the centre line of the same strip. The model proved to be very successful for unswept and high aspect ratios wing applications.

The MSC/NASTRAN Flight Loads code that will be used for the computation of the aeroelastic model of the GRAF design, is also based on the Küssner and Schwarz (1940) models.

The numerical analysis is based on the resolution of a two DOF system, whose expression in the two variable dependent equations may be written as:

$$\begin{cases} m\ddot{h} + S_\alpha \ddot{\alpha} + m\omega_h^2 h = Q_h \\ S_\alpha \ddot{h} + I_\alpha \ddot{\alpha} + I_\alpha \omega_\alpha^2 \alpha = Q_\alpha \end{cases} \quad \text{with} \quad (2.39)$$

$$\begin{cases} Q_h = \int_{-b}^{b} (p_U - p_L) dx = -L \\ Q_\alpha = \int_{-b}^{b} (p_U - p_L)[x - ba] dx = M_y \end{cases} \quad (2.40)$$

where,

m – mass per unit span;

I_α - mass moment of inertia;

S_α - static mass moment;

$\omega_h = \sqrt{K_h / m}$ - uncoupled natural bending frequency;

$\omega_\alpha = \sqrt{K_\alpha / I_\alpha}$ - uncoupled natural torsional frequency;

and where the terms on the right hand side of the lift and pitching moment equations of system (2.39), Q_h and Q_α, are respectively the system representation of the external forces, namely the Generalized Aerodynamic Forces (GAF), depending on the heave "*h*" and pitch "α" variables. The numerical techniques adopted to carry out the flutter analysis will be presented in Chapter 3.

2.8.1 Aeroelastic tailoring and aeroelastic effect

The typical *modus operandi* of the aeroelastic structures is entirely based on controlling and handling the effect of the deformations generated by the aircraft's aerodynamics-structure interaction and avoiding and preventing flutter, divergence, reversal and buffeting instabilities. Due to the natural elasticity of the materials, the aeroelastic deformations, although more likely to be generated by local loadings

variations, modify the shape of the entire aerodynamic surface. In order to withstand all critical loads and instabilities, the adopted solutions include stiffening the box structures, balancing masses on critical parts, the aeroelastic tailoring of the panels of composite structures or even using stiffer materials with thicker sections, or applying stringers and stiffener reinforcements. One different solution with a novel original option is the one adopted for the Active Aeroelastic Wing (AAW) technique used on board the NASA F/A-18AAW, presented in this paragraph. The AAW design concept exploited the induced deformations rather than stiffening the wing structure. However, apart from a few cases where flexibility is considered to be a structural advantage, most of the aeronautical designs based on composite materials make great use of the aeroelastic tailoring technique to safely keep under control all unwanted instabilities. Shirk and Weisshaar [158] define the aeroelastic tailoring technique as *"the intentional use of advanced composite directional stiffness to control the structural deformation and resultant aerodynamic forces that act upon a wing or a rotor blade"*. Aeroelastic tailored design applications are used to control dynamic stall, alleviate gust and cyclic fatigue loads, reduce deformation and also to increase flutter speeds. Aeroelastic tailoring is indistinctly applied on fixed and rotary wings, and wind turbine blades as well as proposed in [78]. It is primarily used to reduce to their minimum extent the aeroelastic deformations generated by in-flight loads and structural elasticity. However, aeroelastic tailoring is not a recent technique used in modern aircraft projects; aeroelastic planform tailoring was already adopted on the Handley Page HP80 Nimrod wings. The Nimrod project was the first application of tailored wing design done without the assistance of any computers. Hertz *et al.* in [88] studied and tested the design of a composite forward swept wing for enhancing the flight performance of jet fighter aircraft. The flying demonstrator of this unconventional configuration was the DARPA/NASA X-29. Forward swept wings enhance handling quality in terms of speed and rolling manoeuvres, in particular by reducing drag at transonic speeds but, unless they are properly designed and built, they may be subjected to hazardous damage and failures. The first cause of failure is linked to the static aeroelastic condition, specifically to divergence phenomena. Swept wings under loading actions may bend and twist. Structural configurations of isotropic aft swept wings tend to twist, pitching down the airfoil leading edges and

reducing the wing angle of incidence, and so the loads. This phenomenon is called the *wash-in* effect. Conversely, the *wash-out* effect is produced when the wing sweep angle is negative, with the wing profiles pitching up. As published in the results of Diederich and Budjansky [52], regarding swept forward wings, these considerably suffer divergence conditions which can dramatically further increase the twist, thus increasing the incidence and aerodynamic load, and leading to structure failure. Bisplinghoff shows how the divergence speed is a direct function of the wing sweep angle. A moderate forward sweep angle can dramatically lower the divergence speed of wing surfaces, whereas the aft angle beneficially increases the divergence speed limit.

It was in the 1960's that studies started focusing on exploiting and developing the fibrous properties of composite materials. In 1971 the Grumman Corporation initiated a research programme to evaluate the possibility of controlling and enhancing the aeroelastic response of wing structures by applying the aeroelastic tailoring techniques of composite materials. Krone [106] published one of the first studies to eliminate aeroelastic instability by means of aeroelastic tailoring. In detail, he showed that a forward swept wing structure could avoid aeroelastic divergence simply by tailoring the composite fibres used for the laminates without any weight penalty.

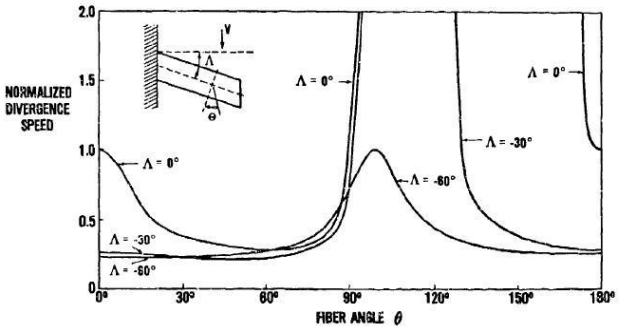

Figure 2-50 Normalized divergence speed vs. fibres orientation [106].

In practice, examples of modern applications of this technique can be found in the work of Guo *et al.* [81, 82], in which they demonstrated the beneficial effects of tailored designs by proposing a composite optimised layup for maximum flutter speeds. By tailoring the layup of a studied composite wing box, the results showed an increase of 18% of flutter speed and a consistent weight reduction for the whole

box of 13% compared to an untailored design. Guo in [83, 84] applies the same technique to enhance the wing structure and aerodynamic performance of an aerobatic aircraft. By using a gradient based deterministic method (GBDM), the objective function $f_v(x)$ is minimised to solve the optimisation problem. The objective function is expressed as:

$$f_v(x) = \left[1 - \frac{V_f(x) - V_f(\vartheta_0)}{V_f(\vartheta_0)}\right]^2 \tag{2.41}$$

Where $V_f(x)$ is the wing flutter speed and x is the vector containing all the fibres orientation, with ϑ_0 representing the fibres orientation of the initial laminate. The optimisation process generated good results for the tailored layout increasing the flutter speed by 37% and reducing the weight, compared to the aircraft's original metallic wing structure of 40%. The GDBM technique, although giving a slight inaccuracy of the solution for optimisation problems, represented at the same time a positive aspect of the design process. The inaccuracy of the model is attributable to the fact that the objective function has low sensitivity to a deviation of the fibres orientation from the optimum solution. However, that turns out to be exploited in a positive way and within a certain amount of tolerance from manufacturers to adapt the industrial manufacturing process of the plies stacking sequence to accurately optimise tailored fibres orientation.

The study of sweep angle influence on diverge phenomena for composite wing boxes has also been tackled by Librescu *et al.* in [111, 112] from whom the following divergence pressure formulation has been taken:

$$(q_n)_D = \frac{(a_{77})_R (q_n)_D^{PT}}{(a_0)_R c_R e_R L^2 \left[1 - \tan\Lambda \left(\frac{a_{77}}{a_{33}}\right)_R \frac{L}{e_R} \frac{(q_n)_D^{PT}}{(\tilde{q}_n)_D^{PB}}\right]} \tag{2.42}$$

The denominator of Eq. (2.42), from [111], also takes into account the sweep angle of the wing. It provides two important conclusions. The one is that with a forward swept wing layout (i.e. negative values of Λ), the denominator becomes more

dominant and contributes to lowering the divergence pressure. Therefore, it lowers the critical divergence speed for such a forward wing configuration.

The second conclusion is that from their formulation, it is easily possible to define the sweep angle for which the wing may be defined theoretically as divergence free. That is the angle Λ_{crit} when the denominator becomes zero. The a_{ij} coefficients of Eq. (2.42) correspond to bending and torsion stiffnesses of the composite box. For the sake of brevity they are not fully listed here, but may be found in detail in [112]. The superscripts PT and PB recall the terms related to pure-torsion and pure-bending analysis theories, respectively; while the subscript *R* refers to values related to the wing root section and a_0 is the lift-curve slope of the profile sections.

Aeroelastic deformations and tailored designs were also exploited by Thuwis *et al.* to study a self-adaptive configuration for a composite F1 car rear wing. The aim of their research was to design a self-adaptive structure able to passively reduce the induced drag of the car wing. Due to the aerodynamic loads and the tailored orientation of the fibres, the car wing was deforming in a beneficial way to smoothly create an optimised wash-out effect and adaptively trim the wing for a reduced induced drag. Their research [173] successfully proved that at high speed the tailored rear wing could reduce the induced drag coefficient by 10-15%.

Similarly Weisshaar in his wing model studied in [193] exploited aeroelastic deformation to reduce the induced drag generated by a wing surface.

Popelka *et al.* [144] studied an 18% *t/c,* thickness chord ratio tailored wing design for high speed tilt-rotor configurations for the Boeing V-22 wing. The new tailored wing with the 18% thickness ratio, and thinner than the original 23% design, showed improvements in structural stability up to 71%. However, it had a little weight penalty of 1.2% with respect to the overall wing weight. Weisshaar conducted an important study on aeroelastic tailoring designs for improved performances on UAVs [192]. He showed that passively tailored designs cannot reach the optimum effect in drag reduction unless the control surface on LE and TE assist the wing in being aeroelastically trimmed or twisted to optimise the performances at any point of the flight envelope. Hence, he highlighted the importance of a morphing device for LE and TE parts and wholly cambering sections on aerodynamic surfaces that want to act like actively aeroelastic structures.

Classical aeroelastic tailoring is also widely applied on modern wind turbine blades as with helicopter blades. Although wind turbines' rotational speeds are lower than helicopter rotor-heads, the considerable dimension of those blades still generate high cyclic loads for the blade structures. That brought engineers to adopt tailored designs to alleviate structures and self-adaptively control the operational speeds of the blades.

Aeroelastic tailored blades can deform according to a predetermined configuration when speeds exceed the design limit speeds. The passively induced deformations contribute to generate the dynamic stall effect over the blades' surfaces which is used to control and slow down the wind turbine speed, as described in the study of Veers *et al.* in [184].

A different technique to reduce inappropriate displacements of wing surfaces is presented in the experiments of Chattopadhyay *et al.* in [45]. Their research studies focused on actively controlling wing deformations not by tailoring the composite plies of the wing laminates but by embedding a series of piezoelectric sensors/actuators into the structure. The piezoelectric devices were used to control and dampen the wing oscillation or attitude variation during flight. They managed to reduce wing tip displacement by 36% with respect to the conventional layout and even more for acceleration and twist distortions.

Also Weisshaar *et al.* in [191] and Rocha *et al.* in [149] conducted experiments with embedded smart materials. Rocha included piezoelectric patches in between composite layers of a wing structure. The piezoelectric laminae were actively working to control the aeroelastic instabilities of the wing, especially for flutter circumstances. Once activated, they could responsively control and reduce the deformations induced by flutter conditions. With this technique, the engineers increased the wing model flutter speed of 12.5% without using directional tailoring for the composite fibres.

A total different philosophy is the one followed by other engineers, who in the 1980's were researching for methods to enable the exploitation of aeroelastic instabilities to create more performing aircraft configurations. The studies focussed on wing structures able to use the aeroelastic effect to deform structures for command surfaces usage. As already explained, it was the Active Aeroelastic Wing

(AAW) programme [2, 3, 26], primarily conducted by NASA on the modified version of an F/A-18 AAW, shown in Figure 2-51 that successfully introduced this novel flight technique.

Figure 2-51 NASA F/A-18 Active Aeroelastic Wing [2, 3].

Engineers wanted to investigate new control techniques to avoid reversal phenomena at transonic and supersonic speeds. The idea was to use the effective reversal circumstances to further twist the wing structure and use it as an entire, unified, big command surface, rather than using simple mechanically hinged activated ailerons. In order to allow such a performance, a few structural modifications were made to the F/A-18's wing. Stiffened panels were replaced by thinner and more flexible composite panels, and new actuation mechanisms were installed to actively control the leading and trailing edge deflections at each of the flight speeds. LE and TE were operated to initiate the reversal condition and perform the twist distortion upon the wing. Figure 2-52 shows the concept adopted on the AAW wing.

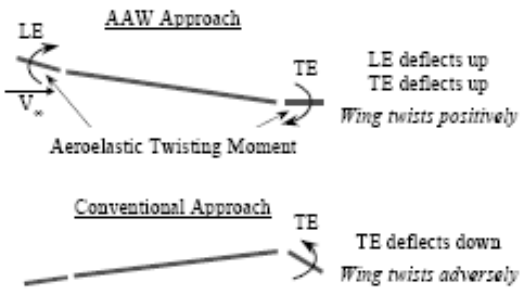

Figure 2-52 Aeroelastic wing concept description [26].

Whereas in normal wings the aileron varies the wing camber and generates the manoeuvring aerodynamic forces, in the AAW the LE and TE device co-operate to camber the wing profile in such a way that the pitching moment coefficient produced will start twisting the whole wing in the desired direction. When the wing is twisted it has changed incidence on all its aerodynamic sections, thus now the entire wing is working as a control surface rather than a single conventional aileron. The goal of the AAW control laws is to maximise performance using the wing flexibility. The AAW system works, with credit due to the series of mechanical LE and TE flaps whose deflection was able to induce the necessary forces and trigger the twist for the final aerodynamic effect, details of the model validation and test of the aeroelastic wing are discussed by Brenner in [31].

Clarke *et al.* [46] and Lizotte *et al.* in [114] synthesised the F/A-18 AAW ten years project, highlighting the results obtained from this study. They successfully developed a flight control system with adequate laws to control the LE and TE sections, either differentially or together, for aeroelastically activating the wing at various flight speeds. They assessed that the modified version of the aircraft, with improved flexibility of the wing, did not cause any reversal condition on the F-18AAW wing. Conversely, it has imposed usage limitations at supersonic speeds: high pressure flight conditions could not be reached by the vehicle. Proper modification of the control laws had to be done to take into account all possible manoeuvres and load reduction conditions, so the FCS prediction at subsonic speed was not matching the real situation, but the concept was successfully proved and flight tested aboard. All these issues proved the extreme complexity of an aeroelastic design, under the perspectives of FCS, structures, handling qualities, flight mechanics, aerodynamics and actuation systems. But it proved the feasibility of the aeroelastic effect principle, and just needed more advanced designs and materials to make it more reliably possible. Flick *et al.* in their work [70] studied the influence of the AAW approach in the conceptual aircraft design phase. They investigated the design of wings with different aspect ratios and found that possible aeroelastic advantages might be gained from such flexible configuration, although a weight penalty due to the complexity of the integration and mechanical systems was more likely. A more powerful mechanism to activate LE and TE surfaces to control the

wing's aeroelastic behaviour will be necessary to counteract the increased loading actions, and thus the increased weight. That is also an assumption the author has constantly acknowledged since the beginning of the doctoral project, thus making this study more challenging in finding a novel solution to overcome even simple technological issues such as weight and material problems.

Amprikidis *et al.* [10] proposed a different approach for varying the structural flexibility of a wing in order to exploit the aeroelastic effects. They did not force the structure to accomplish the desired deformations. They, instead, designed an internal structure whose stiffness could be tuned and changed by rotating spars to easily allow twist and bending deformations of the wing. Their design was based on classical rib and spar components. They proposed two variants of the same concept idea, one with spars sliding inside the ribs, and the other with rotating spars. They could adjust the level of required stiffness to attain the desired deformations by linear or angular movements of the spars. The variable stiffness design can automatically control the wing deformation, and consequently the aerodynamics of the surface, optimised according to different flight loads and circumstances.

Finally, in order to conclude this section, the only three cases of aeroelastic effect applications on vertical control surfaces are presented next. The first aeroelastic vertical tail study, shown in Figure 2-53, is about the case studied within the 3AS research programme [1, 159].

Figure 2-53 3AS Programme: Aeroelastic fin concept [1, 159].

The project evaluated the possibility of designing an all-moving tail whose internal shaft could vary the fin torsional stiffness and also its chord location between the 30% and 50% of the root chord. Those features allowed the tail to be mechanically tailored in stiffness according to the flight speeds and load conditions to enhance its flight effectiveness for different conditions. The variable stiffness shaft attachment could regulate the rotation of the whole tail, increasing and reducing the torsional freedom and so the tail efficiency with the varying flight speeds. As shown in Figure 2-53 (picture on the right), due to the beneficial exploitation of the aeroelastic characteristic, their novel design, because of the effectiveness gained in terms of stability and directional control, presented a smaller size than the original classical fin-rudder version. Based on the same aeroelastic principle of the 3AS design is the work presented by Amprikidis and Cooper in [8, 9, 11] who studied the possibility of exploiting the aeroelastic effect on vertical tails by implementing mechanical or magnetorheological fluid options, respectively, as adaptive stiffness attachment for the whole empennage. Similar techniques and principles, but with a different concept layout, are adopted by Allegri *et al.* in reference [6]. This design has already been introduced in the cambering device paragraph, and is based on the "belt-rib" concept of Campanile. The design exploits the sideslip circumstance to augment the directional stability derivative's effectiveness of the unconventional empennage. The assembly is mounted on top of a spring-damper support which can release the fin to enhance the stability weathercock effect by rotating under the pressure of the external loads. At the same time the fin, via the belt-rib elements activated by SMA wires, can also camber its profile. The torsional stiffness also varies with the flight speeds and attitudes of the aircraft.

The last work discussed in this section shows the aeroelastic effect application on different types of vertical surface. Nagel *et al.* in reference [128] proposed the concept design for actively and passively adaptive winglets. The passive adaptability was based on the aeroelastic tailoring technique used to orient the fibres of the composite main wing box and the winglets too. It allowed the whole assembly to withstand higher loads by reducing the wing root bending moment. The fibres' orientations allow both the fin and the wing to twist adequately to beneficially reshape and minimise the loads distribution over the wing surface, while the active

control of the winglet, used for wake vortex reduction, was actuated by a deflecting active control surface attached to the fixed part of the winglet, as shown in Figure 2-54.

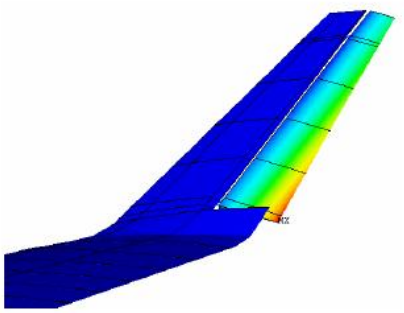

Figure 2-54 Active aeroelastic winglet [128].

The mobile part of the winglet trimmed the wingtip device for optimising drag generation and furthermore inducing a twist deformation on the whole wing, which helped with the trimming effect and further reduction of the induced drag.

Chapter 3 – Research Methodology and Model Analysis

3.1 Chapter Introduction & Methodology Description

The third chapter will describe the methodology study and disciplines applied for the design and modelling of the GRAF empennage. In detail, the next paragraphs will focus on the methods used to evaluate the fin aerodynamics, compute the loading actions, size the structural components to stiffness and strength requirements, and verify the in-flight directional fin performance. The research objectives aim at transforming a classical fin-rudder configuration into a seamless and gapless aeroelastic empennage with enhanced performance. The investigation and design process set within this methodology describes the path followed to study and work out the challenging technical aspects posed by the GRAF features. It was acknowledged from the earliest stage of the project that the technical aspects of the engineering process relating to both structural and aeroelastic designs in order to guarantee stiffness and strength requirements would have not represented the most challenging part of the study. The real hurdle was foreseen as making such a very low aspect ratio structure morph without the usage of open gaps and smart materials, and, above all, with a composite light frame layout. In detail, the real issue was to enable large movements of a fin shape with reduced degrees of freedom, due to its fixed root and no hinged connection. Therefore, there were apparently no ways of producing the manoeuvring side forces necessary to equate the effectiveness of conventional hinged rudders or slab tails.
The research investigation was subdivided into five different areas:

- Directional control and stability performance;
- Aerodynamic configuration and loading actions;
- Conceptual and composite structural design;

- Aeroelastic effect and actuation system;
- Manufacturing process.

Manufacturing wise, although this aspect has not been technically investigated in this research project, a brief discussion on the fin construction process will be illustrated in the fin prototyping section, in Chapter 7. The technical areas closely investigated in the thesis are illustrated in Figure 3-2. Those areas integrate all the steps described by Fielding in its 'design spiral', shown in Figure 3-1, related to conceptual and preliminary design processes [65] into three main ones.

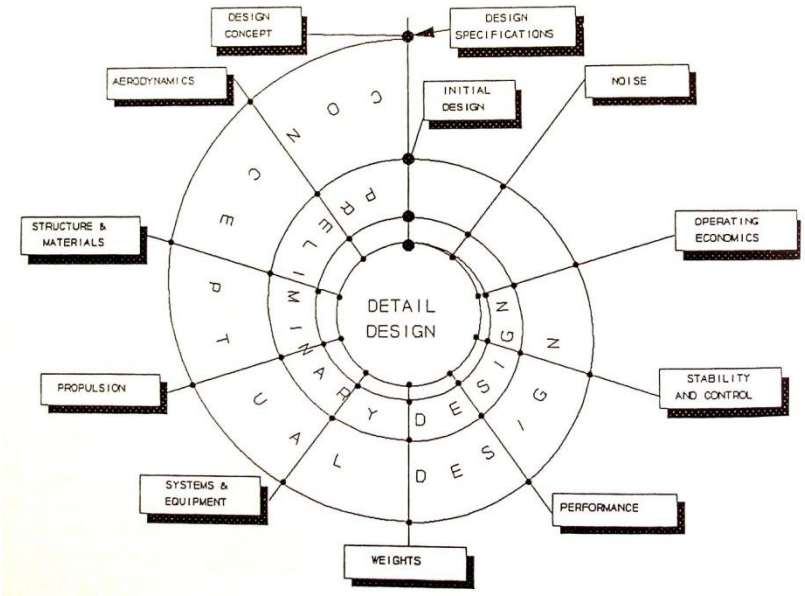

Figure 3-1 Fielding's design spiral [65].

Although in the specific case of the fin design, some stages such as 'propulsion, costs and noise' are not taken in consideration, the reader will notice that every single step, introduced by *Fielding's* diagram, has been followed during the study of this research project. Nevertheless they must be jointly developed as shown in the Figure 3-2 where the five technical disciplines are grouped in three different circle which jointly merge into the unique design of the unconventional GRAF empennage. The first two of the five different research areas have been enclosed into a unique circle referred to as the flight mechanics and aerodynamic performance, dealing with all those aspects related to the profile's aerodynamic efficiency, loadings and handling

qualities of the tail. A different technical area is the circle which integrated the conceptual and structural modelling of the novel. The third circle – needed to define the final technical configuration of the fin – is the area studying the integration of the aeroelastic effect and actuation systems into the unique form of the GRAF empennage.

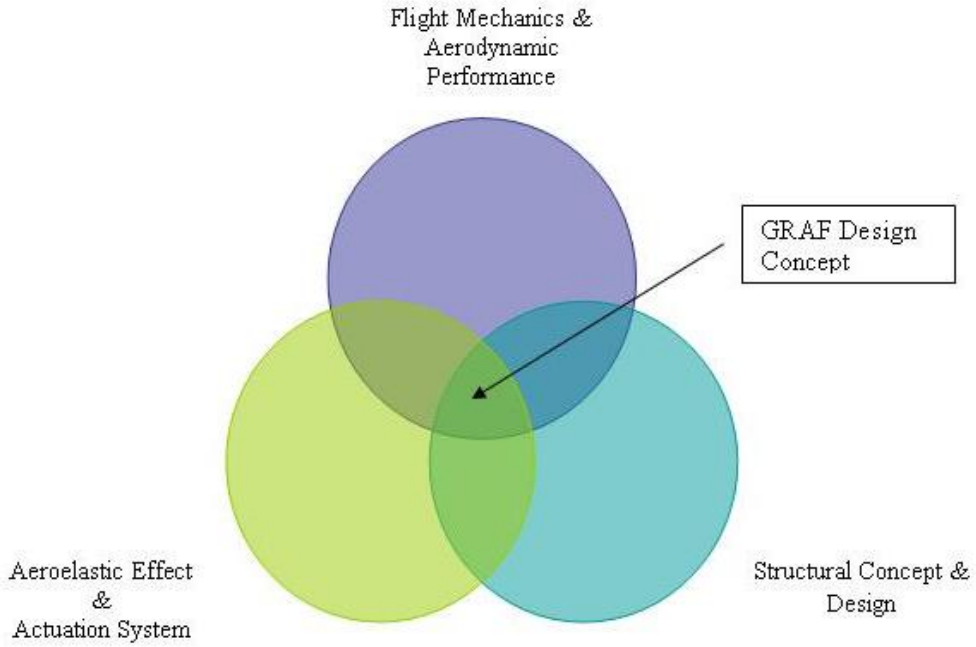

Figure 3-2 Multidisciplinary integration of the studied areas.

As anticipated in Chapter 1 with the musical analogy, all these areas as represented by the circles must be studied and applied together in order to decree the success of such an unconventional configuration. The lack of analysis in one area might compromise the effectiveness of the whole design.

The figure below – the 'Waypoints Chart', Figure 3-3 – anticipates the way the results will be presented in Chapter 5 and 6. It shows the technique adopted by the author to collect and present the results obtained from each phase of this research project. In particular, an aviation analogy relating to flight mission and waypoints is used to explain the path followed by the design study in collating those results and information necessary to enable the GRAF assembly to work and perform as required. Each stage and set of results must be completed and achieved before moving to the next waypoint.

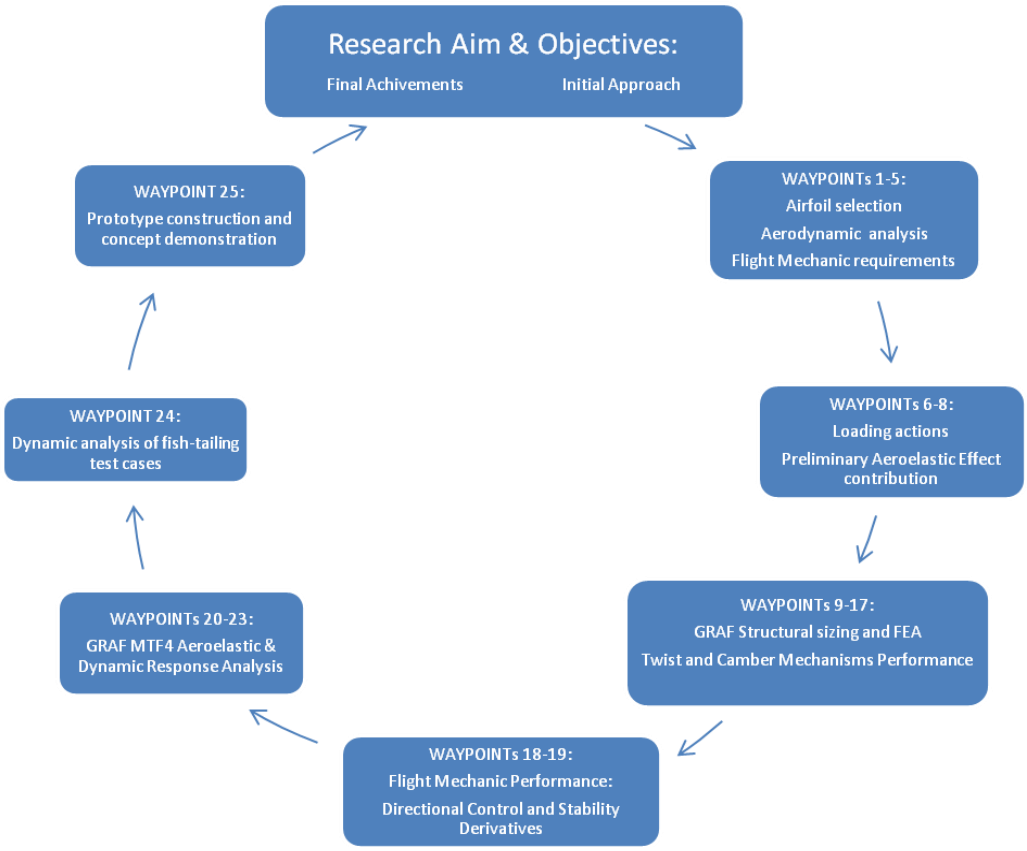

Figure 3-3 Waypoints chart

Different areas of the study correspond to numbered and sequenced results, namely waypoints. In order to complete the design, as a mission flown by an aircraft, all waypoints must be reached. If only one waypoint is missed, then the technical consequences might compromise the other waypoints and so the final outcome and performance of the GRAF structure.

Let us start by going into the technical aspects of the first part of the research study, by tackling the understanding of the aerodynamic and flight mechanic issues related to the novel empennage configuration.

3.2 Aircraft directional control and stability requirements

Before starting with the technical details of theories and methodologies, it must be said that the two definitions of lift and side force will be both interchangeably used in this thesis. The more familiar definition of lift concept is used, especially, to describe or explain aerodynamic phenomena referred to in the generic airfoil sections. While the side force expression is more properly adopted when it is specifically referring to the vertical tail assembly application and manoeuvres generation.

As already introduced in Chapter 2, the fin rear position, its surface area and its profile sections are the primary elements which sensibly affect the fin effectiveness for the directional stability and controllability of the whole aircraft. Let us take as the main reference coordinate systems for the aircraft flight mechanics study, the systems described by Roskam in [150], and shown in Figure 3-3. The subscript '*s*' denotes the stability reference system with respect to the body reference fixed to the aircraft structure.

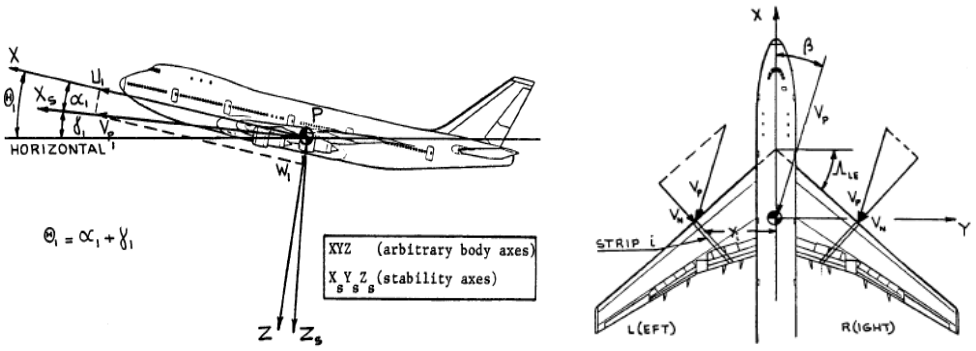

Figure 3-4 Rigid body and stability coordinate systems [150].

The primary stability task that vertical tails are predominantly designed for, is to counteract sideslip circumstances. The sideslip condition occurs when the lateral velocity $V_y \neq 0$. This phase is characterised by the sideslip angle $\beta \neq 0$, shown in Figure 3-3, which tends to move the vehicle nose from its original heading. This angle is the lateral-directional equivalent of the longitudinal angle of attack. The angle is defined as positive when the velocity vector lies on the right hand side of the *xy*-plane. In that case, it causes the aircraft to turn its nose to the left side, requiring the fin to counteract the disturbance with a clockwise yawing moment. Either for

stability or control mode, in order to produce the necessary yaw, the fin must generate, according to sign convention, a negative side force if a positive sideslip angle is met. Every time the fin operates in either of both modes, it generates three actions which correspond to these three following force and moments: the rolling moment L_1, the side force F_Y and the yawing moment N . Normally, the sideslip angle caused by a steady crosswind or lateral gusts is also responsible for inducing rolling motions on the entire airplane. This is mainly due to the fact that the fin's centre of pressure, where the side force applies, is usually located above the longitudinal axis of the fuselage and the wing plane. Therefore that distance acts as a moment arm for the side force generated by the fin surface, thus initiating a roll manoeuvre. Despite its importance in lateral stability performance, for the purpose of this study, this investigation will not focus on the rolling moment effect that such a bank-sideslip angle's interaction may have on the aircraft's attitude, but only on the directional attitudes. However, before starting with the details of the directional stability and control study, a brief description of the fin's contribution to the lateral effect, to highlight the fin's influence on rolling manoeuvres, is presented through equations (3.1 and 3.2a). By assuming a positive side wind circumstance, the lift (i.e. side force) coefficient generated on the vertical tail can be written as:

$$C_{L_V} = C_{L_{\alpha V}}(\beta - \sigma) = C_{L_{\alpha V}}\left(1 - \frac{d\sigma}{d\beta}\right)\beta \qquad (3.1)$$

where $C_{L_{\alpha V}}$ represents the lift-curve slope of the vertical tail and σ is the side-wash induced by the aerodynamic wing-body interference. Thus the rolling moment induced by the tail force is:

$$\Delta L_V = -z_{V_S} C_{L_{\alpha V}}(\beta - \sigma)\overline{q_V} S_V \quad (3.2a) \Rightarrow C_{L_{\beta V}} \beta \overline{q_\infty} S b = -z_{V_S} C_{L_{\alpha V}}\left(1 - \frac{d\sigma}{d\beta}\right)\beta \overline{q_V} S_V \quad (3.2b)$$

from which it yields:

$$C_{L_{\beta V}} = -C_{L_{\alpha V}}\left(1 - \frac{d\sigma}{d\beta}\right)\eta_V \frac{S_V}{S}\frac{z_{V_S}}{b} \qquad (3.3)$$

with $\eta_V = \dfrac{\overline{V_V}}{\overline{V_\infty}}$, where S_V is the fin surface area, S and b are the surface area and span of the main wing, and z_{V_S} is the height of the fin *CP* with respect to the aircraft

CG. V_V and V_∞ are respectively the airflow velocity on the vertical tail and at infinite distance in the free stream condition. Equation (3.2b) highlights the importance of the role played by the tail surface during rolling manoeuvres. The larger the tail size, the greater the rolling effect when a crosswind occurs. That means in order to reduce its effect and increase the lateral stability, airplanes should be provided, in the extreme case with no tails, or otherwise with as small as possible configurations. However, the fin size is generally defined and chosen in accordance with the necessary and required directional control and stability performance.

Let us focus now on what characterises the side force generation and which the parameters are that affect the control and stability tasks of vertical fins. The total airplane side force F_Y and the non-dimensionalised side force coefficient C_Y generated by a generic vertical tail can be written as:

$$F_Y = C_Y \overline{q_\infty} S \tag{3.4}$$

with C_Y depending on different factors expressed as:

$$C_Y = C_{Y0} + C_{Y\beta}\beta + C_{Y\delta_R}\delta_R + C_{Y\delta_A}\delta_A \tag{3.5}$$

where according to Roskam's definition:

C_{Y0} - is the side force coefficient for zero angle of sideslip and zero angle of rudder deflection. Its value is zero if the XZ plane is a plane of symmetry;

$C_{Y\beta}$ - is the change in side force coefficient due to a unit sideslip angle, also called a side force derivative due to sideslip;

$C_{Y\delta_R}$ - is the change in side force coefficient due to a unit change in directional control deflection;

$C_{Y\delta_A}$ - is the change in side force coefficient due to a unit change in lateral control deflection.

Each of those terms sensibly influences the sideslip attitude and the stability performance of the empennage. Their effect will directly influence the flight dynamic and comfort of the whole aircraft. The first coefficient is zero for fins with symmetric airfoil sections. It is different from the zero for helicopters' tails where asymmetric airfoil sections are cleverly chosen to assist the tail rotor by producing an asymmetric side force to counteract the main rotor torque. The second non-

dimensional coefficient contains the side force derivative contribution of the fin due to a sideslip angle. The detailed expression of $C_{Y\beta_V}$, has already been presented in equation (3.3). The third coefficient is linked to the side force generated by a rudder deflection through the following formula:

$$F_{Y_{Rudder}} = C_{Y\delta_R}\delta_R \bar{q}\ S \tag{3.6}$$

from which the expression of the side force coefficient due to rudder deflection can be obtained as:

$$C_{Y\delta_R} = C_{L_V} = \frac{\partial C_{L_V}}{\partial \delta_R}\delta_R = \frac{\partial C_{L_V}}{\partial \alpha_V}\frac{\partial \alpha_V}{\partial \delta_R}\delta_R = C_{L_{\alpha V}}\alpha_{\delta_R}\delta_R \tag{3.7}$$

where α_{δ_R} is the effective change in angle of attack for a unit change in rudder deflection. Therefore substituting equation (3.6) for equation (3.7) yields:

$$F_{Y_{Rudder}} = C_{L_{\alpha V}}\alpha_{\delta_R}\delta_R \bar{q}_V S_V \tag{3.8}$$

hence,

$$C_{Y\delta_R} = C_{L_{\alpha V}}\alpha_{\delta_R}\eta_V \frac{S_V}{S} \tag{3.9}$$

finally, a further contribution to the side force generation also comes from the influence that aileron deflection has on directional stability via the $C_{Y\delta_A}$ coefficient. For the purpose of this study and also because its order of magnitude compared to the others is negligible, the ailerons effect has not been taken in account in the GRAF performance evaluation.

Hence, as soon as the side force is generated, it causes the aircraft to react with a rotational moment with respect to the *CG* of the vehicle, namely the *yawing moment*. The yaw effect will tend to rotate the aircraft nose in the opposite direction to the one which the side force is pointing to. The expression for the airplane yawing moment is:

$$N = C_N \overline{q_\infty} S b \tag{3.10}$$

and, as similarly expressed for the side force, its total effect comes from the contribution of several terms, listed as:

$$C_N = C_{N0} + C_{N\beta}\beta + C_{N\delta_R}\delta_R + C_{N\delta_A}\delta_A \tag{3.11}$$

where:

C_{N0} is the yawing moment coefficient for zero angle of sideslip and zero angle of rudder deflection. Its value is zero if the *xz*-plane is a plane of symmetry;

$C_{N\beta}$ is the change in yawing moment coefficient due to a unit sideslip angle, also called a directional stability derivative;

$C_{N\delta_R}$ is the change in yawing moment coefficient due to a unit change in directional control deflection, also known as directional control power derivative;

$C_{N\delta_A}$ is the change in yawing moment coefficient due to a unit change in lateral control deflection.

Also in the case of the yawing moment effect, the first coefficient, C_{N0} is zero when the fin and the aircraft have symmetric shapes. The third coefficient $C_{N\delta_R}$ depends on the extent of the rudder deflection or TE deformation, while the last coefficient, $C_{N\delta_A}$, depends on the aileron's deflection. This last contribution is very effective on large aspect ratio wings, such as on gliders, because of the generated drag effect induced by the deflection and the consequently caused yaw, but it is neglected at this stage of the research as it is not required for the specific purpose of this study. The most important and effective of the four coefficients is the $C_{N\beta}$. It encloses three components:

$$C_{N\beta} = C_{N\beta_{WB}} + C_{N\beta_V} = C_{N\beta_W} + C_{N\beta_B} + C_{N\beta_V} \qquad (3.12)$$

The first one on the right hand side of the equation is the wing contribution to the yawing moment. The $C_{N\beta_W}$ is usually very small compared to the other coefficients; it is produced when either a positive or negative sideslip angle occurs. In that case, with a positive sideslip angle, the airflow velocities on the right side of the wing are higher than on the left side, thus creating more drag on the right wing panels than on the left ones. In this way a positive yawing moment to the right side is generated. Its contribution tends to directionally stabilise the aircraft. However, the most effective term of Eq. (3.12) is the one directly related to the element purposely designed for this scope, the vertical tail, with the $C_{N\beta_V}$. The combination of positive sideslip and side-wash angles increases the aerodynamic force generated by the fin. That further contributes to a positive yawing moment, which rotates the aircraft around its CG in

a clockwise fashion. This phenomenon, as consequence of an external disturbance diverting the aircraft heading, is responsively sensed and autonomously restored through the aircraft fin side force generation effect which is technically termed as the "*weathercock effect*" [48]. It stabilises the aircraft heading in side wind circumstances trying to point and keep its nose into the head-wind direction. This effect gives the airplane the tendency to yaw back until the sideslip angle is reduced to zero and it is also the primary task for which vertical stabilisers are designed. Therefore, by considering the side force and yawing moment coefficients determined in the case of sideslip and rudder deflection, and neglecting at this stage of the research the aileron contribution in Eq. (3.6 and 3.11), then it is possible to write:

$$N_{V_{Sideslip}} = C_{L_{\alpha V}} \left(1 - \frac{d\sigma}{d\beta}\right) \beta \overline{q_V} S_V x_V \tag{3.13}$$

then, as the yaw moment is equal to:

$$N_{V_{Sideslip}} = C_{N_{\beta V}} \beta \overline{q_\infty} Sb = C_{L_{\alpha V}} \left(1 - \frac{d\sigma}{d\beta}\right) \beta \overline{q_V} S_V x_V \tag{3.14}$$

it is possible to extract the final *directional stability derivative* of the airplane as:

$$C_{N_{\beta V}} = C_{L_{\alpha V}} \left(1 - \frac{d\sigma}{d\beta}\right) \eta_V \frac{S_V x_V}{Sb} \tag{3.15}$$

and by substituting the side force coefficient for rudder deflection from equation (20) into Eq. (3.15), it is possible to express the *directional control power derivative* as:

$$C_{N\delta_R} = C_{L_{\alpha V}} \alpha_{\delta_R} \eta_V \frac{S_V x_V}{Sb} \tag{3.16}$$

in which the quantity $\frac{S_V x_V}{Sb}$, as introduced in the previous chapter, is the volume coefficient of the vertical tail. In the particular case of this research project, the fin area and fin distance from the aircraft centre of gravity are parameters already fixed in the design specifications. They have already been determined in the original configuration of the baseline aircraft, the Eclipse UAV, chosen as the case study for this research. Although the fin area is kept identical to the original empennage, the planform geometry of the novel design will change from the baseline configuration. The actual Eclipse fin shows a trapezoidal shape, whilst the new aeroelastic design

will assume a simpler, rectangular planform. The rectangular shape has been imposed at this stage for structural and mechanical reasons which are explained later in the text.

From the previously described signs convention, as well as indicated by Roskam in [150] and Phillips in [140], it transpires that the mandatory condition to have directionally stable aircraft is established by the relation:

$$C_{N_\beta} = \frac{dC_n}{d\beta} > 0 \qquad (3.17)$$

This translates into the fact that when a positive sideslip angle affects the aircraft heading, by rotating its nose on the left hand side, the stabilising yawing moment must generate an opposite rotation on the right hand side of the *xy*-plane. The clockwise rotation corresponds to a positive yawing moment which determines the sign of Eq. (3.17). Two more derivatives also exist for both aileron and rudder deflection circumstances. Neither will be considered here because no effect of the aileron will be taken into consideration in this study, and no deflecting rudder will be included in the new fin model. However, although a morphing TE section is included within the GRAF design and expected to work similarly to a hinged rudder, its effect is not considered in the rudder deflection coefficient. Its contribution is, instead, taken into account in the lift-curve slope coefficient. Eventually, the seamless TE deformation changes the profile camber line and so the $C_{L\alpha}$ of the whole airfoil section, which takes into consideration the increased efficiency of the cambered profile.

This flight mechanic analysis has given the information needed to assess and enhance the stability performance of the GRAF empennage. The research will focus the attention on developing a system able to improve the effectiveness of the $C_{N\beta}$ and $C_{N\delta_R}$ derivatives. That will primarily consist of increasing the contribution of the $C_{N\beta}\beta$ term in Eq. (3.14), which definitively represents one of the objectives of the novel aeroelastic design. Two ways of enhancing the $C_{N\beta}\beta$ contribution are explored. The first method investigates the possibility of modifying the lift-curve slope of the fin airfoil sections $C_{L_{\alpha V}}$. The airfoil efficiency can be changed by simply shaping the symmetric airfoil sections into a more lifting asymmetric profile. A

morphing TE section, later explained in this chapter, will be purposely designed and integrated into the GRAF tail to increase the side force generation effect. The second factor, used to improve the stability effectiveness, is the sideslip angle β. The simplest way to increase the sideslip angle is to rotate the whole fin structure opposite to the wind direction. The fin rotation will make the entire structure work as a sail on a sailing boat, offering the largest portion of wet surface to the wind pressure. That means the rotated fin might feel an angle of incidence larger than the initial sideslip angle. However, because of the gapless constraint, the fixed root fin layout will limit this capability. The GRAF design is not totally free to rotate, because of its root section sealed onto the fuselage back skin, and, unless the joining is made of extremely elastic materials, it cannot move from that position. Therefore, at this stage of the research it was clear that the fin rotation could be achieved in only a partial way. The GRAF design eventually deforms in a twist shape. The twist effect will add a further angle of attack to the one already generated by the sideslip incidence. Therefore, the fin aerodynamic resultant, originally supposed to be generated only by the β angle, is now incremented because of the added incidence due to the twist angle ϑ. Figure 3-4 shows the two angles and the technique the fin will use to open its asset to a larger angle of deflection $\alpha = \beta + \vartheta$.

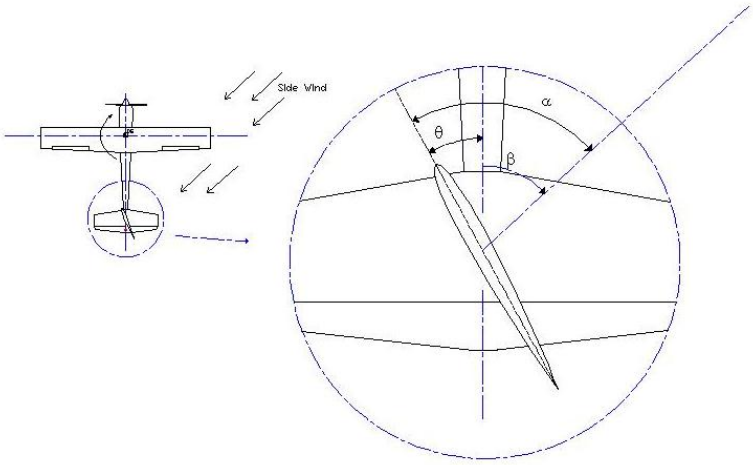

Figure 3-5 CAD illustration of increased AOA due to side slip and twist angles.

The same techniques applied for the stability tasks, with similar principles but different activation mechanism, are involved in the study of the directional control authority. The objectives of the directional control study focus on the second and

third terms of Eq. (3.5). The second term has already been discussed for the stability performance, whilst the third term – $C_{Y\delta_R}\delta_R$ – whose detailed expression is written in Eq. (3.9), leads directly to the study of the two terms $C_{L_{\alpha V}}$ and α_{δ_R} contained in Eq. (3.16). The reason why other parameters are not considered in the study is because the rest of them are already defined in the specification of the selected case study of the Eclipse UAV. The $C_{L_{\alpha V}}$ will be varied in the same way that has been suggested for stability purposes in order to seamlessly emulate a rudder deflection. The camber line modification enhances the effectiveness of the fin profiles for side force generation. In addition, it also positively influences the α_{δ_R} term. As a matter of fact, any rudder deflection which corresponds to the α_{δ_R} term in Eq. (3.16) varies the angle of incidence for the entire airfoil section. Moreover, the warping deformation, which in the case of control purposes is induced by mechanical servo actuators rather than by external disturbances, will further increase that angle by gradually rotating the fin profiles during twist. The angled sections, plus the cambered shape, eventually substitute the control authority of a deflecting rudder, by sorting out the desired effect of side force generation under the mechanical input of the actuation system. The command inputs sent to the actuators, together with the self-adaptive exploitation of the aeroelastic effect, are the only differences between the GRAF stability and control modes. The two modes are governed by identical aerodynamic and flight mechanic principles. When the control authority tasks are performed, the actuation system can restrain the fin from deforming under the external pressure of side wind circumstances. While in the stability mode, the fin, released to freely warp, engages a self-adaptive mode by sensing and twisting according to the side wind circumstances.

The fifth chapter will present and discuss the results of the performance investigation. The analysis is conducted using aerodynamic panels method programs, such as JAVAOIL [101] and ESDU-b1v95010 [60] for the side force and yaw computation. The Flight Loads tool of the MSC/ NASTRAN package will be used, instead, to compute the controllability and stability derivates of the whole model.

This section of the study has been carried out with the scope of evaluating whether and in what way such a novel tail design, with apparently more constraints and

limitations than classical layouts could generate the same or even an improved level of performance from the GRAF technology adoption.

The next section of the chapter continues with the performance study, describing in greater detail the ways the aerodynamic efficiency of the whole fin might be improved by reducing the drag force production.

3.3 Enhanced aerodynamic efficiency by reducing drag

This section investigates those potential factors which might contribute to the reduction of drag generation on the vertical tail. By considering the horizontal components of the whole aircraft aerodynamic resultant, it is possible to express the total drag force as:

$$D = C_D \bar{q}_\infty S \tag{3.18}$$

with

$$\overline{q_\infty} = \frac{1}{2}\rho V_\infty^2 \quad and \quad S = S_{Body} + S_{Wing} + S_{H-tail} + S_{V-tail} \tag{3.19}$$

and where the total drag coefficient may be written as:

$$C_D = C_Z \sin\alpha + C_X \cos\alpha \tag{3.20}$$

where C_Z and C_X are the vertical and horizontal components of the aerodynamic resultant force respectively, projected onto the xy-plane offset by the angle of incidence α. The terms in equations (3.19) represent the free-stream dynamic pressure and the total wet surface area respectively. The non-dimensional drag coefficient for a generic aircraft can be further expressed as:

$$C_D = C_{D_0} + C_{D_\alpha}\alpha + C_{D_{iH}} i_H + C_{D_{\delta E}}\delta_E \tag{3.21}$$

where the last two terms of the equation refer to stabiliser and elevator parameters which will not be taken into account in the study because they are part of the

longitudinal performance. Also the second term, linking the drag intensity to the aircraft's angle of attack, has not been considered here for the same reason. The C_{D_0} coefficient, instead, contains the drag contributions of all components of the aircraft such as the fuselage, wings and empennages. It is easily rewritten as:

$$C_{D_0} = C_{D_{Body}} + C_{D_{wing}} + C_{D_{H-tail}} + C_{D_{V-tail}} \tag{3.22}$$

Specifically, this study aims at reducing the contribution of the $C_{D_{V-tail}}$ to the total drag force effect. From a vertical tail standpoint, the aerodynamic drag force can be split into two terms, which are the two force components related to viscous (parasite) and induced drag:

$$D_{V-tail} = D_{0_{V-tail}} + D_{i_{V-tail}} \tag{3.23}$$

from Eq. (3.23), the non-dimensional coefficients can be extrapolated as:

$$C_D = C_{D_{V-tail}} = C_{D_0} + C_{D_i} \tag{3.24}$$

therefore, having identified the vertical tail as the primary object of the study, the "*V-tail*" subscripts will no longer be used in the rest of the text, unless necessary when other components are discussed.

There are three main reasons which create most of the drag effect onto an aerodynamic section. Included in the two coefficients of Eq. (3.24), they are:

1. flow separation;
2. parasite/form effect;
3. vortexes induction.

The first two types of drag are enclosed in the 'C_{D_0}' component, while the third one, by linking the drag to the lift circulation around the airfoil section, is described by C_{D_i}. In detail they are:

1. Flow separation: there are different circumstances which lead to this phenomenon. In particular, flow separation occurs in situations of high angles of attack, flight speeds approaching stall speeds, large angles of deflection for command surfaces, unsealed gaps, and shock waves. By dealing with low subsonic vehicles, shock waves can be excluded from this study. Likewise, stall speeds and high angles of attack are excluded once it is assumed the flight control system (FCS) will keep the aircraft within safety aspects of speeds and incidences. Therefore, the final aspect regarding large surface deflections and unsealed gaps must be investigated yet. Plain command surfaces deflected at large angles can create uneven pressure distribution over the entire aerodynamic surface letting the flow stall and separate. Thus, the vortexes generated by the flow separation contribute to the drag force by increasing the aerodynamic resistance and the loss of control authority. A similar reason is the cause which generates vorticous flow on open gaps between mobile parts and rigid bodies. The vorticous flow detaches from the aerodynamic surface and contributes to a worsening of the drag effect. In order to smooth this effect, plain and rigidly deflected surfaces are intended to be integrated and converted into seamless morphing layouts. Moreover, sealing all the gaps in the design will avoid pressure leaps in the flow due to surface discontinuity. That will also smoothly distribute the airstream from the LE to the TE without separation and drag vortexes effects. The two charts of Figure 3-5 show the RAE 101 airfoil section with 10° of deflection for both plain and cambered flap.

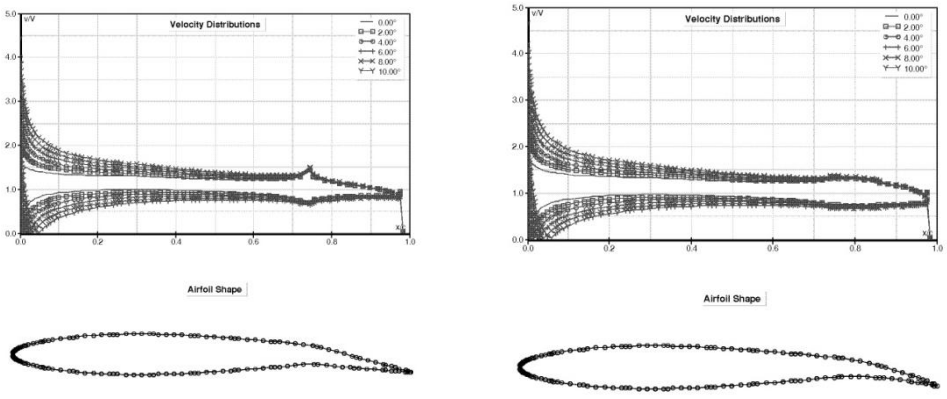

Figure 3-6 Pressure distribution on plain rigid (a:left) and seamless (b:right) flap.

Although no gap has been included in the model of Figure 3-5(a), its Cp diagram distribution already denotes a peak corresponding to the hinge line, where abruptly the surface varies its inclination. The presence of an unsealed gap will further stress that same point.

2. The parasite drag is represented by the friction between the airflow and the surface of the aerodynamic element. It is simply due to the aerodynamic encumbrance of the structure in the free stream. There are two elements which can considerably affect and improve this aspect: the fin geometry and the airfoil sections. The former can lower the fin aerodynamic resistance if the size of the tail is reduced. The latter might contribute to it if selected with a thinner profile. The airfoil choice is not of interest to this project as the same airfoil section adopted in the original tail of the Eclipse vehicle is used.
The adoption of a scaled down tail version might be an applicable solution for drag reduction, but an accurate study must guarantee a smaller fin can provide the same control and stability requirements as a conventional one.

3. Finally, the induced drag is the component strictly related to the lift generated by the airfoil section. This drag force contribution is created by the wake-induced flow. As explained, by Katz and Plotkin in [103], through the lifting-line theory, the lift and drag force are not independent of each other:

$$D_i = \rho \overline{q_\infty} \int_{-\frac{b}{2}}^{\frac{b}{2}} \alpha_i(y)\Gamma(y)dy \tag{3.25}$$

$$L = \rho \overline{q_\infty} \int_{-\frac{b}{2}}^{\frac{b}{2}} \Gamma(y)dy \tag{3.26}$$

The induced drag, expressed via the integral form (3.25), is strictly dependent on the produced lift. The linking element is the flow circulation $\Gamma(y)$. It is the element responsible for generating the lift force on the airfoil section, but at the same time it is also causing the vortexes to detach from the surface extremities and induce drag.

The induced drag coefficient can be expressed as:

$$C_{Di} = \frac{C_L^2}{\pi S e} \tag{3.26}$$

where C_L is the lift coefficient of the fin airfoil sections, and S the surface area. Although Wright and Cooper [200] suggest the Oswald's number 'e' be chosen between 0.85 and 0.95 in order to better optimise the induced drag, its value, in the case of the GRAF design, will not be changed at this stage and will rely upon the already defined configuration of the baseline Eclipse vehicle. From Eq. (3.26) it is evident that the only two parameters that can undertake any modification for improvements of the fin aerodynamic efficiency are the surface area 'S' and the lift coefficient C_L. On the one side a larger tail will positively influence the induced drag reduction, but on the other one, a bigger fin will affect the parasite drag and, more seriously, the vehicle lateral stability. Hence at this stage, neither the fin surface nor the lift coefficient will be changed. The optimisation study to find the best compromise between the C_L and the C_{Di} effect has not been taken in consideration in this research study. Therefore, in order to decrease the penalising effect of the C_{D_0} term in Eq. (3.23), two technical solutions are considered and applied. A cambered profile shape for a smooth aerodynamic transition will be created by a morphing trailing edge device and a compliant structure will be designed to gradually deform the trailing edge part of the fin. In addition, all the gaps normally existing on control surfaces with classic hinged configurations will be sealed.

Before concluding this section, there is one last parameter which is discussed here that might aerodynamically influence the fin performance, i.e. the fin sweep angle. The novel empennage has a rectangular planform geometry rather then the Eclipse original trapezoidal shape. The new tail then lacks front and rear swept edges in favour of two right ones. Although the new shape was primarily dictated by structural and conceptual design reasons, it is believed that due to the low subsonic flight speeds the advantage of having swept fin edges is negligible. In the particular circumstance of a low subsonic fin, as shown in the diagram of Figure 3-6 developed

by Roskam, for both cases of the existing Eclipse vertical tail and the novel aeroelastic fin with AR=1.34, the sweep angle has a minimal influence on the flight performance.

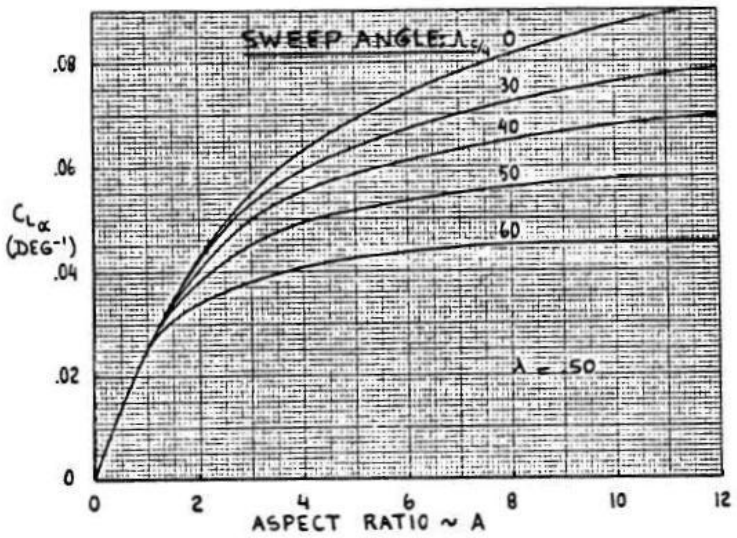

Figure 3-7 Roskam study on sweep angle for various AR surfaces [150].

However, even with right edges some assembling tricks may eventually be adopted to provide for the lack of a swept angle. The solution consists of inclining upwards the fin mount inside the fuselage connection. In this way the GRAF following the inclined position of the fuselage support, will tilt backwards, simulating a provisional swept angle configuration, as shown in Figure 3-7.

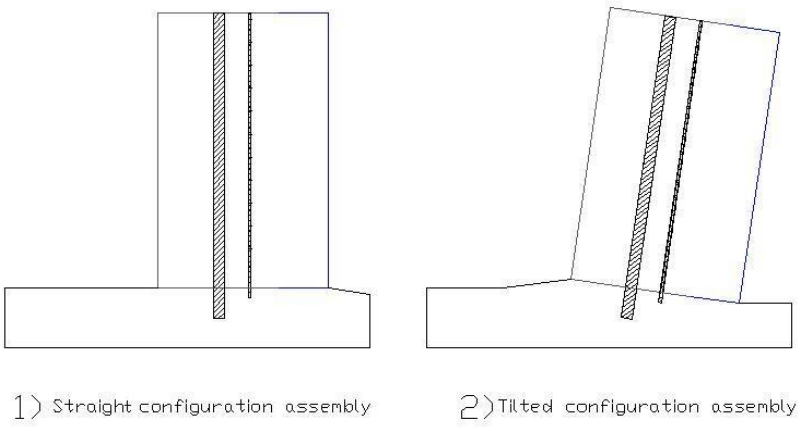

Figure 3-8 CAD illustration of the GRAF assembly variants.

3.4 Aerodynamic loading actions

The structural design of the GRAF model starts with the analysis and investigations into the aerodynamic loading actions generated on the GRAF tail. The RAE 101 profile of the original fin configuration is also considered for the novel design. The rectangular planform geometry of the GRAF presents an identical span, surface area and mean aerodynamic chord to the Eclipse's fin. The reason for keeping the same parameters within a different shape is to prove that the enhanced effectiveness can be, in practice, generated with identical aerodynamic characteristics to the preceding configuration but with a reengineered layout and a more performing concept design.
The aerodynamic analysis of the fin has been carried out using the open source program JAVAFOIL and the FORTRAN based code ESDU b1v95010. These codes run 2-D analyses and have been used to identify both the pressure distribution around the airfoil section and the loading actions estimation over the fin surface. They have also been used to compute the aerodynamic coefficients necessary to calculate the side force and the yawing moment performance of the novel fin. The section of the thesis dedicated to the results will present a comparison of the side force performance generated by the conventional Eclipse fin with hinged rudder and the GRAF model. It will discuss differences and beneficial effects gained from potential GRAF applications. The JAVAFOIL tool is a 2-D aerodynamic program that uses potential flow analysis (details of the potential flow theory are included in Appendix A), via a high order panel method (linear varying vorticity distribution) for inviscid flow. It also, via an integral method, takes into account the boundary layers analysis and considers the separation and transition implemented according to the procedures explained by Eppler in [61, 62]. The ESDU program is based on the Multhopp-Richardson solution for steady lifting surface theory [126]. The program calculates the spanwise loading distributions of local lift and pitching moment coefficients for varying incidences, camber and twist. Furthermore, the program can also take into account the deflection of command surfaces on the LE and TE of the surface. The flow chart in Figure 3-8 describes the procedure followed to estimate the aerodynamic performance and load distribution for the selected airfoil shapes. The

load distribution has been investigated using the ESDU program. It can take into account the AR of the wing and give the loads per unit span all over the fin surface.
From the preceding flight mechanic and aerodynamic study it has been defined that in order to perform properly, the GRAF will need both a twisting and cambering actuation of the fin profiles. The flow chart below illustrates the steps followed during the first phase of the aeroelastic fin study.

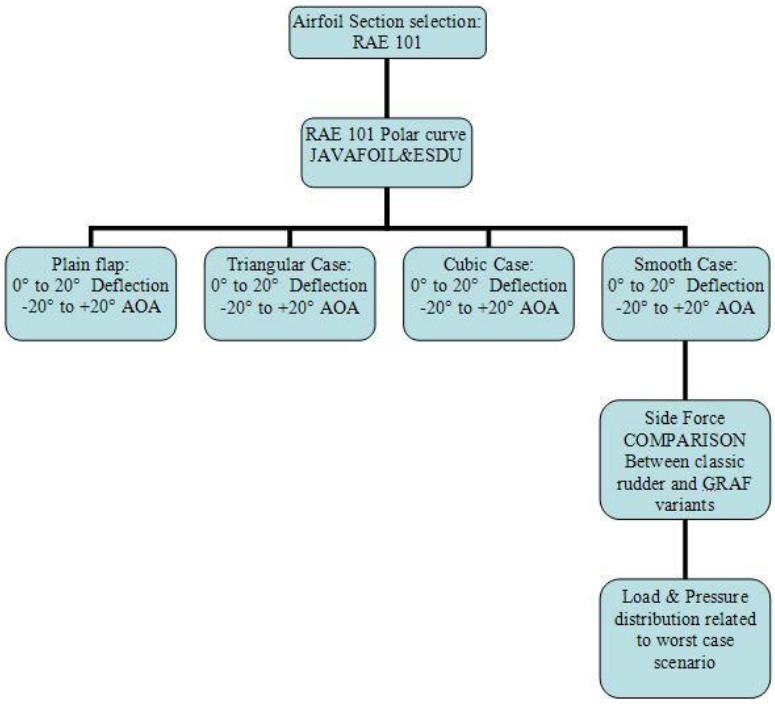

Figure 3-9 Flow chart for the aerodynamic configuration & loading definition.

Before dealing with the structural sizing corresponding to the worst loading case scenario, the analysis has started with the aerodynamic evaluation of four different configurations for the cambered TE sections of the GRAF design. A MATLAB code has been purposely written to study the diverse options for the seamless TE shape of the rudderless profile. The code works by allowing the user to deform any portion of the airfoil chord according to four different shapes. The four different types of deflection are:

- Classic plain flap (plain, conventional rigid surface);
- Cambered option 1 (triangular): assumed to be generated by a triangular load distribution;

- Cambered option 2 (cubic): following a third order equation curvature;
- Cambered option 3 (smooth): setting a uniform curvature distribution.

(for the sake of explanation the word “flap” will be used in this text to refer to any generic mobile surface). The first option simply replicates the conventional plain command surface rotating around the hinge line. The second option instead tries to follow the deformation that a typical triangular load distribution over a flap surface might produce, as shown in Figure 3-9 from Howe [96]. The third option has been input using a third order curvature equation, whose starting point can be arbitrarily decided by the user in the MATLAB program. The fourth option can also be specified by the user by arbitrarily distributing the curvature on the TE chord to simply define the number of the segments in which the TE will be subdivided for the deformation. The default case used to run this last analysis case has set two main points of curvature at 1/3 and 2/3 of the TE chord. In all four cases the flap angle of deflection is conventionally defined as the line joining the very end of the trailing edge with its imaginary centre of rotation, normally represented by the hinge line.

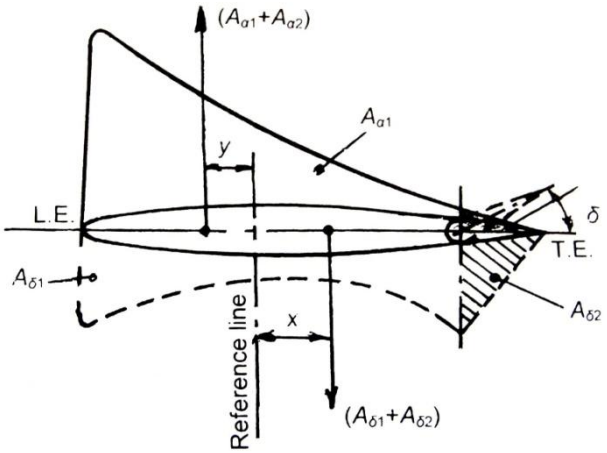

Figure 3-10 Classic airfoil pressure distribution [96].

The coordinates of the four diverse airfoil sections are then input into the JAVAFOIL database in order to run the analysis to get the lift, drag and pitching moment coefficients for the different shapes at various angles of attack. Amongst the four cambered options, the *smooth* curvature is eventually chosen as the most effective TE shape for a good compromise of lift and low drag generation. The aerodynamic results of the four cases, which will be discussed in Chapter 5, will explain the

technical reasons for this choice. The aerodynamic coefficients are then used to compute both the side force and the yawing moment of the GRAF model. A comparison with the classic hinged rudder performance and the novel configuration is made and presented in the results section. For the novel design, several different combinations of twist angles and TE camber deflections are tested in order to optimise the two types of system actuation with the side force effectiveness. The intention of the study is to establish the minimum required twist angle to ensure the needed control authority and stability to safely manoeuvre the aircraft. After having established the loads and the forces' requirements, the structural design will start focusing on sizing and developing the concepts needed to accomplish the desired stability and control tasks on the unconventional tail. A series of assumptions are made at this point of the GRAF study:

- all the loading cases induced by the yaw motivator (i.e., the conventional rudder on a classical configuration, and the warping and cambering devices on the GRAF model) start and end with steady level flight conditions;
- the extent of the twist rotation will be limited by aerodynamic and structural requirements;
- the activation of full camber deflection of the morphable TE section and maximum twist angle of the fin structure will not be coupled to correspond with the maximum design speed, i.e. to avoid high loads;
- only low subsonic speeds will be considered for the case study (i.e. $\leq 90 m/s$).

In normal flight operations, the full deployment of conventional rudders is operated only at low speed, just to increase the yaw motivator effectiveness during critical flight phases such as landing, take off, and engine failure circumstances. At high speed the full activation of the control surface will induce two problems: firstly, high loads on the structure and secondly, considerable lateral acceleration. These two problems are severe circumstances which can affect both the structure integrity and also the on board passengers' and crews' comfort when subjected to extreme lateral g-forces. The lateral acceleration for manned aircraft is normally limited to 2g [96, 152], based on pilot resistance to lateral g-forces. Conversely, these factors might be

increased when unmanned systems are taken into consideration. The only problem with those vehicles limiting the lateral acceleration is related to structural and manoeuvrability issues. In the particular case of the GRAF configuration the only factor limiting the fin deformation is the stall angle of the profiles. Two mechanical springs and stoppers will block the fin to the maximum twist angle. Normal operational recommendations suggest that the dynamic stall angle of vertical tails is usually 1.5 times the static one, as discussed by Howe. The GRAF profile stall angle increases when the section camber is activated. Thus cambering the airfoil, in addition to the twist effect, raises the limit angle of the whole fin. Due to the twisted shape, the fin tip will stall first, especially when sideslip angles are also taken into account. In detail, the stall angle for the RAE101 with cambered profile can achieve up to 13° AoA. This translates into a dynamic stall angle of about 19.5°. All this information, together with the results obtained from the aerodynamic analyses, have been used to define the worst loading case scenario related to the most effective twist and camber deflections and operating speeds of the aircraft.

The fin structure has undergone two different loading case scenarios. They have been divided into static and dynamic cases. The first set of loads comes from the ESDU analysis and refers to steady aerodynamic conditions. The second set of loads, related to unsteady aerodynamics, has been computed for the aeroelastic instabilities and for the dynamic and gust response analyses using the Flight Loads Tool of the MSC/NASTRAN package.

3.4.1 Steady aerodynamic loading case

As already introduced, the static load condition corresponding to the worst case scenario has been applied to size the structural components of the GRAF assembly and verify that stiffness and strength criteria are satisfactorily met. The aerodynamic pressure related to the worst loading condition has been applied to size the skin panels of the fin and its primary shaft, and to estimate the actuation power needed for the GRAF activation. The GRAF research study primarily focuses on the conceptual design and performance analysis of the novel tail, by involving several different

technical aspects of the design. Hence, the reason for choosing simpler and quicker 2-D aerodynamic codes to run the loadings and aerodynamic simulations, rather than using more sophisticated 3-D computational fluid dynamic (CFD) models and programs for this part of the study. Although more accurate, those CFD models, besides taking a longer time to run, also need more complex and detailed aerodynamic meshes for the simulations. As already mentioned, in addition to the JAVAFOIL and ESDU programs, another specific aerodynamic tool has been used to investigate the properties of the novel aeroelastic fin: the Flight Loads tool of the MSC/NASTRAN package. This tool allows the integration of the entire FE model of the fin structure with the Doublet Lattice Method (DLM) analysis used to assess the flight performance of the fin and the whole vehicle. In order to calculate the flight dynamic derivatives and the forces to be applied to the structure, the NASTRAN tool defines its own load distribution over the aerodynamic boxes specifically built and introduced to integrate the aerodynamic DLM model with the structural FE model of the tail.

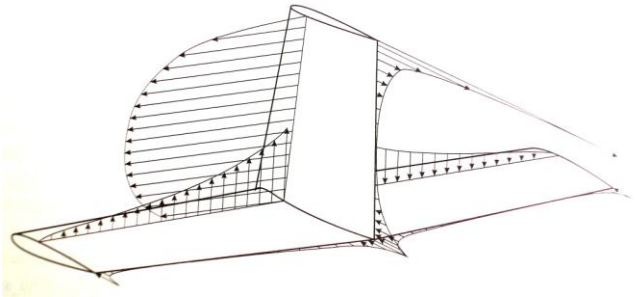

Figure 3-11 Classic tailplanes aerodynamic loads distribution [140].

Figure 3-10 shows the typical distribution of the external loads on rigid conventional vertical tailplanes. That typical load distribution was utterly changed by the adaptive flexibility of the GRAF empennage. The twisted shape and cambered profile generate a less symmetric load distribution which, according to the twist degrees and TE deflection, may differently affect the various areas of the tail. Once calculated, the load pressure corresponding to the worst case scenario is then input into another MATLAB code to calculate the displacements of the panels under the operating side loads. The code can establish the number of skin layers needed to withstand the loads and the space in between two adjacent ribs. The same type of load has been applied to size the other primary components of the tail. The primary shaft will, therefore, be

designed to withstand the whole loading action derived from the aforementioned pressure distribution. All the static loads are applied to the structure with a load safety factor equal to 1.5, in accordance with the ultimate load requirements for aeronautical structures. In order to assess the validity of the computed loads, a comparison with the empirical formula suggested by Howe in his text has been conducted during the sizing of the primary shaft of the fin. Howe's expression for vertical tail loads comes from operational and practical experience over past and current design projects. The formula calculates the total vertical tail load as:

$$L_{Fin} = \frac{n_1 mg}{8} \tag{3.27}$$

where n_1 is the maximum design vertical load factor of the whole vehicle; m is the mass of the aircraft at MTOW, and g is the gravity acceleration. The comparison between the empirical formula and the loading results obtained from the theoretical real distribution are presented in Chapter 5.

3.4.2 Unsteady aerodynamic loading case

The part of the study investigating the dynamic loading actions due to discrete gust loads and structural fin responses to frequency and time dependent forces is presented here. Three different typologies of investigation are conducted on the GRAF model:

1. Modal frequency response analysis;
2. Modal transient response analysis;
3. Discrete *1-cos* gust response analysis.

The first considers a sudden activation of the fin to its maximum displacements in order to generate the worst load case scenario. The loading excitation frequency varies within a set of specified frequencies of interest. The corresponding frequency response of the fin structure is then analysed to verify that the rapidly varying set of forces do not dangerously excite the structure in resonance phenomena resulting in

the consequent failure of the whole assembly. The second type of analysis is the modal transient response analysis. The same typology of worst load scenario is engaged by the fin for a finite period of time. The investigation studies its response during the rapid and transitory changes of attitude of the model. For both analysis cases the results data are presented in Chapter 6. They will discuss the displacements of the structural and aerodynamic grids nodes and the reaction forces of the fin constraints. Finally, the last type of dynamic loading case is the discrete gust response. As introduced at the beginning of the thesis, this project aims to design a novel fin configuration for small-medium UAVs. Although, to date, there is not yet any specific regulation for airworthiness certification of unmanned aerial vehicles, the CS-23 regulations have been studied and taken into consideration as baseline references to assess the structural requirements of the novel fin design when sudden lateral gusts occur. In particular, as specifically required in the 'Subpart C – Structure - Vertical Tail' of CS 23, and in detail within sections CS-23.443 'Gust and Turbulence Loads' and CS-23.333 'Flight Envelope', there are two options to be considered for the application of gust loads relating to dynamic load conditions. One is based on a semi-empirical formula contained in section CS-23.443 and to be used when a not analytical approach is applied. The second one is based on the analytical computation of the '*1-cos'* curve shape for the gust case required in paragraph "Gust and Turbulence Loads" of section CS-23.333 (a copy of the paragraph is attached in Appendix C). The scope of this type of analysis consists of evaluating the fin and aircraft responses to the external disturbance, in terms of the fin and of the whole aircraft time response, to counteract the sudden gusty perturbation. The second section of Chapter 6 will present the aeroelastic dynamic response results of the GRAF model undergoing such a type of disturbance.

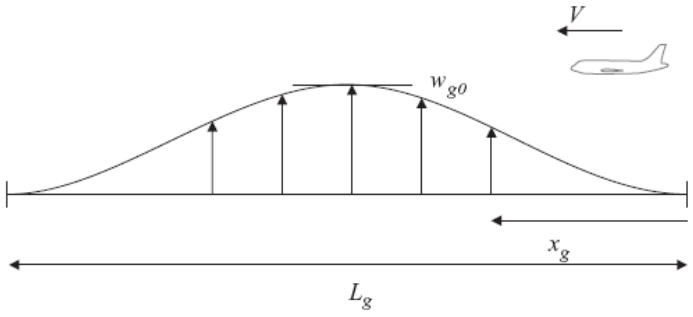

Figure 3-12 Illustration of 1-cos gust load velocity distribution for vertical case.

The "*1-cos"* lateral gust speed distribution can be written as follows:

$$\begin{cases} U = \dfrac{U_{ds}}{2}\left[1-\cos\left(\dfrac{\pi s}{H}\right)\right] & for\ 0 \le s \le 2H \\ U = 0 & for\ s > 2H \end{cases} \tag{3.28}$$

That gives the shape of the *1-cos* gust wind speed that must be taken into consideration for the dynamic analysis, where *s* is the distance penetrated into gust, U_{ds} is the designed gust velocity, and *H* is the gradient of the gust (specifying where the gust reaches its peak). The regulations, according to CS-23.333, establish the gradient of the gust as $H = 25\bar{c}/2$, where $\bar{c}$ is the wing mean geometric chord. The *1-cos* gust condition, as well as the other typology of dynamic load cases, have been implemented in the FE models of the GRAF design and solved by using the NASTRAN Flight Loads package. The results are presented in Chapter 6.

3.5 Structural Design and GRAF Modelling

This section of the methodology focuses on the structural development of the GRAF model. The novel aeroelastic fin will be designed and built to satisfy the structural stiffness and strength requirements while accomplishing the primary four targets necessary to enhance the flight performance. These are listed as follows:

- To increase the aerodynamic side force coefficient by increasing the profiles $C_{L\alpha}$;
- To reduce the aerodynamic drag force;
- To generate bigger angles of attack to augment the control and stability effectiveness and response;
- To design a rudderless structure lighter than conventional empennages.

The first point aims to develop a compliant structural layout that will enable the fin to seamlessly camber and increase the effectiveness of its profile sections. The

second objective highlights the importance of sealing all the gaps of the aerodynamic surface by designing the tail into a one-piece structure. The third objective refers to a concept structure able to perform the warping deformation necessary to augment the profile's angle of attack for improving the side force generation to enhance control and stability tasks. The final point outlines the need for using lighter materials, likely to be composites, to reduce the novel fin weight. The most challenging part of the design was to gather all these characteristics within a unique design simultaneously. Although innovative, the characteristics of a rudderless configuration reduce the available options to realise a performing vertical control surface without any movable part. Whereas on board conventional fins, the directional control task is normally entrusted to a hinged surface, i.e. the rudder, here, in the GRAF variant, that same control attitude must be obtained from a smart operating mode of the whole tail in conjunction with an unconventional compliant design of its internal structure. The primary elements constituting the GRAF empennage are the external skin, the primary shaft, working as the main carrying load beam, and the rotating ribs which allow more warping freedom.

The GRAF conforming structure will be designed using composite materials. The choice of glass and carbon fibres, rather than metallic alloys, has been made in favour of the desired objective of a lighter fin structure. The structural design commences by defining the most appropriate thickness for the unitised covering skin. The cladding will withstand the lateral external loads and will be flexible enough to simultaneously allow twist deformations and TE camber deflections. The structural modelling and analysis is based on the 3-D models of the entire fin and components built for the numerical analysis carried out via the finite elements method (FEM). In order to guarantee the GRAF meets the stiffness and strength requirements, the failure criteria, as listed in Chapter 2, will be applied. In particular, for the finite elements analysis (FEA) the reference parameters adopted to evaluate the safety or failure of the entire GRAF model, are the maximum strength-to-stress ratio '*R*' and the fibres failure index '*k*':

$$k = \left[G_{ij}\varepsilon_i\varepsilon_j\right]\left[\frac{1}{k}\right]^2 + \left[G_i\varepsilon_i\right]\left[\frac{1}{k}\right] = a\left[\frac{1}{k}\right]^2 + b\left[\frac{1}{k}\right] = 1 \qquad (3.29)$$

In the specific case of the FEM models run via the NASTRAN processor, the adopted criterion for the failure inspection has been that of Hoffman .

3.5.1 Introduction to the GRAF structure composite design

The notation and symbols used in this section of the methodology use predominantly the convention adopted in reference [175]. For the purpose of this project and at this current research stage, only the linear behaviour of composite materials has been taken into account. No thermal or moisture effects are considered for the current model application. Eight assumptions have to be made before proceeding with the composite design description:

- the laminate thickness is very small compared to its other dimensions;
- the layers of the laminate are perfectly bonded together;
- the line perpendicular to the middle plane remains straight and perpendicular to it even after the deformation;
- the laminae and laminates are linear elastic;
- the stresses and strains through the thicknesses are negligible;
- only case studies for linear FEA have been run;
- glass fibre material is chosen for the skin construction;
- carbon fibre material is chosen for the rib and stringer parts.

Dealing with isotropic materials is easier because mechanical properties are identical in all directions. Composites instead, as introduced in the literature section, have properties which are very likely to vary even from lamina to lamina, and the property of the final laminate depends on the sum of the properties of single plies. However, they have the remarkable advantage of a high strength-to-weight ratio compared to other metallic compounds. Laminate theory is based on the study and analysis of the properties of each single lamina constituting the final composite laminate.

The constitutive laws for the lamina are now presented. Let us start by introducing first the total in-plane displacements at any point in the plate following the classical laminate plate theory already introduced in Chapter 2. The plate in-plane displacements are the sum of the normal displacement plus the displacements introduced by bending. Hence, they can be written as:

$$u = u_0 - z\frac{\partial w}{\partial x} \quad (3.30a) \qquad \text{and} \qquad v = v_0 - z\frac{\partial w}{\partial y} \quad (3.30b)$$

where the "*0*" denotes displacements along *x* and *y* of the plate mid-plane and $\frac{\partial w}{\partial x}$ and $\frac{\partial w}{\partial y}$ the bending of the plate in the *x*- and *y*-directions respectively. From the constitutive laws the following can be expressed:

$$\varepsilon_x = \frac{\partial u}{\partial x} = \frac{\partial u_0}{\partial x} - z\frac{\partial^2 w}{\partial x^2}; \quad (3.31)$$

$$\varepsilon_y = \frac{\partial v}{\partial y} = \frac{\partial v_0}{\partial y} - z\frac{\partial^2 w}{\partial y^2}; \quad (3.32)$$

$$\gamma_{xy} = \frac{\partial u}{\partial y} + \frac{\partial v}{\partial x} = \frac{\partial u_0}{\partial y} + \frac{\partial v_0}{\partial x} - 2z\frac{\partial^2 w}{\partial x \partial y} \quad (3.33)$$

and by defining:

$\frac{\partial u_0}{\partial x}$ as ε_x^0; $\frac{\partial v_0}{\partial y}$ as ε_y^0; and $\frac{\partial u_0}{\partial y} + \frac{\partial v_0}{\partial x}$ as γ_{xy}^0

to be the mid-plane strains, as well as defining:

$\frac{\partial^2 w}{\partial x^2}$ as K_x; $-\frac{\partial^2 w}{\partial y^2}$ as K_y; and $-2\frac{\partial^2 w}{\partial x \partial y}$ as K_{xy},

to be the plate curvature, the notation can be made easier and yield

$$\begin{Bmatrix} \varepsilon_x \\ \varepsilon_y \\ \gamma_{xy} \end{Bmatrix} = \begin{Bmatrix} \varepsilon_x^0 \\ \varepsilon_y^0 \\ \gamma_{xy}^0 \end{Bmatrix} + z\begin{Bmatrix} K_x \\ K_y \\ K_{xy} \end{Bmatrix} \quad (3.34)$$

where K_x and K_y are the rate of change of slope of the bending plate in both direction *x* and *y*, respectively, whilst the term K_{xy} represents the amount of bending in the *x*-direction along the *y*-axis. This finally leads to the determination of the stresses in each ply of the laminate. Therefore by substituting Eq. (3.34) in

$$\{\sigma\} = [Q]\{\varepsilon\} \tag{3.35}$$

The stress strain relation can be written as

$$\begin{Bmatrix} \sigma_x \\ \sigma_y \\ \tau_{xy} \end{Bmatrix} = \begin{bmatrix} \overline{Q}_{11} & \overline{Q}_{12} & \overline{Q}_{16} \\ \overline{Q}_{12} & \overline{Q}_{22} & \overline{Q}_{26} \\ \overline{Q}_{16} & \overline{Q}_{26} & \overline{Q}_{66} \end{bmatrix} \begin{Bmatrix} \varepsilon_x^0 \\ \varepsilon_y^0 \\ \gamma_{xy}^0 \end{Bmatrix} + z \begin{bmatrix} \overline{Q}_{11} & \overline{Q}_{12} & \overline{Q}_{16} \\ \overline{Q}_{12} & \overline{Q}_{22} & \overline{Q}_{26} \\ \overline{Q}_{16} & \overline{Q}_{26} & \overline{Q}_{66} \end{bmatrix} \begin{Bmatrix} K_x \\ K_y \\ K_{xy} \end{Bmatrix} \tag{3.36}$$

Because diverse plies may have different mechanical properties, the stresses can also be different and varying through the thickness of the laminate. Hence, it may be convenient to sum up all the contributions in a unique term of an equivalent force acting on the middle surface of the laminate, thus defining the stress and moment resultants as:

$$\begin{cases} N_x \equiv \int_{-h/2}^{h/2} \sigma_x dz \\ N_y \equiv \int_{-h/2}^{h/2} \sigma_y dz \\ N_{xy} \equiv \int_{-h/2}^{h/2} \tau_{yx} dz \\ V_x = \int_{-h/2}^{h/2} \sigma_{xz} dz \\ V_y = \int_{-h/2}^{h/2} \sigma_{yz} dz \end{cases} \tag{3.37a}$$

$$\begin{cases} M_x \equiv \int_{-h/2}^{h/2} \sigma_x z dz \\ M_y \equiv \int_{-h/2}^{h/2} \sigma_y z dz \\ M_{xy} \equiv \int_{-h/2}^{h/2} \tau_{yx} z dz \end{cases} \tag{3.37b}$$

The first two moments are responsible for the bending deflections, while the combined action of the bending in the *xy*-direction induces twist distortions over the laminate. Subdividing the laminate into a finite number of layers and then performing the integration through the laminate thickness, yields:

$$\begin{Bmatrix} N_x \\ N_y \\ N_{xy} \end{Bmatrix} = \sum_{k=1}^{n} \left\{ \begin{bmatrix} \overline{Q}_{11} & \overline{Q}_{12} & \overline{Q}_{16} \\ \overline{Q}_{12} & \overline{Q}_{22} & \overline{Q}_{26} \\ \overline{Q}_{16} & \overline{Q}_{26} & \overline{Q}_{66} \end{bmatrix}_k \begin{Bmatrix} \varepsilon_x^0 \\ \varepsilon_y^0 \\ \gamma_{xy}^0 \end{Bmatrix} (h_k - h_{k-1}) + \begin{bmatrix} \overline{Q}_{11} & \overline{Q}_{12} & \overline{Q}_{16} \\ \overline{Q}_{12} & \overline{Q}_{22} & \overline{Q}_{26} \\ \overline{Q}_{16} & \overline{Q}_{26} & \overline{Q}_{66} \end{bmatrix} \begin{Bmatrix} K_x \\ K_y \\ K_{xy} \end{Bmatrix} \frac{1}{2} \left(h_k^2 - h_{k-1}^2 \right) \right\} \tag{3.38}$$

and,

$$\begin{Bmatrix} M_x \\ M_y \\ M_{xy} \end{Bmatrix} = \sum_{k=1}^{n} \left\{ \begin{bmatrix} \overline{Q}_{11} & \overline{Q}_{12} & \overline{Q}_{16} \\ \overline{Q}_{12} & \overline{Q}_{22} & \overline{Q}_{26} \\ \overline{Q}_{16} & \overline{Q}_{26} & \overline{Q}_{66} \end{bmatrix}_k \begin{Bmatrix} \varepsilon_x^0 \\ \varepsilon_y^0 \\ \gamma_{xy}^0 \end{Bmatrix} \frac{1}{2}\left(h_k^2 - h_{k-1}^2\right) + \begin{bmatrix} \overline{Q}_{11} & \overline{Q}_{12} & \overline{Q}_{16} \\ \overline{Q}_{12} & \overline{Q}_{22} & \overline{Q}_{26} \\ \overline{Q}_{16} & \overline{Q}_{26} & \overline{Q}_{66} \end{bmatrix} \begin{Bmatrix} K_x \\ K_y \\ K_{xy} \end{Bmatrix} \frac{1}{3}\left(h_k^3 - h_{k-1}^3\right) \right\} \quad (3.39)$$

These two systems can be finally grouped into the compacted form equation that has already been introduced in the literature of Chapter 2, as:

$$\begin{bmatrix} N \\ M \end{bmatrix} = \begin{bmatrix} [A] & [B] \\ [B] & [D] \end{bmatrix} \begin{bmatrix} \varepsilon^0 \\ K \end{bmatrix} \quad (3.40)$$

where the matrices terms are:

$$A_{ij} = \sum_{k=1}^{n} \left[\overline{Q}_{ij}\right]_k t_k \;\; ; \qquad B_{ij} = \sum_{k=1}^{n} \left[\overline{Q}_{ij}\right]_k t_k \frac{\left(h_k + h_{k-1}\right)}{2} \;\; ; \qquad D_{ij} = \sum_{k=1}^{n} \left[\overline{Q}_{ij}\right]_k \left(\frac{t_k^3}{12} + t z_k^{-2}\right)$$

where t_k is the thickness of the *k*th ply. The matrix **A** is the extensional stiffness matrix and A_{ij} are the in-plane stiffnesses. When the terms A_{16} and A_{26} are not zero and a shear strain is applied onto the laminate, then normal stresses will result and vice versa. When they are zero, there is no shear coupling effect. The matrix **B** is defined as the coupling stiffness matrix, and B_{ij} are the in-plane-out-of-plane coupling stiffnesses. They relate bending strains with normal stresses and vice versa. The matrix **D**, instead, is the bending stiffness matrix relating the curvatures of the plate to bending moments, and D_{ij} are the bending stiffnesses. When the elements D_{16} and D_{26} are not zero, bending moments cause twisting of the laminate. All these terms vary for each different laminate whether a symmetrical, balanced, unbalanced or angle-ply lay-up is set within the composite plate. The COALA program has been applied to find out the **A**, **B** and **D** matrices corresponding to the composite layup of the covering skin. In particular, the values of the flexural rigidity of the laminate will be applied to compute the thickness and layout configuration of the fin skin. These values are input into the MATLAB code specifically written to define the best compromise between the skin thickness and the ribs pitch on the empennage under the worst loading case scenario.

3.5.2 The Skin Structure

This section of the chapter is dedicated to describing in detail the process that has been used to determine the properties and thickness of the GRAF skin. The fin panels are key elements of the fin, the characteristics of which ensure the successful outcome of the warping design. An adequate ratio of stiffness and elasticity is demanded to the skin in order to safely withstand the external loads while allowing warping and cambering flexibility to the rest of the structure. The glass fibre skin runs across the ribs and the LSS stringers. The glass fibre materials, despite their higher density compared to carbon fibres, have been selected for the cladding skin of the GRAF because of their greater elasticity compared to the carbon fibres' elastic modulus. A more flexible external shell is a fundamental element for warping requirements. The skin flexibility also comes from its very thin layup and from the fact that the skin is not rigidly attached to the ribs. The skin panels simply lean on the ribs flanges. They are connected to each other via brackets and pins which allow tiny, either chord-wise or vertical displacements, of the parts. Those little movements reduce the restraining effect of the attachments, lower the stress level in the joints areas and improve the angle of twist.

The FEM, along with the plate and composite theories, are used to define the initial size and thickness of the skin. The analysis is carried out complying with the boundary conditions and the external aerodynamic loads of the GRAF model. The classic laminated plate theory initially discussed in Section 2.4.1 is applied to the skin model. The plate theory, originally studied for isotropic material models, is then readapted and presented in this text through Levy's and Kirkhoff's assumptions which were made to take into account composite plates [174]. Despite the fact that the plate model works well for medium-thin plates, a few more corrections to this theory are added when the case studies look at very thin shells, as in the case of the GRAF external skin and TE panels. Their behaviour tends to be closer to those of membrane characteristics rather than of a 3-D plate. The plate theory implies that plates react by bending and transverse shear forces, whereas the shell theory implies that thin shells resist external transversal loads by reacting with membrane forces, tangential to the shell mid-plane.

The membrane model and its assumptions are followed in this analysis.

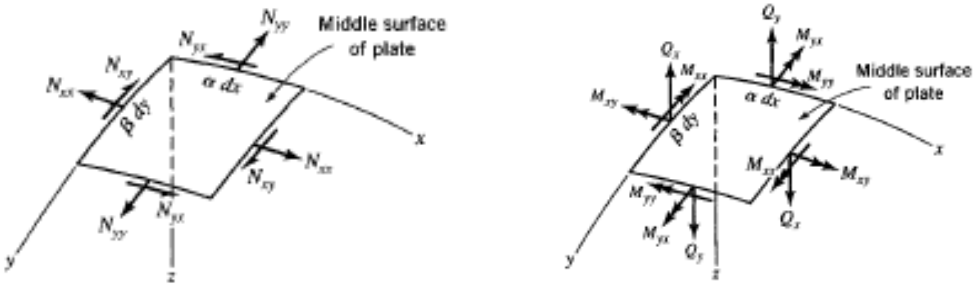

Figure 3-13 Resultant traction, shear and moments on a reference surface [32].

Following the formulation of the plate theory for the analysis of thin shell, as expressed in reference [104], the set of equations of equilibrium for a generic panel of the GRAF composite skin can be reduced to:

$$\begin{cases} N_{xx} = \int_{-h/2}^{h/2} \sigma_{xx}\left(1+\frac{z}{R_y}\right)dz \qquad N_{yy} = \int_{-h/2}^{h/2} \sigma_{yy}\left(1+\frac{z}{R_x}\right)dz \\ N_{xy} = \int_{-h/2}^{h/2} \sigma_{xy}\left(1+\frac{z}{R_y}\right)dz \qquad N_{yx} = \int_{-h/2}^{h/2} \sigma_{yx}\left(1+\frac{z}{R_x}\right)dz \end{cases} \tag{3.41}$$

where R_x and R_y are the radii of curvature in the *x*–*z* and *y*–*z* planes, due to membrane deflection. Kirkhoff's reduction theory for plates assumes the sections that are normal to the reference plane remain normal and straight even after the plate or shell have undertaken a deformation. It is the same principle applied in the beam theory by Bernoulli's hypothesis and formulation for transverse cross sections' deformation and rotation of beams. Therefore the three-dimensional plate problem is reduced to a more tractable two-dimensional study. There is no extension or angular rotation of the sections normal to the middle plane. That reduces the degree of freedom and therefore the order of the system, which yields:

$$\begin{aligned} &\frac{\partial N_{xx}}{\partial x} + \frac{\partial N_{xy}}{\partial y} + P_x + hB_x = 0 \\ &\frac{\partial N_{xy}}{\partial x} + \frac{\partial N_{yy}}{\partial y} + P_y + hB_y = 0 \\ &\frac{\partial Q_x}{\partial x} + \frac{\partial Q_y}{\partial y} + P_z + hB_z = 0 \\ &\frac{\partial M_{xx}}{\partial x} + \frac{\partial M_{xy}}{\partial y} - Q_x + R_y = 0 \\ &\frac{\partial M_{xy}}{\partial x} + \frac{\partial M_{yy}}{\partial y} - Q_y - R_x = 0 \\ &N_{xy} = N_{yx} \end{aligned} \tag{3.42}$$

giving the momentum equilibrium equation of the plates as:

$$\frac{\partial^2 M_{xx}}{\partial x^2} + 2\frac{\partial^2 M_{xy}}{\partial x \partial y} + \frac{\partial^2 M_{yy}}{\partial y^2} + P_z z = 0 \tag{3.43}$$

where P_z is the vertical component of the external force resultant. The terms in equation (3.43) can be substituted by the bending and twisting moment expressions:

$$M_{xx} = -D\left(w_{xx} + \nu w_{yy}\right) \tag{3.44}$$

$$M_{yy} = -D\left(w_{yy} + \nu w_{xx}\right) \tag{3.45}$$

$$M_{xy} = -(1-\nu)D w_{xy} \tag{3.46}$$

Consequently their substitution in equation (3.43) with $P_z = p$ (external distributed load: pressure), gives under a compact formulation the following expression:

$$\nabla^2 \nabla^2 w = \nabla^4 w = \frac{p}{D} \tag{3.47}$$

That is the fourth-order partial differential equation of the plate, whose solution can be found once the boundary conditions at the edges of the plate are satisfied. Intermediate passages can be verified in references. This formulation has considered, until this stage, only isotropic materials, by expressing in equation (3.47) the flexural rigidity as:

$$D = \frac{Eh^3}{12\left(1-\nu^2\right)} \tag{3.48}$$

It contains Young's modulus and Poisson's ratio of isotropic materials. In order to allow for Kirkhoff's plate theory, as expressed above, to take into consideration the anisotropy of composite laminates with normally distributed loads, two more assumptions are introduced. The first is related to the study of a generic composite panel for the skin or the trailing edge application. This defines the anisotropic elastic behaviour of composite materials by taking into account the flexural rigidity of the subject laminate through the **D** matrix terms of the corresponding composite plate layout. In the specific case of the composite skin subjected to the external load pressure and observed between two adjacent ribs, the solution for the normal-to-plane displacements problem is proposed by a Navier-Stokes double series development in the form:

$$w(x,y) = \sum_{m=1}^{\infty}\sum_{n=1}^{\infty} A_{mn} \sin\frac{m\pi x}{a}\sin\frac{n\pi y}{b} \qquad (3.49)$$

The analytical model expressed in Eq. (53) is then implemented into a MATLAB program used to study and size the skin thickness of the fin. The MATLAB program determines also the ribs pitch as a function of the skin thickness. The anisotropic material properties, obtained from the COALA code, provide the necessary stiffness data to be substituted in the plate bending theory for composite laminates. In particular, the flexural stiffness D_{11} and D_{22} are taken into account to estimate the bending stiffness for the composite plate. The final expression of the flexural stiffness for the composite skin, in the case of asymmetric angle ply laminates, can be defined as $D = D_{11} - B_{16}^2 / A_{66}$, where $D_{11} = \frac{E_{xx}^b h^3}{12\left(1 - \nu_{xy}^b \nu_{yx}^b\right)}$. The plate strip investigated with the MATLAB model represents the generic panel of the fin assembly. The plate is simply supported at the four edges. This configuration simulates the real boundary condition on the fin model. In fact, in the real GRAF design, the skin panels just lean on ribs without any type of rigid constrain restraining the plate deformation. The code allows the user to vary the panel stiffness and also adjust the thickness of the plate and the reciprocal distance between the supporting ribs. The program outcomes are finally plotted in the thickness vs. ribs pitch curve presented in Chapter 5.

The results will show two different lay-up sequences for the glass fibre skin. Because no optimisation process has been carried out for the study of the composite panels of the skin, the initial basic configuration of quasi-isotropic layup following the Hart-Smith 10% rule [97] has been applied with the plies oriented as $[0/\pm 45/90]$ in the four layers laminate. Due to the fact that the extent of deformations under the maximum loading case scenario has induced vertical displacements of the plate element less than the 3% of the biggest dimension of the plate, a further investigation with a reduced three layers layup has been carried out. The three layers layup study with plies oriented as $[0/45/90]$ has revealed that the more loaded side of the skin deflects about 6% of the longest edge of the panel. This configuration, however, as discussed in the results section, due to its flexibility and despite having doubled the deformations, it has been picked up as the final configuration of the GRAF model.

The final thickness is then kept constant for the whole skin structure and verified later under more accurate stiffness and strength perspectives with the FEA of the entire GRAF model using the MSC/NASTRAN package. Both three- and four-layer skin variants are tested for flutter analysis in order to investigate any higher flight speed applications.

The second assumption is made when loading actions and composite characteristics apply to the TE section. Levy's bending plate formulation is used to simplify the order of the equation through the cylindrical bending theory for plate strips expressed via the displacements equation in Eq. (3.51). It reduces the order of two-dimensional plate problems by treating them as a one-dimensional case. Details of Levy's theory are described in detail in reference [148]. The cylindrical bending theory implies that the plate strip is very long along its y-axis and has a much shorter finite dimension on the x-axis. Both must be considerably greater than the plate thickness. Levy has established an empirical formulation to verify whether or not the cylindrical bending theory may be worth applying to the considered plate strip. If the following equation is verified, then the theory applies:

$$\frac{L_y}{L_x} > 3\sqrt[4]{\frac{D_{11}}{D_{22}}} \tag{3.50}$$

In the specific case of the three glass fibre layers used for the skin layup, with the trailing edge dimensions equal to $L_x = 0.08m$ and $L_y = 0.425m$ and by taking the flexural stiffness from the D matrix included in Appendix A, it yields $L_y > 3.39L_x = 0.27m$, which verifies the assumption. That allows us to reduce the order of the problem as shown in Eq. (3.51) where the load is assumed to be constant along the y-axis, while varying only along the x-axis:

$$w(x,y) = X_n(x)\sin\frac{n\pi x}{a} \tag{3.51}$$

Therefore, assuming the load varies only chordwise, and by considering simply supported boundary conditions (*BCs*) at $x = 0$ and $x = a$ as:

$$\left.\begin{array}{c} w = 0 \\ M_{xx} = -D(w_{xx} + \nu w_{yy}) = 0 \end{array}\right\} at\ x = 0, a \tag{3.52}$$

then with all the constants $X_n(x)$ found and substituted in Eq. (3.51), it is possible to compute the final result. However, in order to complete the solution of equation (3.51), the external load *p* must also be expressed in the appropriate form of the series solution. The external load pressure is expressed as follows:

$$p(x,y) = p_0 \sum_{n=1}^{\infty} f_n(x) \sin \frac{n\pi x}{a} \tag{3.53}$$

Substituting Eq. (3.51 and 3.53) in Eq. (3.47), leads to the set of ordinary differential equations:

$$D\left[X_n'''' - 2\left(\frac{n\pi}{a}\right)^2 X_n'' + \left(\frac{n\pi}{a}\right)^4 X_n \right] = p_n f(x), \quad n = 1, 2, ... \tag{3.54}$$

and finally gives the solution of equation (3.54) in the form of:

$$X_n(x) = \frac{p_n}{D}\left(\frac{a}{n\pi}\right)^4 \left[1 + (A_{1n} + xA_{2n}) \cosh \frac{n\pi x}{a} + (B_{1n} + xB_{2n}) \sinh \frac{n\pi x}{a} \right] \tag{3.55}$$

where the constants $A_{i,n}$ and $B_{i,n}$ are obtained from the BC*s* of the system. Once X_n is known, then the final vertical displacement can be found by substituting its expression in equation (3.51) to find *w(x,y)* . Due to time constraint the Levy's simplified model has not been implemented in the MATLAB code. However, the assumption expressed in Eq. (3.50) has been used to verify whether the TE section of the GRAF model can be subjected to the cylindrical bending theory and consider the relating flexural stiffnesses to evaluate the torque necessary to bend the TE panels, via the M_e term in Eq. (3.56).

3.5.3 The morphing TE section: the L-shape Stringers (LSS) device & the “swivel-edge” closure

The L-shape stringers (LSS) device has been developed to work as a skin-integrated mechanical system to transform the linear forces from the servo-actuators into applied bending moments for the deflection of the panels of the GRAF rudderless section. The LSS device is designed to camber the trailing edge of the GRAF tail, either for trimming or control purposes, to help the aerodynamic surface increase its effectiveness. The original idea behind this design concept was to seamlessly camber 25% of the fin chord to contribute to side force generation when the twist effect only cannot guarantee the required performance. The CAD illustrations of Figure 3-13 show the conventional systems adopted on aircraft to activate the deflection of any command surface.

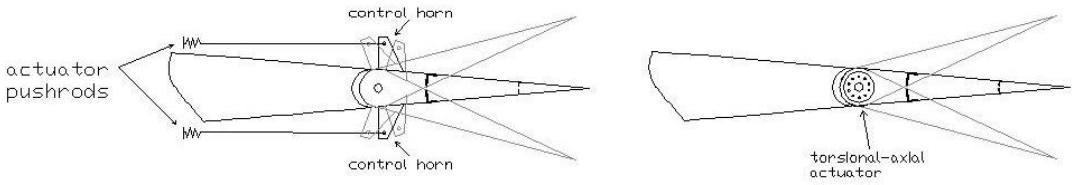

Figure 3-14 CAD illustration of TE actuation mechanisms.

The first system on the left hand side relies upon an external support/control horn and linkages to be connected to the actuation mechanism. The type of linkages used varies with the aircraft size and class. Small, general aviation aircraft use cables and leverages for their actuation. A larger typology of surfaces and aircraft are instead directly connected to the hydraulic/pneumatic/mechanical arm of the actuators and fly-by-wire technology.

The Eclipse conventional fin adopts the external control horn-pushrod mechanism, as shown in Figure 3-14.

The second type of mechanism, on the right side of the drawing, expects the actuator to be installed inside the wing or tail structure to perform its actuation task by generating an axial torque directly aligned with both the actuator’s shaft and the command surface hinge line. This configuration allows the aerodynamic body to

mount all the linkages and supports internally to the section, thus not affecting the external aerodynamics of the surface, and so reducing the drag force.

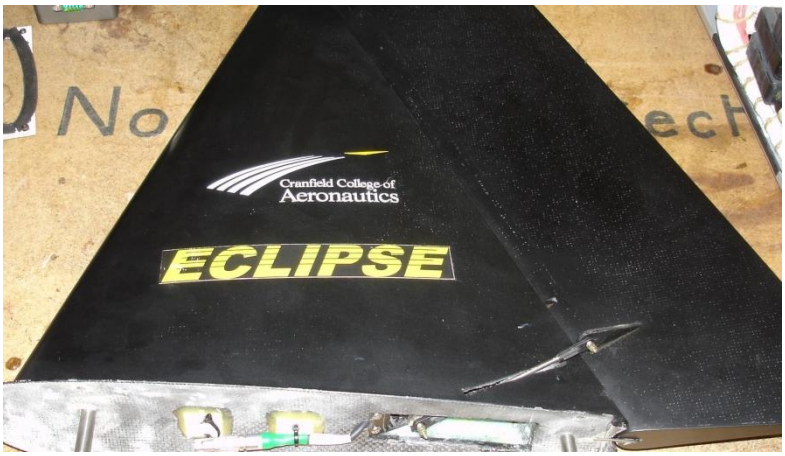

Figure 3-15 Eclipse UAV fin-rudder control horn.

In a similar way, in order to seamlessly bend the TE surface of the GRAF fin, a series of torsional actuators is embedded throughout the profile section and distributed chordwise along the TE chord, as shown in Figure 3-15 (top one). The actuators could be fixed at the root of the fin or on the fuselage mount and activate the TE deflection throughout the torsional rods as extensions of the actuators shafts.

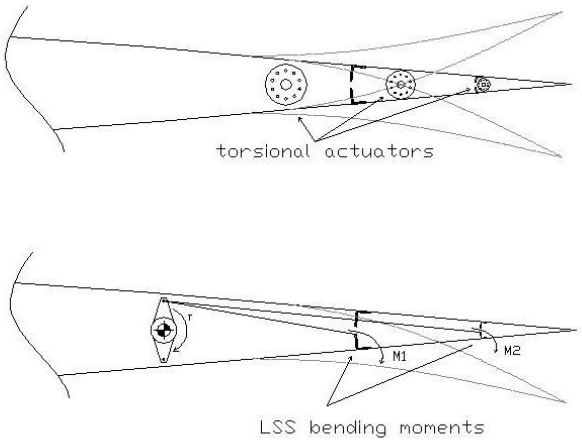

Figure 3-16 Integrated mechanism for seamless TE actuation.

Mechanical and weight issues of multiple torsional actuators decreed that option not to be a valuable solution for this configuration. The out-of-plane TE deformation induces the servo-mechanism to follow the curvature line of the TE part while fixed at the support frame. The actuator's shaft will impede the TE deflection unless very flexible rods are used to transfer the actuation torque. As shown in Figure 3-15, as

soon as the TE moves in deflection (light gray line), the fixed servo-mechanism cannot follow its deformation. Only the shaft aligned with the imaginary hinge line of the cambering TE will stay straight during actuation, while the rest of them will fail. Therefore, a simpler concept design was tried, studied and then proposed to be specifically adapted for the GRAF model, i.e. the LSS. It works similarly to the in series torsional actuators displaced inside the TE section. With this system, the torque can be transferred to the surface panels from a unique actuator. The applied moments are obtained by converting the linear forces of the pushrod linkages into rotational moments via the L-shaped stringers connected to the TE panels. The single servo-mechanism, located at the bottom of the fin, is connected to a secondary shaft placed inside the fin, slightly behind the primary shaft and through the ribs' cut-outs. Then the rigid pushrods link this secondary shaft to the stringers for pushing or pulling them to force the bending deformation. The location of the LSS and the actuator power needed to deform the panel are discussed below.

The TE section can be gradually deformed in a wide variety of curved shapes. For each configuration, a precise load distribution applies. The extreme case of maximum deflection will, therefore, be studied. The determination of the load pressure for the precise case will help define the torque needed by the actuators to deflect the panels. At this stage of the analysis, for the preliminary estimation of the required torque, the classical triangular TE loading distribution is taken as the case study. Let us assume a downward deflection is imposed to the command surface. Due to the linear load distribution, the curvature of the TE panels follows a differential equation of the third order, with its final shape deflected as shown in Figure 3-16. Although a downward deflection is imposed, as a consequence the resultant pressure distribution is pressing upwards. The same figure shows also the same panel under only the effect of the actuator forces applied onto the LSS device. The deflection may be distinguished by two segments with different curvatures. The first segment from the inner edge of the TE to the LSS application point follows a third order curvature equation, while beyond the LSS location to the outer edge of the section, the panel should theoretically deflect in a straight line. It will, however, assume a curved shape as well because of the reciprocal interaction of the two side panels of the TE undergoing deflection.

They will induce a reciprocal deformation to each other.

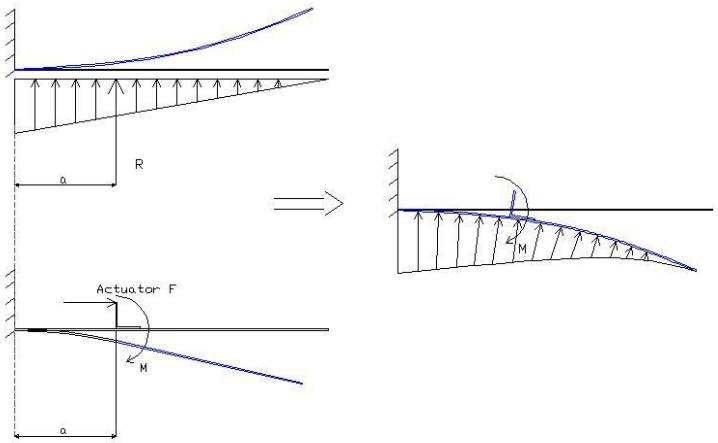

Figure 3-17 CAD exemplification of TE deflection under loads.

The superposition of the external load- and mechanically-induced deformations generates the final shape of the cambered TE. The FEM analysis has later revealed that the TE stiffness and the LSS location do not satisfy the shape requirements. The TE is supposed to assume the cambered profile as defined by the MATLAB selection of the four different variants already discussed in the aerodynamic paragraph. Therefore a modification of the whole TE assembly was needed. The objective was to reproduce the "*smooth*" curvature profile by using the LSS activation. Thus two solutions have been outlined. The first was to include a second row of stringers between the first row and the edge of the panel. The second solution was to create a smart connection for the closure of the TE panels. At the beginning of the conceptual design phase of the LSS, the idea was to include only one set of stringers inside the TE. The reason for that was because the rudderless profile of the GRAF section does not guarantee a large enough space at the back of the airfoil in which to mount several elements for the actuation device. At the very end of the TE section, only a few millimetres separate the two side panels. However, the second LSS was used to increment the radius of deflection for the TE in the same way the *smooth* camber is attained in the MATLAB program.

In order to increase the effectiveness of the actuator forces, a particular technique to transfer the forces more efficiently from the actuation mechanism to the stringers was adopted. The solution is shown in Figure 3-17. The pushrods used to transfer the

forces are not aligned with the airfoil chord. They are inclined and x-crossing each other in the middle of the TE section, as shown in Figure 3-17.

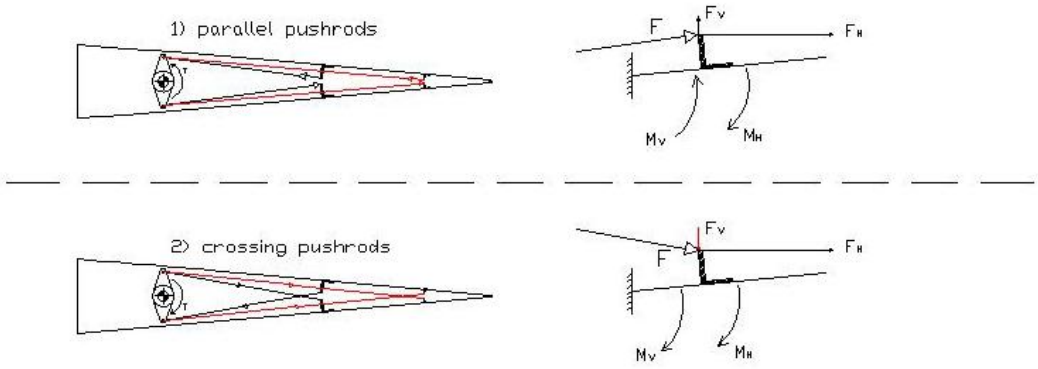

Figure 3-18 Two variants for push-rod type linkages.

This technique allows the actuator force to be decomposed into two more effective horizontal and vertical components. In this way, the vertical component of the actuator force acts directly in the same direction as the resultant of the external triangular load. That component, despite being a very small force, significantly improves the bending moment effect because the effective arm distance '*a*' measured from the hypothetical hinge line to the LSS stringer is fixed at 1/3 of the TE chord, equal to 2.6cm. The horizontal component, although greater than the vertical one, has a much shorter arm moment of less than a centimetre, corresponding to the height of the vertical wall of the LSS stringer. In the case of the triangular load distribution, the first stringer location coincides with the application point of the external load resultant. The second row of the LSS is then mounted between the first LSS and the trailing edge closure, at 2/3 of the TE chord, Figure 3-18.

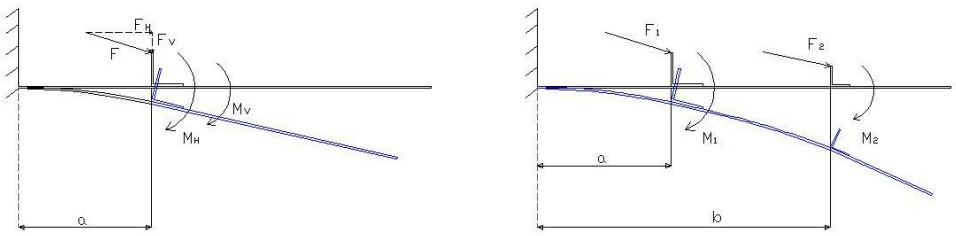

Figure 3-19 CAD illustration of single and double rows of LSS devices on TE panel.

This study allowed the possibility of establishing the minimum required torque necessary to activate the deflection of the TE. The pressure distribution for the RAE 101 obtained with the maximum angles of deflection and attack via JAVAFOIL analysis is applied to each panel. Thus, simply multiplying the resultant force by the distance from the inner edge of the TE section, will give the corresponding bending moment the actuator should produce to counteract just the resultant of the external aerodynamic pressure.

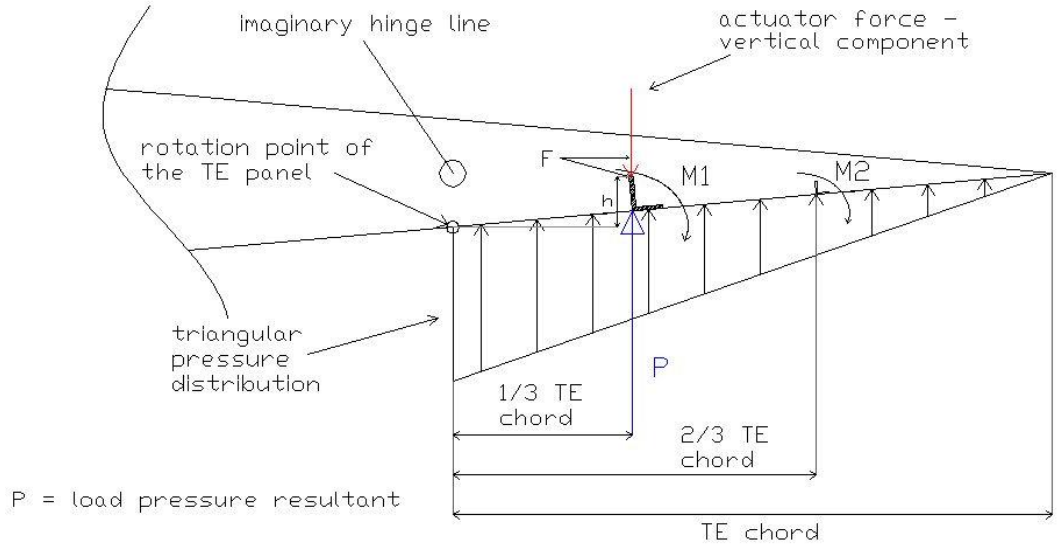

Figure 3-20 Push-rod force and external load interaction on the TE system.

The preliminary torque estimation is carried out considering the equilibrium of the vertical forces and the bending moments acting on each panel of the TE section, see Figure 3-19, as described by the system below:

$$\begin{cases} actuator\ Torque\ (i.e.\ LSS\ bending\ moment) = F_H \cdot h + F_V \cdot 1/3TEc \\ pressure\ bending\ moment = P \cdot 1/3TEc \\ Minimum\ required\ Torque: F_H \cdot h + F_V \cdot 1/3TEc \equiv P \cdot 1/3TEc + M_e \end{cases} \quad (3.56)$$

The last equation of the system (3.56) establishes the moments equilibrium between the bending moment produced by the actuator force components and both the moment induced by the eternal pressure and the elastic reaction of the panel, 'M_e'. The elastic reaction of the panel can be calculated by using the equation of the

vertical displacements already described in the cylindrical bending theory given in the previous paragraph. Although the design study of the LSS has shown the necessity for having at least two sets of stringers in order to guarantee a smoother curved deflected shape, the analytical computation presented with system (3.56) refers only to one set of stringers. The system needs to be activated and tested to work safely at its maximum deflection even with only one stringer attached to the panel, in case of failure of the farthest one. The option of a second row of LSS does not increase the servo mechanism load, but simply redistributes more uniformly the unique force over the TE.

Before concluding the TE conceptual design section, another novelty has to be mentioned in this paragraph, i.e. the 'swivel edge' closure device, shown in Figure 3-20. This is a novel concept used to keep the TE edges together while being free to slide and rotate over each other. The reason for its introduction is mainly because unless the TE is made of extremely elastic materials, a rigidly closed TE box cannot bend to follow large deflections of the section without buckling or overstressing the materials.

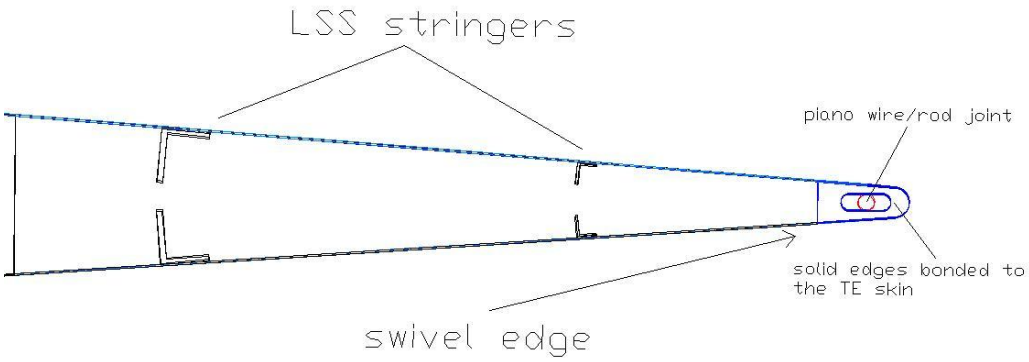

Figure 3-21 CAD side view illustration of the "swivel edge closure" device.

Each time the TE section initiates a deflection, the rigid closed edge forces the TE side panels to double curve and buckle. The rigid closure will hinder the deformation of the two sides of the morphing surface. During bending the upper and lower panels follow two different curvatures with different radii. Let us take for example the downward deflection of a horizontal TE profile, such as the one shown in Figure 3-

21. In this case the external panel reduces its radius and apparently shortens its length whilst the edge of the internal one “travels for a longer distance”. To demonstrate this, the reader is asked to join his/her hands and bend them together on one side. In the straight position all fingers match the reciprocal one on the other hand, whereas once bent the reciprocal fingertips do not touch each other any more. The fingers on the external hand have extended less than the internal ones. Therefore, as described in the hands analogy, the “longer” inner panel pulls and stretches the “shorter” outer one while the ‘shorter’ one pushes and compresses the “longer” panel.

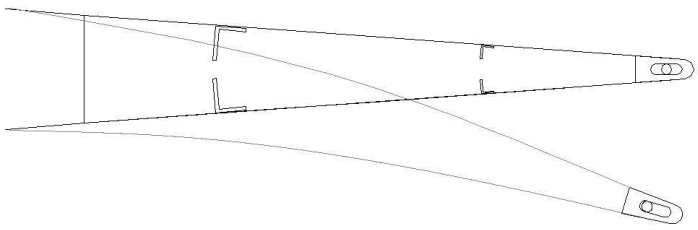

Figure 3-22 TE flexibility with operating swivel edge device.

This condition can lead to buckling of the TE section into an s-shaped curvature, with a very poor aerodynamic efficiency. Moreover, the force necessary to deform a closed box section is much greater than that needed to bend an open section. Hence, a solution to avoid these problems and still respect the initial objectives of a gapless configuration was proposed by introducing the swivel device.

The swivel connection is divided into two halves bonded on to the two panels of the TE section skin. The edges are kept joined by a tiny rod or piano wire that passes through the oval hole drilled into the solid edge, as shown in Figure 3-20. The oval cut-out allows the rod to work as a hinge line for the rotation of the parts, and at the same time, permits the connecting rod to move chordwise in the limited space of the hole. This sliding degree of freedom allows the two skin panels to move and slide over each other during deflection. The absence of a rigid edge releases the stresses caused by the bending deformation and increases the angles of deflection. More technical drawings are presented in Chapter 4.

3.5.4 The structural design of the primary shaft and the ribs

This paragraph covers the description of two components of the GRAF assembly which are fundamental to accomplish the warping tasks of the fin, i.e. the rotating ribs and primary shaft. A detailed analytical study and numerical validation of the rib elements has not been conducted at this stage of the research. Due to the technical complexity of the whole design, it has been decided to focus the research and analysis on other components of the project. Therefore, the ribs design study has been simplified by adopting a composite-based layout comprised of a set of four, or multiple of four, layers of carbon fibre. The reason why four is the number of layers chosen as the default number is directly linked to the layup sequence of the plies. The selected layup sequence is [0/+-45/90]. The reason for this choice is to follow the 10% rule, in order to deal with a quasi-isotropic configuration. No optimisation has been carried out on the orientation and number of plies applied for the ribs element. The stiffness and strength of the ribs have been assessed through the FEA models run for the whole GRAF using the NASTRAN framework. More details about the ribs design is presented in the next Chapter.

The primary shaft works as the support for the ribs and main load carrying beam. Its tubular profile has been designed in carbon fibre too. Also this component has not undergone a detailed analytical study in the design phase. Off-the-shelf (OTS) components such as the tubular beam, already available commercially, have been considered for application on the GRAF design. According to the fin airfoil section thickness, the room available at 0.4c can house a carbon tube with a radius of 11mm, leaving a thickness of 5mm on both sides of the ribs between the skin and the shaft. In order to verify whether the composite shaft satisfies the structural stiffness requirements to withstand the load under the worst case scenario of the GRAF tail, an FE model of the same shaft has been created and tested using the NASTRAN package. An equal number of layers to represent the thickness of the commercially available carbon tube have been applied to the model by using unidirectional carbon fibre prepregs with a thickness of 0.125mm each. The number of twelve layers has been used to build the FE model implemented in NASTRAN with a balanced layup sequence. Although the real load is not linearly distributed over the fin surface, the

maximum loading case has been applied, uniformly distributed, for the shaft study. The reason for the more conservative uniformly distributed load comes from a practical consideration based on the shaft geometry. The shaft has a circular cross section to favour the assembly of the rotating ribs and their roller bearings. Furthermore the thickness of the shaft wall is constant and not tapered within the shaft length, and above all neither is its outer diameter. The shaft, due to its double geometric and thickness symmetry, may be arbitrarily mounted on either of the two ends inside the fuselage mount. The symmetry of the element and the constant characteristics identify both ends of the shaft as top or bottom end of the tubular beam, according to the way it will be installed on board. Therefore, both sides of the tube are equally sized for the highest load and can be mounted as convenient. Also, a carbon tube with a constant diameter and wall thickness, as opposed to tapered ones, has lower manufacturing costs.

The results of the FE analysis regarding the displacements and stress analysis of the composite shaft are presented in Chapter 5.

More technical details about the assembly and function of the shaft are presented in the next Section.

3.6 Fin torsion & slot connection novelty study

The design philosophy and analysis of the twist concept model for the study of the warping aeroelastic structure is presented here. The flight mechanics requirements have already explained the motivations for inducing the twist deformations on the novel aeroelastic tail. This analysis studies the method to be utilised in order to twist the fin without increasing the actuator's torque, or weakening the structural stiffness of the assembly. Moreover, it must be guaranteed that the empennage will safely deform by meeting all the stiffness and strength requirements without causing any linear or non-linear instability. The amount of twist angle achieved by the fin depends on:

- the stiffness and layout of the fin structure;
- the torque generated by the actuation system and the aeroelastic effect;
- the type of constraint at the base of the tail.

The very low aspect ratio of the empennage reduces the spanwise elasticity of the entire structure, thus its tendency to twist more easily. Structurally speaking, all vertical empennages look more like compacted and rigid boxes than flexible and slender bodies. Their configuration provides a good resistance against torsional loads; thereby they are not the best configuration to undergo torsion without generating either structural or geometrical instabilities. Dealing with conventional fin structures, the only way of producing large deformations on the tail is either by applying a considerable amount of torque to the unitised box of the empennage or by making the fin itself of very flexible and elastic materials. Both of these options are discarded in this research. The first is because a greater torque requires big actuators and so, more than likely, powerful and heavy systems. The other is because although highly flexible materials might work for morphing purposes, the resulting structure will be too weak and unstable under the loading due to the external aerodynamic pressure.

Torsion and, in detail, warping theories represent the core of the twist design study and the basic principles on which are based the GRAF model conceptual analysis and the fin featuring tasks. As introduced in Chapter 2 in the section dedicated to the warping theories and mechanisms, up to a few decades ago, all the phenomena associated with torsional instability on aircraft structures were categorically avoided in aeronautical designs. Stiffer frames and reinforced wing boxes were built to avoid in-flight structural and flight instabilities such as command reversal, divergence and flutter conditions. To date, with modern morphing technology and aeroelastic effect techniques, those phenomena instead of being avoided, are purposely going to be exploited. The main objective of this study is to enhance the fin capability during twisting deformation. An unconventional way to allow the fixed root and gapless empennage to twist for stability and control purposes is investigated. The twist is needed to increase the angle of attack of the airfoil sections but it must be performed with the root section fixed and sealed to the fuselage mount. The unitised and gapless features impede the configuration to be released to freely rotate around its vertical

axis. The Bredt-Batho torsion theory [123] for thin-walled closed sections will be considered for the specific study of this part of the design. Saint-Venant's assumption for the redistribution of the stresses at the extremities of the element and the elastic-membrane analogy of Prandtl [33] are also applied for the case.

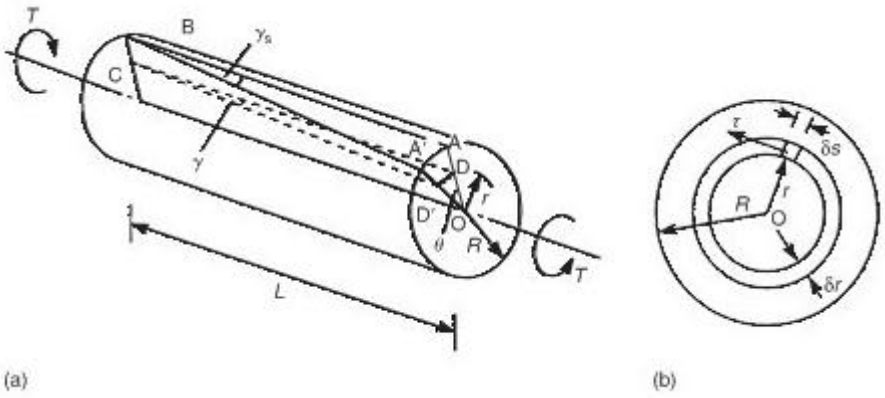

Figure 3-23 Isometric and front views of cylindrical bar under torsion [123].

The analysis focuses on finding out those factors which may increase torsion flexibility while retaining the stiffness of the fin elements. Let us start by considering the basic principles of torsion theory. The illustration in Figure 3-22(a) shows a symmetric circular section bar of length L subjected to equal and opposite torques at each end. The torque at any section of the bar is therefore equal to T and is constant along its length. Due to the twisting action of the torque, the generator AB on the surface of the cylindrical bar will displace the end A to A'. That implies the radius on the top section will rotate from OA to OA'. By indicating with ϑ the radius rotation angle, the shear strain on the top surface related to the distortion of the $OABA'$ section can be written as:

$$\gamma_S = \frac{AA'}{L} = \frac{R\vartheta}{L}; \tag{3.57}$$

and similarly, for a generic section and point of the bar, it yields:

$$\gamma = \frac{DD'}{L} = \frac{r\vartheta}{L} \tag{3.58}$$

hence, the expression of the shear stress, τ, at the radius r, may be written by rearranging the following equation:

$$\gamma = \frac{\tau}{G} = \frac{r\vartheta}{L} \tag{3.59}$$

and substituting it into the shear stress formula, as:

$$\frac{\tau}{r} = G\frac{\vartheta}{L} \tag{3.60}$$

from Eq.(3.60) it is possible to obtain the total torque on the bar. That is done by summing all the contributions from each annulus in the cross section. On a single annulus, as that represented in Figure 3-22(b), the torque on a single element may be written as:

$$\delta T = \int_0^{2\pi r} \tau \delta r \, r \, ds \qquad \Rightarrow \qquad \delta T = 2\pi r^2 \tau \delta r \tag{3.61}$$

and finally the total torque,

$$T = \int_0^R 2\pi r^2 \tau \delta r \tag{3.62}$$

by integrating and substituting for τ in Eq. (3.62), the following is obtained:

$$T = \frac{\pi R^4}{2} G\frac{\vartheta}{L} \qquad or \qquad T = JG\frac{\vartheta}{L} \tag{3.63}$$

where $J = \pi R^4/2$ is the polar second moment of area for the bar cross section. Although the expression in equation (3.63) represents the result of the torque analysis of a solid circular bar, and so is extremely different from the final objective of the GRAF thin-walled cross section shape, it already gives important information on which parameters might increase or reduce the twist performance on the novel design. Before discussing those parameters let us finalise the torsion theory for the GRAF case and move a step forward by considering the torsion theory for hollow sections rather than solid bars. Adapting the equation (3.63) to a simple hollow circular bar section gives:

$$T = \frac{\pi}{2}\left(R_o^4 - R_i^4\right) G\frac{\vartheta}{L} \tag{3.64}$$

that is the torque expression for a circular section bar with outer and inner radii R_o and R_i respectively. For both preceding cases, the angle of twist may be expressed as:

$$\vartheta = \frac{TL}{GJ} \tag{3.65}$$

Equation (3.65) establishes that, given a constant actuation torque *'T'*, in order to increase the twist angle performed by the section, there are only three factors which

can be modified in the equation. They are:

- the shear modulus of the material;
- the polar moment of inertia of the cross-sectional area;
- the length of the body.

The length of the body influences the elasticity of the assembly and also the torsion angle. In the GRAF application, the very low aspect ratio of the surface reduces the effect of the length contribution to the axial distortion. The length of the fin has not changed from the original Eclipse configuration. A higher aspect ratio with a longer vertical tailplane will risk being too flexible in bending deformations. The GRAF fin is thought to remain straight during twist. The reason for that is to avoid dangerous structural and flight dynamic consequences due to the aerodynamic coupling induced by bending and torsional deformations occurring at the same time. The other factor listed in the three twist angle variables is the shear modulus. That depends on the mechanical properties of the selected materials. This parameter has been determined by the minimum skin thickness, already defined in the preceding paragraph. Hence, the only parameter left to play a key role in the torsional displacements of the novel design is the polar moment of inertia of the fin cross sections. However, the torsion theory of solid sections must be adapted first to the study of hollow sections with thin-walled cross sections in order to better represent the unitised mono-coque shell constituting the GRAF empennage.

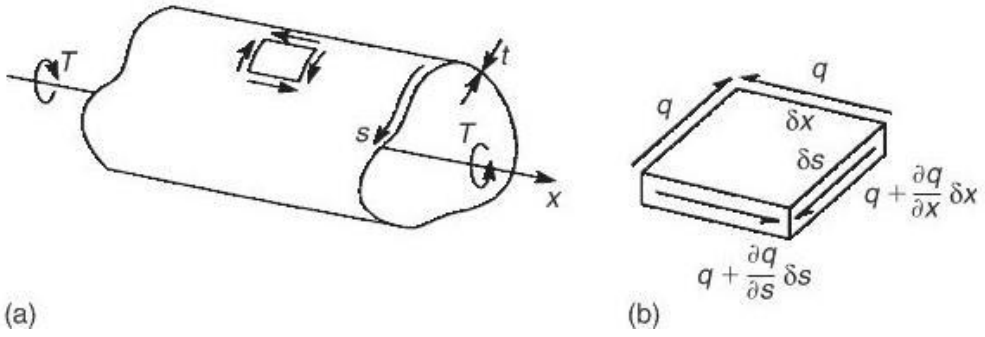

Figure 3-24 Torsion and shear flow on a thin-walled structure external surface [172].

The pure torque application on thin-walled sections that are not restrained generates only a shear stress system in the walls of the beam. Different types of stress are instead produced when axial constraint effects, or when eccentric or discontinuous

loading or diverse typology of support, are included on the beam. From the equilibrium of the wall element in the *x* and *s* direction of the beam shown in Figure 3-23(a), and discussed in detail by Megson in reference [123], the result is that the shear flow $q = \tau \cdot t$ must be constant all round the single element contour of Figure 3-23(b). Thus, due to its generic expression, it will also be constant on the whole beam wall. However, it may vary with the thickness value which might be a function of the coordinate *s*. Considering the equilibrium of the element in the *s* direction, it yields:

$$\left(q + \frac{\partial q}{\partial x} \delta x \right) \delta s - q \delta s = 0 \tag{3.66}$$

from which

$$\frac{\partial q}{\partial x} = 0 \tag{3.67}$$

Eq. (3.67) demonstrates how the application of pure torque on the thin-walled section induces a constant shear flow around the tube wall.

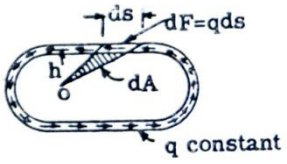

Figure 3-25 Shear flow distribution on thin-walled section [33].

For each single infinitesimal element area *dA* of the thin-walled section illustrated in Figure 3-24, it is then possible to calculate its single contribution to the torque of the whole cross section as: $dF = qds$. Taking an arbitrary point *'O'* with arm distance '*h*' from the element area, it transpires that the torsional moment contribution of *dF* around the generic point due to the element of length *ds* equals:

$$dT = qhds = 2qdA \tag{3.68}$$

by integrating Eq. (3.68) around the contour section, that brings the final expression of the total torque around the wall sections, often known as the Bredt-Batho formula:

$$T = \int_A 2qdA \tag{3.69}$$

once all these values are known it is possible to calculate the twist angle ϑ.

According to Castigliano's theorem which utilises the energy deformation theory to finalise the twist angle expression it may be expressed that:

$$\vartheta = \frac{\partial U}{\partial T} = \oint \frac{T}{4A^2 Gt} ds \tag{3.70}$$

and by assuming that all values, except the wall thickness '*t',* are constant for a tube of length '*L',* and substituting the general expression for the twist angle, it can be rewritten as:

$$\vartheta = \frac{TL}{GJ} = \frac{qL}{2AG} \oint \frac{ds}{t} \tag{3.71}$$

where *G* is the material shear modulus and *A* the area enclosed within the mean periphery of the wall sections, where

$$J = \frac{4A^2}{\oint \frac{ds}{t}} \tag{3.72}$$

is the generic expression of the polar moment of inertia. It is remarkable how this influences the torsion effect and stiffness of the entire cross section. Hence, by having excluded the option of varying either the body length or the material properties of the GRAF design, the only way to increase the torsional deflection consists of reducing the cross section polar moment of inertia of the novel aeroelastic fin. The aeroelastic fin, differently from the original Eclipse fin design, which is based on a foam core structure, will be devoid of a rigid core. The foam element is replaced by other smart and compliant components. The internal layout of the GRAF will see rotating ribs mounted on the primary shaft to twist the empennage, minimising the resistance to the torsion and warping effect. The other fin element undergoing warping deformation is the glass fibre external skin. The Table below shows the cross-sectional properties of two diverse thin-walled RAE 101 airfoil sections. The main difference between the 'open rib section' and the 'closed' one is in the trailing edge closure. The former presents a very flexible edge simulating a sealed gap with extreme flexibility and freedom in movements. The latter is rigidly connected and as it may be seen from the data in Table 6, the polar moment of inertia for the 'open' configuration, demonstrates a reduction of 15%. That might definitively result in an increase of the twist angle when the same torque is applied to open and closed sections. Besides reducing the power needed to attain the required

twist angle, the ‘open’ profile fin also reduces unexpected distortion due to the restraining effect of closed boxes under warping deformations. Therefore, as demonstrated by the data in the table, a compliant TE joint type able to reduce the torsional stiffness of the whole cross section was needed.

Table 3 - RAE101 Airfoil cross section properties

Thin-walled Section Properties:

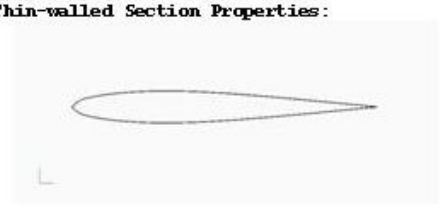

Closed Rib Section		Open Rib Section
0.0097054	=A Area A=	0.0092024
-0.0075 (Cy) 0.037329 (Cz)	Centroid (from leading edge)	-0.0075 0.028945
0.000084649 (Iyy) 1.8198E-7 (Izz)	Moment of Inertia	0.000072158 (Iyy) 1.7255E-7 (Izz)
0.093391 (Ry) 0.0043301 (Rz)	Radius of Gyration	0.088551 (Ry) 0.0043301 (Rz)
0.000084831	Polar Moment of Inertia	0.000072331
0.037228	Shear Centre (from leading edge)	0.028842

The trailing edge, represented by the flexible connection of the ‘open’ profile is, in practice, the swivel edge closure device already introduced in the preceding paragraph. It joins and closes the two edges of a thin composite skin which has been mounted on compliant ribs and smartly joined to the fuselage in order to avoid buckling and out-of-plane warping instabilities during twist. A single mono-coque shell made of a thin-walled closed section with fixed root and without any internal rib element will result in a very weak configuration during deformation. Such a single cell shell structure will buckle and warp under torsion in the same way as when we try to twist an empty soft drink can by applying pure torsion to its top and bottom. Providing the fin with internal rib elements might help to support the external shape but it will not increase the twist deformations. Conversely, the ribs will further increase the torsional stiffness of the entire structure. More powerful actuators will necessarily increase the overall weight, against the other initial primary objective of a lighter fin design.

The rigid TE closure was not the only element impeding the empennage of large deformations. Another element of the design, if not properly studied, can hinder the

twist of the whole tail, i.e. the connection between the fin root and the fuselage mount. The gapless feature implies the root section of the fin must be sealed to the aircraft body. The fixed root connection further augments the torsion rigidity of the empennage by restraining the structure from free warping. This phenomenon has already been described in the warping theory and studies presented in the literature section. For the sake of explanation let us assume the x-axis is aligned with the fin span (i.e. aligned with the shaft axis) and consider only a torsion load applied to a restrained configuration. Hence, the root section stress of a warping fin may be expressed as:

$$\sigma_{xx} = \frac{B}{C_W}\psi \tag{3.72}$$

where B and C_W are the bi-moment and warping constant of the cross section respectively. The aim of the study is to find a type of connection able to lower the stress level at the root of the fin or even cancel it out. If the fin can be twisted without stressing the structure due to warping deformation, then the final expression of the torsion equilibrium, by assuming $dB/dx = 0$, may be rewritten as:

$$M_t = GI_t \frac{d\varphi}{dx} \tag{3.73}$$

by recalling Eq. (2.34) from Chapter 2 it is evident that the absence of the bi-moment in Eq. (3.73) considerably reduces the torque necessary to twist the fin structure with the angle ϑ expressed from Eq. (3.71).

The expression of the warping stress in Eq. (3.72) refers to the torsion theory applied to generic isotropic materials. In order to consider the correct expression for composite thin-walled sections undergoing torsion, the formulation suggested by Loughlan and Ata has been assumed and written as:

$$\sigma_\Gamma = -\frac{\omega_{eff}(s)T}{\mu_s (E\Gamma)_{BS}}\left[\frac{\sinh[\mu_s(L-Z)]}{\cosh(\mu_s L)}\right]E^a_{x_i} \tag{3.74}$$

where the warping rigidity $(E\Gamma)_{BS}$ and the μ_s coefficient values have already been introduced in Section 2.6, while the sectorial coordinate distribution of the closed box may be expressed as:

$$\omega_{eff}(s) = \int_0^s \left(P_R - \frac{\psi_{eff}}{t_{eff}} \right) ds \qquad (3.75)$$

where $\psi_{eff} = \dfrac{2A}{\oint \dfrac{ds}{t_{eff}}}$, with t_{eff}, in this case of identical mechanical properties of all the walls of the box, coinciding with the real thickness of the skin, and $E^a_{x_i} = E_x / \left(1 - \nu_{xy}\nu_{yx}\right)$ being the effective elasticity of the *i*-th wall of the box.

In order to minimise the warping stiffness, and consequently the stresses induced on the skin structure, and enhance the torsional displacements of the ribs, two techniques have been applied. The first is to design a smart fin-fuselage connection to increase the torsional flexibility of the fin without weakening the stiffness. The second refers to locating the primary shaft position as close as possible to the shear centre of the fin structure. This solution allows the beneficial exploitation of the aeroelastic effect contribution during twist.

The first technique regards the solution adopted to deceive the fin to be like a fixed root and sealed configuration, while simply leaning on the fuselage joint and being actually unrestrained by the connection. The engineered method applied to join the GRAF to the fuselage is unveiled by the introduction of the *slot-connection* novelty. It basically reduces the connection site to a slot where the fin is slid in without being clamped. The system simply slides the fin assembly into a profile shaped slot on the fuselage section. The connection does not restrain the skin panels but clamps only the primary shaft inside the fuselage while allowing only rotational freedom. The covering skin is just slid into the aircraft and leaned on the edge of the slot. The simple surface contact between the fin skin and the slot border avoids any horizontal displacement or rotation of the fin base, while keeping it free to twist. Moreover, the biggest benefit of such an assembly is the fact that during twist the skin can slightly displace in the vertical direction. This movement, which will cause opposite displacements on the two sides of the skin, further reduces the torsional stiffness of the tail by cancelling out the warping stress and so increases the twist angle. This freedom is attained because there are no constraints at the root section restraining the skin edges. The consequence of that freedom means the model cancels out

longitudinal (spanwise) tensile and shear stresses caused by the warping effect and expressed in Eq. (3.74).

The second method applied to increase the twisting flexibility of the GRAF design, concerns the location of the primary shaft. It represents the main supporting element of the assembly and also the pivoting point for the rotating ribs during warping. The shaft location has been chosen in the area with the maximum airfoil section thickness, in order to offer the largest and most effective section to withstand the bending loads. Nonetheless, it is located as close as possible to the elastic axis of the whole structure, thus mostly withstanding pure torsion effects and avoiding unexpected bending coupling between aerodynamic and twisting moments. The coincident location for the shaft and the EA induces pure torsion loads on the structure. In this way, coupled deformations inducing out-of-plane distortions might be avoided. According to the rib configuration, described in the next Chapter, the ribs shear centre is located at 0.136m from the leading edge. While the primary shaft is placed at 0.125m from the LE. The difference between the two locations is about 3.5% of the geometric chord. This little eccentricity might be avoided by shifting the shaft position further rearwards, towards the trailing edge. However the rearwards shifting of the shaft has not been considered because moving from the 40% of the airfoil chord to the trailing edge of the profile, the airfoil thickness starts decreasing considerably till it becomes null at the closure edge. That means the only way to accommodate the shaft was by reducing its external diameter. Thus a consequent reduction in the cross-sectional stiffness. Therefore, although a small margin of coupled deformations might be expected from the slightly misalignment of the fin EA and the shaft location, the shaft position has been fixed at 0.4c. That is the airfoil section area offering the highest profile thickness. Hence, the larger shaft may be placed inside to be better exploited from a structural standpoint. The shaft has been placed as close as possible to the fin elastic axis in order to involve the structure only in pure torsion deformations minimising the out-of-plane distortions.

The FEA results on the GRAF model will show good and successful results obtained from the application of this type of fin-fuselage connection when compared to a rigid one. The warping is also facilitated by the presence of the rotating ribs which follow the twisting deformation of the fin shape without representing rigid obstacles

hindering the fin motion. The twist operations are managed by a single actuator placed at the bottom of the primary shaft, releasing and governing the rotations of the assembly in flight. Furthermore, the rearward location of the shaft helps the aeroelastic effect generation to act effectively on the GRAF configuration. The distance between the AC of the profile and the shaft position works as an arm moment for the aerodynamic forces. That is the cause which creates the twisting moment used to warp the empennage. The results of Chapter 5 will show the beneficial effect of the twisting moment produced by the aerodynamic loads applied onto the AC of the profile. The aeroelastic moment is exploited for both the self-adaptive mode and the control authority activation of the fin. The aerodynamic deformations also achieve the effect of reducing the actuation power needed to warp the structure for side force generation.

The servo-mechanical actuator responsible for the control and activation of the warping mode of the GRAF will be mounted at the bottom of the main shaft. That is not the only way the fin may initiate the twist. The aeroelastic effect, better explained in the next paragraph, will also contribute to the deformation.

3.6.1 The GRAF FEM Structural Model

This section describes in detail the FE modelling of the GRAF structure used to run the numerical analysis with a commercial finite elements method-based program. The entire fin structure with all its detailed components has been built into a 3-D model for FEM analysis carried out by using the MSC/NASTRAN processor. The FEM analysis is used to verify that the GRAF can safely withstand the operating loads and perform the required deformation without stress failure. Stiffness and strength criteria are applied. After the preliminary surface model construction, the entire surface area has been meshed using quadrilateral ‘CQUAD4’ elements. Triangular mesh elements ‘CTRIA3’ are used instead as transition elements to connect finer mesh areas to coarser meshed regions. Finer mesh regions are concentrated where a high stress gradient is expected, such as the circular cut-out

connecting the ribs with the roller bearing to the main shaft. It is suggested, for accuracy of the mesh results, that the side ratio of the CQUAD4 elements is kept in a range between 2:4 and 4:4 [125]. The majority of the elements of the GRAF model present a squared 4:4 ratio. Only a small percentage of the mesh shows a 3:4 ratio mesh. That is because a unit proportionality of the element sides was not possible due to the articulated geometry of the surface. The FEM model of the GRAF has been built with 18,600 elements of mesh and 21,899 nodes. The CQUAD4 and CTRIA3 elements represent the composite plate elements of the fin skin, ribs, stringers and main shaft. The internal part of the leading edge has been built with 3-D solid elements to replicate the presence of a lattice edge used to soften the front nose of the fin in favour of a more compliant and flexible behaviour.

At the bottom end of the primary shaft is located the constraint restraining the entire fin DOF but not the rotational one. The 5-degrees restrained constraint simulates the bearing clamp placed inside the fuselage which firmly holds the whole assembly. The other element of the assembly that also works as a compliant constraint is the slot connection. Two-dimensional spring elements, 'CELAS2' with variable DOF, have been utilised to model the slot-connection features. These elements are spring connections attached with one extremity to a fixed constraint, in this case represented by the aircraft fuselage, and with the other end in contact with a dependent node on the fin skin, corresponding to where the slot edge joins the empennage. The mechanical properties of these elements can be defined by the user to decide which degree of freedom must be fully or partly released either in translation or rotation. In order to properly model the flexible characteristics of the slot-connection, the spring elements have been constrained in the x- and y-axis translation, while left free in the rest of the DOF. The model uses spring elements rather than rigid connections because it wants to simulate the presence of a flexible material in between the surface parts. In order always to have a sealed gap during twist activation, a strip of elastic material is placed between the fuselage slot and the fin skin. The expansion and contraction of the elastomeric strip allows the material to always be in contact with both parts and keep the gap sealed. Therefore, its elasticity is modelled by the spring constants.

The other GRAF elements included in the FEM model, such as the roller bearings, the sliding connection and the rest of the linkages, have been modelled by using rigid elements 'RBE2'. These elements rigidly connect two or more nodes allowing partial degrees of freedom in the required direction. Rigid elements have also been used to simulate the leverages used for the mechanical push-rods connection with the actuation system, while other RBE2 elements featured with chordwise translational and spanwise rotational freedoms have been applied to model the characteristics of the swivel edge closure for the cambering tasks of the TE section.
The structural analysis on the GRAF model has run linear static cases. They have been carried out running the solution SOL 144 of the MSC/NASTRAN processor. Solutions SOL 145 and SOL 146 have been respectively applied for the flutter and dynamic aeroelastic response study of the models.

3.7 Aeroelastic effect and aeroelasticity of the GRAF design

This part of the chapter discusses those aeroelastic phenomena which might occur on this type of aerodynamic element, and how some of them are investigated to be avoided while others are instead tried to be exploited to enhance the flight performance of the novel fin configuration. Both steady and unsteady aerodynamic effects are considered for static and dynamic aeroelastic studies. The major distinction in aeroelastic phenomena is the time domain. When the time does not appear as an independent variable, then static aeroelastic instabilitites can be investigated, otherwise the domain of time-dependent dynamic phenomena must be taken into consideration. In the first group there are divergence, control effectiveness and reversal phenomena. In the other group there are flutter, buffeting and aeroelastic dynamic response cases. Clear explanations of all these phenomena, their assumptions and theories are provided in detail in references [24]. For the purpose of this project, only those aeroelastic aspects directly involved into the performance, stiffness and strength characteristics of the GRAF empennage will be studied. In the specific case, these are the reversal, divergence and flutter instabilities. In particular,

the controlled development of diverging circumstances is the aeroelastic effect condition sought for the GRAF design. The exploitation of this technique permits the utilisation of the deformations derived from the aerodynamic loads onto the flexible structure for increasing flight stability and controllability performance. The mechanical and aeroelastic induced deformations are the two ways used by the unconventional fin to accomplish its tasks. However, the aeroelastic effect exploitation is generally a riskier approach than classical rigid designs and is normally avoided in conventional wing and tailplanes structures. It requires the unusual characteristic of implicit flexibility or compliancy in the undertaking structure, with the risk of degenerating into loss of control and structural failures. These types of problem are normally avoided by stiffening the components and strengthening the design. In order to safely withstand reversal, divergence and flutter circumstances, aeronautical structures rely upon stiff and robust torsion boxes. The main tasks they are asked to accomplish are to protect from failure the primary box undergoing pure torsion loads and bending-coupled deformations.

Let us explain more in detail the phenomena originating such conditions either for a generic aerodynamic surface or the GRAF design. For the scope of this study let us define the angle of attack, for the generic airfoil section, written by means of two separate components, as follows:

$$\alpha = \alpha^r + \vartheta \tag{3.76}$$

where α^r refers to the initial angle of attack of the aerodynamic surface, while ϑ is the elastic twist angle due to the spanwise structural flexibility of the sections.

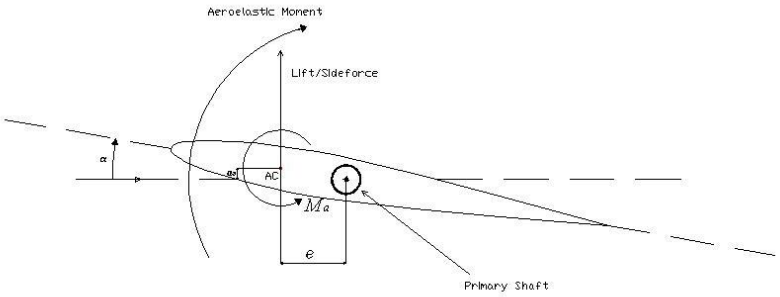

Figure 3-26 Airfoil CAD illustration of the GRAF induce aeroelastic moment.

The twist angle is easily computed from the equilibrium between the total aerodynamic torque generated by the external loads and the elastic reaction of the

structure. The aerodynamic torque evaluated about the elastic axis of the aerodynamic surface is:

$$T = (C_L e + C_{mAC} c) qS \tag{3.77}$$

where C_L is the lift coefficient (i.e. the side force coefficient for vertical empennages), C_{mAC} is the aerodynamic pitching moment of the profiles, whose surface area is indicated by *S*. The dynamic pressure is included in the parameter *q*. By taking into account the structural expression of the twist, previously expressed through the polar moment of inertia formulation, and by considering once again a more compact expression for the torsion angle, using the flexibility influence coefficient, $C^{\vartheta\vartheta}$, the final twist angle can be written as:

$$\vartheta = C^{\vartheta\vartheta} T \,, \tag{3.78}$$

substituting the aerodynamic torque for the elastic twist of the wing, it becomes:

$$\vartheta = \frac{C^{\vartheta\vartheta}\left[\left(\partial C_L \big/ \partial\alpha\right) e\alpha^r + C_{mAC} c\right] qS}{1 - C^{\vartheta\vartheta}\left(\partial C_L \big/ \partial\alpha\right) qSe} \tag{3.79}$$

as evident from equation (3.79), the twist is directly proportional to the distance "e" between the AC (i.e. 0.25c) and the EA of the profiles. The closer the EA is to the AC, the lesser the torsional effect generated by aerodynamic force variation. The value of "*e*" influences the torsion effect on the twist deformation of the GRAF model. It changes the moment arm that causes the aerodynamic moment to twist the structure. That distance in the GRAF tail model is increased up to 15% of the fin chord, from the AC location. The shorter the arm the lesser the aeroelastic effect produced. Furthermore, a shorter arm might favour an opposite twist effect than the one expected, determining the reversal condition of the tail. That situation occurs when a too flexible wing is subjected more to the torsion generated by the airfoil pitching moment coefficient rather than the one produced by the lift. A farther location of the shaft in the GRAFT model would have been more effective for the

aeroelastic effect generation. However, as has already been discussed in the previous section, geometric issues impeded the rearwards shifting of the shaft. From the aeroelastic static standpoint, equation (3.79) allows the definition of an important result valid for all types of aerodynamic structures. It determines the first instability condition of torsional divergence, occurring when the denominator of expression (3.79) tends towards zero. That circumstance is well defined by its characteristic flight speed, namely the divergence speed, which may be obtained from the divergence dynamic pressure:

$$q_D = \frac{1}{C^{\vartheta\vartheta}(\partial C_L/\partial\alpha)Se} \tag{3.80}$$

which finally results in:

$$U_d = \sqrt{\frac{1}{C^{\vartheta\vartheta}(\partial C_L/\partial\alpha)\left(\rho/2\right)Se}} \tag{3.81}$$

The divergence speed is independent from both the initial angle of attack and the airfoil camber effect (there is no contribution from the C_{mAC}). But it is directly dependent on the profile's lift-curve slope and the surface structural stiffness, through the flexibility coefficient $C^{\vartheta\vartheta}$.

Although the GRAF design technology implies, in a controlled fashion, the exploitation of the divergence attitude of semi-flexible aerodynamic surfaces, the novel empennage has been tested to avoid unexpected divergence instabilities at any point of its flight envelope. Therefore, in order to guarantee safe application of the GRAF, all the aeroelastic analyses have been carried out to assess the safety of the unconventional design against all the unstable flight conditions. The MSC/NASTRAN Flight Loads package has been used to verify the aeroelastic stability of the novel fin against those differing situations and critical speeds. Flexibility of structural components is always a risk if not properly controlled. That applies not only to divergence instability but also to other problems associated with

weak torsional stiffness of the structures, such as the surface control reversal.

When the yaw motivator, either in the form of a conventional hinged rudder or a cambering trailing edge, is activated in deflection by an angle δ, then the lift and pitching moment coefficients start to change. Their contributions influence the twist angle of the aerodynamic surface according to the torque expression responsible for inducing the deformation, which is written as:

$$T = qs\left\{e\left(\frac{\partial C_L}{\partial \delta}\delta + \frac{\partial C_L}{\partial \alpha}\vartheta\right) + c\frac{\partial C_{mAC}}{\partial \delta}\delta\right\} \tag{3.82}$$

and substituting again equation (3.82) for (3.78), it is possible to express the elastic twist-to-surface motivator displacement ratio, as:

$$\frac{\vartheta}{\delta} = \frac{e\left(\partial C_L \big/ \partial \delta\right) + c\left(\partial C_{mAC} \big/ \partial \delta\right)}{\left(1 \big/ C^{\vartheta\vartheta} qS\right) - e\left(\partial C_L \big/ \partial \alpha\right)} \tag{3.83}$$

This result allows the estimation of the unit twist distortion per unit degree of command surface displacement. It can also be rewritten to give the lift coefficient value when the command surface is deflected. It becomes:

$$C_L = \frac{\left(\dfrac{\partial C_L}{\partial \delta}\dfrac{1}{(\partial C_L/\partial \alpha)C^{\vartheta\vartheta} qSe} + \dfrac{c}{e}\dfrac{\partial C_{mAC}}{\partial \delta}\right)\delta}{\dfrac{1}{(\partial C_L/\partial \alpha)C^{\vartheta\vartheta} qSe} - 1} \tag{3.84}$$

This expression in Eq. (3.84) helps define how much lift is generated by a control surface deflection. Meanwhile, it can also be used to evaluate the reversal point condition of the tailplane surface. That is the value of C_L at which the deflecting command surface becomes utterly ineffective, thus producing C_L = 0. That circumstance occurs only when the twist angle is such that the numerator of the equation above tends towards zero. Thereby, it finally gives a reversal speed of:

$$U_R = \sqrt{\frac{-\frac{\partial C_L}{\partial \delta}}{\frac{\partial C_L}{\partial \delta}\frac{\partial C_{mAC}}{\partial \delta} C^{\vartheta\vartheta} \frac{\rho}{2} Sc}} \tag{3.85}$$

this speed depends only upon the aerodynamic characteristic shape of the airfoil section influenced by the deflected section. The reversal speed is totally independent from the elastic axis location, defined by the "*e*" distance. However, as the results will show, this type of instability is not a concern of the aeroelastic tail. The reversal effect does not occur on the GRAF model because the aeroelastic effect on the fin starts twisting its shape in the desired directions before reversing its torsion. In classic configuration, the reversal phenomenon may occur because the twisting moment generated by the pitching coefficient is unbalanced by the lift produced moment and by the torsional stiffness of the structure. Conversely, in the GRAF model, as soon as the fin generates side force, the joint combination of flexibility, compliant design and shaft location, starts rotating the entire shape around the shaft axis in the same direction as the side force. The angle of attack starts increasing, thus further contributing to the side force generation and so to the twisting moment effect generated by it. The aeroelastic effect in the GRAF design is used to keep the fin twisting once the deformation is initiated, whether it has been actuated by servo mechanism or external force, as illustrated in Figure 3-26.

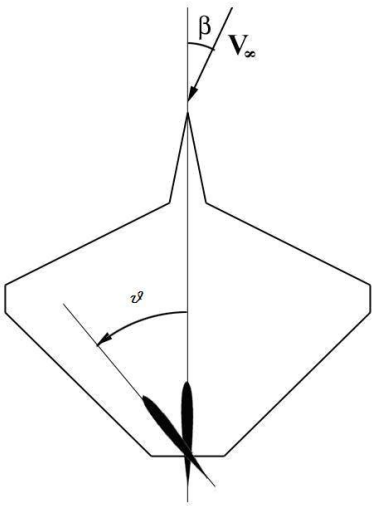

Figure 3-27 Eclipse CAD illustration of effective side wind and twist angles.

The aerodynamic section of Chapter 5 will present the value of the generated aeroelastic moments with varying flight speeds. It quantifies the diverging effect of the GRAF design at different speeds and twist angles. The minimum level of necessary torque to counteract the aeroelastic effect on the fin in order to control, hold and rotate back the twisting fin will be assessed.

Besides the already mentioned divergence and reversal studies for the static aeroelastic analysis of the GRAF model, the flutter and the aeroelastic dynamic response studies of the structure have been performed too. The flutter study carried out using the NASTRAN model has been based on solving the equation of system (3.86), which has been introduced with the Theodorsen model already anticipated in Chapter 2.

$$\begin{cases} m\ddot{h} + S_\alpha \ddot{\alpha} + m\omega_h^2 h = Q_h \\ S_\alpha \ddot{h} + I_\alpha \ddot{\alpha} + I_\alpha \omega_\alpha^2 \alpha = Q_\alpha \end{cases} \tag{3.86}$$

in order to predict the flutter behaviour of an aircraft structure, the dynamic variation of h and α must be studied. Hence, by considering the solutions of the type as:

$$h = \overline{h_0} e^{i\omega t} \qquad \text{(3.87a)} \qquad \text{and} \qquad \alpha = \alpha_0 e^{i(\omega t + \phi)} = \overline{\alpha_0} e^{i\omega t} \qquad \text{(3.87b)}$$

and then by taking the low speed flow and substituting it for the harmonic motions in equations (3.86), it is possible, by rearranging both lift and moment equations, to get to the dimensionless flutter equations in the form of:

$$\frac{\overline{h_0}}{b}\left\{\frac{m}{\pi\rho b^2}\left[1-\frac{\omega_h^2}{\omega^2}\right]+L_h\right\}+\overline{\alpha_0}\left\{x_\alpha\frac{m}{\pi\rho b^2}+\left[L_\alpha-L_h\left(\frac{1}{2}+a\right)\right]\right\}=0 \tag{3.88}$$

$$\begin{aligned}\frac{\overline{h_0}}{b}\left\{x_\alpha\frac{m}{\pi\rho b^2}+\left[\frac{1}{2}-L_h\left(\frac{1}{2}+a\right)\right]\right\}+\overline{\alpha_0}\left\{r_\alpha^2\frac{m}{\pi\rho b^2}\left[1-\frac{\omega_\alpha^2}{\omega^2}\right]+\right.\\ \left.+M_\alpha-\left(L_\alpha+\frac{1}{2}\right)\left(\frac{1}{2}+a\right)+L_h\left(\frac{1}{2}+a\right)^2\right\}=0\end{aligned} \tag{3.88b}$$

this is a homogeneous system as a function of the reduced frequency *k*, constituting an algebraic eigenvalues problem stated by the characteristic determinant created by the two equations (3.88a) and (3.88b). Generally, when speaking of flutter, the unsteady aerodynamics is taken into account to consider the dynamic behaviour of

the structure merged in the aerodynamic forces fluctuation. The *reduced frequency "k"* is introduced in the dynamic aeroelastic phenomena in order to consider the unsteadiness of those circumstances compared to the quasi-steady lift generation cases. The effect of a varying frequency and the unsteadiness of the phenomena could reduce the lift's magnitude and also introduce a phase lag between the airfoil motion and the related unsteady forces. When the frequency of oscillations increases, the amplitude of the unsteady forces decreases. The mentioned reduced frequency can be written as:

$$k = \frac{\omega b}{V} \tag{3.89}$$

where b is the airfoil semi-chord. The reduced frequency characterises the Theodorsen's function [171] used to model the variation of amplitude and phase for a sinusoidal unsteady behaviour of the aerodynamic forces around a section for specified frequency values. It works as a transforming filter to convert the input of quasi-steady lift for an airfoil to the final output of unsteady aerodynamic forces related to the frequency. The function can be expressed as:

$$C(k) = F(k) + iG(k) = \frac{H_1^{(2)}(k)}{H_1^{(2)}(k) + iH_0^{(2)}(k)} = \frac{K_1(ik)}{K_0(ik) + K_1(ik)} \tag{3.90}$$

with $K_j(ik)$ and $H_n^{(2)}(k)$, as a Bessel and Hankel function of the second kind. Bisplinghoff and Fung give an approximate expression for $C(k)$ written as:

$$\begin{cases} C(k) = 1 - \dfrac{0.165}{1 - \dfrac{0.045}{k} i} - \dfrac{0.335}{1 - \dfrac{0.3}{k} i} & k \le 0.5 \\ C(k) = 1 - \dfrac{0.165}{1 - \dfrac{0.041}{k} i} - \dfrac{0.335}{1 - \dfrac{0.32}{k} i} & k > 0.5 \end{cases} \tag{3.91}$$

This approach of studying a harmonic oscillating airfoil allows the solution of the flow around the section to be split into two parts:

- Circulatory terms: lift and moment due to vorticity of the flow, and related to Theodorsen's function;

- Non-circulatory terms: usually interpreted as apparent inertia not connected to flow vorticity but due to acceleration of mass of air around the airfoil during pitch and heave motion.

Hence, the lift and moment expressions as a function of the reduced frequency can be written as:

$$L = \pi\rho b^2\left[\ddot{h} + V\dot{\alpha} - ba\ddot{\alpha}\right] + 2\pi\rho VbC(k)\left[\dot{h} + V\alpha + \left(\frac{1}{2} - a\right)\dot{\alpha}\right] \tag{3.92a}$$

$$\begin{aligned} M &= \pi\rho b^2\left[ba\ddot{h} - Vb\left(\frac{1}{2} - a\right)\dot{\alpha} - b^2\left(\frac{1}{8} + a^2\right)\ddot{\alpha}\right] + \ldots \\ &\ldots + 2\pi\rho Vb^2\left(a + \frac{1}{2}\right)C(k)\left[\dot{h} + V\alpha + b\left(\frac{1}{2} - a\right)\dot{\alpha}\right] \end{aligned} \tag{3.92b}$$

where the first parts of the two equations embody the non-circulatory terms, while the second parts with the Theodorsen functions take into account the circulatory ones. Considering a further transformation with the oscillatory aerodynamic derivatives and coordinate substitution, the two equations system can be expressed in a more compact form as:

$$\begin{Bmatrix} L \\ M \end{Bmatrix} = \rho V\begin{bmatrix} bL_{\dot{h}} & b^2L_{\dot{\alpha}} \\ b^2M_{\dot{h}} & b^3M_{\dot{\alpha}} \end{bmatrix}\begin{Bmatrix} \dot{h} \\ \dot{\alpha} \end{Bmatrix} + \rho V^2\begin{bmatrix} L_h & bL_\alpha \\ bM_h & b^2M_\alpha \end{bmatrix}\begin{Bmatrix} h \\ \alpha \end{Bmatrix} = \rho V\,\mathbf{B}\begin{Bmatrix} \dot{h} \\ \dot{\alpha} \end{Bmatrix} + \rho V^2\mathbf{C}\begin{Bmatrix} h \\ \alpha \end{Bmatrix} \tag{3.93}$$

where ***B*** and ***C*** are the aerodynamic damping and stiffness matrixes respectively. The classical form of the aeroelastic problem can also be posed through the expression of the equation of motion, as:

$$\mathbf{A}\ddot{\boldsymbol{q}} + \left(\rho V\mathbf{B} + \mathbf{D}\right)\dot{\mathbf{q}} + \left(\rho V^2\mathbf{C} + \mathbf{E}\right)\mathbf{q} = 0 \tag{3.94}$$

where **A, B, C, D, E** are the structural inertia, aerodynamic damping, aerodynamic stiffness, structural damping and structural stiffness matrices respectively, and ***q*** is the generalised coordinates vector. It is common notation in aeroelasticity to name the structural inertia, damping and stiffness matrices as **A, D, E,** rather than being

conventionally adopted in simple structural dynamics **M, C** and **K** notation. Then, by introducing the identity NxN matrix **I**, the equation (3.94) can assume the partitioned form:

$$\begin{Bmatrix} \dot{\mathbf{q}} \\ \ddot{\mathbf{q}} \end{Bmatrix} - \begin{bmatrix} \mathbf{0} & \mathbf{I} \\ -\mathbf{A}^{-1}\left(\rho V^2 \mathbf{C} + \mathbf{E}\right) & -\mathbf{A}^{-1}\left(\rho V \mathbf{B} + \mathbf{D}\right) \end{bmatrix} \begin{Bmatrix} \mathbf{q} \\ \dot{\mathbf{q}} \end{Bmatrix} = \mathbf{0} \tag{3.95}$$

this system is now transformed in the classical eigensolution form of the kind:

$$\left(\mathbf{A} - \mathbf{I}\lambda\right)\mathbf{x} = \mathbf{0} \tag{3.96}$$

where the complex conjugate pairs of the eigenvalue solution λ contains the system's natural frequencies and damping ratios coefficient. The aeroelastic model is now, through the **B** and **C** matrices, reduced frequency-dependent. However, those two matrices cannot be numerically formed without knowing the values of some specified reduced frequency of interest. However, that condition cannot be defined unless an eigensolution of the system (3.95) is found, where the **B** and **C** matrices are directly involved. Therefore in order to sort out this "chicken and egg" problem, a few numerical approaches known as "frequency matching" methods have been developed. The most used ones are the American "*k-method*" and the British "*p-k method*". The former, introduced by Theodorsen, was based on including the aerodynamic loads in the frequency domain as mass terms. The latter was introduced by Hassig and based on the idea of Frazer and Duncan [24, 125] of including the aerodynamic loads in the frequency domain as stiffness and damping terms. Both methods are based on the assumptions that at the flutter speed the aerodynamic response is strictly dependent upon a harmonic behaviour. The *p-k method* also implemented in the Flight Loads tool of MSC/NASTRAN is the one selected to evaluate the aeroelastic instability of the novel fin design. The *p-k method* carries out the analysis by making, as first step, an initial guess of the frequency as $p_0 = \delta_0 + jk_0$. Then, it evaluates the general aerodynamic matrix with this guessed frequency and the *p-k* approximation to find out the new root $p_1 = \delta_1 + jk_1$ obtained from the eigenvalue solution of the characteristic determinant. The previous steps must be continuously iterated until the imaginary part of the root becomes invariant

as $k_n \cong k_{n-1}$. At that condition a precise velocity will correspond that will decree the flutter speed of the examined structure.

This procedure is implemented by the NASTRAN solution SOL 106. The model results are presented in Chapter 6.

3.7.1 Dynamic response analysis

The dynamic response analysis applies loads varying within the time or the frequency domain. This analysis widely differs from those static aeroelastic phenomena where time dependent variables were absent from the equations and from those flutter case studies where harmonic variations of displacements with the time were included. This type of analysis shows how the structure dynamically reacts to instantaneous changes and unexpected external solicitations to restore equilibrium and stable conditions.

Rapidly applied forces can be split into two different categories. Mainly, the distinction can be made by classifying the way the forces are generated and applied on the structure. One group is linked to rapidly applied forces induced by rapid manoeuvres of the aircraft, as per sudden command surface deployment for disengaging actions, changing direction or sudden correction of the aircraft heading. These actions may cause the instantaneous forces on the structure generated by the rapid variation of the external pressure distribution. In the other group, applied forces more related to external and natural circumstances, such as gusts, aerodynamic interference with other aircraft wakes and shock waves, might be recognised. Both groups of perturbations equally affect and concern any class of aircraft from structural and handling quality standpoints.

In the specific case of this research study, four different types of investigation are conducted on the aeroelastic fin. The first two analyses regard the modal frequency (FRA) and transient response analysis (TRA). These two types of analysis are used to assess the structural stiffness of the design within a more dynamic loading scenario. In the particular case of the GRAF model, both the modal and transient

response analyses will excite the fin with the set of loads corresponding to the worst case scenario. Both models are run using the aeroelastic modal analysis performed by the Flight Loads tool of the NASTRAN framework. In the case of dynamic analysis, there are usually two different numerical methods which can be applied to examine the cases: direct and modal dynamic analysis. The direct method solves the equation of motion in terms of forcing frequency, while the modal method utilises the mode shapes of the tested structure to reduce the order and uncouple the equations of motion. The modal type of analysis has been preferred to the direct type because it is more adaptable when complicated FE models with a large number of nodes are taken into consideration. By using the same notation adopted in [125] then Eq. (3.97) indicates the transformation from physical coordinates to modal coordinates operated by the numerical method for both frequency and transient response analyses, as:

$$\begin{aligned} FRA \quad \{u(\omega)\} \quad &\rightarrow \quad \{x\} = [\phi]\{\xi(\omega)\}e^{i\omega t} \\ TRA \quad \{u(t)\} \quad &\rightarrow \quad \{u(t)\} = [\phi]\{\xi(t)\} \end{aligned} \tag{3.97}$$

where $[\phi]$ are the mode shapes used to link the problem to the behaviour of the global modes rather than to the single structural grid points. If all modes are used than the system results in an equality with the direct mode analysis. Usually, just a few modes are used to represent the real model and compute the dynamic response. That is also the reason why in Chapter 6 only a precise range of frequency has been taken into account, including the first four shape modes of the fin.

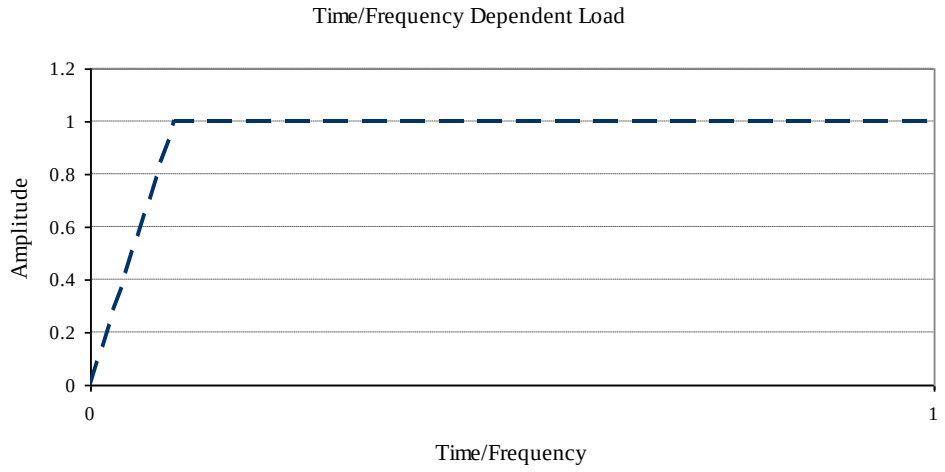

Figure 3-28 Unit scale factor diagram for time/freq. varying forces and loads.

The dotted line shown in the above diagram, Figure 3-27, illustrates the way the dynamic loads are applied upon the fin model for both types of frequency and transient response analyses. The curve indicates the scale factor by which the overall load is multiplied when applied on the structure according to the corresponding value in abscissa representing either the frequency (Hz) or the time (sec).

In the case of the GRAF model, attention to the analysis results has focused predominantly on the displacements of the fin structure under frequency and time dependent varying loads, and on the fin root node bending moment and shear force reaction. The stress level of the entire structure has not been computed because of the considerable number of elements present on the FE model, and the analysis may result in a very time demanding process outside the timeframe of this research study.

The last two types of dynamic response analyses regard the *1-cos* type discrete gust analysis, as already anticipated in the aerodynamic section. One analysis has tested the GRAF model to evaluate displacements and node reaction of the fin assembly when a sudden lateral gust hits the fin surface. The other has tested the aeroelastic fin, integrated with the entire aircraft, and subjected to cyclic lateral gusts to compare the yaw response of the whole vehicle with the one adopting the rigid fin configuration.

Rapid external disturbances, if not adequately damped, can translate into discomfort for all passengers and an unpleasant, unstable flight attitude of the vehicle. In particular, poorly damped directional oscillations may degenerate in such a stability phenomenon normally called fish-tailing.

The results of this part of the study are included in Chapter 6.

3.7.2 The FEM aeroelastic model

This section of the chapter describes the way the structural components and the aerodynamic features of the GRAF have been integrated to run the aeroelastic

dynamic cases. The cases investigated in this section through the FE aeroelastic model of the fin will consider:

- the divergence and flutter study (although the divergence case belongs to the static aeroelastic analysis, it is enclosed in this section because its model must be mandatorily integrated with the aerodynamic grid included with the rest of the model);
- the frequency and transient response analysis; and,
- the discrete gust response cases;

The model analyses have been carried out using the Flight Loads Tool of the NASTRAN package. However, a few more elements and information had to be added to the FEM model of the fin in order to take into account the implementation of the aerodynamic grid. A new set of nodes is included to identify and build the aerodynamic grid of the structural mesh. The aerodynamic grid will be formed by a chordwise and spanwise distributed finite number of boxes which will represent the aerodynamic panels for the Double-Lattice-Method (DLM) model analysis used by Flight Loads. This grid, representing an aerodynamic flat surface, will lie in the middle plane of the structural sections of the fin. Its task will be to generate and feel all the external variations of the surrounding airflow. In order to transfer the external aerodynamic solicitations from the aerodynamic grid to the nodes on the structural grid, a specific type of constraint is applied. The multi-point-constraint (MPC) elements of NASTRAN allow the user to mutually link the two grids together with a specifically defined set of equations to describe the mechanical properties of this type of connection. In the particular case of the GRAF FE model, the MPCs have been defined with the following equation specified for each MPC element:

$$0.5ynode_1 + 0.5ynode_3 = -1ynode_2 \tag{3.98}$$

Equation (3.98) states that when the aerodynamic grid node "2" moves according to an external excitation or internal input, then the other two nodes (nodes 1 and 3) located on the structural grid of the fin must move accordingly and proportionally to node "2". The aerodynamic node is at the centre of the MPC, and exactly on the in-plane aerodynamic surface, while the two structural nodes are attached at the two

opposite ends of the MPC and, due to the symmetry of the fin section, are one on each side of the section (i.e. on the skin panels). Those nodes allow the MPCs to transfer the aerodynamic grid nodal displacements to the structural model. They eventually create the deformation of the structural grid and allow the identification of the structure's nodal displacements and stresses. In order to connect the deformations of the finite number of nodes belonging to the aerodynamic grid to those on the structural grid, a harmonic and smooth distribution of the displaced aerodynamic nodes is created by the NASTRAN model by applying an interpolation method termed splining. This technique is also used to take into account their mutual interaction during the aeroelastic deformation and analysis, and also the mechanical properties and stiffnesses of the structural model. The MSC/NASTRAN processor peaks up the structural degrees of freedom as the independent set of DOF, while considering the aerodynamic DOF as dependent ones. Then, a few transformations are required to pass from one system to the other and connect the two grids together. One of these passages creates the relationship between the aerodynamic forces and the structurally equivalent forces on the structural grid points, necessary to compute the aero-structure interconnection. The splining method relates the components of the structural grid point deflections $\{u_g\}$ to the deflections of the aerodynamic grid $\{u_k\}$ via an interpolation matrix $\lfloor G_{kg} \rfloor$ as follows:

$$\{u_k\} = \lfloor G_{kg} \rfloor \{u_g\} \tag{3.99}$$

where, in the particular case of the GRAF design, the matrix *G*, due to the complexity of structural model, is based on a surface spline. A line spline option is also available for the aeroelastic solution, but it is more appropriate when a fewer number of nodes and a more simplified geometry constitutes the model. A surface spline is a mathematical tool used to find a surface function, $w(x, y)$, which covers all points of the grid and that are numerically known only for a finite number of a discrete set of points, (x_i, y_i). The solution of the function $w(x, y)$ is computed by interpolation of the single solutions w_i found for the discrete set of points. Once the

surface function $w(x, y)$ is obtained, then, by applying the virtual work principle to equation (uu), the final force transformation is also attained and written as:

$$\{F_g\} = [G_{kg}]^T \{F_k\} \tag{3.100}$$

with $\{F_k\}$ being the aerodynamic force and $\{F_g\}$ the structurally equivalent ones ready to be transferred to the entire structure. As said before, the effect of these applied forces will be presented in the stresses and displacements results of the static and dynamic aeroelastic analysis.

Let us now explain the modelling details of the aeroelastic model built for the GRAF design. As already introduced, the aerodynamic grid is formed by a series of quadrangular elements representing the aerodynamic boxes used to compute the aerodynamic forces of the built lifting surface. Figure 3-28 shows the generic chord- and span-wise distribution of the aerodynamic boxes.

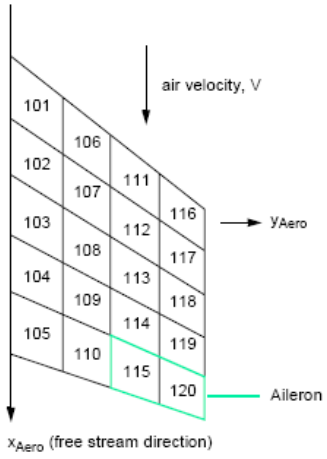

Figure 3-29 MSC.NASTRAN exemplification of aerodynamic boxes model [125].

A local reference system termed “aero” is included to simplify the construction and the sign convention of the aerodynamic grid. The aero x-axis is oriented parallel to the wind direction and pointing in the same direction as the airflow, see Figure 3-28. The aero y-axis points to the starboard of the aircraft and the z-axis follows the rule of the right hand to form a coordinate reference system, and point downwards with respect to the aircraft body. As shown in the model example of Figure 3-28, in order to perform the aeroelastic analysis, the NASTRAN tool requests all the aerodynamic boxes to be numbered and sequenced per column. The nodes at the corner of each

box are the ones connected to the structural grid via the MPC elements. The centre of each box, instead, contains the aerodynamic grid points, free in plunge and pitch, that will establish the aerodynamic effect on each panel. The aerodynamic boxes have been manually input in the aeroelastic code using the entry 'CAERO1'. It specifies the input for the coordinates, dimensions and numbers of the boxes on each aerodynamic surface used for the analysis. In the GRAF aeroelastic model there are 42 aerodynamic boxes. They are distributed upon the fin surface with seven boxes across the chord line and six boxes along the fin span. For a better accuracy of the analysis, the DLM application recommends a minimum of four boxes chordwise, whose length must be equal to: $\Delta x < 0.08V / f$. Where V and f are respectively the maximum flight speed and frequency (in Hz) of interest. The GRAF model boxes verify that condition by having a larger number of boxes chordwise. Figure 3-29 shows the aeroelastic FE models of the GRAF empennage (on the right) and the entire model of the Eclipse UAV integrated with the aeroelastic fin.

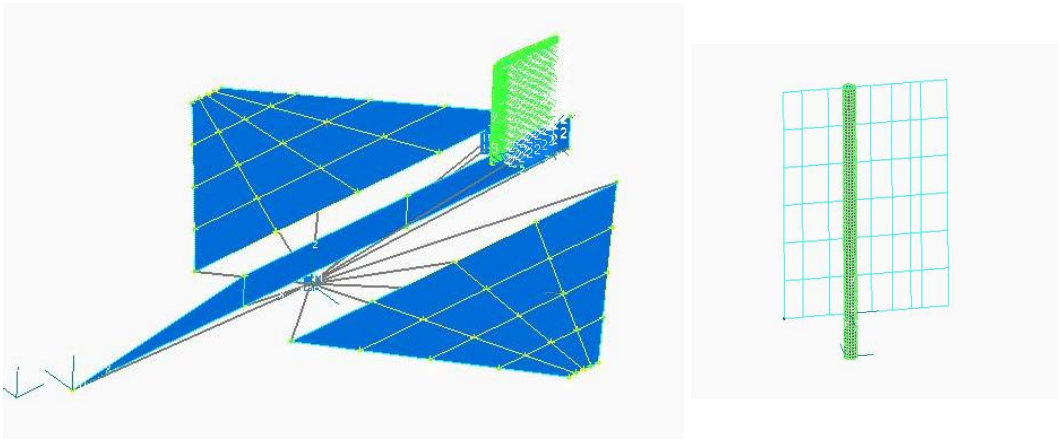

Figure 3-30 MSC.NASTRAN Flight Loads GRAF empennage (right) and Eclipse UAV with GRAF (left) models.

The whole Eclipse UAV model shown in Figure 3-29 was used only for the directional stability derivates and gust response analyses. The model has taken into account the inertia and aerodynamic interference of the wing and fuselage components integrated with the novel fin concept. The divergence, flutter and dynamic response cases have been analysed using only the fin model. These aerodynamic boxes are then all linked together via the SPLINE1 entry which specifies which CAERO1 group of boxes must be associated with the defined sets of points on the structural grid. Further aerodynamic data and information are then input

via the AEROS and AERO entry, respectively for the static and dynamic aeroelastic analyses. They specify the aerodynamic reference system, reference air density, flight speed and the wing reference chord necessary to run the analysis. Other entries such as SET1, SPC, MPC and SUPORT define further inputs requested by the aeroelastic model. The SET1 entry contains the list of sequenced nodes which form the aerodynamic grid. It tells the SPLINE1 entry which nodes must be identified with the aerodynamic boxes. The MPC entry, as already explained, defines the set of elements which links those nodes to the ones on the structural grid. The Single Point Constraint (SPC) entry declares which of the structural nodes have any DOFs retained by a rigid constraint. Eventually, the six rigid-body modes of the whole model must be restrained. Those modes which are left unrestrained by SPC, are then enclosed within the SUPORT element. This element is specifically applied by NASTRAN for aeroelastic and dynamic studies. It virtually reduces the DOFs of the model without rigidly constraining them. The SUPORT entry provides a frame of reference for the computation of the rigid modes. It substitutes the unrestrained DOFs using an element with large mass and inertia moment to avoid large movements of the structure during external disturbances but capable of sensing little accelerations which will change the asset and flight attitudes of the entire configuration if totally released by the constraining supports. Those little movements and accelerations are converted into forces used to provide the lateral/directional stability and controllability derivatives of the subject model.

In the specific case of the GRAF analysis, the SUPORT element was linked to the CG of the aircraft model with unrestrained DOFs in the 2-, 4-, and 6-direction. That translates into restraining the translational freedom along the y-axis and the rotational one along the x- and z-axes of the aerodynamic reference system. The numbers correspond to the convention used to name the DOFs in the FEA: the x-, y- and z-translations are identified by the T1, T2 and T3 entries, and listed in the SPC, MPC and SUPORT elements as 1, 2 and 3; while the respective rotational freedoms, termed as R1, R2 and R3, are listed as 4, 5 and 6. So the GRAF model, through the SUPORT element, is partially free to sense any y-plane translation (side force effect), also the rotations in rolling and yaw along the aircraft’s longitudinal and vertical axes (rolling and yaw effect).

In order to finally run the analysis, the TRIM entry also has to be included in the NASTRAN file. This command lists the initial conditions of the model related to its DOF and SUPORT entry. For the study of the GRAF stability and controllability derivatives, the TRIM entry contains the values of the initial sideslip angle, any initial lateral, translational or either rolling or yawing acceleration, the dynamic pressure and the Mach number. The MSC/NASTRAN processor finally estimates the aircraft stability derivatives by considering small perturbations with respect to the user specified trim condition.

Due to the low subsonic flight speeds of the Eclipse, all the aeroelastic analyses have been carried out under the assumption of incompressible flow, so the Mach number influence is neglected. After this type of entry command, the geometry and mesh of the model are listed. The TRIM entry is substituted by the FLUTTER, GUST, TABLED1 and FREQ1 entries for the other types of aeroelastic analysis. The FLUTTER entry specifies the method to be used for the flutter analysis. The p-k method is chosen for the GRAF model. It is also associated with two other entries the MKAERO1 and the FLFACT. They have been included to input respectively the reduced frequency and the flight speeds at which the analysis had to be performed. The GUST entry, instead, has been used to define the typology of the discrete gust taken into account in the gust response study. The *1-cos* gust typology, the vehicle velocity and the gust angle of attack (i.e the ratio of the lateral gust velocity to the aircraft velocity) are included in the same command. The *1-cos* gust is defined by the DLOAD1 entry which for the particular case lists all the points of the gust curve expressed through the recommendations of the CS-23 regulations. The last two commands FREQ1 and TABLED2 are used to run the modal dynamic frequency and transient analysis. The first one defines the range of frequencies of interest to be used for the in-frequency domain case. A TABLED1 entry is used in this case to specify the amplitude and frequency of the external input related to rapidly applied forces varying within the input frequency spectrum. The TABLED2 entry, instead, is used for the transient response analysis, and defines the time dependent load in amplitude and duration period. All these dynamic cases are presented in detail in the section on the dynamic analysis results of Chapter 6.

Chapter 4 - The GRAF MTF4 fin: graphical illustration and components details

4.1 Chapter Introduction

This section is entirely dedicated to presenting the details of the GRAF model, specifically named MTF4 after the author's initials, where the 'F' stands for 'fin' and the number simply identifies this novel concept as the fourth design project developed by the author during his education and career in aviation. This part of the thesis introduces the technical features of the MTF4 under the two main perspectives of the structural assembly and its operating flight modes for stability and control tasks. The following paragraphs will present the characteristics of the vehicle chosen as the reference baseline for the case study, and the way all the technical features are integrated into the novel fin. In particular, the technical descriptions of the MTF4 fin will outline how all the technical novelties introduced within this thesis are eventually combined into the final GRAF assembly.

4.2 The Eclipse UAV as a Case Study

The Eclipse UAV is a flying demonstrator designed and built by part time students at the Department of Aerospace Engineering of Cranfield University. It was, later, included within the Flapless Air Vehicle Integrated Industrial Research (FLAVIIR) programme. This was a research programme funded jointly by BAE SYSTEMS and EPSRC, managed by Cranfield University and included nine other university partners [68]. The Eclipse was the first of two prototypes built as technology demonstrators, and later succeeded by the 15% larger scale version of the Demon. At the time of the doctoral research, the Eclipse vehicle was chosen as the baseline case

study because it was a platform already built, and ready and waiting to be flight tested. The interest in the FLAVIIR research programme and the aim of the GRAF project were matching each others' interests and technologies which might be jointly developed in the near future. The illustration of Figure 4-1 shows the side and top views of the Eclipse vehicle. As can be seen from those figures, its diamond wing shape and the absence of a horizontal tailplane are the main distinguishing characteristics of the aircraft. The vehicle is provided with conventional control surfaces acting as ailerons and elevators. Those surfaces are expected to be substituted, in the second phase of the project, with more technological trailing edge devices for controlling the aircraft attitude by flapless systems.

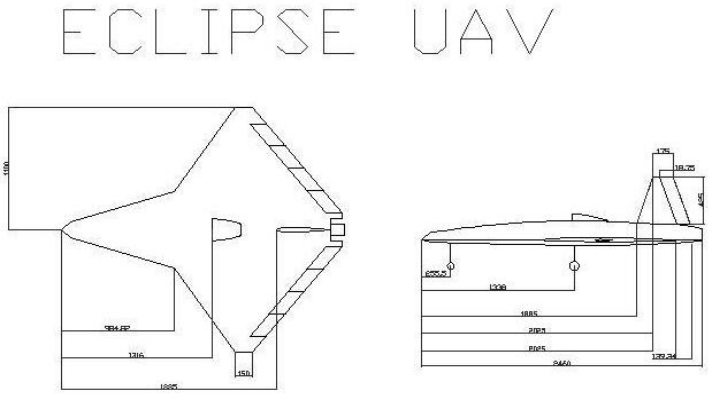

Figure 4-1 Top and side CAD views of the Eclipse UAV model.

The aircraft is built with a mono-coque shell of carbon fibres. Only the engine intake, the nose cone and the vertical empennage are components separated from the main fuselage structure. The vertical fin has a trapezoidal geometry with swept back leading edge and swept forward trailing edge. It is mounted onto the aircraft's back by two steel spikes coming out from the fin root chord. They are inserted into two circular slots on the fuselage. The whole fin-fuselage assembly is then held rigidly together by using four stainless screws which connect the root fin skin to the fuselage panels.

Table 4 - Eclipse specifications [77, 97]

Eclipse UAV specifications:

Wingspan (m)	Mean Aerodynamic Chord (m)	Wing Area (m^2)	Wing AR	MTOW (kg)	Fuselage length (m)	Stall speed (m/s)	Take off speed (m/s)	Cruise speed (m/s)	Dive speed (m/s)
2.2	1.34	2.36	2,047	45	2.5	25.6	41.8	40.8	60

As shown in Table 4, the total length of the aircraft is 2.5m with a maximum take-off weight of 45kg. The weight of the vertical tail is 0.67kg, which includes the rudder actuator. The current Eclipse version of the fin is made of a blue foam core embedded into a carbon fibre shell. The fin also has a hinged rudder running across the entire span of the tail. The rudder has a chord of 0.118m. Its dimension is constant, but due to the tapered geometry of the fin, its rudder chord-to-fin mean chord ratio varies with the span. Its percentage, with respect to the tapered chords of the fin, varies from 0.25c at the root section to 0.75c at the tip chord. The fittings for the attachment of the four hinges are equally spaced through the span and visible through the gap separating the fin from the rudder.

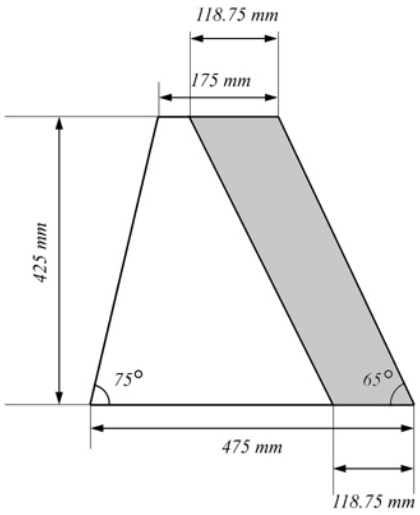

Figure 4-2 Eclipse UAV trapezoidal fin [179, 180].

Table 5 presents the geometric and reference features of the Eclipse fin, Figure 4-2. The fin shape is tapered in span and thickness but keeps the same aerodynamic profile for all the sections; this is the RAE 101, with a maximum airfoil thickness of 10%.

Table 5 - Eclipse fin details [77, 97]

Fin details:

Finspan (m)	Mean Aerodynamic Chord (m)	Root chord (m)	Tip chord (m)	Fin Area (m^2)	AR	Weight (kg)
0.425	0.375	0.475	0.175	0.154	1.32	0.670

The aspect ratio, fin area, finspan and the mean geometric chord are identical in both original and novel aeroelastic designs. The only difference between the GRAF version and the fin-rudder model is in the planform geometry. The novel variant has changed it into a rectangular shape with a constant chord of 0.325m.

4.3 Materials properties and actuation system

As already introduced in this thesis, the structural design of the GRAF is entirely made of composite lightframes. In particular, the primary and secondary shafts, six ribs and the stringers of the LSS device are made of carbon fibres. In order to match the same strength and weight properties of the conventional Eclipse fin, the same type of carbon fibre utilised on the hinged rudder tail has been used for the aeroelastic design; this is the carbon fibre prepreg ACG MTM-46, whose mechanical properties are presented in Table 6.

Table 6 - Carbon fibre properties

Material Details:	MTM46/HTS(12K)-145-35%RW Unidirectional HTS-5631 carbon prepreg				
Cure Details:	1 hour at 121°C, 6 bar autoclave pressure No postcure Zero bleed process achieving 57% Fibre Volume All results (except shear) normalised to 60% Fibre volume				
			Test Conditions for Data		
Property	Test Method	Units	20°C Dry		
Tensile Modulus	D 3039	GPa	128.3		
Compressive Modulus	D 3410	GPa	118.8		
Trans. Tensile Modulus	D 3039	GPa	9.0		
Trans. Comp. Modulus	D 3410	GPa	10.3		
Tensile Strength	D 3039	MPa	2278		
Compressive Strength	D 3410	MPa	1352		
Trans. Tensile Strength	D 3039	MPa	33.9		
Trans. Comp. Strength	D 3410	MPa	210		
Tensile Strain to Failure	D 3039	%	1.79		
Comp. Strain to Failure	D 3410	%	1.12		
Trans. Tensile Strain	D 3039	%	0.40		
Trans. Comp. Strain	D 3410	%	2.12		
In-Plane Shear Modulus	D 3518	GPa	3.95		
In-Plane Shear Strength	D 3518	MPa	98.1		
Maj. Tensile Poisson's Ratio	D 3039	-	0.32		
Maj. Comp. Poisson's Ratio	D 3410	-	0.33		
Min. Tensile Poisson's Ratio	D 3039	-	0.02		
Min. Comp Poisson's Ratio	D 3410	-	0.02		
Flexural Modulus	CRAG 200	GPa	114.2		
Flexural Strength	CRAG 200	MPa	2262		
ILSS	D 2344	MPa	99.9		

Table 7 shows the material properties of the glass fibre chosen for the skin and leading edge modelling and manufacturing.

Table 7 – Eglass fibre properties

Material: E-Glass Unidirectional Property	Units	
Tensile Modulus	GPa	42
Transverse Modulus	GPa	15
Shear Modulus	GPa	4
Poisson's Ratio	-	0.3
Tensile Strength	MPa	1310
Compressive Strength	MPa	750
Shear Strength	MPa	67
Trans. Tensile Strength	MPa	73
Trans. Compressive Strength	MPa	165
Tensile Strain to Failure	%	0.031
Compressive Strain to Failure	%	0.018
Trans. Tensile Strain	%	0.005
Trans. Compressive Strain	%	0.011

The leading edge of the GRAF will embed the flexible airfoil section nose made of lattice material. A strip of lattice will also constitute the sealing edge surrounding the slot connection profile. The elastomeric material forming the edge of the fuselage-fin slot works as a sealing flexible cushion between the fin root and the fuselage attachment. The whole fin, once inside the slot-connection, is firmly clamped at the bottom end of the primary shaft by a roller bearing mounted on the fuselage. In order to activate the warping and cambering mechanism, two servo-actuators Hitec HS-7980TH and HS-7950TH [93] are used to generate the necessary torque on the primary and secondary shafts respectively. From Eq. (3.56) in Section 3.5.3 the preliminary torque requirement for the 0.25c TE camber actuation has been determined by assuming the elastic reaction of the three layers panel subjected to an overall displacement of 0.027m at the tip of the panel which corresponds to 21° of TE deflection, as $M_e = w'' D$. By assuming a linear deformation of the panel at this stage, in order to simplify the integration, it gives:

$$M_e = \frac{2 w_{\max}}{(a)^2} D \qquad \rightarrow \qquad M_e = 0.43 Nm \tag{4.1}$$

By adding the external contribution from the aerodynamic pressure acting upon the TE panels, the resultant forces are $P_{lower} = 29.1N$ and $P_{upper} = 34.7N$, both applied at $1/3$ of the TE chord (i.e. 0.026m) on their respective panels. They give a total bending moment of $0.75Nm$ and $0.9Nm$ respectively. Therefore, the actuator, via

the secondary shaft transmission, must be able to provide the pushrods forces which, once applied on the LSS elements, must guarantee the following minimum values of bending moment:

$$\begin{aligned}\left(0.43Nm + 0.9Nm\right)_{upper} &= 1.33Nm \\ \left(0.43Nm + 0.75Nm\right)_{lower} &= 1.18Nm\end{aligned} \tag{4.2}$$

By considering an inclination of 10° between the x-crossing pushrods and the LSS stringers, the total actuator/pushrod bending moment computed in Eq. (3.56) must be equal to:

$$F_H \cdot h + F_V \cdot 1/3TEc = F\cos 10° \cdot h + F\sin 10° \cdot 1/3TEc = \begin{cases}1.33Nm \\ 1.18Nm\end{cases} \tag{4.3}$$

from Eq. (4.3) is calculated the force needed to be applied on the pushrods acting on the lower and upper panel. The established forces are $F_{upper} = 147N$ and $F_{lower} = 131N$. Obviously the bigger value is taken into account as the minimum requirement for the actuator sizing. Regarding the primary shaft, the actuator sizing has not been analytically determined because of the considerable number of degrees of freedom of the fin assembly. Hence, the servo actuator with the maximum torque available in the same class of actuators as the one on the original Eclipse rudder mechanism has been adopted. The actuator torque is then implemented and tested in the FEM simulations to verify the servo twisting capacity under external loading actions.

Table 8 - Actuators specifications

Hitec HS-7980TH	
Specifications	
Motor Type:	Coreless
Bearing Type:	Dual Ball Bearing
Speed (6.0V/7.4V):	0.20 / 0.17
Torque kg./cm. (6.0V/7.4V):	38.0 / 46.0
Size in Millimeters:	43.69 x 22.35 x 39.88
Weight g.:	76.54

HS-7950TH	
Specifications	
Motor Type:	Coreless
Bearing Type:	Dual Ball Bearing
Speed (6.0V/7.4V):	0.15 / 0.13
Torque kg./cm. (6.0V/7.4V):	29.0 / 35.0
Size in Millimeters:	39.88 x 20.07 x 38.10
Weight g.:	68.04

As shown in Table 8 the former has 380Ncm torque at 6V, while the latter has 290Ncm at the same voltage with a weight of 0.0765kg and 0.068kg respectively.

The conventional Eclipse fin, conversely, mounts a Futaba servo S92004 which provides a maximum torque of 95Ncm and an overall weight of 0.064kg.

4.4 The MTF4 empennage assembly and components

As already described, the GRAF design is based on a unified fin structure with the main feature of having a fixed root section and being devoid of conventional hinged control surfaces. The warping-morphing capability of the GRAF is achieved via a smart internal arrangement of rotating ribs, circular central shaft and flexible composite skin. The use of smart materials for either the structure or the actuation system has not been taken into consideration because of the likely weight penalty encountered with those systems once integrated into a similar design. As acknowledged from past projects and studies, those materials require a considerable amount of power supply, thus increasing the aircraft weight. Nonetheless, some of them, such as the magneto rheological fluids (MRF), also have a very high specific density. However, despite these technical inconveniences, their potential application on one GRAF configuration was considered, but was soon discarded during the conceptual design process. The smart concept was based on creating a one-piece composite cladding skin with an internally embedded ramification of thin hollow tubes filled with MRF. The complex systems of capillary veins systematically organised under the external fin skin can vary the stiffness and flexibility of the whole shell structure by simply varying the magnetic field around the fluid. When the field surrounding the MRF changes by turning it on, the liquid becomes solid and stiff in the assembly. Conversely, when the field is not activated, the MRF flows as a fluid, thus lowering the capillary stiffness and making the structure more flexible and prompt for morphing actions. The complexity of the MRF veins and the heavy density eventually discarded any further developments for the scope of this project.
The figure below shows the final version of the GRAF modelled for the design analysis, the MTF4. Figure 4-3 illustrates the external shape and the skeleton structure of the novel fin, whose detailed geometric features are listed in Table 9.

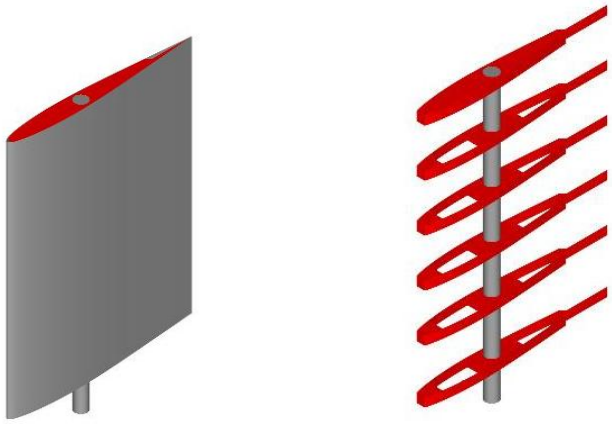

Figure 4-3 CAD illustration of covered and naked view of the GRAF assembly.

Table 9 – GRAF MTF4 geometry

GRAF MTF4 details:

Finspan (m)	Root chord (m)	Tip chord (m)	Fin Area (m²)	AR
0.425	0.325	0.325	0.138	1.32

The rectangular planform shape has been chosen to facilitate the integration and testing of the warping mechanism and aeroelastic layout into a novel and simple design. A diverse shape, perhaps optimised from an aerodynamic perspective with profiles tapered in thickness and chords, would certainly have increased the complexity of the entire design at this stage of the research. Therefore the conceptual phase of the study considered the simplest modelling and manufacturing tailplane shape for the novel aeroelastic empennage.

The GRAF assembly has 21 primary components which constitute the main body of the fin structure:

- x1 main shaft for warping actuation and support;
- x1 secondary shaft for the LSS device actuation;
- x6 rotating ribs;
- x1 glass fibre shell – main body skins;
- x4 LSS stringers;
- x1 lattice LE;

- x5 roller bearings;
- x1 swivel TE closure;
- ancillaries.

The last category of the fin components includes mainly non-structural elements such as push-rods, piano wires, linkages, clips and screws necessary to guarantee the firm assembly of the whole aeroelastic tail. The red elements in Figure 4-4 are the fin ribs connected via the roller bearing (in yellow) to the main shaft (in grey), while the blue shaft is the one needed for the trailing edge camber control where the stringers of the LSS device are attached (in blue).

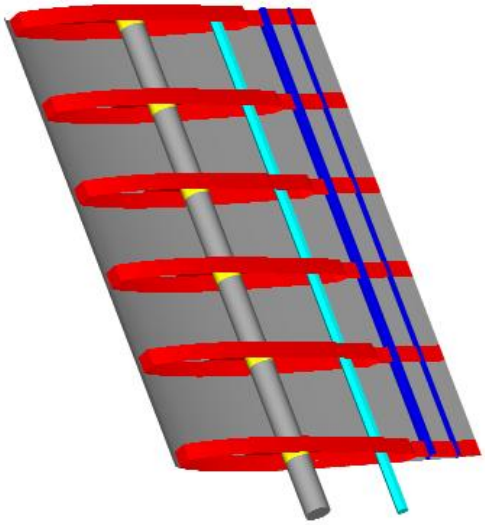

Figure 4-4 Global CAD illustration of ribs, shafts, LSS stringers and skin of the MTF4 model.

4.4.1 The primary shaft and the master rib elements

The main shaft represents the pivoting point for the ribs and the whole fin structure. It is designed to be the main carrying load beam to withstand the entire set of loads acting upon the tail. The shaft's symmetrical round shape guarantees equal stiffness in all radial directions and is designed to minimise the bending deflection in order to avoid coupling with the twist deformation. The coupled distortion might affect the

side force generation and consequently the yaw effect, and might induce more severe deformations and load scenarios which could lead to structural failure or flutter excitation of the entire empennage. Nonetheless, a bent shaft will force the clamp-bearing mount at its bottom end to obstruct any further rotation of the fin.

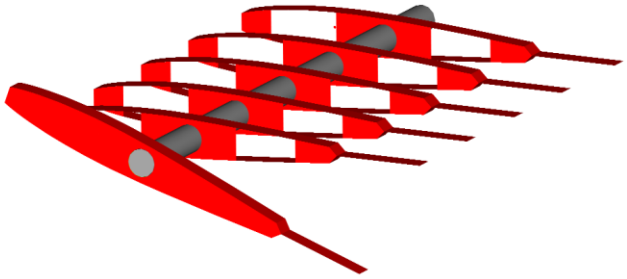

Figure 4-5 CAD ribs and shaft view during actuation of master-rib.

Figure 4-5 shows the main shaft solely fixed to the second most important component of the design, the master-rib (the one rotated). The master-rib, rigidly connected to the main shaft, drives all the mechanical deformation of the warping GRAF. The shaft is then fixed at the fuselage mount via a bearing which restrains all DOFs but the rotation along the shaft vertical axis, see Figure 4-6.

The task of the top rib is to transfer the actuation torque from the servo mechanism to the whole fin every time the shaft is activated in rotation. The master rib displacement will force the side skin to deform by dragging all the other components into a twist motion.

Figure 4-6 CAD view of the twisted fin mounted in to the fuselage support.

Different warping actuation occurs when a side wind circumstance is met by the GRAF. In that case the lateral aerodynamic pressure tends to deform the fin by pressing upon its skin surface. That pressure induces all the ribs to rotate independently from the master rib. Obviously, the ribs closest to the fuselage, because of the constraint, rotate through a smaller angle than the central ones. The master rib can rotate to follow the distortion of the pressed skin and thus increase the whole twist but only if the shaft is released and free from the actuator.

4.4.2 The central and bottom ribs

All the central and bottom ribs have an identical quasi-isotropic carbon fibre design. The ribs have two cut-outs forward and aft of the 0.4c shaft location. The ribs section has a chordwise dimension equal to 75% of the mean chord, reducing the remaining portion to a 25% central web, called the '*tail*', which is used to keep separate the push-rods on the two sides of the TE. Figure 4-7 shows a detail of the rib design.

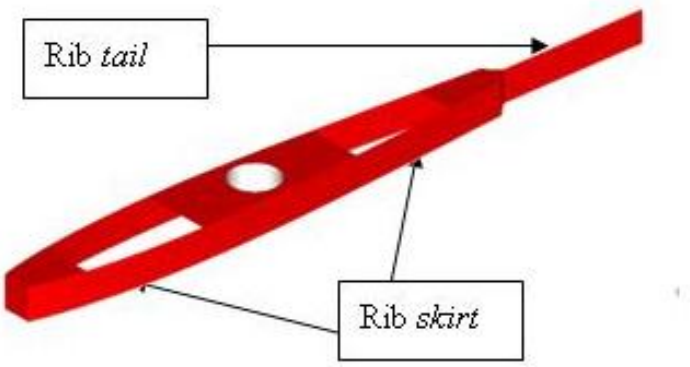

Figure 4-7 CAD illustration of the rib design.

Each rib is surrounded by a 1.5cm height edge, termed the rib "skirt". It works as a structural reinforcement for the potential out-of-plane distortions, but at the same time also acts as a support for the covering skin. The external skin will lean on the rib's skirt. The elasticity of the edge of those flanged ribs is, in practice, exploited as

an elastic band working as a spring to help the fin recover the straight shape once the twisting and cambering effect have ceased. Figure 4-8 shows how the skin is connected to the central and bottom ribs.

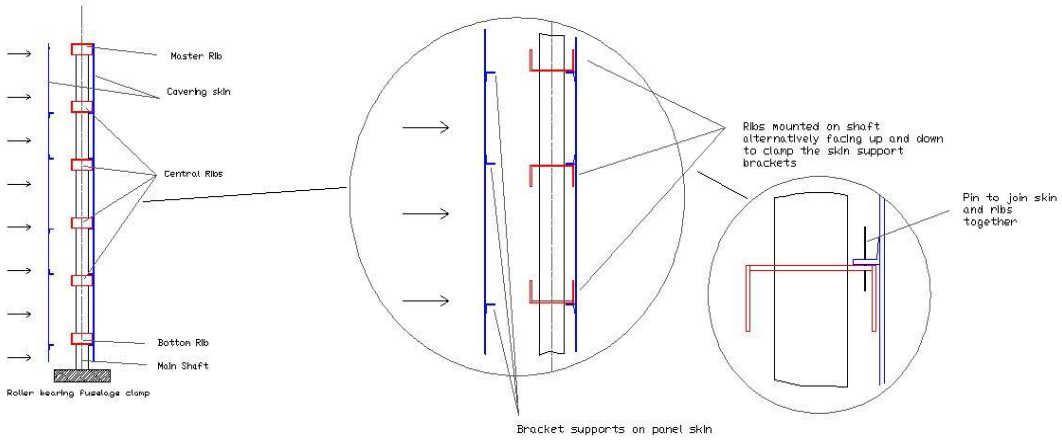

Figure 4-8 CAD exemplification of panel skin and ribs assembly.

The ribs can be mounted all in the same position or as shown in Figure 4-8, alternately rotated and mounted upside down in order to have, by pair, the top faces of two adjacent ribs surfaces looking at each other to work as support and clamp for the mounting brackets bonded on the fin skin. This assembling technique can be used if the slot-connection is allowing too much freedom in vertical translation. This system prevents the skin from sliding vertically, even though very minimal displacements are allowed to work in conjunction with the warping task of the base slot connection.

The two cut-outs, on the one side, help to make the ribs section lighter; on the other side, besides the elastic function, they allow the secondary shaft for the TE actuation to pass through the ribs.

The leading edge of the fin is made with a soft lattice core covered by a stiffer glass fibre skin, the same as for the whole fin. The soft material enables it to be more compliant with twist deformation while the thin composite skin is applied, to avoid buffeting and fluttering of the flexible edge and above all to guarantee stiffness against foreign object damage (FOD) impact. An entirely composite glass fibre leading edge without a soft core would have needed more layers of composites,

considerably increasing the ribs cross-sectional stiffness and the torque necessary to twist the tail.

4.4.3 The skin

The cladding skin of the GRAF, made of three layers of glass fibres, is internally provided with L-shaped brackets to harness the skin panels to the supporting ribs. These brackets lean on each rib and are held together by means of pins (diameter of 1-2mm) slid into the holes, drilled in both parts, and working like pivots. The covering skin also encompasses the rear part of the profile – the stringers of the LSS device used to activate the morphable trailing edge section and the swivel edge closure. The skin is also firmly anchored to the master rib by screws, whereas, at the other end of the covering, panels are not constrained by any support.

4.5 Integration of the technical novelties on the MTF4 design

This section of Chapter 4 presents more about the perspective of the assembly of the five major novelties introduced within the MTF4 design. They are presented in the following order: first is the L-shape Stringer device (LSS), then the “swivel edge” device closure, followed by the original device used to connect the fin structure to the fuselage, the slot-connection, whilst the fourth novelty is the shaft and the rotating ribs of the compliant structural layout of the assembly. The fifth novelty is the technique used to warp the fin structure, exploiting the aeroelastic effect deformations.

4.5.1 The LSS and swivel edge devices integration

The L-Shape Stringers (LSS) concept idea was specifically designed by the author for the cambering task of the GRAF TE section. However, the LSS design might resemble a similar, but lower performing concept model, proposed by Campanile *et al.* in the morphing structure presented in reference [38]. The LSS device is a mechanism designed to convert linear forces from actuators into applied bending moments. It has been originally applied on closed TE sections of the GRAF design, but as is visible from the final deformations attainable with a fully sealed configuration, and shown in Figure 4-9 and 4-10, it was impossible to obtain the desired cambered shape.

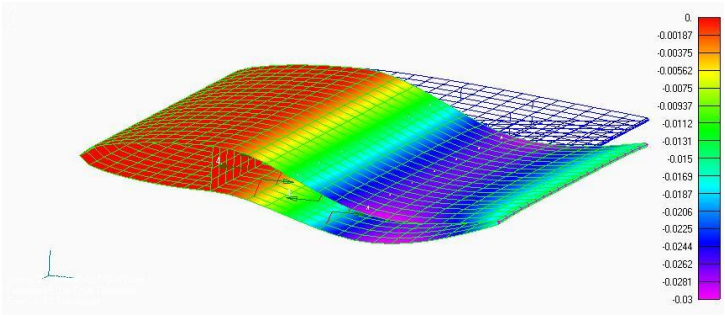

Figure 4-9 Camber deformation with rigidly closed TE.

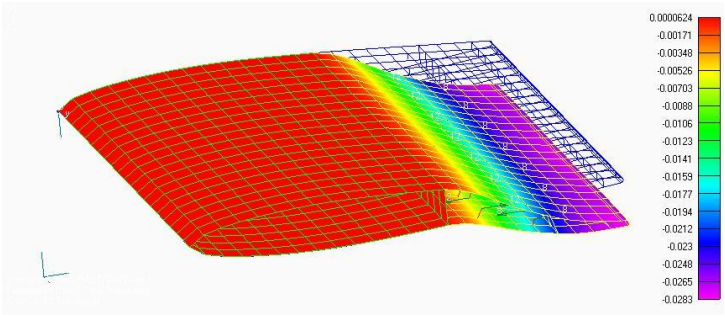

Figure 4-10 Camber deformation with elastomeric material TE.

These figures anticipate the FEA results of the next section but they represent three different variants of the TE section. The first model is the fully sealed and rigid TE section. The applied forces on the LSS generate an unexpected double-curved TE.

The second model is identical to the first one with the only difference being the closure edge of the TE is made of elastic rubber. Despite the smoothness of the deformed profile, the double-curvature still effects the final shape. The third variant

keeps the flexible edge closure of the second model and in addition has vertical spar webs running across the span of the TE which are made of elastic material and join the two sides of the TE skin. The flexible webs help orient the deflection with the same curvature but as soon as tension and compression are produced, because of the large deflections, the TE double-curves, generating the necessity to introduce a smart connection to create more freedom on the edges of the TE panels while keeping them united. The assembled and exploded views of the CAD models shown in the figures below present the swivel edge closure concept used to release tension on the TE skin and achieve the expected deformations.

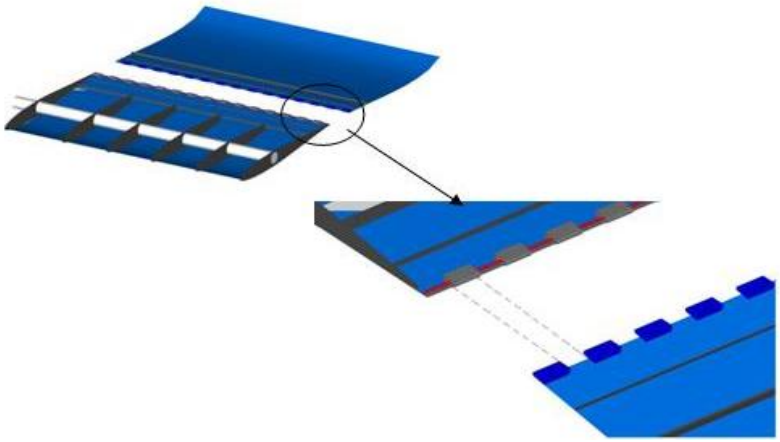

Figure 4-11 CAD swivel closure device view on the two sections of the TE.

The CAD illustrations of Figure 4-11 show the exploded view of the fin assembly with disassembled trailing edge connection. The detail of the figure shows how the swivel edge parts on the two sides of the skin will be joined together to form a unique solid edge. The dashed lines indicate the position of the grey edge component in between the reciprocal ones in blue on the other edge of the skin.

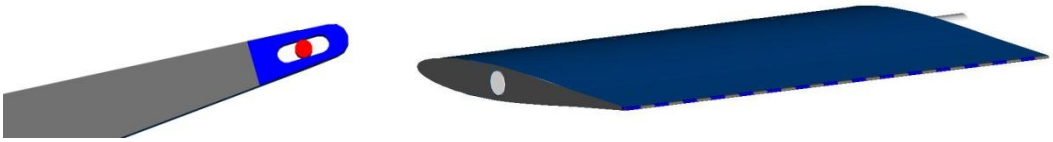

Figure 4-12 Assembled swivel device: CAD TE top and rear views.

Figure 4-12 shows the joint edge from a side and rear view of the assembly. The red element inside the blue area is the internal rod used to keep both panels united and allow relative motion of the parts for the cambering effect.

4.5.2 The slot-connection assembly

The novel slot-connection system has been intuitively designed to join the vertical empennage to the aircraft fuselage without restraining any of its compliant components, and in particular its flexible covering skin.

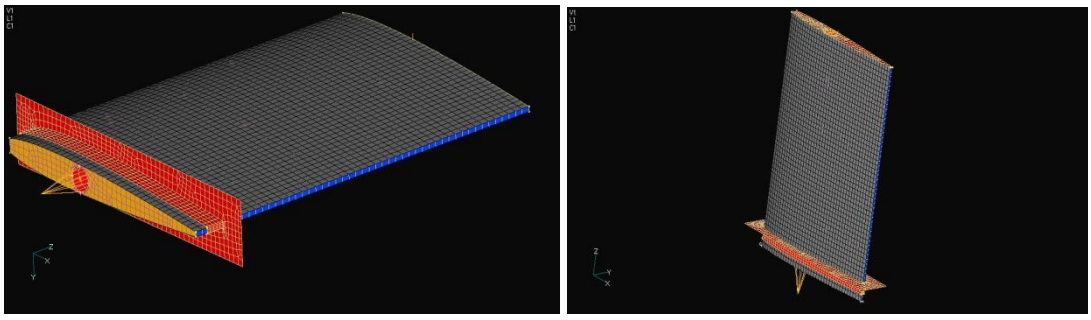

Figure 4-13 CAD views of the fin-fuselage slot-connection assembly.

Figure 4-13 shows two different views of the MTF4 tail joined to the fuselage section of the slot connection [drawn with red elements],. The edges of the slot also work as lateral support for the fin, which leans on the flexible sealing positioned between the fin skin and the rigid edge of the fuselage frame. Structurally, the slot edge reacts to the shear forces generated by the aerodynamic loads on the fin as well as to those forces due to the warping deformations. However, no structural analysis has been carried out on the fuselage section of the slot edge because it is assumed it has already been assessed in the original Eclipse design. In practice the slot-connection restrains the external panels of the skin to horizontally translate in the x- and y-axes directions. However, the compliant joint does not exclude the skin panels from sliding vertically. The lattice strip is used to create a sealed joint with the fin assembly, working also as a damper for vibration and loads due to the fin's external

disturbances and its twist activation. The next chapter, Chapter 5, will prove the dynamic effect of the slot-connection-skin capability with the FEA results of the whole GRAF performance. As explained in the Methodology Chapter, the reason for this augmented freedom comes from the absence of constraints at the fin root, thus cancelling out the shear and axial stresses that will reduce the morphing capacity of the structure if conventionally attached.

4.6 How the MTF4 empennage performs stability and control tasks

This is the last paragraph of the section dedicated to the technical novelties introduced with the MTF4 design. It briefly discusses the stability and controllability operating modes such an unconventional adaptive structure can perform, by applying mechanical actuation and aeroelastic effect exploitation. The description of the applied techniques can be split into two typologies related to the specific roles of the fin:

- Mode 1: stability;
- Mode 2: control authority.

The two tables below list the circumstances in which vertical fins are requested to guarantee safe conditions of lateral/directional stability and control performances. For the purpose of the study, only the directional task will be taken in consideration.

Mode 1 – Stability	Mode 2 – Controllability
• Cross wind and sideslip circumstances • Lateral gust • Damping effect in rolling motion	• Flight manoeuvres: ➢ Heading correction ➢ T/O and Landing ➢ Cross wind ➢ Rapid disengagement • Rolling motion • Trimming for further stability effect

Both operating working modes share the consequent deformations induced by the aeroelastic effect phenomenon. The differences in the way it engages the warping of the empennage are presented in detail in the next Sections.

4.6.1 Mode 1: stability

Mode 1: this operating mode is naturally performed by the fin shape generating the yawing moment needed to stabilise the aircraft nose when in the presence of lateral external disturbances such as lateral wind conditions, gusty cross-winds, and even rolling manoeuvres. Normally, in most of those cases, the upset condition is resolved by simply entrusting the fin generated ‘weathercock effect’, which is the primary purpose vertical empennages are designed for. Only in the case of extreme windy scenarios, in order to enhance the natural fin stability effect, does the control mode intervene by further twisting and cambering the empennage for trimming purposes.

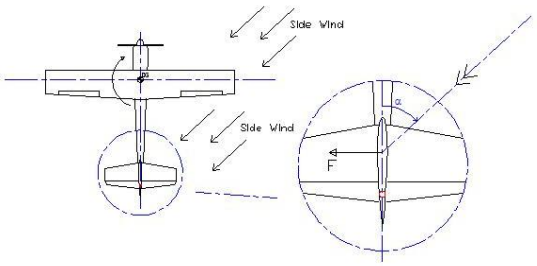

Figure 4-14 Side wind circumstance on conventional vertical fin.

However, even during the autonomous self-adaptive role, the GRAF results appear to be more effective than with the original rigid tail. The MTF4 can, under the pressure of the external wind, beneficially twist its shape, thus increasing the tail effectiveness in side force and yaw generation for a more precise and immediate response. The bigger the angle of attack, obviously within the stall limitations, the more effective is the fin performance, thus further enhancing the aircraft handling qualities.

4.6.2 Mode 2: controllability

Mode 2: this is the function mode normally operated by the pilot or the flight control system when a decisive and rapid yaw manoeuvre must be engaged by the aircraft. Control authority effectiveness is essential for a rapid change of direction or to contrast strong side wind disturbances both in flight and in near-the-ground operations. In order to produce the correct amount of control force, the MTF4 design activates both twist and camber deflection of the GRAF systems. The twist is activated by the shaft actuator and as soon as the deformation initiates and side force develops, it is assisted by the aeroelastic effect influence in the warping deformation. Meanwhile if the side force generated only via twist is not sufficient to guarantee the heading control of the vehicle, then the camber is activated too. Although twist and camber devices are designed as two independent mechanisms they can in practice work together if requested. Because of the rapidity, directional control is normally requested; this operating mode of the fin is more demanded and entrusted to the

mechanical actuation than to the slower effect generated by the external dynamic pressure. However, external forces are exploited to reduce the actuator power consumption during twist.

The figure below shows the procedure applied to activate and combine the control authority devices on board the MTF4. The shaft rotates the master ribs, dragging the fin skin into a twisted shape, identified in Figure 4-15. The initiating side force generation contributes to keep twisting the empennage, while, if needed, the trailing edge camber starts morphing for enhancing the yaw effect of the tail. The servo mechanisms are used to hold the elements in position and to bring back to the neutral 0° angle the whole configuration, once the command input has ceased its effect.

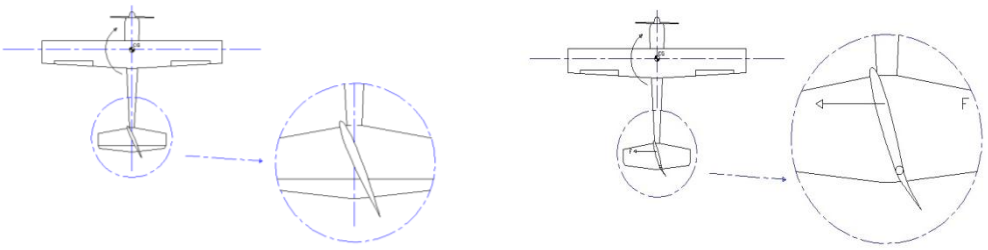

Figure 4-15 Twist and camber activation on the aeroelastic fin.

Mode 1 relies upon the combination of flexibility of the fin due to the compliant structure design and the deformation induced by the aeroelastic effect.

Mode 2, instead, although still takes into account the contribution of the external aerodynamics, entrusts more the mechanical application of the systems utilised to rapidly activate the GRAF seamless deformations.

Chapter 5 - Aerodynamic and Structural Results

5.1 Data collection, numerical analysis and results

The fifth chapter is the first of two sections dedicated to presenting and discussing five different groups of results from the GRAF model analysis. The subdivision is based on the following groups:

1. aerodynamic investigation;
2. static linear structural analysis;
3. flight dynamic performance;
4. aeroelastic instability phenomena;
5. aeroelastic response.

In particular, this chapter will focus on the first three types of results. The others will be presented in Chapter 6. This section opens the data presentation by first discussing the results derived from the aerodynamic investigation and loading actions analysis. The initial part of the aerodynamic section explains, with the help of diagrams and data tables, the reasons for selecting the 'smooth' cambered airfoil section variant for the final MTF4 design rather than the other possible options. All of them are presented and compared in the text. The second part of the aerodynamic results introduces the performance data attained with such an unconventional configuration. The side force generation for control authority purposes is, in this section, compared to the outputs coming from the conventionally hinged Eclipse rudder. An evaluation of whether a warping-cambering fin can match a fin-rudder layout is presented at the end of the second paragraph. After the aerodynamic analysis results, the other sections will then present the results obtained from the structural analysis of the GRAF assembly and its components. The chapter concludes with the collection of

data obtained using the MSC/NASTRAN Flight Loads tool package for the evaluation of the flight mechanic performance of the MTF4 tail integrated aboard the Eclipse vehicle model.

Before starting with the presentation of the results, some of the assumptions made on the following analyses are listed at this point. These assumptions include hypotheses, boundary conditions and constraints which have characterised the study of the GRAF model. They are:

- the baseline reference specification refers to the Eclipse vehicle as discussed in references [30, 77, 97];
- the maximum dynamic stall angle, as recommended by Howe in reference [96] is equal to 1.5 times the static stall angle of a normal airfoil section;
- the aircraft is thought to start and end any type of lateral/directional manoeuvre from and to a steady condition;
- no interaction with any rolling motion of the aircraft is taken in consideration for the directional study of the whole vehicle, either for control or stability;
- the drag force estimation has been carried out adopting the semi-empirical model implemented in the JAVAFOIL program;
- all the structural analysis has been carried out for linear static cases;
- the twist deformation is supposed to follow a linear distortion from root to tip, where the maximum twist angle is achieved;
- the detailed kinematics of the secondary shaft-pushrods-LSS assembly has not been modelled inside the FE model of the GRAF design.

Other assumptions, already presented in Chapter 3, are also taken in consideration during the model analysis.

5.2 Aerodynamics & loading actions results

As already described in the introduction of this chapter, this aerodynamic section is mainly divided into two parts. At first, all the collected data and results are presented to demonstrate the choice of the selected ‘smooth’ airfoil shape for the cambered

version of the TE section. Four profile variants are presented here. The MATLAB code ‘TE-camber’ has been used to create the coordinates database for the three morphed shapes and the baseline rigid plain rudder of the Eclipse fin. The four variants have been run in JAVAFOIL for the selection of a better profile shape. Once the cambered TE version is chosen, then the detailed aero-loading actions upon it are computed. In parallel, a performance analysis has been carried out to verify whether the GRAF model with twist and camber activation can match, in control authority, the side force effect generated by the Eclipse rudder version fin. Operational flight speeds and maximum deflections of the GRAF design will determine the worst case scenario for the loading action assessment.

The maximum twist angle of the fin tip has been limited to 10°. That value derives essentially from both structural and aerodynamic considerations. From an aerodynamic standpoint, the main intention is to try to avoid fin tip stalls due to the high angle of deflection generated by a twist and sideslip combination. Structurally speaking, instead, the reason is because larger warping angles might induce unstable deformations and very high levels of stress on the thin laminates.

The results presentation starts with a discussion of the four TE variants, termed in the MATLAB code as:

- plain;
- triangular;
- cubic;
- smooth.

The figures below will show the MATLAB outputs highlighted in the red profile, with the blue line representing the undeformed airfoil shape based on the original RAE 101. The figures illustrate both the baseline section with plain flap and the three cambered variants with a positively deflected surface of 10°. The 10° deflection angle is the one used as the reference value for the performance comparison. Each section has undergone aerodynamic analysis via the panel method and lifting line theory, conducted respectively with the two programs JAVAFOIL and ESDU 95010. Figure 5-1 illustrates the baseline plain rudder deflection.

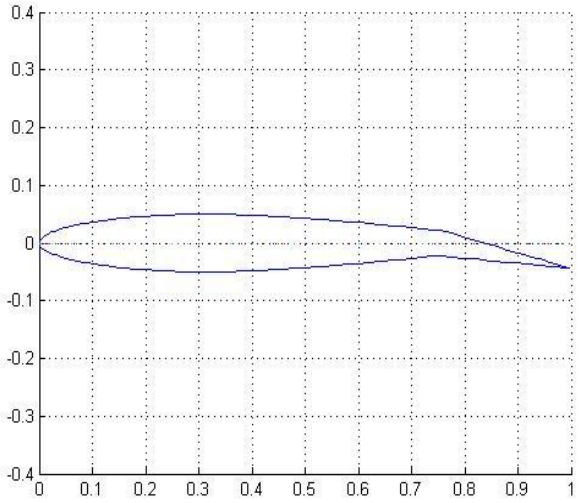

Figure 5-1 MATLAB plain flap deflection.

Figures 5-2, 5-3, and 5-4 illustrate respectively: the cambered trailing edge under a unit triangular load distributed on its 0.25c section; the TE version adopted following a cubic polynomial-based curvature deflection; and the 'smooth' morphed variant where the displacements and rotation of the section are uniformly distributed along the TE length.

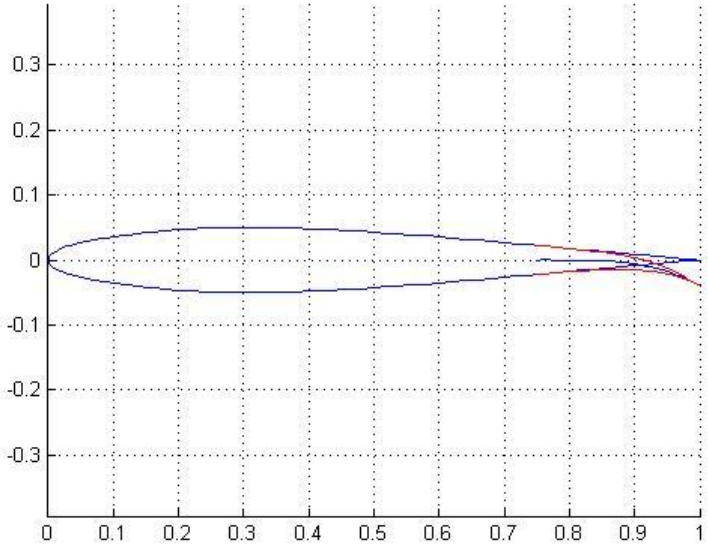

Figure 5-2 MATLAB triangular flap deflection.

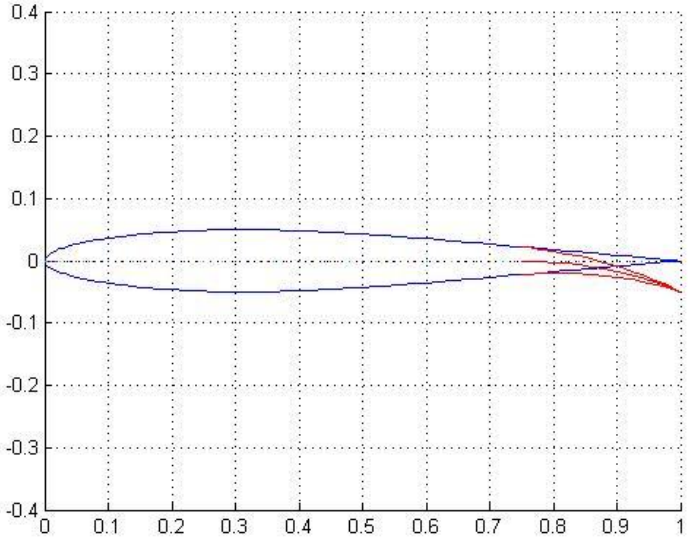

Figure 5-3 MATLAB cubic flap deflection.

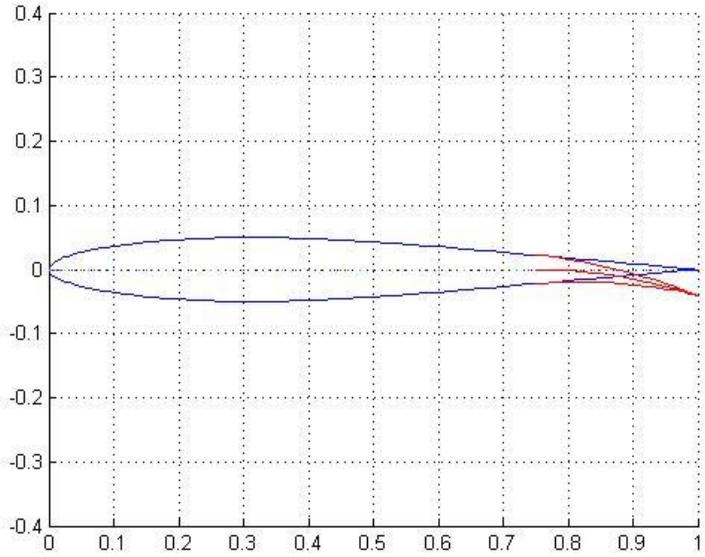

Figure 5-4 MATLAB smooth flap deflection.

The following three diagrams show the 2D JAVAFOIL results for the lift, drag and pitching moment coefficients vs. the angle of attack (AoA) of the three morphed surfaces and the plain rudder version. The comparison of the lift coefficients curves included in Figure 5-5 also includes the case of an all-moving profile configuration.

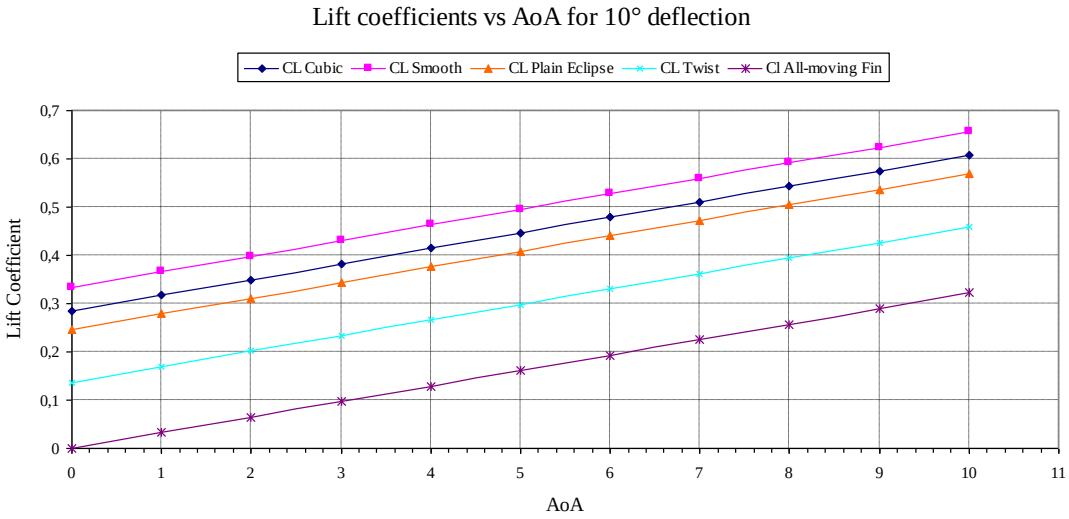

Figure 5-5 Lift coefficients curves for 10° flap deflection vs. AoA.

The aerodynamic coefficients for the three cambered sections have been compared to the simple plain deflected rudder of the Eclipse configuration in Table 10.

Table 10 – Lift coefficients vs. AoA

AoA:	0°	1°	2°	3°	4°	5°	6°	7°	8°	9°	10°
C_L Cubic	0,29	0,32	0,35	0,38	0,41	0,45	0,48	0,51	0,54	0,58	0,61
C_L Smooth	0,33	0,37	0,40	0,43	0,46	0,50	0,53	0,56	0,59	0,62	0,66
C_L Plain Eclipse	0,25	0,28	0,31	0,34	0,38	0,41	0,44	0,47	0,50	0,54	0,57
C_L Twist	0,14	0,17	0,20	0,23	0,27	0,30	0,33	0,36	0,39	0,43	0,46
C_L All-moving Fin	0,00	0,03	0,06	0,10	0,13	0,16	0,19	0,23	0,26	0,29	0,32

The values plotted with the pink curve in Figure 5-5 are the coefficients related to the *smooth* TE. The second line from the top is the conventional plain rudder. The plain surface curve gives better results than both ‘cubic’ and ‘triangular’ sections, but they are not as good as with the ‘smooth’ profile. Finally, at the bottom of the plot is the curve plotting the lift coefficients obtained from an all-moving fin configuration.

The results associated with the ‘smooth’ curve give the information to draw conclusions for the first waypoint (WP) of this navigation through the design path of the GRAF MTF4 model.

WP1: The ‘smooth’ profile shape gives better results in terms of lift coefficients for a seamless deformation of the TE.

Figure 5-6 shows the drag force coefficient results, while Figure 5-7 focuses on presenting the pitching moment coefficient results obtained from the same investigation.

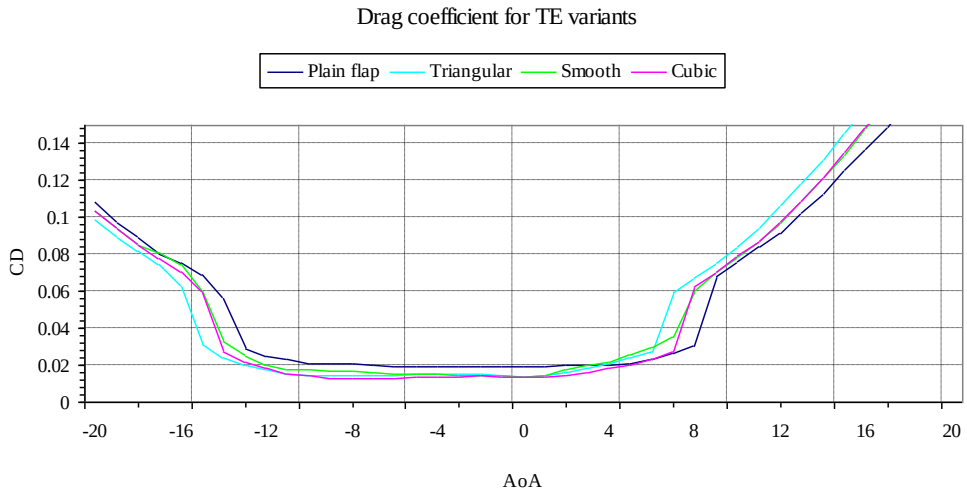

Figure 5-6 JAVAFOIL drag coefficients for the four flap variants.

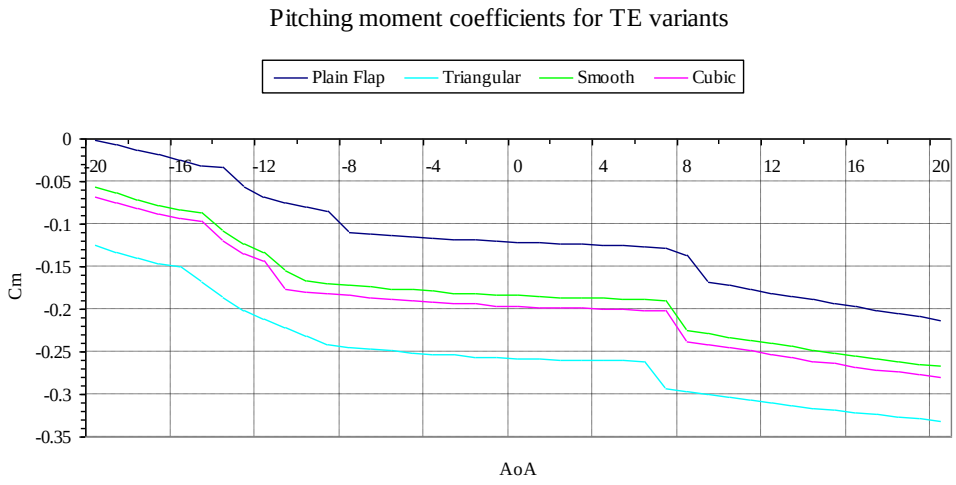

Figure 5-7 JAVAFOIL pitching moment coefficients for the four flap variants.

In terms of aerodynamic drag force, by looking at the coefficients in Figure 5-6, it can be seen that the smooth section performs better than the plain rudder. At 0° of AoA it has a drag coefficient between 15-25% lower than the plain rudder. Therefore, another important conclusion can be drawn.

WP2: There is a 15-25% drag reduction by adopting a seamless *smooth* morphing TE section rather than with a plain deflected surface.

However, the same plots show better values related to the triangular and cubic profile curves, by presenting even lower drag coefficients. Unfortunately, although they have a further drag reduction advantage, those two last variants do not have the same lifting performance as the smooth one. The pitching moment diagram shows the coefficients calculated with respect to the AC profile at 0.25c. The negative values indicate that the profile variant with the greatest tendency to pitch down the nose for a positive lift up force generation, is the triangular one. The less sensitive, instead, is the plain rudder. The smooth variant follow soon after the plain rudder configuration with a modest tendency to rotate the entire nose section down. For the aeroelastic purposes of the design, on one side a cambered profile shape with a high tendency to pitch down would result in generating the moment to help the fin structure to twist back and retrieve its neutral position. On the other side, however, it might represent an impediment to activating the twisting deflection expected with the aeroelastic effect exploitation of the fin. The rotation generated by the pitching moment counteracts the aeroelastically induced distortion.

WP3: The lack of a very effective pitching moment to retrieve the fin to its neutral position will be overcome by the actuation system used to initiate the fin twist deformation.

WP3 concludes the first part of the aerodynamic investigation. The following section will discuss the capability of the GRAF model to match the effectiveness of the conventional Eclipse fin in terms of side force generation.

The diagram in Figure 5-8 plots the result from the ESDU analysis used to measure the lifting (i.e. side force) coefficients obtained with the GRAF configuration. Two different sets of data are considered in relation to two diverse variants of the rudderless TE section. The two TE versions undertaking the analysis have sealed and unsealed gaps in between the TE chord and the fuselage body. They are named fixed root (FR) and detached root (DR) respectively. The study of these two configurations investigates how much the benefit is, in terms of performance, gained by the same gapless fin configuration but with only an unsealed slit included at the root of the morphing TE section.

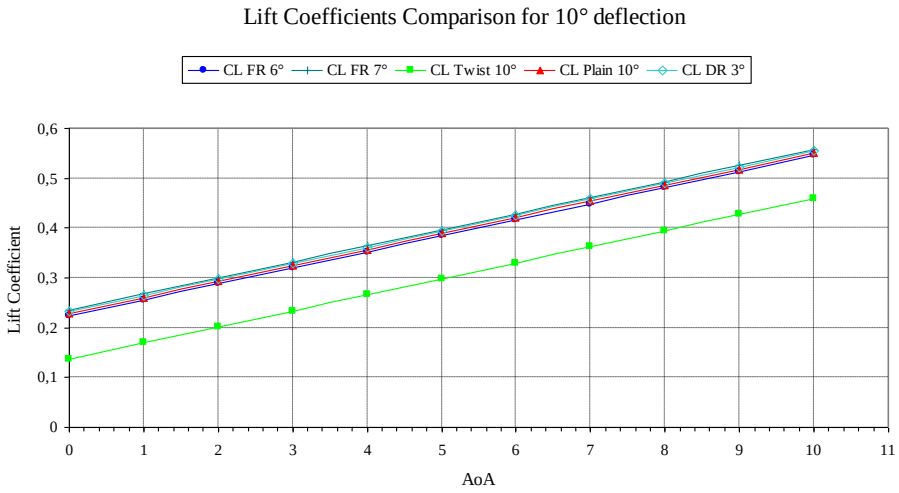

Figure 5-8 Lift coefficients for twist and camber combination.

Figure 5-8 contains only the most interesting curves obtained from the aerodynamic investigation of the GRAF configuration. In order to match the Eclipse tail performance, the GRAF model must combine together its warping capability with the cambering TE section. The red line of Figure 5-8, which indicates the deflected plain rudder, is in between the 6° and 7° deflection lines representing the fixed root TE variant. The top line, in light blue, shows the unrestrained variant of the TE section deflected to 3°. In addition to the TE deformation, all the curves already include a twist angle of 10°. The freedom gained from the unsealed TE part demonstrates the greater effectiveness in side force generation with a consistent reduction of the cambered degrees. The DR TE version, in addition to the 10° of twist, needs only 3° of deflection to match the Eclipse rudder.

WP4: In order to achieve the same control authority as the Eclipse fin-rudder configuration, the GRAF design must perform at least 7° of cambered TE section and 10° of twist to match the 10° rudder deflection. The effectiveness of this solution might improve when the TE part of the GRAF is separated from the aircraft body with consequent loss of the gapless feature claimed in the aim of this research project. In that case, the TE camber reduces to 3°.

The cases discussed up to this point have dealt only with the 10° camber as the most likely deflection deployed by the fin for most of the points of the aircraft flight envelope. The next part of this section, instead, will discuss the results of another

flight circumstance, where full deployment of the fin devices is requested. In particular this part of the study refers to those event cases of critical taking off and landing in adverse cross wind conditions, where very demanding control authority is asked of the vertical empennage. On the Eclipse tail, that case corresponds to 20° of full rudder deflection. From table 10 and the graph in Figure 5-9, it is possible to see how the novel fin, in order to match the value generated by 20° rudder deflection, struggles to achieve the same performance as a conventional fin with rudder. The warping empennage has to compensate for the loss of effectiveness of the inner section of the tail which is barely twisted because it is restrained by the fuselage gapless joint, thus generating a small amount of side force. However, the 20° hinged rudder deflected across the whole span of the conventional fin is extremely more effective than the twisted and morphed tail. In the FR TE section of the GRAF, only the top area of the cambered profiles can really achieve full deformation of the TE. In fact, the rudderless TE deflection angles at the fin root approach almost 0° because of the base constraint. Therefore, the GRAF model with sealed TE, besides the 10° of twist angle, must deflect its TE camber line up to 21° in order to match the conventional fully deployed rudder. A different value of TE camber is expected when the unsealed TE is free to uniformly rotate across the entire span. That brings down the TE bent angle to 10° for the detached root (DR) case, rather than 21° of the sealed version.

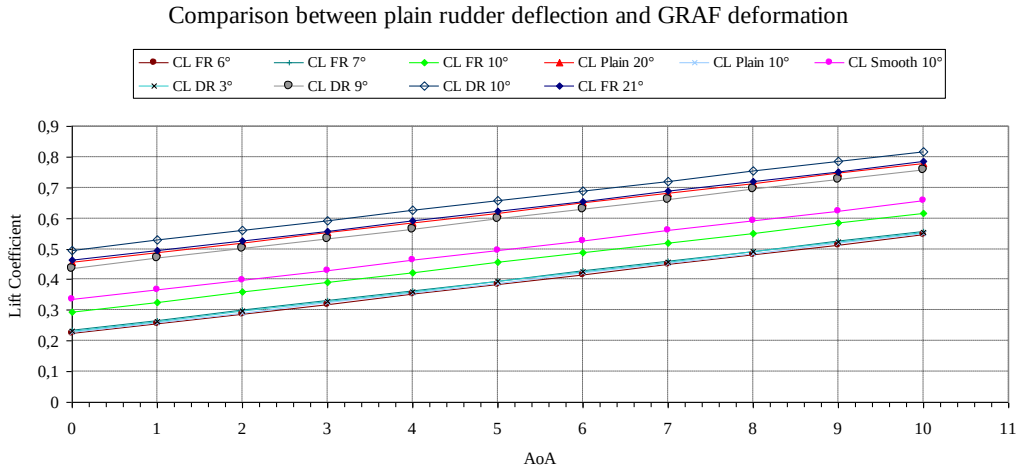

Figure 5-9 Lift coefficients comparison between GRAF & plain rudder.

WP5: The GRAF model with wholly gapless characteristics struggles to achieve the best performance and effectiveness shown by the classical fin-rudder layout. The

gapless configuration, in addition to the 10° of twist, necessitates 21° of TE camber for satisfactory control authority or as little as just 10° in the case of the unsealed TE.

The last two waypoints have given the input for the assessment of the worst case scenario for the fin loading actions. According to the performance results, six loading cases will be investigated. They are grouped by pairs into three separated sets, according to the flight speeds they occur in:

1. The first group includes the analysis conducted at the cruise speed of 40.8 m/s. The GRAF is twisted and cambered to produce the same side force effect generated by the conventional rudder when fully deployed at a 20° angle. This group includes two different cases: '1A' is the TE section with gapless configuration (FR), '1B' is the unsealed (DR) TE case;
2. This group analyses the case of the GRAF tail twisted by 10° and with the cambered section deformed to match the side force generated by 10° deflection of conventional rudder at cruise speed. As with the previous group, this one will also evaluate the sealed and unsealed case with 7° (FR) and 3° (DR) deflection respectively (i.e. 2A and 2B);
3. The third group is potentially the most extreme loading scenario for such a design. It collects the data attained at the dive speed of 60 m/s with the fin twisted by 10° and with a cambered section able to match the 10° rudder deflection. The 7° (FR) and 3° (DR) cases are also discussed here.

The equivalent configuration of 20° rudder deflection at the dive speed is not taken into consideration because it is outside the specifics of the Eclipse design. Moreover, the first two groups also take into account sideslip effects with cross wind at an angle of 10°. No sideslip effect is considered on the dive speed case. By definition sideslip cannot occur during diving. Hence, the six case studies can be compacted and listed as:

1A. 21° FR (Fixed TE Root) @ 40.8 m/s (cruise speed);
1B. 10° DR (Detached TE Root) @ 40.8 m/s (cruise speed);

2A. 7° FR @ 60 m/s (VNE, dive speed);

2B. 3° DR@ 60 m/s (VNE, dive speed);

3A. 7° FR @ 40.8 m/s (cruise speed +10° sideslip);

3B. 3° DR@ 40.8 m/s (cruise speed + 10° sideslip);

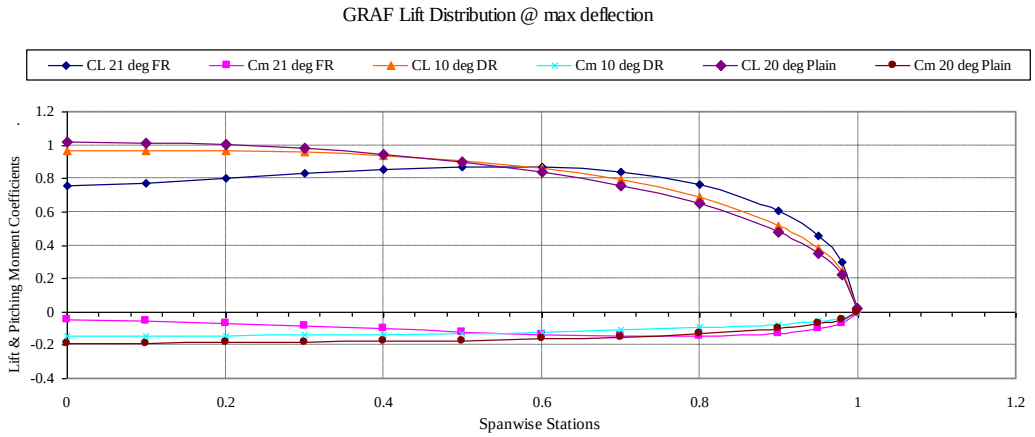

Figure 5-10 Lift distribution for GRAF configuration.

Figure 5-10 shows the values of the lifting coefficients for the mentioned case studies. Their non-dimensional values in the above diagram are independent from the velocities the case studies have been considered to. The flight speed influence and its consequent effects on the load distributions over the fin span are shown in Figure 5-11. The diagram shows the fin load distribution for the three different flight speeds, with varying twist and camber configurations.

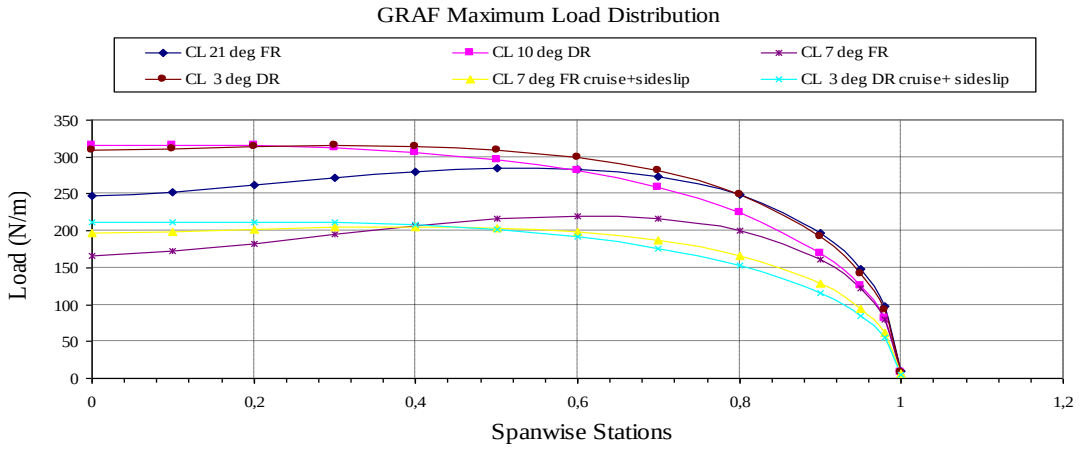

Figure 5-11 GRAF loading case scenarios.

Based on this fin load distribution, the corresponding bending moment has been calculated and is shown in Figure 5-13. The curves plotted in the graph of Figure 5-

11 show the worst loading case scenario for the GRAF empennage is the one occurring with the fin flying at maximum cruise speed, fully deflected and with sealed TE. That translates into the analysis of a 10° twisted fin with cambered TE to either 21° for the FR version or 10° for the DR one, both at 40.8 m/s flight speed. Noticeable here it is the dominant influence of the lift coefficient with respect to the square of the flight speed.

Although the dive speed is much higher than the cruise speed, the reduced deflection of the TE at dive speed produces lower loads than those obtained at cruise speed for full deployment of the GRAF systems, which is shown as the pink and blue curves of Figure 5-11. The blue curve is generated by 21° of FR camber and 10° of twist, while the pink curve represents 10° of fin twist and 10° of DR camber.

WP6: The worst loading case scenario occurs at cruise speed of 40.8 m/s with the GRAF yaw motivator systems simulating the effect of the 20° hinged rudder deflection of the Eclipse UAV.

Note on WP6: this load case scenario has been chosen as worst condition accordingly to the maximum deflection capability of the hinged rudder. However, that represents a rare situation where possibly at cruise speed the Eclipse vehicle might not use a full rudder deflection. Due to the experimental nature of the Eclipse study, flight data, performance and restrictions in order to adjust the case analysis are not available yet.

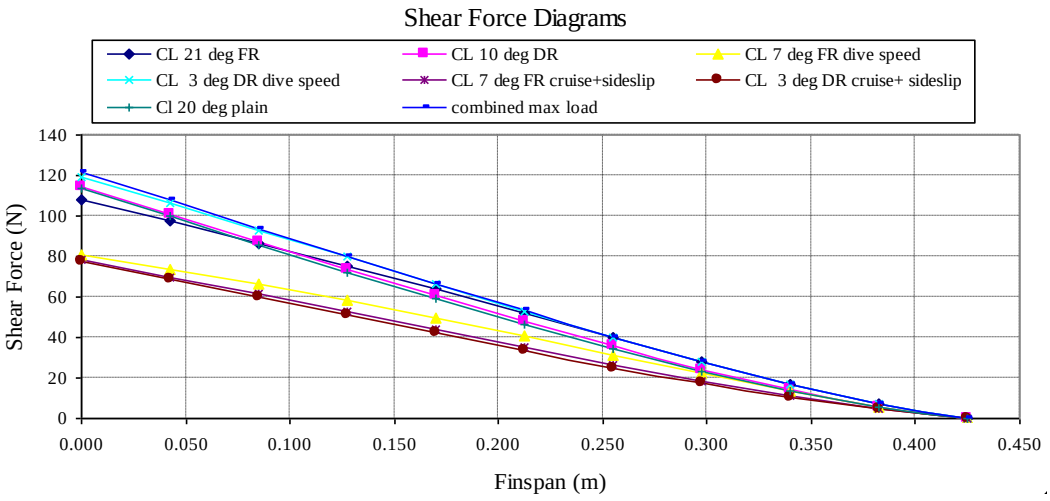

Figure 5-12 GRAF shear force diagram.

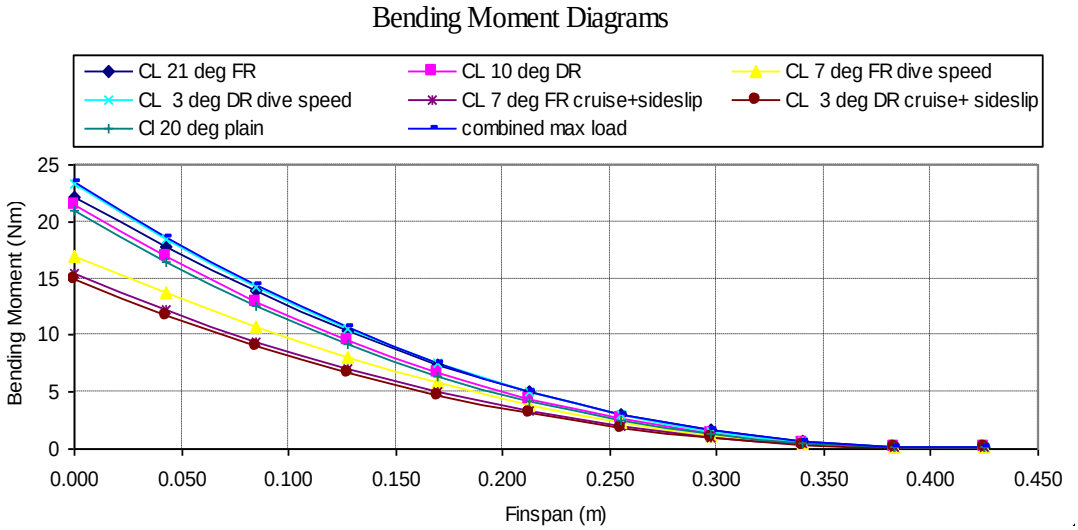

Figure 5-13 GRAF bending moment diagram.

A remarkable conclusion is drawn from the loading action study. Let us look at the curves corresponding to the condition described in WP6; those curves are the top one in pink and the third one from the top in blue of the loads diagram in Figure 5-11. Between the two cases, the higher load is occurring for the pink curve which is plotting the force generated by a root-detached TE section with 10° of camber. The other configuration with the fixed TE root section cambered at 21° shows a different distribution, by having a lower load distribution near the fin root, and higher ones located at around the 70% of the fin span. In both cases the fin is twisted up to 10°. It appears the load distribution is slightly lower when the TE root is anchored to the fuselage than when free to deflect. That difference changes the load intensity and twist distribution on the empennage. The different load distribution could lead to designing those parts near the root to withstand lower cyclic loads and lower levels of stress for the operational conditions of the fin. From the chart of Figure 5-12 it can be seen that the shear force distribution corresponding to the highest load change from the pink curve to the blue one when they intersect at around 30% of the fin span. In the first segment the pink curve (10° unsealed TE) generates a greater shear force, while after that point the dominant force is the one coming from the blue line (21° sealed TE). A similar situation is presented in the bending moment diagram. The resultant force of the load distribution has a distance arm from the root longer than the one compared to the unsealed case. That generates a greater bending moment, and the change of curve level in the shear force diagram. In order to comply

with all possible cases that might occur on the GRAF model during any flight mission and systems operation, a more conservative curve enclosing single segments of the two worst case scenario has been drawn. The global curve is shown in Figure 5-14 with a blue line, namely 'max combined load'.

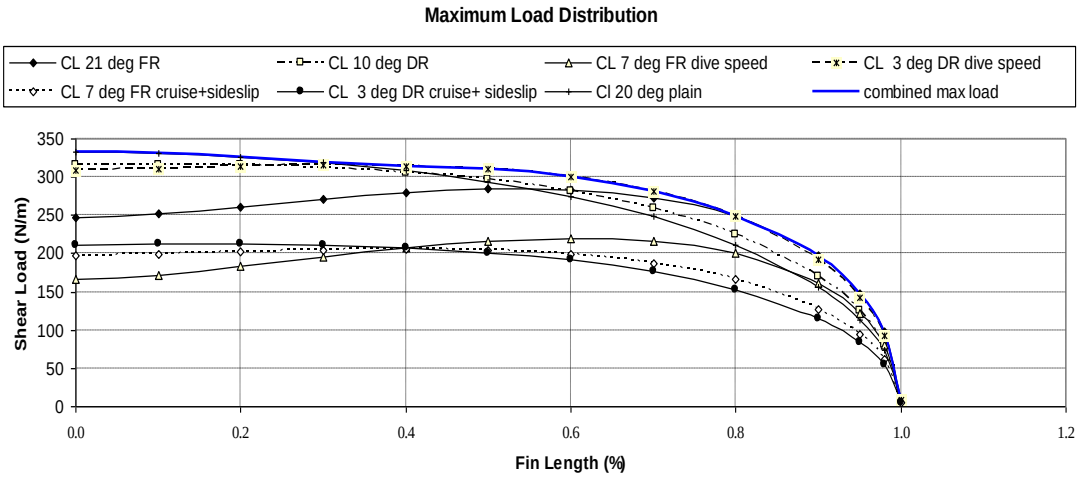

Figure 5-14 Selected worst loading case scenario.

Two clearer charts for the shear force and bending moment distribution corresponding to the above defined maximum combined load distribution are illustrated in Figure 5-15 and 5-16.

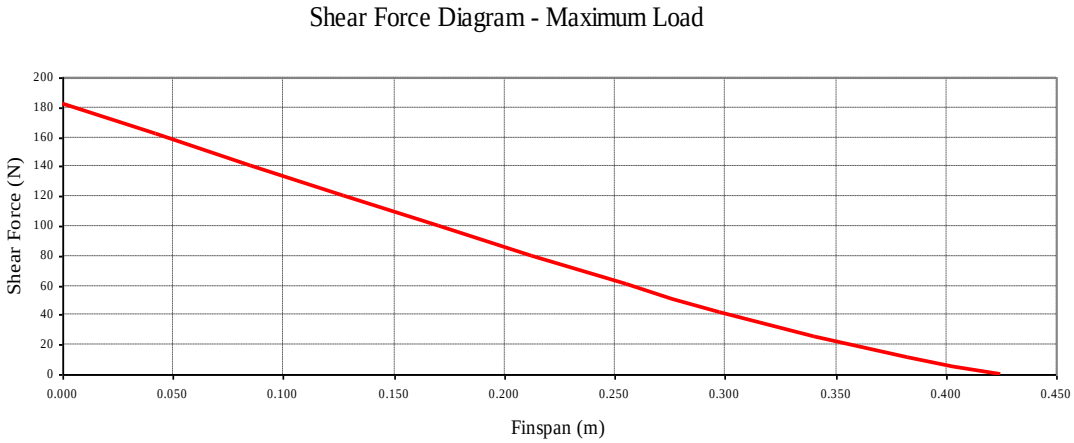

Figure 5-15 Shear force diagram for worst case scenario.

The semi-empirical formula used by Howe, already presented in Chapter 3, establishes that the maximum shear force acting on the vertical tail is:

$$L_F = \frac{4.2\,m/s^2 \cdot 45Kg \cdot 9.8\,m/s^2}{8} = 231N \cdot 1.5 = 346.5N$$

The empirical formulation estimates a resultant load almost coincident with the resultant of the load distribution considered in Figure 5-16.

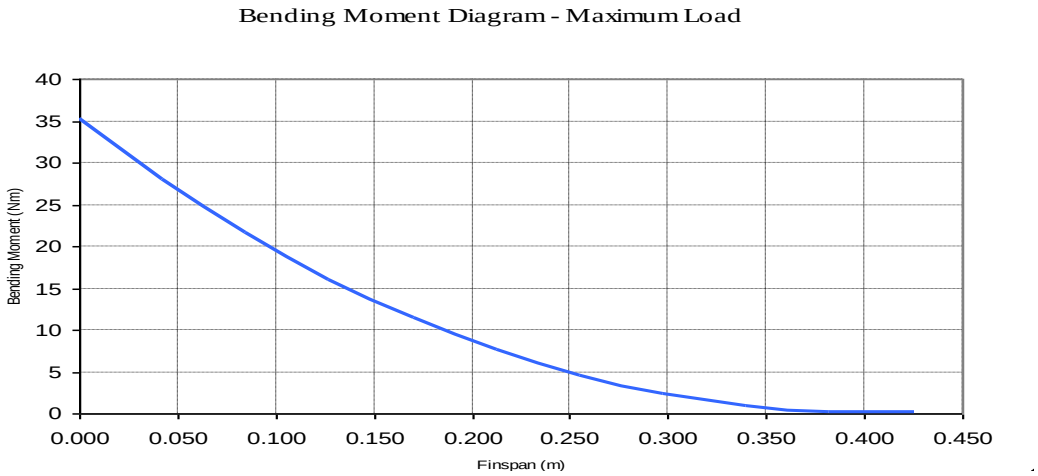

Figure 5-16 Bending moment diagram for worst case scenario.

The same GRAF configuration used to identify the worst load case scenario has been used to compute, via the JAVAFOIL tool, the pressure distribution over the skin panels of the most loaded fin section. This pressure distribution presented with the Cp diagram of Figure 5-17 has been input as external loads in the MATLAB code in order to find the rib pitch and skin thickness. It has also been input, as an external load pressure upon the TE part, in the NASTRAN analysis carried out for the assessment of the morphing TE section design.

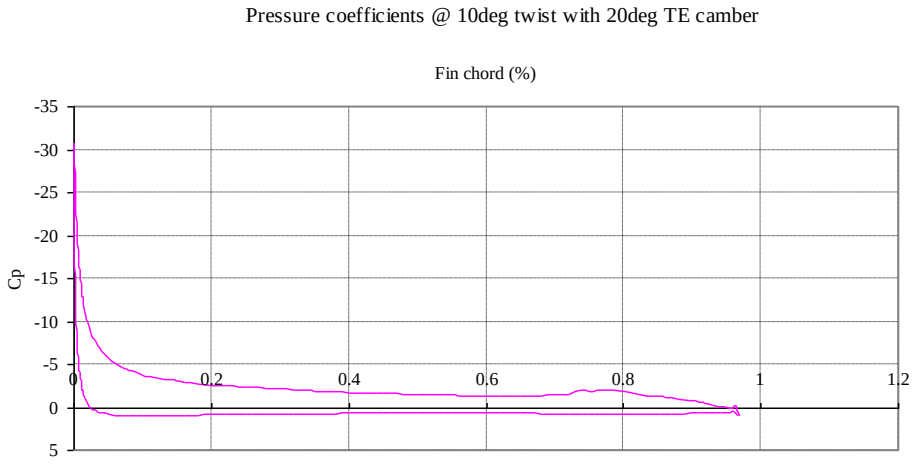

Figure 5-17 Airfoil section pressure distribution under worst loading case.

The Cp-diagram corresponds to a twist angle attitude of 10° with a morphed TE deflected by 20°.

This aerodynamic study has concentrated its analysis on the aerodynamic effect that TE camber and twist angles have on the novel aeroelastic rudderless fin. As with all tail-plane configurations, only the rear part of the profile section, the TE, has undergone seamless deflections, while modern aeroelastic and morphing wing applications are used to deploy leading edge devices for performance purposes, as done by NASA and Boeing with the experiments conducted on board the F/A-18AAW.

The reason why the GRAF design does not include active LE sections is explained here. Aerodynamic simulation of the fin surface provided with LE devices has been carried out via JAVAFOIL models. This investigation has kept the TE section equal to 25% of the fin chord, with an active LE device equal to 15% of the fin chord. For clarity on the sign convention, let us imagine the airfoil section with the chord line parallel to these lines and with the LE pointing to the left hand side of the page, and the opposite TE towards the right hand side edge. Their deflections are termed positive when they deflect both down, negative when bent upwards.

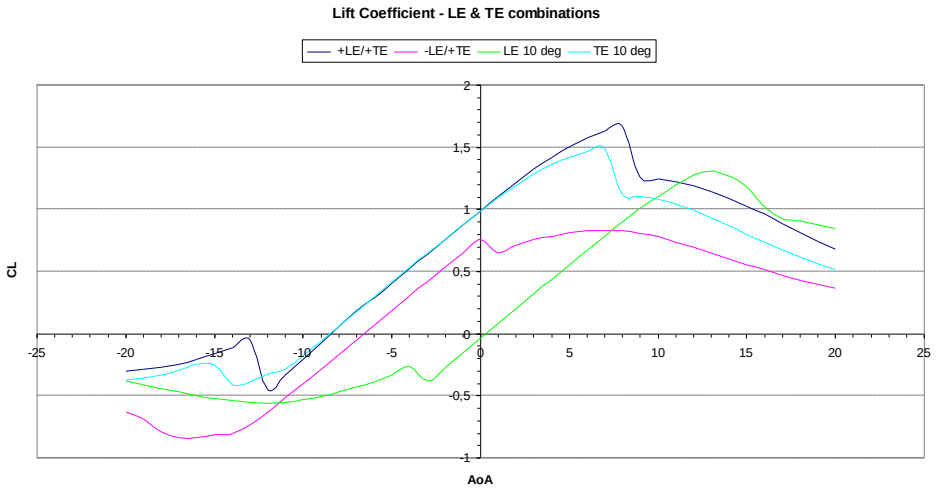

Figure 5-18 Lift curves generated by LE and TE device deployment.

The lift coefficients diagram of Figure 5-18 shows how the LE deflection increases and shifts the lift curve towards higher values of AoA when it is combined with the TE device (blue curve). The positive LE and TE combination gives performance advantages at high angles of attack, while the LE activation, shown by the green curve, helps the profile shift the stall at a higher angle of attack but is not providing better performance in terms of lift generation. Moreover, besides the achieved higher angle of attack, it is performing a little less than the single TE deflection (light blue

curve). However, the combination of both devices rotated in opposite directions (negative LE and positive TE or vice versa) is not generating interesting values of lift coefficients.

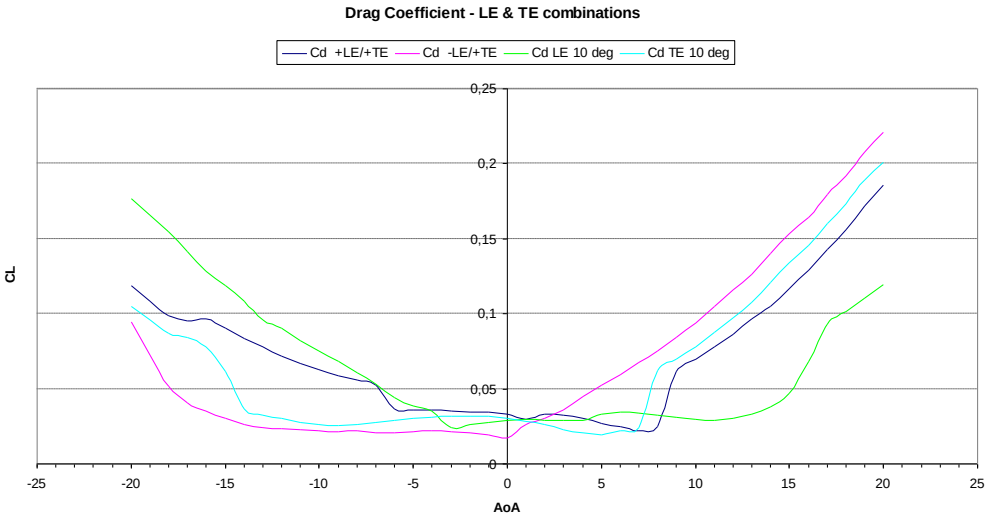

Figure 5-19 Drag curves generated by LE and TE devices deployment.

The drag coefficient diagram of Figure 5-19 indicates that the configuration generating less drag force is the one with the LE and TE activated in opposite ways. The same configuration, however, gives a modest pitching moment coefficient compared to the low values of the only-LE curve and to the one with both LE and TE devices rotated on the same side (+LE/+TE).

Hence, in terms of lifting contribution, the '*+LE/+TE*' variant offers the best performance. However, a penalty in the greater pitching moment effect is paid because of the high camber shape achieved during deformation. The high value of the pitching moment could reduce the diverging effect sought for the aeroelastic actuation of the GRAF, thus reducing the twist capability of the tail. The other device option might see the application of only the LE part. The deployment of the single LE device, on the one side shows low values of the C_M and also presents a modest drag force coefficient generation but on the other side does not perform well in lift generation. Therefore, for the specific case of the GRAF design, the best compromise of C_L, C_D and C_M is offered by activation of only the TE device.

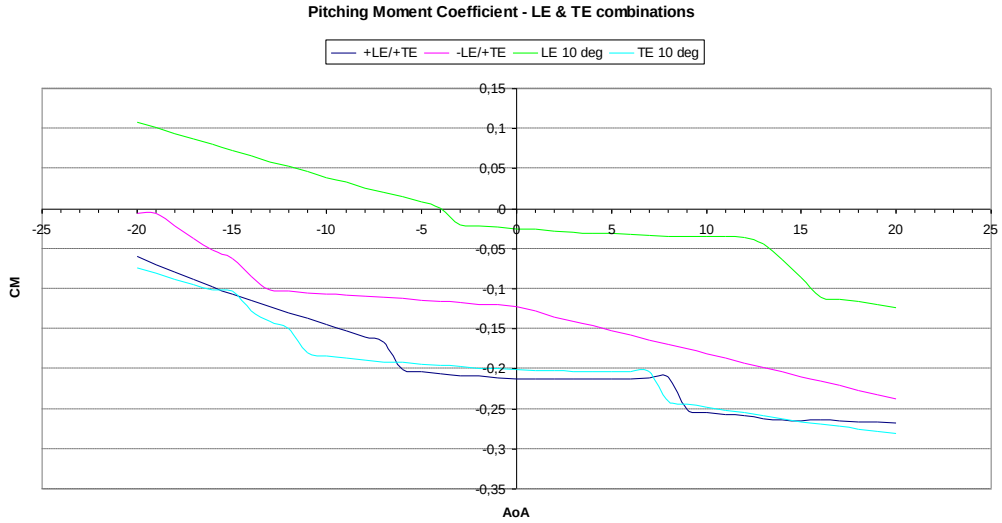

Figure 5-20 Pitching moment curves obtained from LE and TE devices deployment.

There is also another technical reason for discarding leading edge applications on tailplanes, which is the mechanical and structural complexity of the LE integration into a fin structure. The leading edge area of any aerodynamic surface is the most difficult part of the profile to be deformed. The highly curved shape of the short section considerably increases the stiffness of that area. However, there could be three options to make an LE deformation possible. The first is by interrupting the structure continuity with gaps or hinge elements, in order to increase the DOF of the parts. The second is by adopting smart materials, enabling the profile to easily deform the leading edge configuration without breaking or overstressing the material. The third is by adopting an internal mechanism and very powerful actuators able to elastically force conventional materials into the deflected shape. All three options may represent theoretically viable solutions, but with unacceptable drawbacks for the specifics of the GRAF design. The first option will include gaps, thus cancelling out the gapless characteristics of the novel empennage. The second will complicate the internal design and increase the weight of the structure due to the high density of smart materials and heavy weight of related power supplies. The third option, as with the second one, will considerably affect the weight of the vehicle, because of the amount of the necessarily powerful actuators needed to activate and control the very robust profile sections.

WP7: A compromise in performance and complexity has established that the GRAF profile will perform only by entrusting warping and TE section capabilities. No consideration of any LE device implementation has been taken into account. The fact is that the modest margin of the LE advantages will not be worth the application of a more sophisticated design concept.

Table 11 presents the side force values obtained for different combinations of warping and cambering deflections at the various flight speeds of the Eclipse vehicle.

Table 11 - Control authority performance vs. flight speeds

GRAF Side Force

Flight Speed (m/s)	CL 21° FR	CL 10° DR	CL 7° FR	CL 3° DR	CL 7° FR cruise+sideslip	CL 3° DR cruise+ sideslip	CL 20° Plain	Twist only	CL 10° Plain
25.6	25.2	27.1	12.9	12.7	30.4	30.3	24.9	7.5	12.5
30	34.6	37.2	17.6	17.4	41.8	41.6	34.2	10.3	17.1
40.8	64.1	68.8	32.6	32.3	77.3	76.9	63.3	19.0	31.6
41.8	67.3	72.2	34.3	33.9	81.1	80.7	66.4	20.0	33.2
45	77.9	83.7	39.7	39.2	94.0	93.5	77.0	23.1	38.5
50	96.2	103.4	49.0	48.4	116.1	115.5	95.0	28.6	47.5
60	138.6	148.9	70.6	69.8	167.1	166.3	136.8	41.1	68.4

The data contained in the above table are plotted in the "GRAF Side Force" diagram of Figure 5-21.

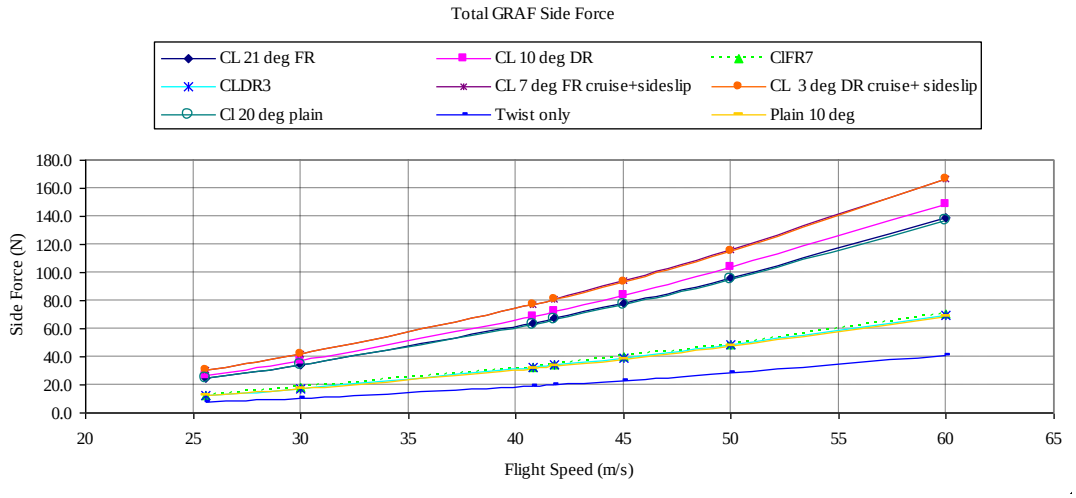

Figure 5-21 MTF4 model side force generation vs. flight speed.

The aerodynamic centre of the profiles is located at 0.25c of the section. It is 0.15c away from the pivoting point of the GRAF shaft located at 0.4c of the root chord. As soon as the empennage moves from its neutral, non-lifting, position with an angle of

0°, then it starts generating the side force and the aeroelastic moment necessary to warp the entire assembly. The distance between the AC and the shaft acts as moment arm for the side force. It generates the aeroelastic moment which tends to twist the whole fin shape. Figure 5-22 shows the twisting moment those side forces are able to generate at different flight speeds. The aeroelastic moment computation has also taken into account the contribution of the pitching moment.

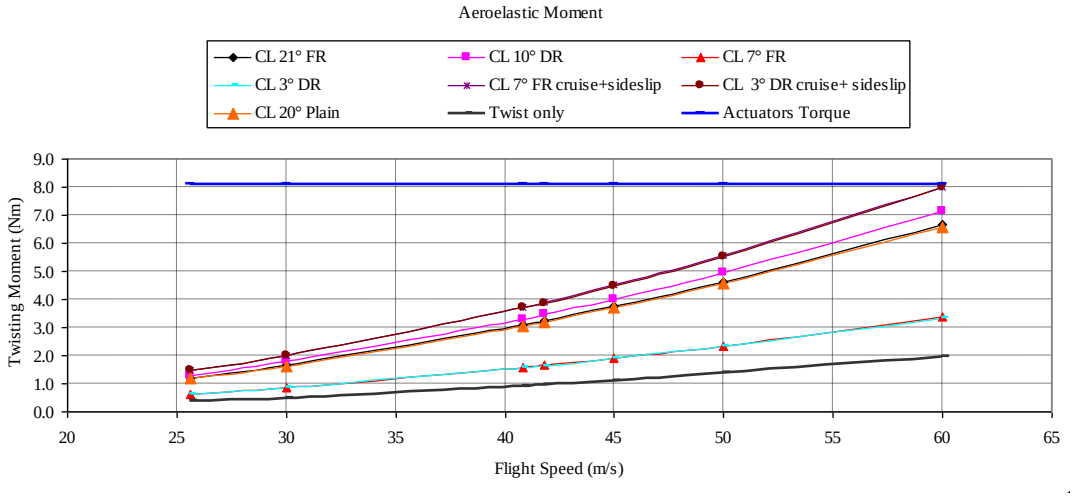

Figure 5-22 Twisting moment induced by the aeroelastic effect.

The thick blue line of Figure 5-22 represents the minimum torque provided by the selected servo mechanism. The mechanical torque is used to initiate, control, damp and hold the twisting phase of the GRAF tail. As noted in the graph, the chosen actuator gives sufficient power to withstand the torque load generated by the aeroelastic effect at different speeds. At the same time it is capable of retrieving the fin to its neutral position whatever its deflecting attitude is, even at a limited dive speed. The actuator torque is also amplified by the leverage system linked to the bottom of the fin shaft, in order to produce the amount of moment needed for the operational cases of the GRAF. The servo-actuator used for the TE device, develops between 290N and 350N of linear force to be applied on the pushrod linked to the levers of 0.03m length fixed at the bottom of the primary shaft. The three centimetres arm helps to amplify the actuator effectiveness by generating a torsion moment varying from 290N x 0.03m = 8.7Nm to 380N x 0.03m =11.4Nm. The servo mechanism assists the fin during the normal operations to control it by preventing and blocking the entire structure from any unexpected diverging twist.

WP8: The aeroelastic moment can contribute to the fin twist once the deformation has been initiated by the actuation system or by an external disturbance. The selected actuators are capable of providing enough torque to counteract the twisting moment induced by the aeroelastic effect.

5.3 Structural design: FEM analysis results

This section begins a discussion of the results obtained from the structural and performance analysis of the key elements constituting the GRAF MTF4 assembly. The section is divided into four paragraphs:

1. Fin skin: structural sizing;
2. Rudderless TE displacement and stress analysis;
3. Primary shaft: structural analysis;
4. Twist effect and slot-connection analysis.

5.3.1 Fin skin sizing

The analysis has been carried out on the skin portion situated between two adjacent ribs. The surface area of the panel has been subjected to the external pressure derived from the worst loading case scenario. The composite laminate properties applied for the skin analysis have been taken from the COALA computations, and are attached in Appendix B. The analysis is used to define the skin thickness and rib pitch of the fin assembly. The diagrams in Figs. 5-23 and 5-24 illustrate the results obtained from the MATLAB analysis related to the four and three layers layups.

Between five and seven (i.e. between 50-80mm) is the number of ribs meant to be included inside the GRAF tail. This study, related to the three and four layers skin variants, helps identify the final value of the skin thickness, the ribs pitch and so the ribs number.

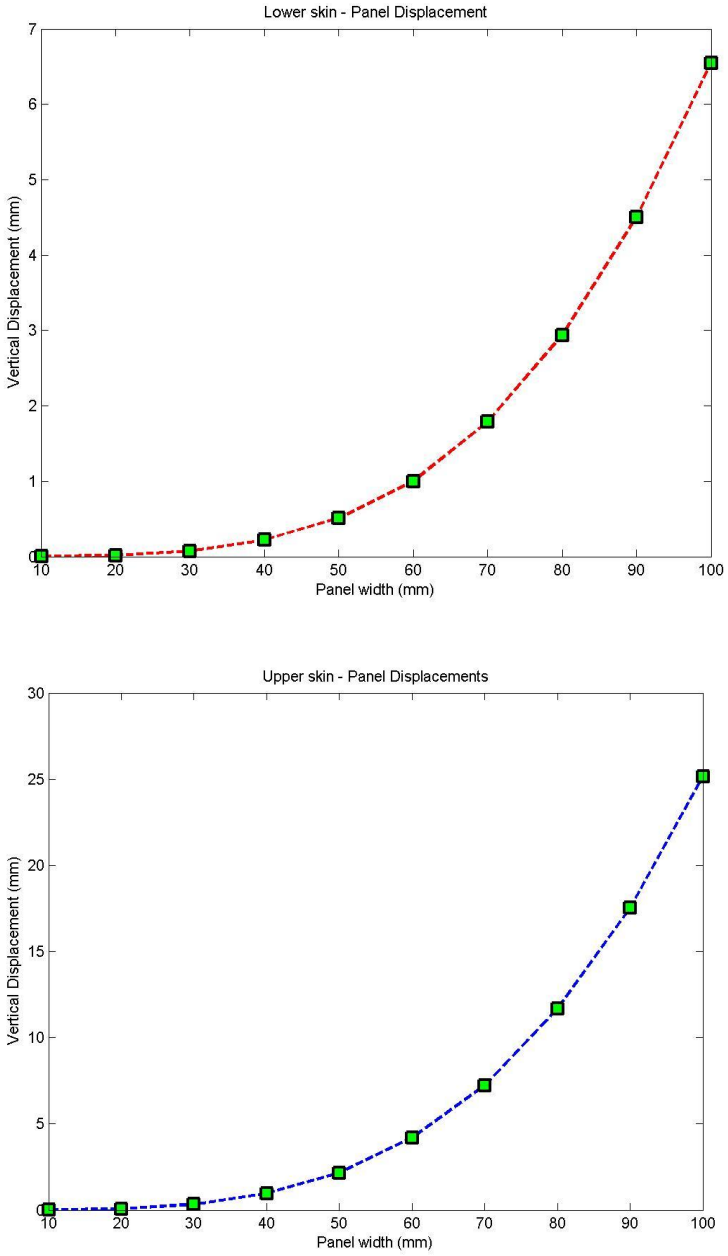

Figure 5-23 Four layers lower (top) and upper (bottom) skin vertical displacements.

Talking about the four layers configuration, as shown in the above diagrams, the best compromise between deflection and rib pitch comes from the 70mm pitch value, which for the worst loaded panels, corresponds to a maximum deflection of 8mm.

The 60 and 80mm ribs pitch cases offer very small and too much deflection, respectively, for this test case. The variant option with reduced number of layers is presented next. The curves in Figure 5-25 will show the 3-D graphic representation of the MATLAB model of the four layers plate.

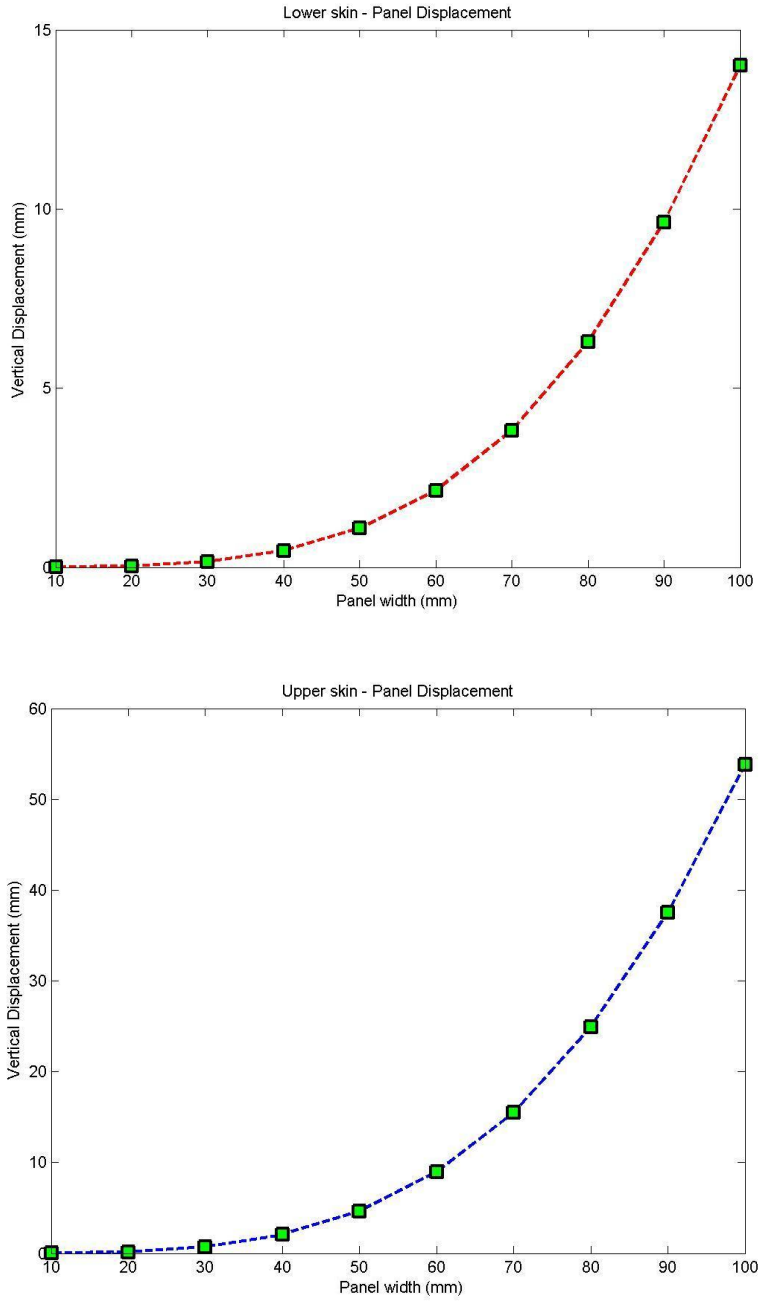

Figure 5-24 Three layers lower (top) and upper (bottom) skin vertical displacements.

The two diagrams of Figure 5-24 identify the deformation curves of the composite skin made only of three layers of glassfibre. As it can be seen from the blue curve of

the upper profile side, the deflection, related to 70mm pitch (i.e. six ribs) has increased to a maximum of 15mm, with the lower side panel displacing only of 4mm. These results have been taken as reference values for the final configuration of the GRAF. Despite the consistent 15mm of vertical displacement for the skin panel, the three layers option with a ribs pitch of 70mm has been chosen to define the internal layout of the fin. This configuration provides a lighter skin and more flexibility to the external cladding. However, a shorter distance between ribs, hence more rib elements inside the fin, will definitively increase the overall weight of the structure. Thereby, at this stage of the fin design the six ribs option, with 70mm rib pitch across the 0.425m fin span, has been adopted for the MTF4 model. Although the panel deformation achieves 15mm of deflection under worst loading case scenario, few assumptions can be made to justify that in practice the deformation will be much less than this case used for this preliminary sizing of the skin. At this stage, the skin analysis has been conducted on a flat composite panel with two simply supported and two free edges boundaries. In practice, the curvature of the airfoil shape and the LE and TE connection will contribute to reducing the extent of the overall plate deformations, by simply stiffening the panel due to its curved shape. Nevertheless, this worst load case scenario occurs only when the fin is fully twisted and cambered, so with the skin stretched under tension, which, as explained by the membrane theory, will further reduce the normal-to-plane displacements of the plate. Eventually, the final distance between the ribs is 85mm. The computed rib pitch has determined an overall distance between the two opposite edges of the single skin panel equal to 70mm. However, it must be taken into account that the rib design also includes the 15mm *skirt* extension which is added to the panel length for a total width of 85mm, 70mm of which represent the free length between the plate edges.

There are other two reasons which addressed the three layers choice. The one is that a stiffer layout would inevitably increase the warping stiffness and so the torque necessary to activate the twist deformations. The other one is that this loading scenario inducing such a large deformation of the panel occurs only at the very top of the empennage. Thus, affecting only a very small area of the entire empennage, due to the fact only a very small portion of the fin tip is subjected to full twist and camber deflections. The rest of it gradually reduces the deformations down to zero where the

root meets the fuselage joint. Moreover, it is also on the suction side of the profile, thus meaning that by bubbling up the skin it may contribute to further twist the fin shape. Although the simply supported plate has been studied to represent the generic skin panel, from a practical point of view, the skin at the fin tip is rigidly fixed to the master rib. That reinforced type of joint brings down the values of the displacements under the subjected load.

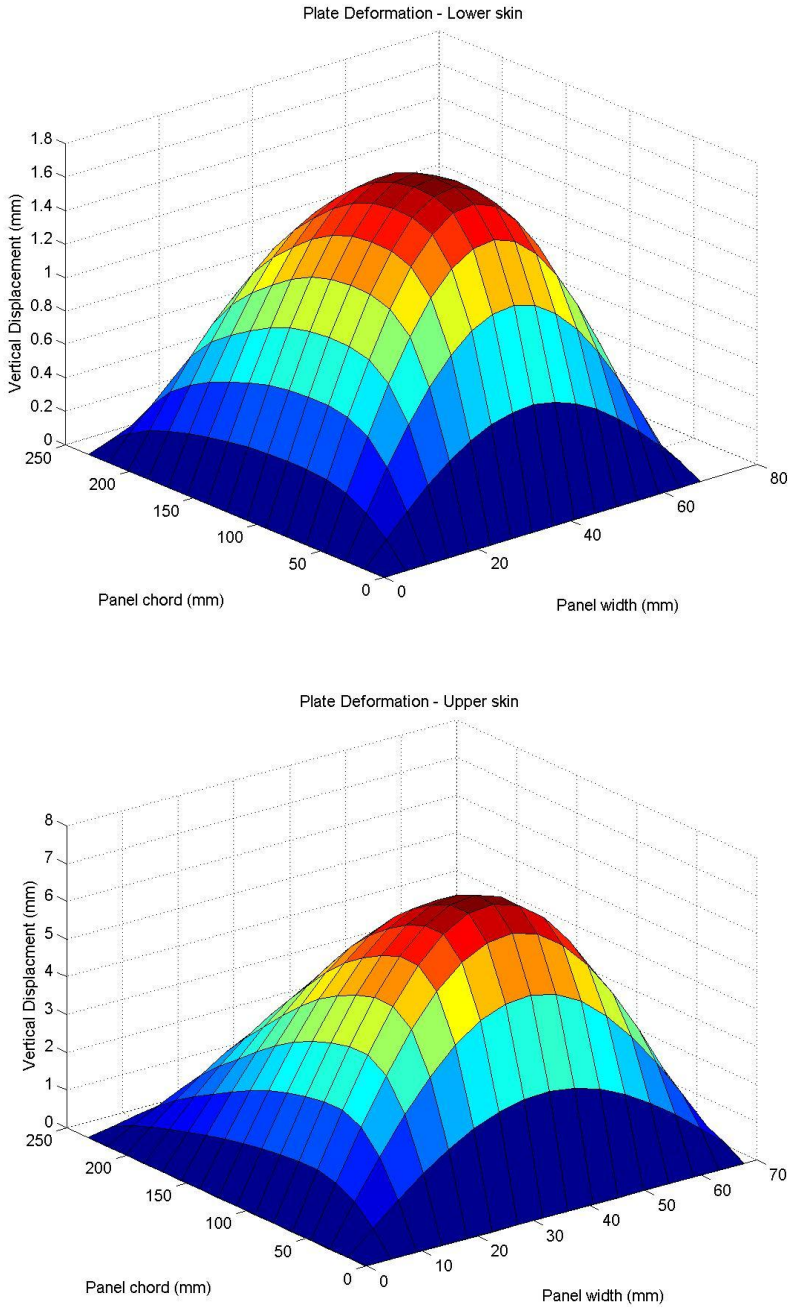

Figure 5-25 MATLAB 3D results for the four layers skin deformation.

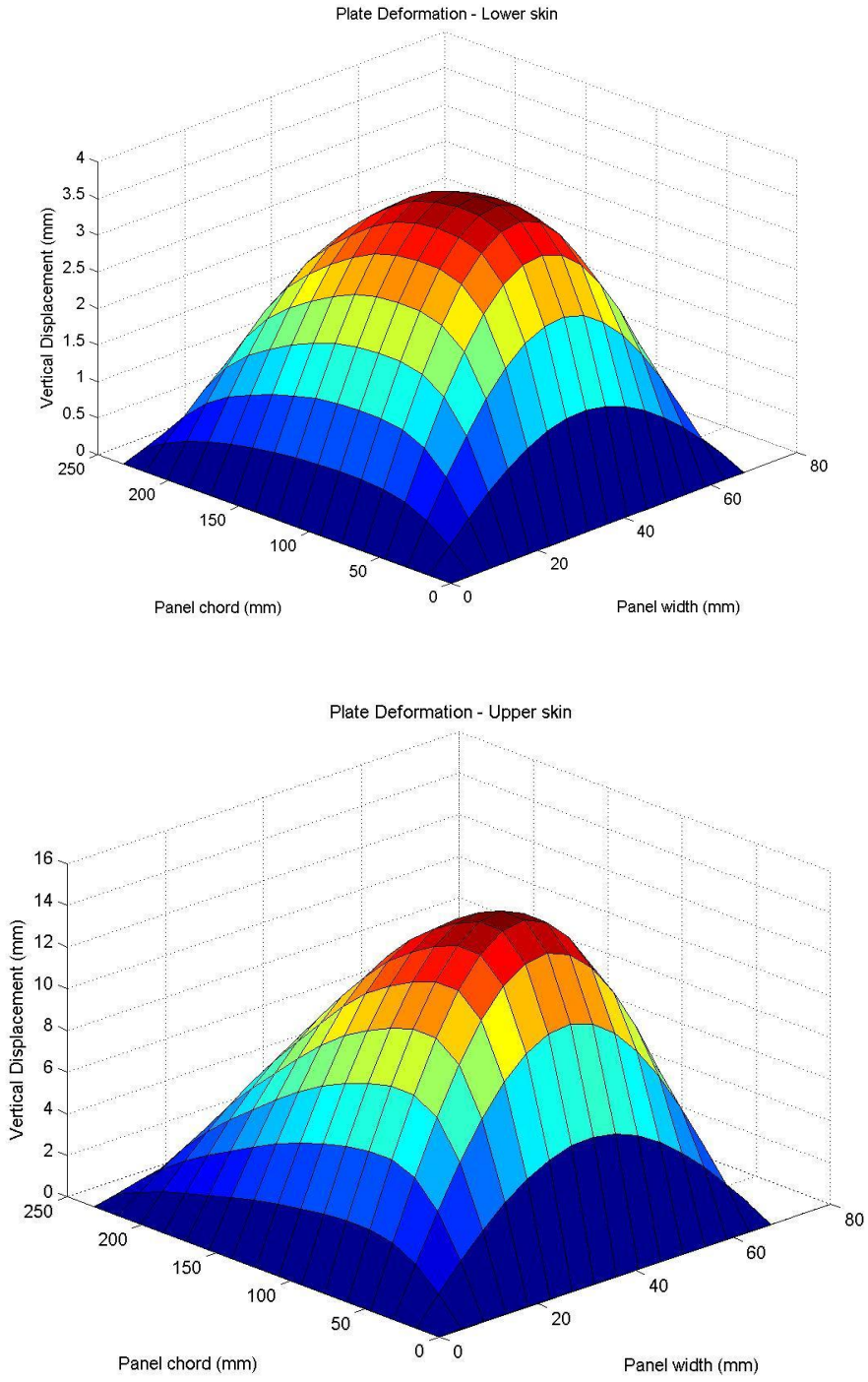

Figure 5-26 MATLAB 3D results for the three layers skin deformation.

Figure 5-26 (top and bottom) shows the 3-D graphical displacements of the upper and lower skins of the fin profile.

WP9: The skin structure of the whole empennage will be constituted by a total of three layers of glassfibre with a total thickness of 0.35mm.

5.3.2 Rudderless TE displacements and stresses results

The second group of the structural design section starts with the presentation and discussion of the FEA results obtained from the camber deflection of both restrained and unrestrained TE configurations. The TE morphing action has reached 10° and 21° for the unsealed and sealed gap configurations respectively. The Figures 5-27 and 5-28 show the TE deformations when activated by the servo-actuator located at the bottom of the secondary shaft for both restrained (FR) and unrestrained (DR) TE cases.

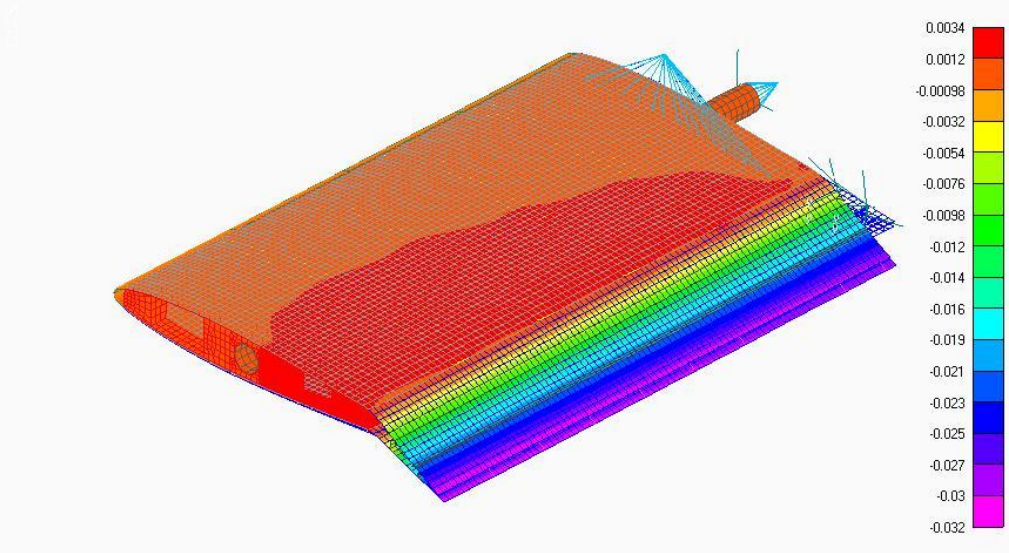

Figure 5-27 TE (DR) deformation with the TE root unsealed and detached from the fuselage.

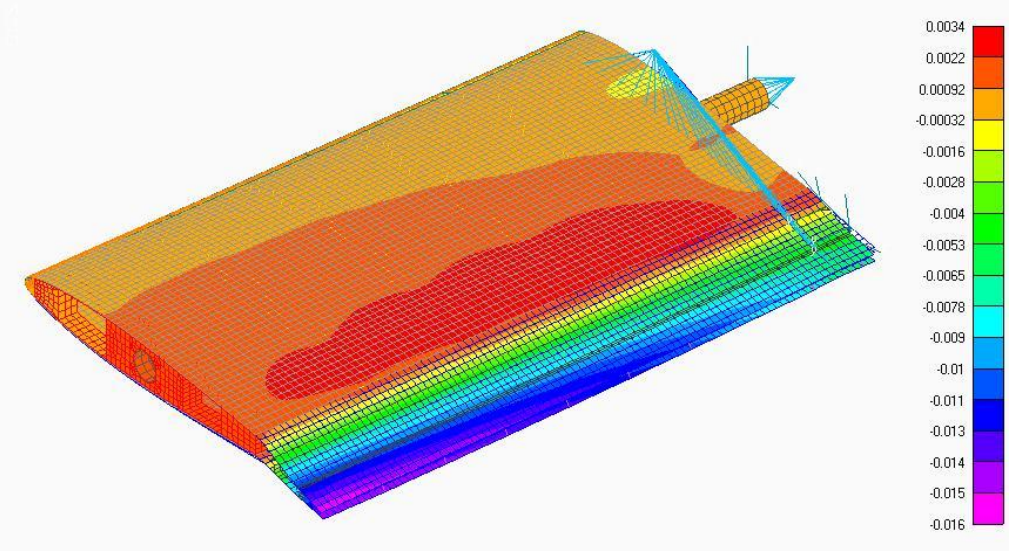

Figure 5-28 TE (FR) deformation with the TE root sealed and connected to the fuselage.

The mechanical torque of 2.9Nm, which is converted and uniformly distributed via pushrods to the LSS bending devices, produces the results shown above. They demonstrate that in the unsealed configuration, the torque is sufficient to evenly bend the TE section up to 22° (i.e. 0.032m, Figure 5-27), while as shown by Figure 5-28, the maximum deflection achieved by the MTF4 fin with the same torque and sealed TE is 0.016m, which translates to less than 11.5° at the top corner.

All the deflection tests are carried out by including the external load pressure distributed normally to the TE surface and corresponding to the worst case scenario obtained in Figure 5-17.

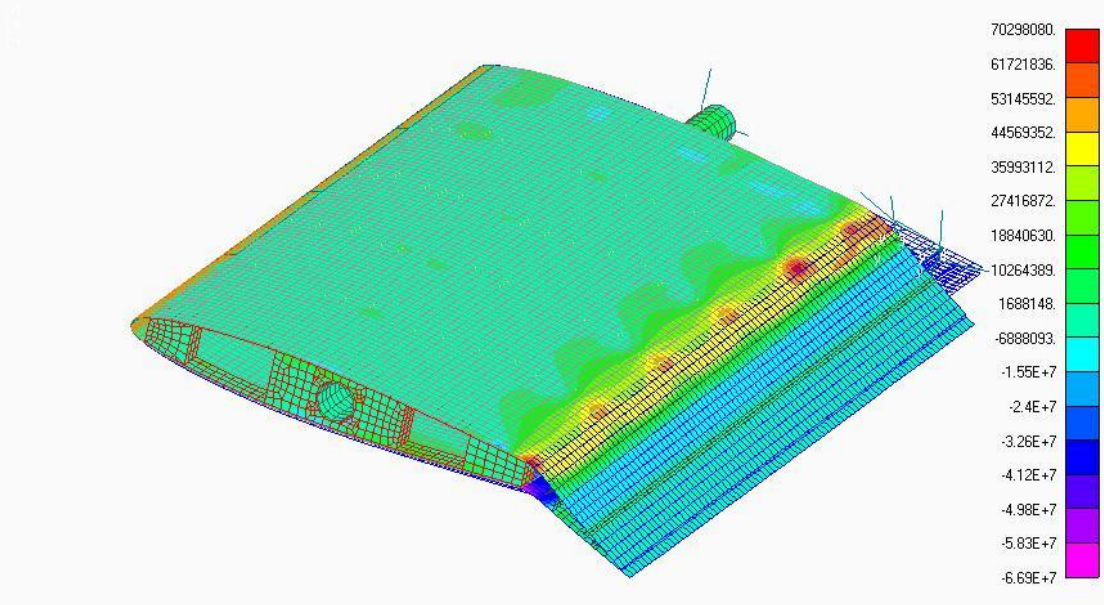

Figure 5-29 Right side skin surface stress level on 0° fibres direction for TE DR variant.

Neither of the restrained (FR) or unrestrained (DR) TE deformations affect the structural strength of the GRAF assembly. As also shown in Figure 5-29, low level of stress is distributed along the bent edge of the TE skin at 0.75c, with a maximum value of 70MPa near the fin root.

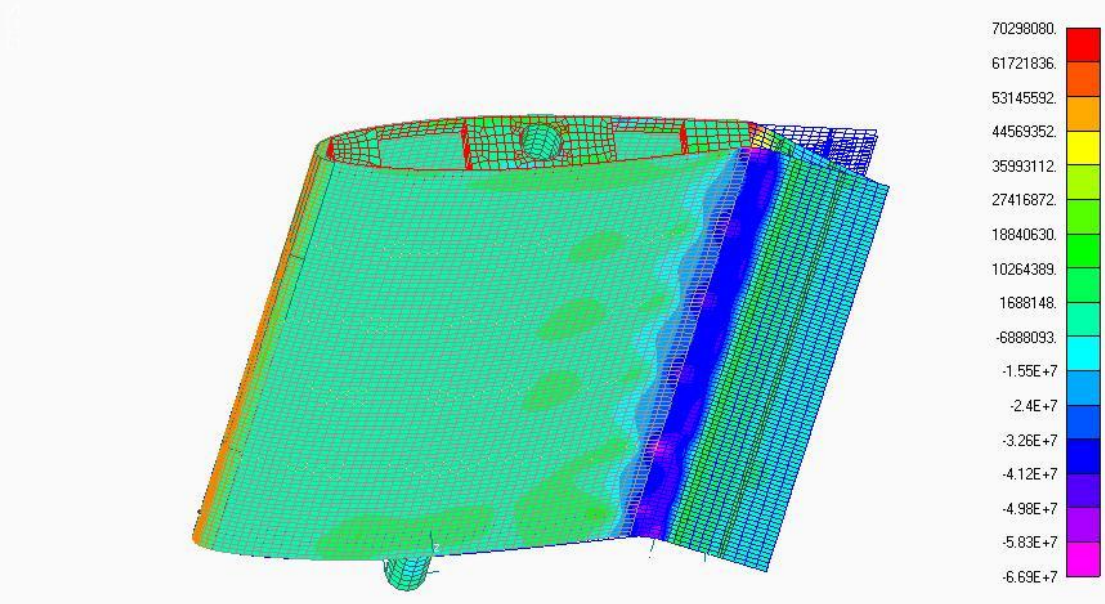

Figure 5-30 Left side skin surface stress level on 0° fibres direction TE DR variant.

As shown in Figure 5-30 and 5-31, the maximum levels of tensile and compressive stress reached during the TE operation are respectively 70MPa and 67MPa for the unrestrained variant, while the sealed constrain generates 74MPa and 70MPa respectively.

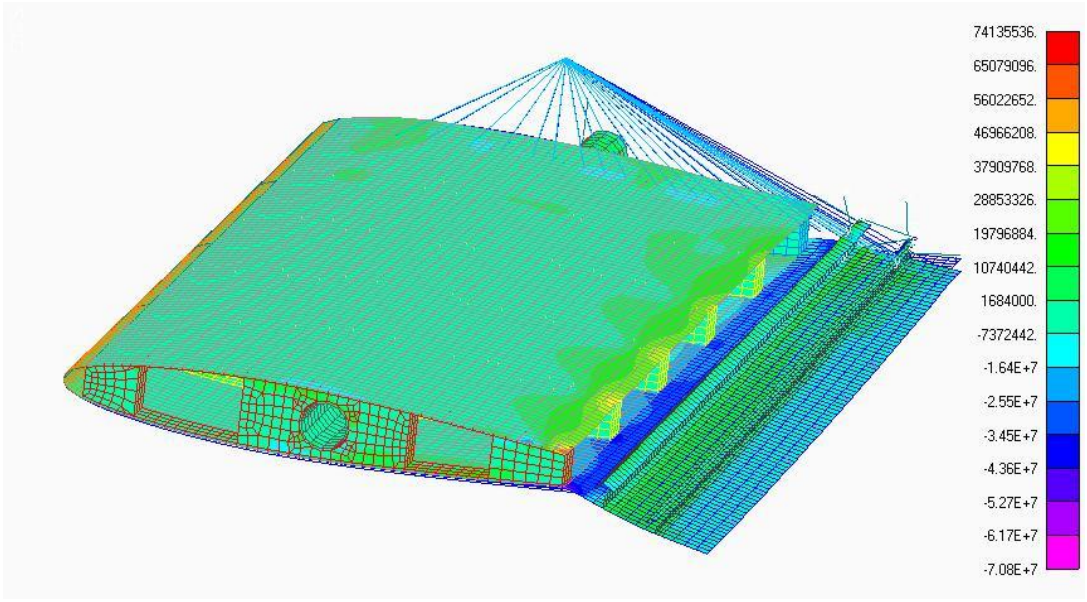

Figure 5-31 GRAF stress level on 0° fibres direction for TE FR variant.

The stresses concentration on both DR and FR TE versions is predominantly located on the skin elements corresponding to the imaginary hinge line of the TE part, where the deflecting panel starts to deform.

The objective of the GRAF design is to perform equally to the hinged rudder version, but, it is hoped, with a full gapless profile layout. Moreover, it has been demonstrated by the aerodynamic investigation, that the GRAF tail needs to generate a camber deflection of at least 21° in order to ensure the same control authority as that provided by the Eclipse conventional rudder. Therefore, in order to achieve the required deflection on the fully sealed TE deflection, the TE-LSS integration mechanism has been engineered in a slightly different way by modifying the current one. The trick used to augment the mechanical system effectiveness, by keeping the same torque as operated in the detached TE case, was to redistribute, but not uniformly, the torque across the TE panels. In the previous test the pushrods (red elements in Figure 5-32), departing from the shaft and linked to the LSS device, were equally spaced and distributed from root to tip.

Figure 5-32 Secondary shaft-LSS push-rods distribution for asymmetric case (2).

In case "2", with the rearranged configuration shown on the right hand side illustration of Figure 5-32, it can be noticed that some of the pushrods on the LSS

stringers are missing. In this way the actuator force redistributes and concentrates its effect only on a portion of the shaft. The top area of the TE is also far away from the restraining sealed gap and therefore much freer to bend the TE panels. Although no direct force applies to the bottom part of the TE, it will be dragged to deform by the rest of the section. The displacements results of this type of TE activation are shown in Figure 5-33.

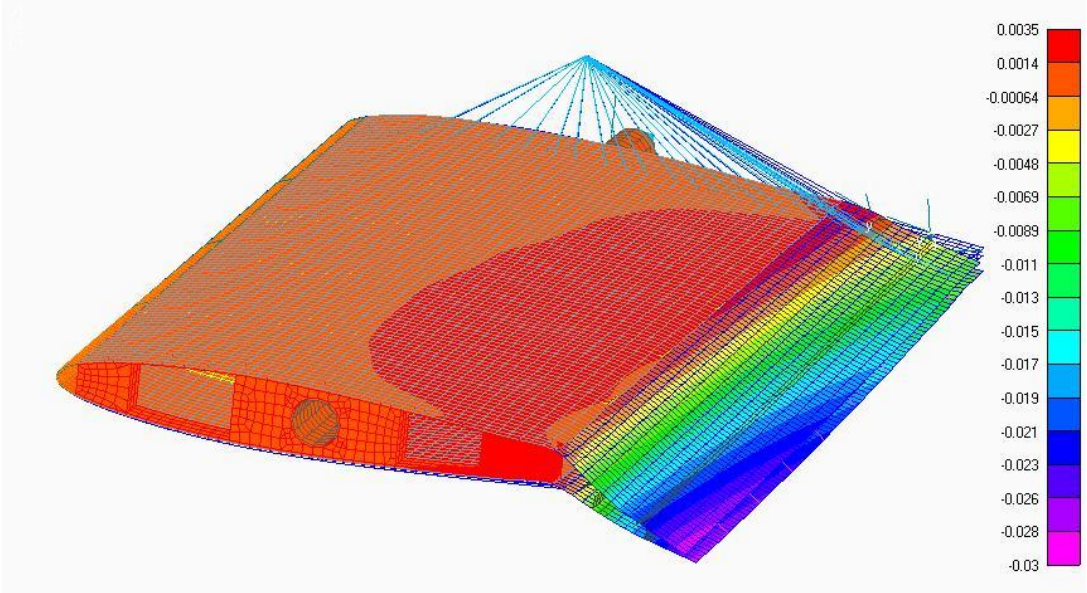

Figure 5-33 Maximum TE displacement for FR variant.

The final 21° camber deflection can be achieved by operating the morphing device with a total pushrods-force of 160N per side. That translates into a total torque of 2.88Nm. This value of torque perfectly suits the range of the Hitec HS-7950TH servo performance. Also in this case of maximum deflection with sealed TE root, the stress level does not present any warning conditions for the structural design. The stresses have risen to a maximum of 96MPa, i.e. still below the allowable values of the used materials. Figure 5-34 plots the FE model results for the stress in the 0° or equally x-direction of the laminate (i.e. the most loaded fibre direction), which coincide with the vertical axis of the fin.

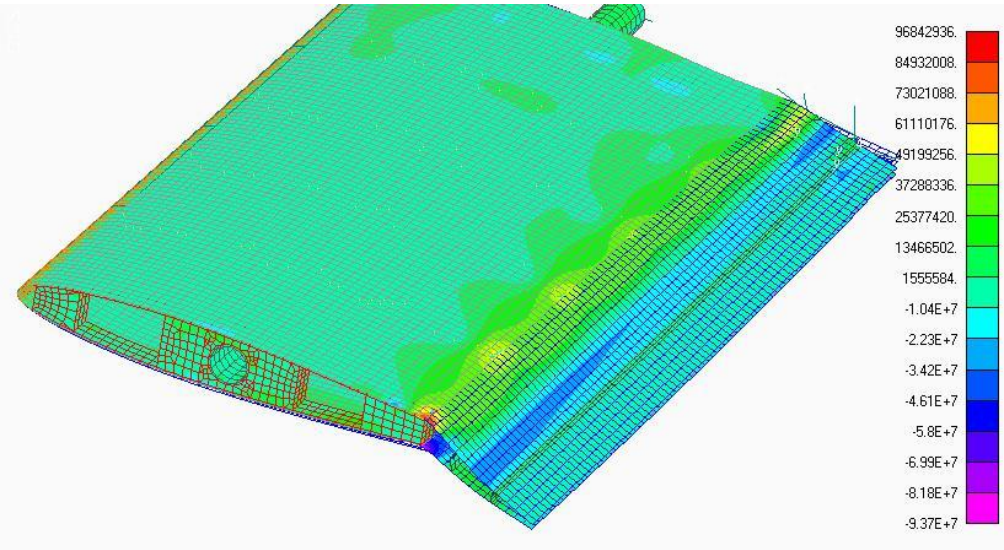

Figure 5-34 Stress results for 21° TE deflection.

WP10: The 21° of TE camber deflection may be achieved with an actuator able to provide a torque of at least 2.88Nm.

At this point of the analysis, the concept has proved that the actuator torque is powerful enough to activate the TE deflection by exploiting the combination of LSS and swivel edge closure devices. It can camber the GRAF TE while withstanding the external load pressure to simulate the rudder 20° deflection. The preceding results have referred to the TE panels activated only by one row of LSS stringers. However, the final TE curvature thought to be achieved with one set of LSS and with the mutual interaction of the deformations coming from both sides of the TE section was not totally accomplished. Therefore the solution of installing another LSS stringer on each panel near the trailing edge was proposed. The second row of stringers helps the forces to redistribute the bending moments on the TE panels. The same total force applied in the previous tests is now split into two set of pushrods. 60% of the force is going to the second row of stringers, while 40% is activating the first row. The reason for that is because the effect of the second LSS is influencing the final shape of the TE more than the first one. Consequently, the deformation induced by the second stringer will automatically drag the rest of the panel up or down.

The pushrods are x-crossing each other inside the TE section. This technique allows the system to transfer to the LSS elements not only a horizontal force component but also a more effective vertical one, as explained in Chapter 3.

The expected *smooth* curvature is clearly more evident in Figure 5-35 with two activated LSS, rather than the parallel case run without the second row of stringers.

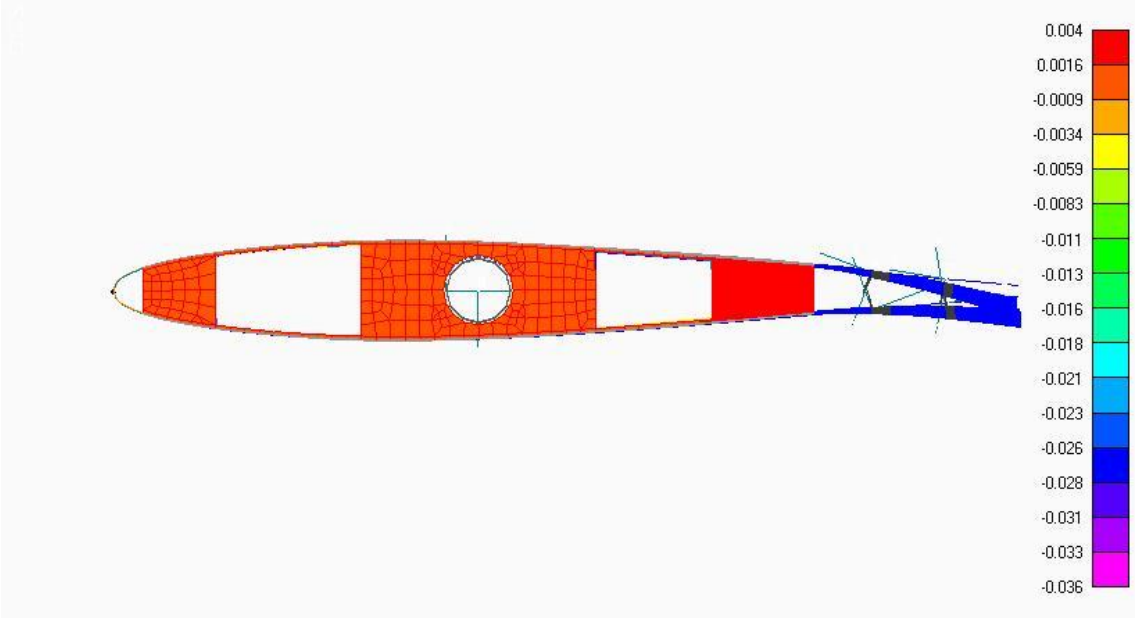

Figure 5-35 TE shape deforming according the smooth configuration.

The effectiveness of the second set of the LSS device in generating the *smooth* shape is beneficially changed with the introduction of the second line of active LSS. As shown in Figure 5-35, the application of the second LSS on each side can theoretically increase the TE deflection up to 36mm. In practice, the linkages and the room available inside the TE section might not allow the system to achieve such a large deflection of the surface. The reason is because there is not enough space inside the TE section to allow larger movements of the rigid push-rods while deflecting.

WP11: The fin can achieve the required maximum deflection to guarantee enough control authority of the aircraft. Whether the seamless cambered smooth shape can be achieved is just a matter of properly distributing the linear forces to optimise the curving bending moments distribution.

The drawings illustrated in the figures below show the technical limitation of the pushrods-LSS system in accomplishing very large deflections, i.e. up to 60°. The main reason resides in the kinematics characterising the motion of the two rods. Two

configurations are shown relating to the scheme used to connect the pushrods. Figure 5-36 shows the type of linkages with the rods x-crossing each other.

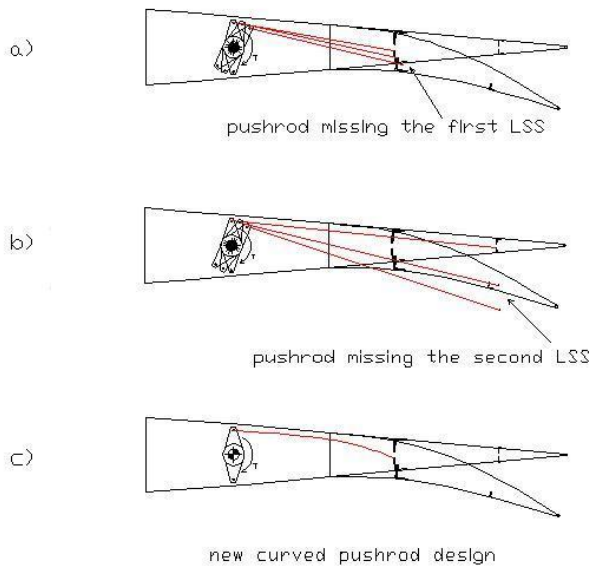

Figure 5-36 Cross linking push-rods design.

This system is the most effective in bending the TE, but it has a limitation due to the rigid length of the pushrod itself. The actuator arm cannot fully rotate and complete its maximum sweeping angle as the pushrod will break through the other component parts. The same situation happens for both stringers as shown in Figure 5-36(b). Thus the only option is to limit the rotation to a more modest TE deflection. The 21° deformation is achieved by adopting the pushrod configuration of Figure 5-36(c). It is still a rigid element but with a slightly curved shape to better follow the TE during bending. Similar issues are met with the second option of the pushrods connection.
Also in this case, the CAD drawing of Figure 5-37 illustrates the rigid push-rods can not go beyond a certain angle of deflection. Moreover, this configuration is also less effective than the previous one. The reason is because having the rods parallel and aligned with the airfoil chord excludes the possibility of engaging the LSS stringer with a vertical component of the actuator force. With this layout, only the horizontal component of the linear force is transferred to the stringers.

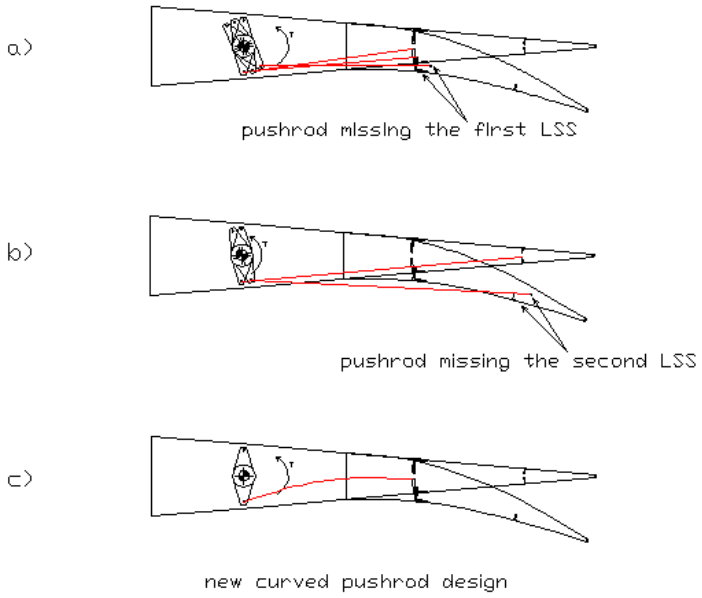

Figure 5-37 Parallel linking push-rods design.

WP12: The pushrods-LSS camber system can theoretically perform up to large angles of deflection whether an appropriate and more articulated pushrod design is studied and provided. Otherwise the kinematics limitation, dictated by the internal geometry and configuration of the current layout, can, in practice, only guarantee the 21° deflection as the maximum angle achievable for its TE camber.

As shown by the figures presented in this section, the stress levels due to the operational cases of the TE cambering deformation are not concerning the structural strength at this level of functionality. There are only a few areas corresponding to the rear corner parts of the ribs which, by pressing on the panels, may raise the stress level on the skin during deformation. However, the highest value of the laminate stresses has been recorded well below the allowable stress of the materials (see Table 7 for the E-glass properties). The main reason why the GRAF structure does not reach very high levels of stress is hidden inside the two most important technical novelties introduced in the design – the slot connection and swivel edge closure. The former reduces the warping and shear stress level during twist operations. The latter, instead, allows the two edges of the TE panels to release any tension and compression stress caused by the morphing deformation.

WP13: the integration of the two novelties – the swivel edge device and the slot connection joint – into the MTF4 empennage allows the structure to reduce the stress level on the fin components and increase the twist and camber angles due to the enhanced warping and bending freedom.

5.3.3 Structural analysis of the primary shaft

The analysis results of the investigation conducted on the primary shaft of the GRAF model are presented here. The load distribution related to the worst case scenario has been applied for the structural analysis of the fin primary shaft. The load distribution has already been presented in aerodynamic Section 3.1.1. The load on the shaft, as in the rest of the components analysis, has been applied with a safety factor of 1.5.

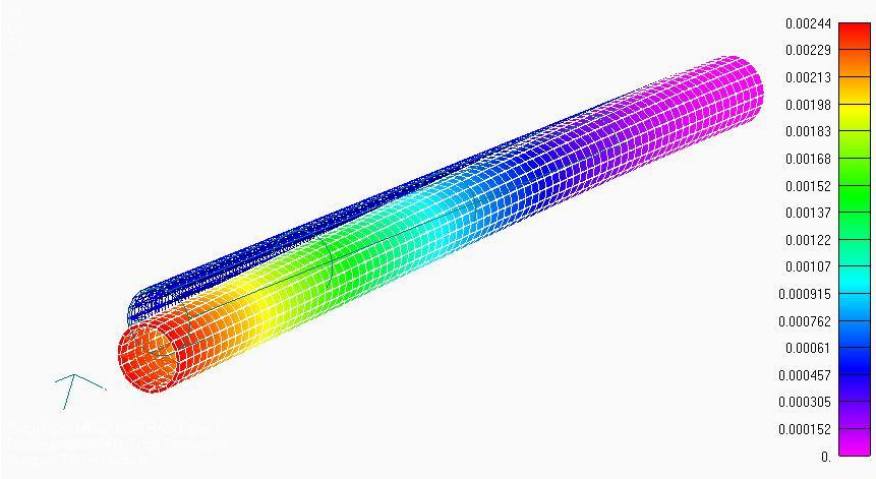

Figure 5-38 Primary shaft vertical displacement under maximum loading.

Figure 5-38 shows that with a distributed load of 332N/m, the maximum deflection of the top end of the shaft is only 2.5mm. While the maximum tensile stress generated by the bending action of the side loads, and recorded along the 0° direction, achieves the value of 106MPa where the shaft meets the bearing clamp,

Figure 5-39 shows the stress level on the part. The 0° fibres and x-direction are aligned with the longitudinal axis of the composite tube.

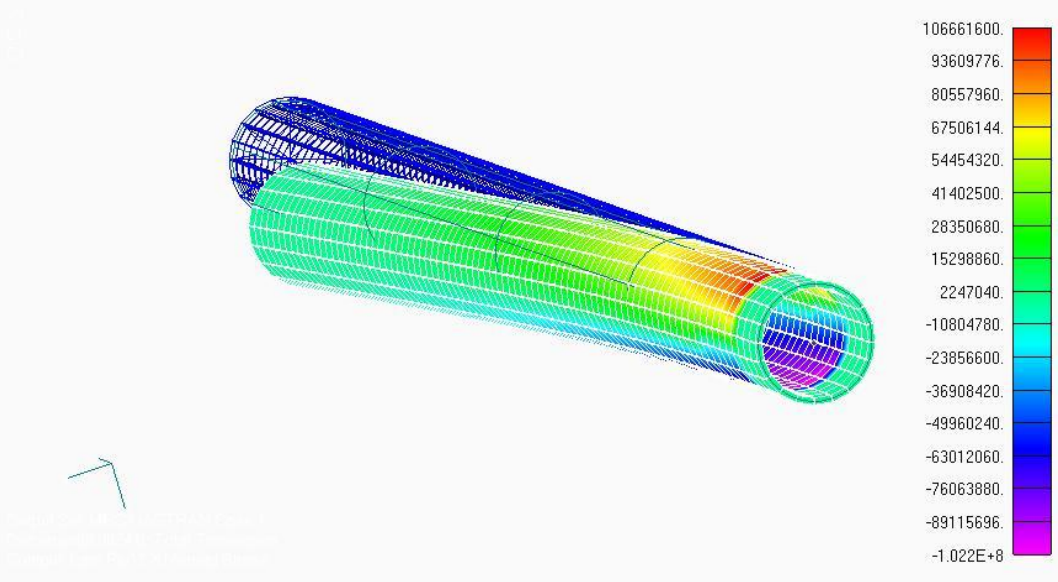

Figure 5-39 Axial stress along 0° fibre direction for worst loading case.

This study did not work out the requirements for the clamp-bearing support needed to hold the main shaft inside the fuselage.

WP14: The extent of lateral displacements produced by the worst loading case scenario reaches only 2.5mm of bending displacements at the tip of the fin.

5.3.4 Twist effect and slot-connection performance results

This paragraph is entirely dedicated to presenting the twist deformations results obtained from the analysis of the warping effect induced on the GRAF design. Two different cases are discussed here. Case-1 presents the MTF4 model with all gaps sealed at the root section of the fin, included the TE root. This configuration reflects

the original design specifications stated in the aim of the research in Chapter 1. Case-2, instead, displays the same sealed gaps configuration as Case-1 with the added option of having only the TE root unsealed and detached from the fuselage joint. Figure 5-40 shows the Case-1 twist deformations obtained using the lowest torque available from the actuation system. The application of a linear force of 145N on each of two control horns at the bottom of the shaft, generates the total twist angle, mesaured at the fin tip of 9.98°. That twist angle corresponds to a lateral displacement of the master rib nose equal to 0.022m. The final torque applied onto the model is 8.7Nm, sufficient to guarantee the required 10° angle.

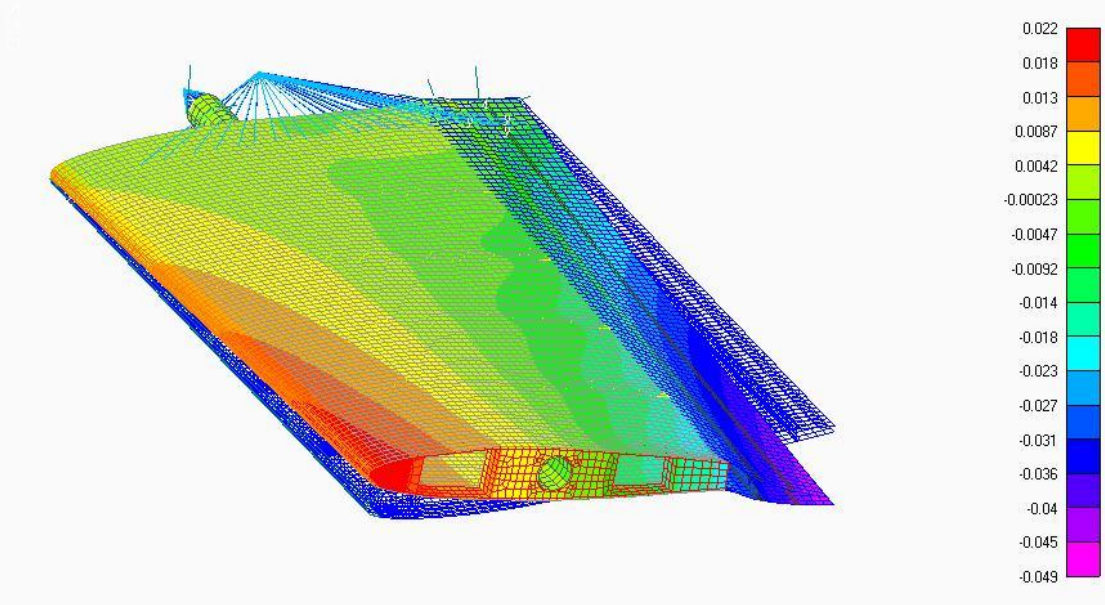

Figure 5-40 MTF4 empennage lateral displacements (twist) with FR TE variant.

The FEA results from Case-2 shown in Figure 5-41, indicate a maximum nose deflection of 0.024m, i.e. almost 11° of twist, achieved by applying the same torque as Case-1, but with unsealed TE root. The reason for the 10% twist angle increase is due to the greater flexibility acquired by separating the root chord of the TE section from the rest of the fuselage connection.

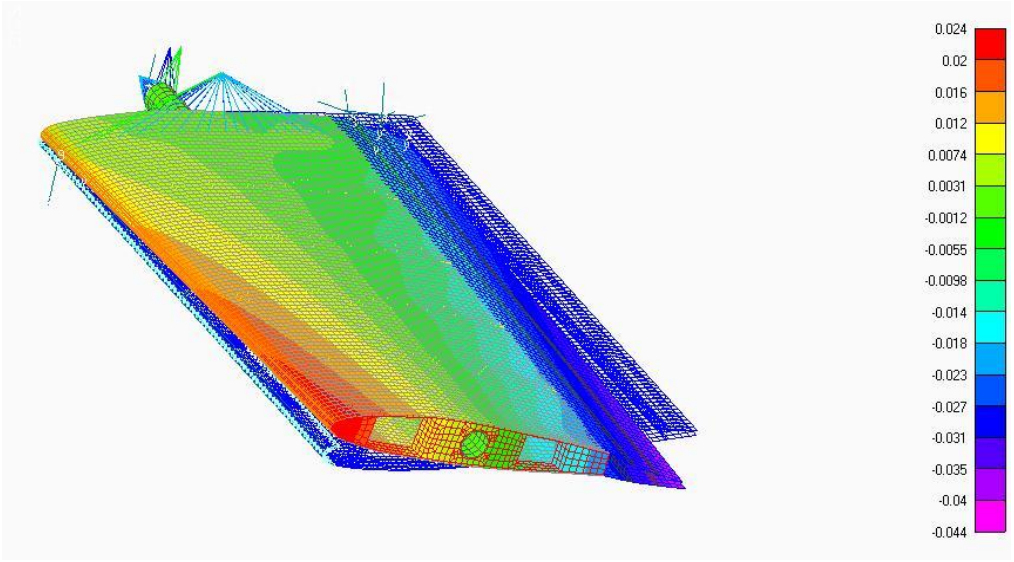

Figure 5-41 MTF4 empennage lateral displacements (twist) with DR TE variant.

The following figures will show the stress level reached by the GRAF structure and its components during twist deformations.

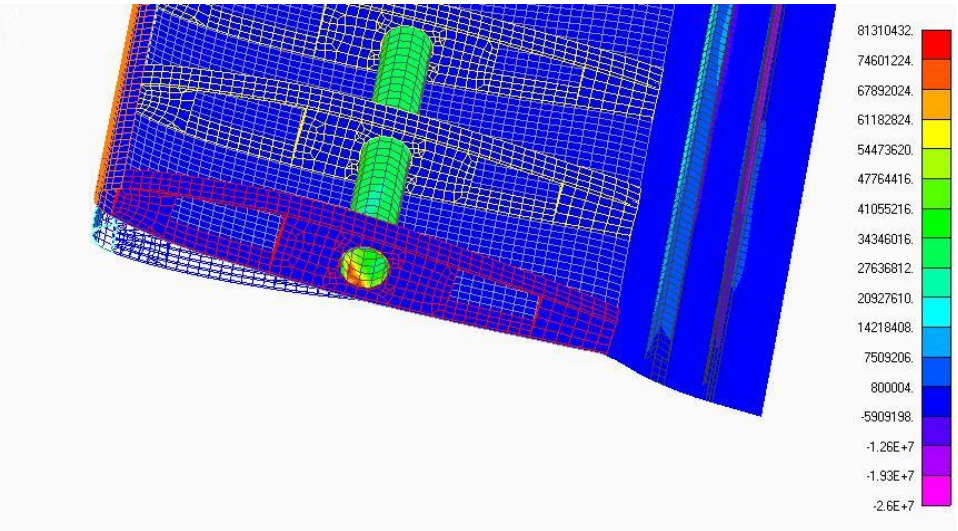

Figure 5-42 Stress concentration on shaft-master rib connection.

In detail, the Figure 5-42 shows the stress level on the shaft element which reaches the maximum value of 81MPa. This refers to the stresses along the 0° direction of the carbon fibres aligned, for this component, with the longitudinal axis of the shaft. As can be noted from the coloured contour plot of the FE model presented in Figure 5-42 and 5-43, the stress concentration is localised in the area where the master rib rigidly connects to the shaft. The top rib is the only one not allowed to freely rotate

around the shaft. The shaft-rib connection is the point where the actuator force and the aeroelastic effect jointly force the GRAF assembly to twist.

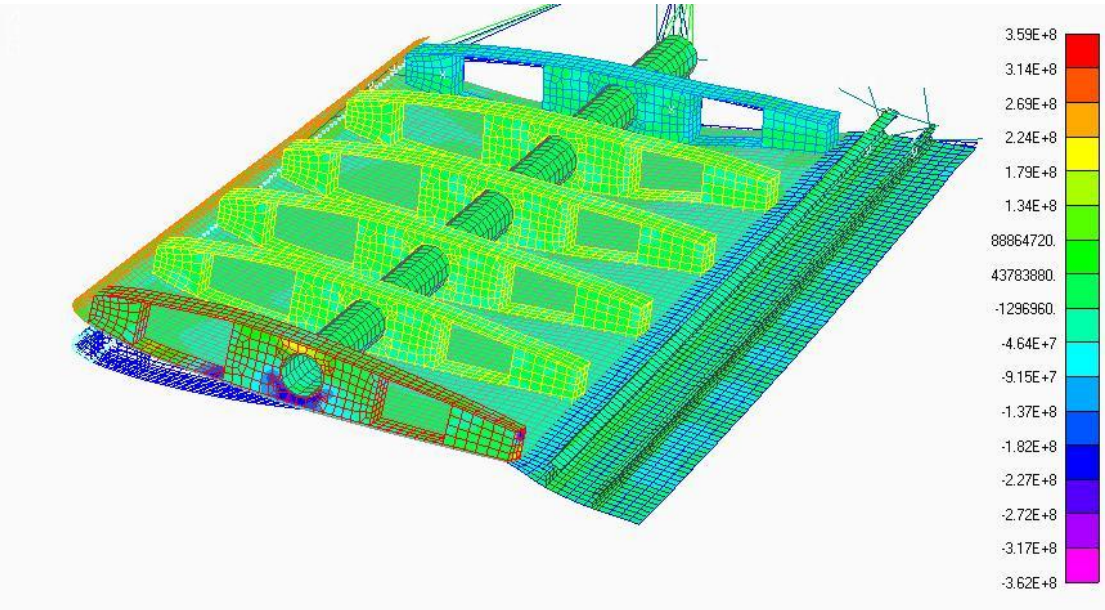

Figure 5-43 Other critical areas on ply-1 of the top rib section.

As discussed in Chapter 3 each rib section has four layers of carbon fibres. The Figure 5-43 shows the highest stress occurring in ply-1 on the master rib near the shaft connection. Those elements of the rib-joint laminate reached a tensile stress of 359MPa in the 0° fibres direction. In the rib elements, the 0° fibres orientation is parallel to the rib chord line.

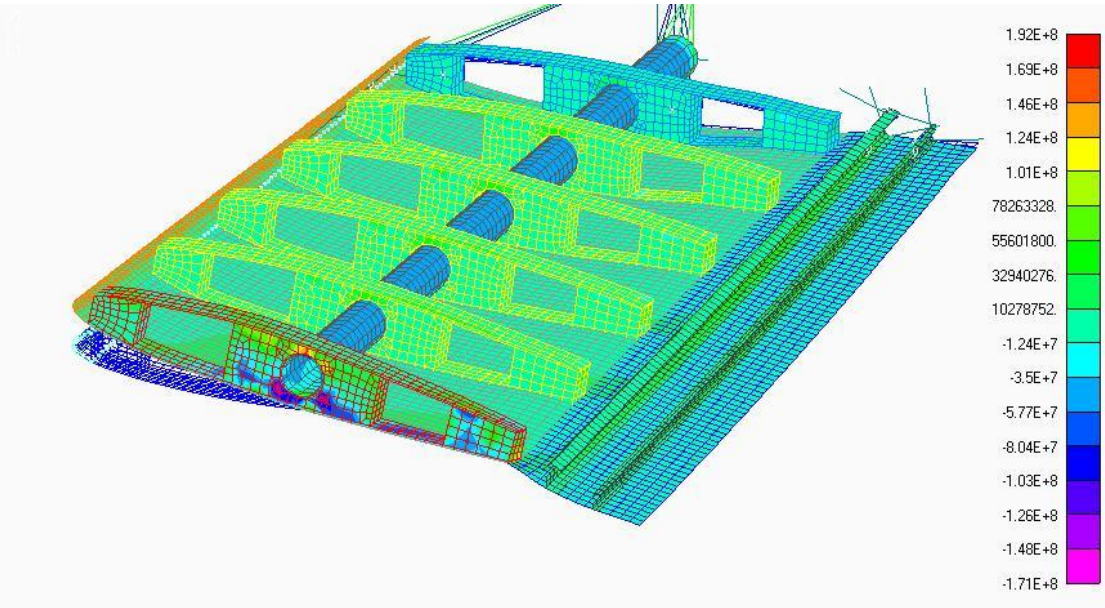

Figure 5-44 Stress results for ply-2.

Figures 5-44, 5-45 and 5-46, instead, show the 0° direction stress level on ply-2, ply-3 and ply-4. The results showed the 0° direction fibres due to be the most loaded fibres of the composite parts.

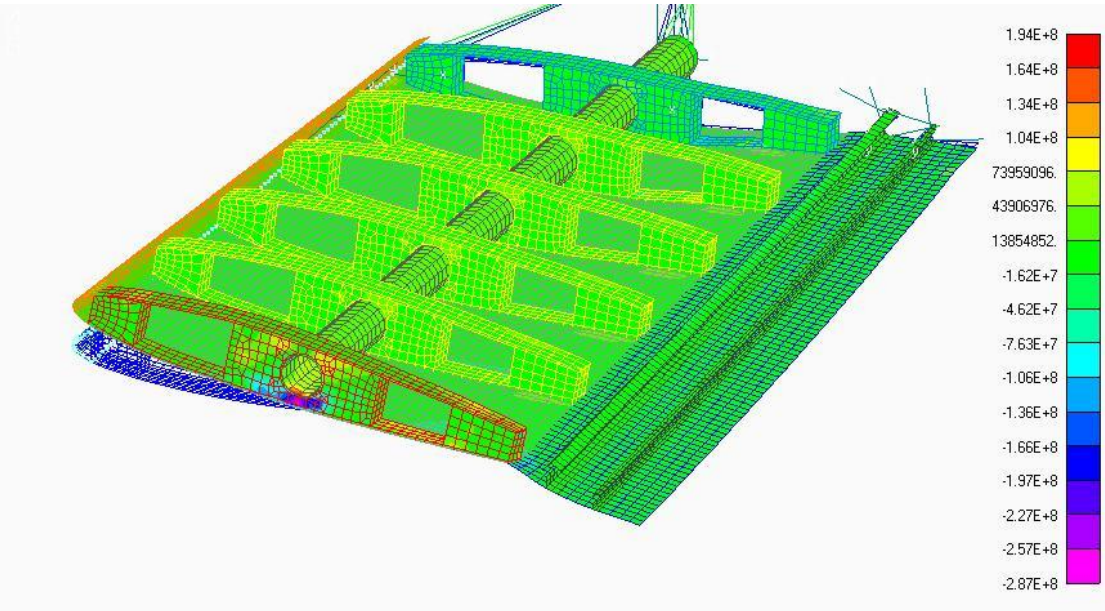

Figure 5-45 Stress results for ply-3.

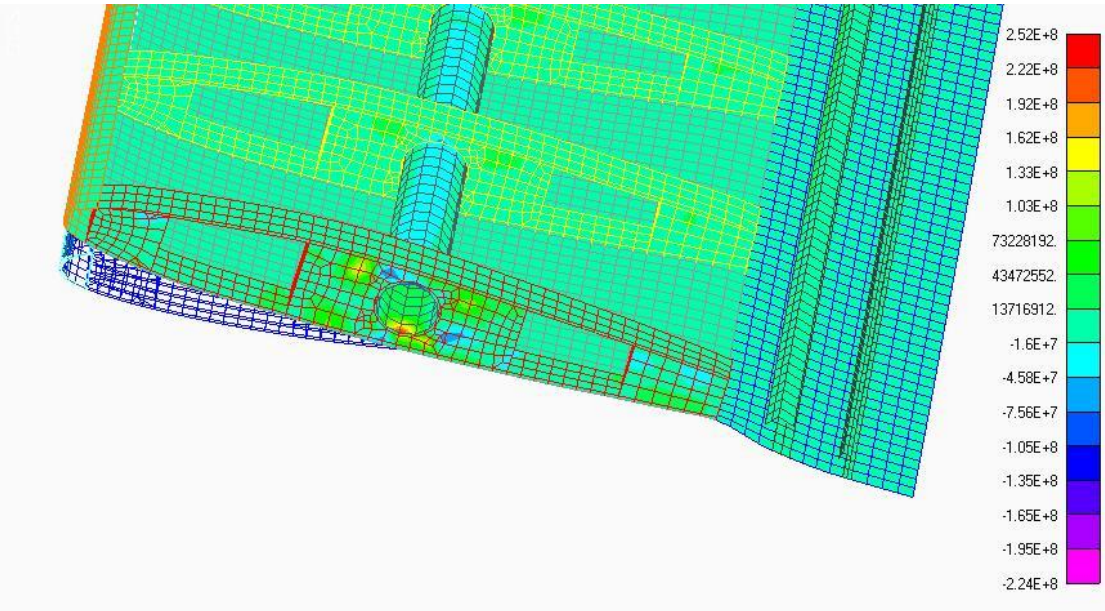

Figure 5-46 Stress results for ply-4.

WP15: The required twist angle is achieved by applying a linear force of 145N on each control horn at the base of the primary shaft. When the TE is not directly in contact with the fuselage joint, the fin can increase its twist angle by 10%. The stress

level has been higher in the shaft-master rib connection but without reaching warning levels.

The application of the slot-connection novelty into the GRAF design has considerably contributed to achieve the final twist angle of 9.98° . Two versions of the GRAF, *i.e.* with restrained and unrestrained root layouts, are discussed here comparing the different results obtained about twist displacements and stresses. The first model, shown in Figure 5-47, represents the GRAF design with the root section rigidly attached at the base of the fuselage connection. It replicates the current fin-fuselage constraint on the Eclipse vehicle used for the conventional fin-rudder tail. Given this type of attachment, the vertical tail cannot perform the necessary twist deformation for control and stability tasks unless a massive torque is deployed to force the structure to warp.

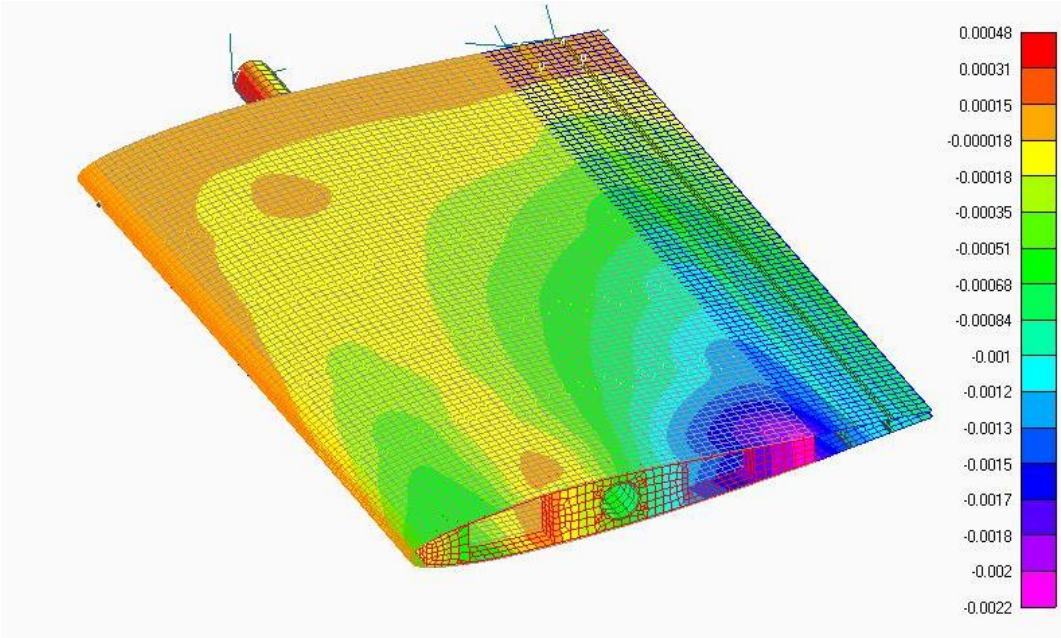

Figure 5-47 MTF4 lateral displacements with the root section entirely fixed to the fuselage.

As it can be seen from the legend on the right side of Figure 5-47, the empennage nose is displacing less than 1.0mm. That translates into a microscopic twist angle of around 0.2°. The very simple yet innovative design of the slot-connection made possible to increase that angle for the whole GRAF. The slot-concept provided a smart and simple solution to extend the deformations, required to guarantee the

GRAF control and stability performance, beyond that limited value of 0.2°. Figure 5-48, shows the displacement of the fin with the slot connection *in situ*.

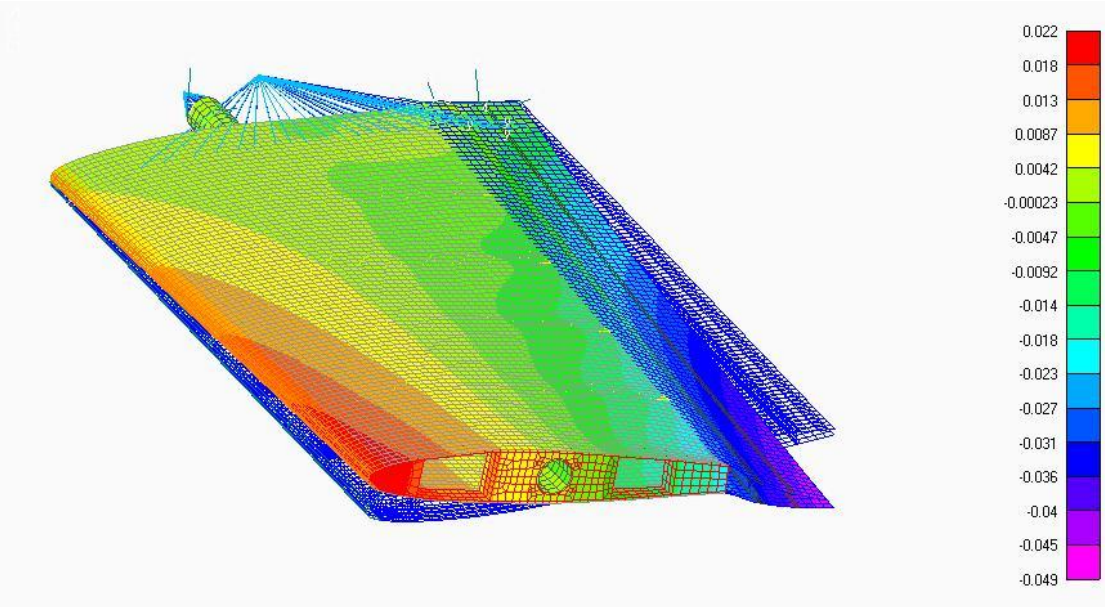

Figure 5-48 MTF4 lateral displacements (twist) with slot-connection joint.

This novel joint system allowed the design to generate twist angle as much as 50 times larger than a rigidly attached root structure by applying to both cases the same 8.7 Nm torque. The slot is physically surrounding the root of the fin but it is not rigidly constraining it. The absence of any restraint allows the structure to further release the longitudinal deformation of the skin thus considerably lowering the stresses over it, and increasing the twist angle.

WP16: The original introduction of the slot-connection allows the vertical empennage to obtain 10° of twist with the same actuator power that would generate only 0.2° of twist if the fin root was rigidly attached to the aircraft fuselage.

5.3.5 Further notes on deformations, material strength and components

Although the area of greatest concern for stress levels has been regarding the shaft-master rib connection, there are other areas of the fin structure that needed to be reinforced.

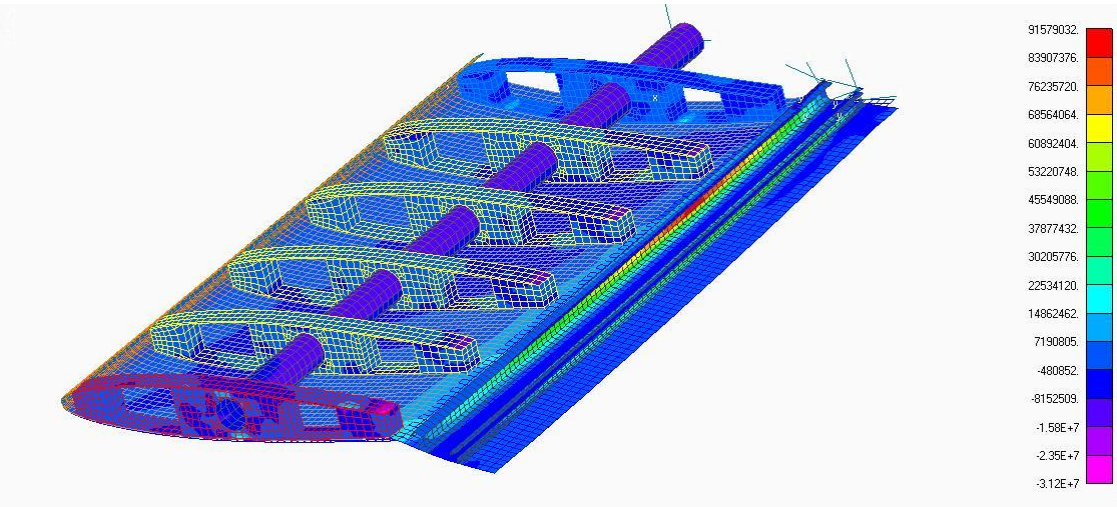

Figure 5-49 Stress area located on the LSS stringers.

The empennage displayed in Figure 5-49 shows the stress results on the carbon fibre ribs and LSS stringers. The level of 91MPa highlighted by the red elements on the FEM model does not represent a highly critical area for the LSS elements themselves. However, it gives some important information about the fact that more likely that specific area is undergoing a considerable amount of coupled distortion due to the combination of camber and twist deformation. Therefore, it might represent a very critical area of structural failure whether both deformations are increased. Further information collected from the FE analysis show the Hoffman failure indexes (FI) related to the plies' fibres. Figure 5-50 shows the FI of ply-1 on the master rib before modification. The original number of four layers applied on the master-rib was not sufficient to withstand the torsion load as the index reached a value of 1.46, well above the unit limit. In order to bring down the FI to a safer condition below 1.0, it was necessary to add two more layers of carbon fibre to the top rib section. Figure 5-51 shows the results of the modified rib. The level of stress on ply-1 is reduced to 310MPa rather than the initial 359MPa.

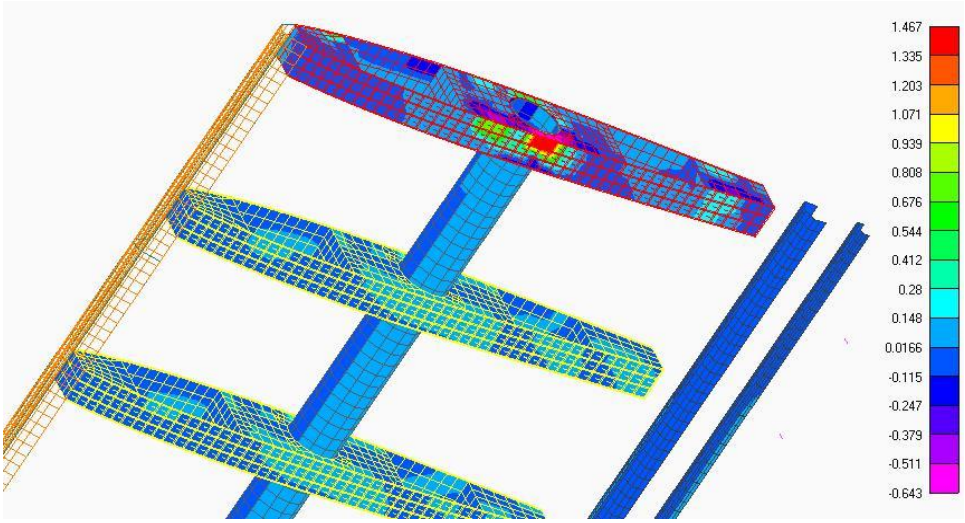

Figure 5-50 Critical failure index detected on the master rib-shaft joint.

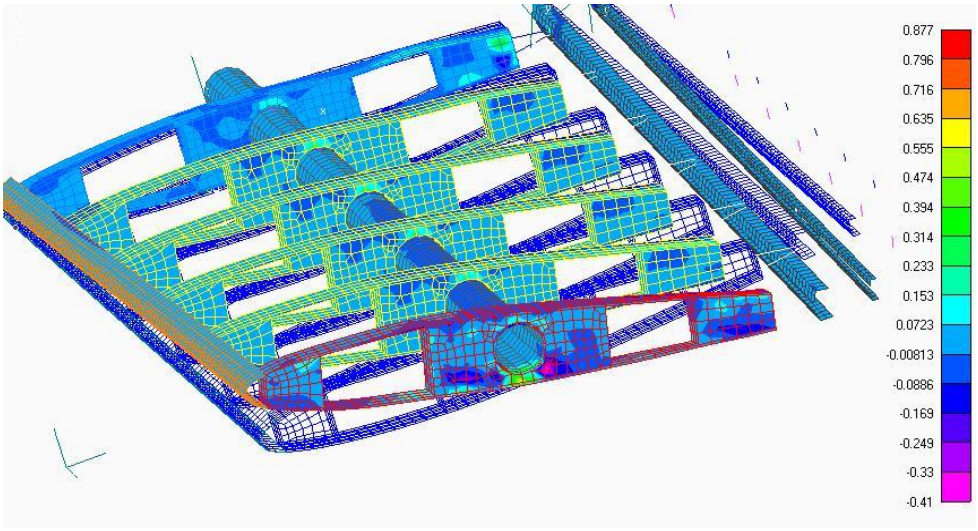

Figure 5-51 Failure index in the master –rib shaft joint with increased thickness.

Table 12 summarises the final weight of the MTF4 empennage structure. The weight of each key element constituting the GRAF assembly is listed below.

Table 12 - MTF4 empennage components weight

GRAF MT4 fin	Master Rib	Central Ribs	Primary Shaft	Secondary shaft	LSS	Swivel edge	Leading edge	Skin	Roller bearings	Ancillaries
Material	Carbon	Carbon	Carbon	Carbon	Carbon	E-glass	Latex	E-glass	Steel	various
Weight	26 gr	16gr	80 gr	25gr	30 gr	20 gr	20 gr	106	8 gr	30 gr
Quantity	x1	x5	x1	x1	x1	x1	x1	x2	x4	x1
Total components weight	26 gr	80 gr	80 gr	25gr	30 gr	20 gr	20 gr	212 gr	32 gr	30 gr

Total structural weight from FEA: 0.555kg	Eclipse Fin weight (w/o actuator): 0.61kg	Saved weight: 10%

As described in the table, the final weight of the GRAF design from the FE model computation was 0.55kg, while the current Eclipse vertical tail weighs 0.61kg. Both weights are considered without actuators. The saved weight of the novel design with respect to the conventional version is 55gr, which is equal to 10% of the total fin weight.

WP17: The empennage strength is successfully verified throughout the Hoffman criterion. The GRAF final weight is 10% lighter than the original Eclipse fin.

5.4 Flight Mechanic Performance Evaluation

Once the design requirements, from the torsion angle, deflection, strength and stiffness standpoints, are satisfied by the FE models of the GRAF MTF4 assembly, the effectiveness results of the flight dynamics of the novel empennage are presented here. The current design has demonstrated that the minimum torque produced by the primary shaft actuator can guarantee sufficient control to activate the fin twist. The area shaded in light blue in Figure 5-52 shows the contribution to the twisting moment on the tail, generated by the aeroelastic effect of the GRAF, varying with the flight speeds. The thick blue line indicates the actuator power is always available to manage the fin twist deformations. That value of torque also represents the minimum torque required to achieve the expected twist of 10° when only mechanical actuators are operated. As explained in Chapters 3 and 4, the twist, after being initiated by the actuation mechanism, can be continued by the aeroelastic effect induced by the aerodynamic forces. Thereby, during deformation the required 8.7Nm torque can initially be produced by the servo actuation and consequently integrated by the torque due to the aerodynamic effect, thus reducing the power consumption for the actuation.

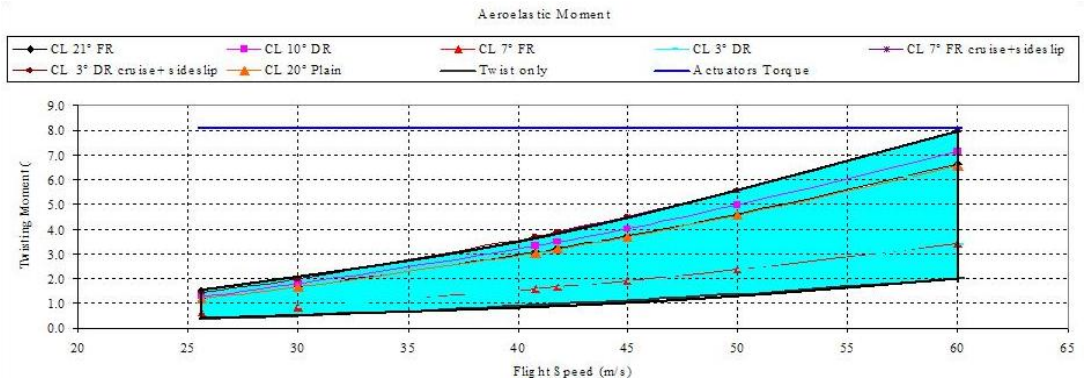

Figure 5-52 Contribution of the aeroelastic effect (blue shaded area) to actuation power.

WP18: Actuation power consumption reduced according to aerodynamic 7load and flight speeds.

This section of the results presents the directional control and stability derivatives analysis carried out utilising the NASTRAN model of the GRAF assembly integrated with the purpose-built NASTRAN model of the Eclipse UAV (see Chapter 3) for the flight performance assessment. Two variants of the MTF4 have been tested: the V1 version has three glassfibre layers constituting the skin of the empennage; the V2 model, instead, has used four layers for a stiffer structure of the fin cladding. There are two sets of results for each version. The directional stability and control derivatives varying with the flight speeds are plotted for both V1 and V2 cases in Figure 5-53 and 5-54 respectively. It can be seen the fin version with the fewer number of layers is the one proving to be more effective in both stability and controllability tasks. The stability derivative value is much higher than its parallel rigid version. The GRAF compliant structure is keener to twist under the side wind loads, thus offering a larger portion of the fin surface to the cross wind pressure for side force generation, rather than a rigid, stiffer, less twistable configuration. This warping flexibility is what beneficially increases the fin effectiveness during the weathercock effect performance. For the same reason the control authority of the GRAF empennage is enhanced by its unconventional architecture and operating mode.

WP19: The main case related to the V1 configuration presents an enhanced effectiveness varying with speed for both control and stability performance, doubling both derivatives values at cruise speed when compared to the Eclipse UAV derivatives.

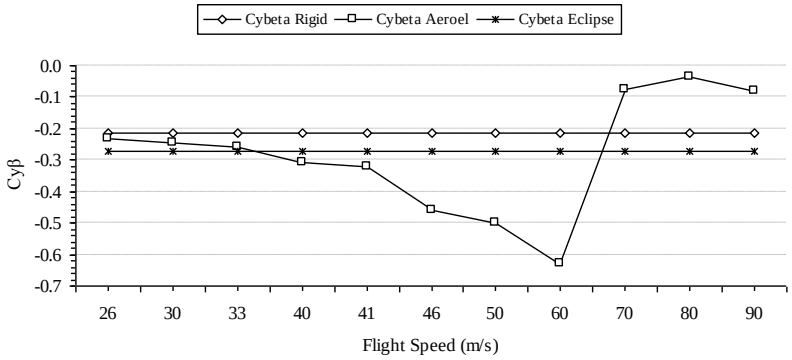

Case V1

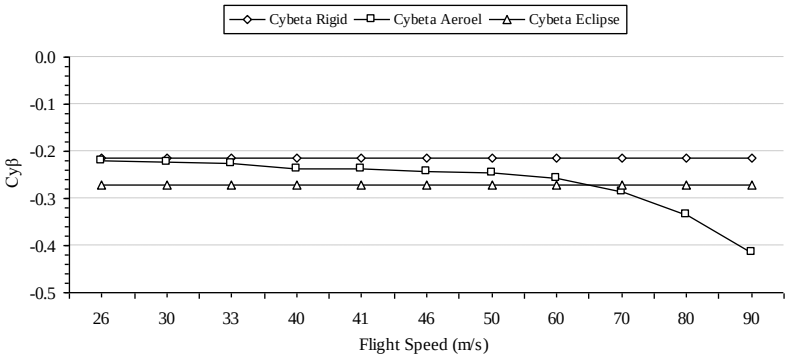

Case V2

Figure 5-53 MTF4 directional controllability derivatives for three (case 1) and four (case 2) layers skin configuration.

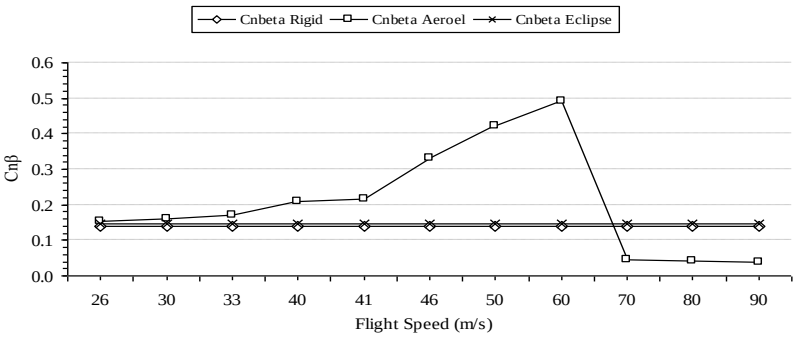

Case V1

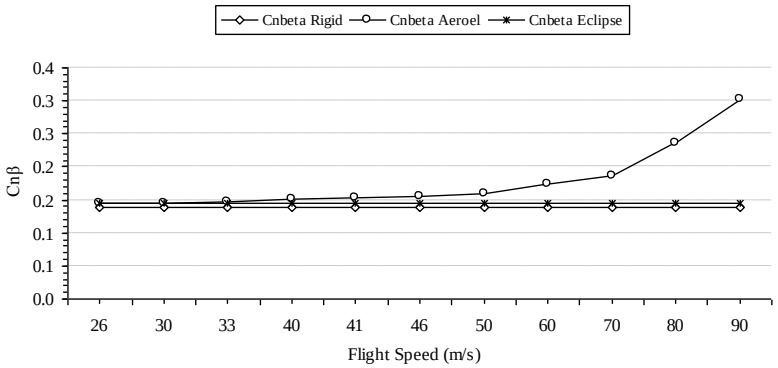

Case V2

Figure 5-54 MTF4 Directional stability derivatives for three (case 1) and four (case 2) layers skin configuration.

Chapter 6 – Aeroelastic & Dynamic Response Analysis results

6.1 Aeroelastic case studies

The sixth chapter of this thesis concludes the section dedicated to presenting the results of the numerical analyses conducted on the MTF4 model. In particular, this part of the thesis will discuss the dynamic aeroelastic instabilities and dynamic response results, computed by using the Flight Loads tool of MSC/NASTRAN. After listing the natural vibration modes of the GRAF structure, the chapter will then present the flutter results analysis and the aeroelastic dynamic response of the GRAF model subjected to sudden loads variation. The dynamic response analysis will investigate the structural model response when a rapid activation of the actuators induces the structure to deform, thus generating the worst load case scenario for the tail. The analysis will also deal with the circumstance of sudden lateral gust loads which affect the structural stability of the model and the vehicle flight dynamic performance. The gust study will close the chapter by presenting the investigation of the fin's quick response to rapid variation of the aircraft directional flight attitude. Table 13 lists the first six natural modes of the GRAF structure:

Table 13 - MTF4 Natural Modes

Natural Modes	Frequency
I	34.2 Hz (Bending Mode)
II	38.9 Hz
III	57 Hz (Torsional Mode)
IV	100.8 Hz
V	117.6 Hz
VI	136.6 Hz

The first bending mode shows a frequency of 34.2Hz, while the first torsional mode occurs at the frequency of 57Hz related to the third eigenvalue extracted by the modal analysis. The first six modes are presented here, and shown in Figure 6-1.

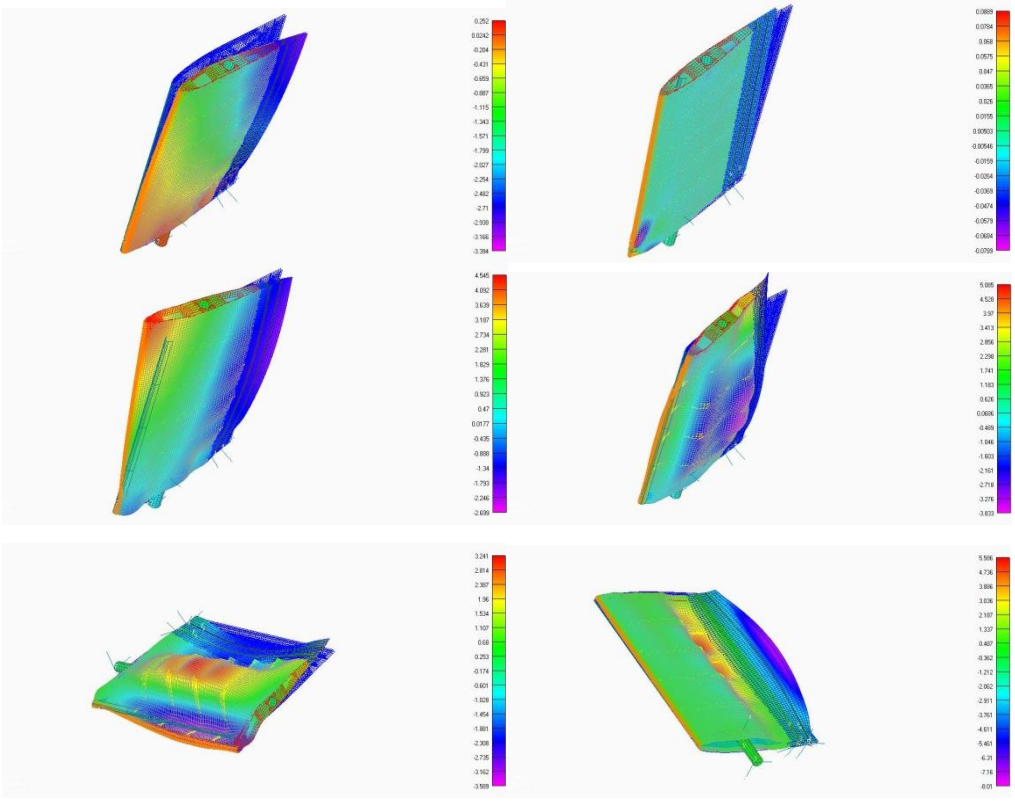

Figure 6-1 First six natural modes: I&II (top), III&IV (middle), V&VI (bottom).

The pre-computation of the natural modes has been used to identify the range of frequency of interest needed for the investigation of the structure's dynamic response. A specified number of modes, i.e. four, within the frequency range of 0-100Hz, have been chosen for the dynamic response analysis.

6.1.1 Divergence and Flutter Analysis

This paragraph presents the results containing the values of the divergence and flutter speeds attained from the static and dynamic aeroelastic analyses respectively. The final results of the divergence speeds obtained from the static aeroelastic model analysis run with the MSC/NASTRAN Flight Loads package are included in Table 14.

Table 14 - MTF4 divergence and flutter speeds

MTF4 fin: Critical Speeds	Units	V1 model	V2 model
Divergence Speed	m/s	74	84
Flutter Speed	m/s	77	87.5
Flutter Frequency	Hz	50.6	48

The results refer to two different versions of the fin with three (V1) and four (V2) layers of glassfibre used to build up the covering skin.

Two models have been scrutinised in the flutter study according to the number of layers applied on the external cladding. The current MTF4 skin is formed by three layers of composite materials oriented as [0/45/90]. The second model, instead, has increased the number of layers to four for a stiffer skin with a quasi-isotropic stack-up sequence $[0/\pm 45/90]$. The results of the p-k method applied for the flutter speeds analysis are plotted in the V-g diagram of Figure 6-2. The MKAERO1 entry, implemented in the NASTRAN aeroelastic code, specifies Mach number m=0.0 for the series of reduced frequencies used for the flutter analysis, set from k=0.001 to k=2.0 in order to cover the frequency range of interest. A constant value of the structural damping coefficient equal to g=0.02 is used throughout the whole range of frequencies. No further investigation on the damping coefficient is carried out at this stage of the research. However, the application of one more layer of glassfibre increases the flutter speed up to 87.5m/s, while the current configuration with three layers reaches a flutter speed of 77m/s.

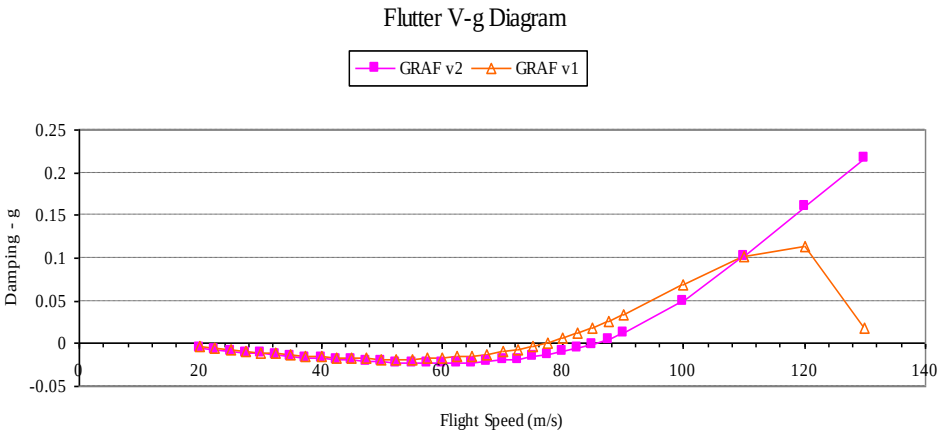

Figure 6-2 V-g diagram for three (v1) and four (v2) layers skin configuration.

Therefore, in case the MTF4 will be applied on an aircraft configuration capable of higher flight speeds (e.g. 90m/s), some changes and modifications to the structure are inevitable in order to make the assembly meet the enhanced performance.
Since the V_d and V_f are about 20% higher than the current Eclipse dive speed of 60m/s, the design requirement for stiffness and aeroelastic stability has been satisfied.

WP20: The analysis has verified that the divergence and flutter speeds for the MTF4 tail have satisfactorily met the structural and aeroelastic requirements of the tail design.

6.1.2 Dynamic Response Analysis

The results discussed in this part of the thesis will be illustrating the structural behaviour of the MTF4 tail under rapidly varying loading actions and gusty environmental conditions. The displacements and the bending moment of crucial nodes of the structure will be shown. Four different sets of analysis are presented:

1. The first group of results illustrates the modal frequency response analysis;
2. The second group is the set referring to the modal transient response analysis;
3. The third section consists of the results attained for a discrete 1-cos gust response analysis;
4. The fourth section discusses the flight dynamic response of the whole aircraft when subjected to rapid changes of heading due to the cyclic application of 1-cos side wind disturbances.

In order to outline and evaluate the fin response in terms of displacements and reaction forces, eight reference nodes have been selected from the structural grid of

the FE model. There are three reference nodes on the leading edge from the bottom rib to the top corner of the vertical tail. These nodes are Node 30000 (bottom rib), Node 30003 (middle rib), and Node 30006 (top rib) located on the leading edge, with other three nodes on the opposite edge of the fin, over the TE section, which are Node 56 (bottom rib), Node 53 (middle rib) and Node 50 (top rib). All the representative nodes are shown in Figure 6-3.

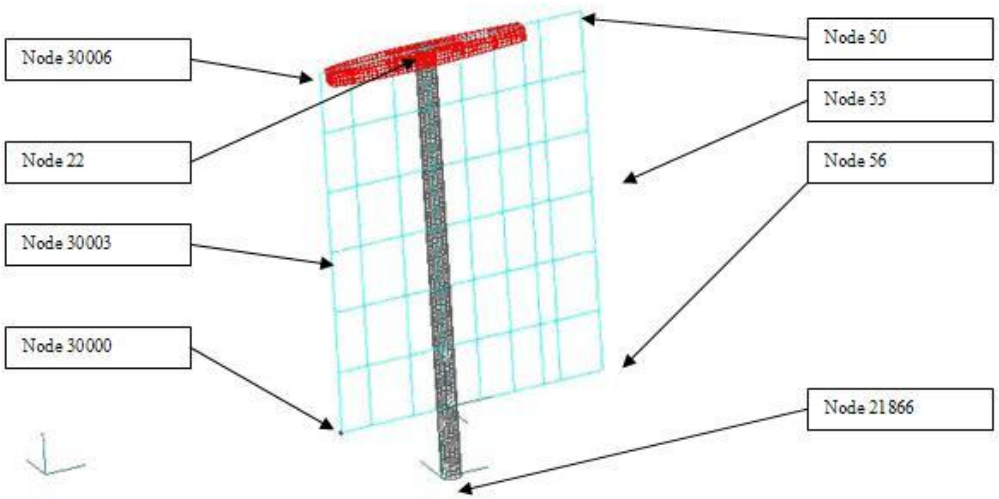

Figure 6-3 MTF4 aerodynamic grid model with reference nodes.

Finally, the last two nodes, used to detect further information about the fin dynamic behaviour, are Node 22 and Node 21866. The former is located on the chord line of the master-rib, at the top section of the main shaft, and centred with the shaft vertical axis. The latter is at the other end of the shaft, located at the bottom of the assembly, where the component is connected to the fuselage mount. This last node will pick up the bending moment of the entire structure during the time varying loadings. The node at the top of the shaft will give an indication of the lateral displacements of the fin. The other six nodes on the LE and TE sections will be used to plot the twisting and the hinge-less TE deformation of the GRAF. Two more nodes are listed in the last diagram of this section. They are the nodes located at the nose and tail of the Eclipse FE model. They are used to plot the yaw motion of the aircraft when upset by any external condition.

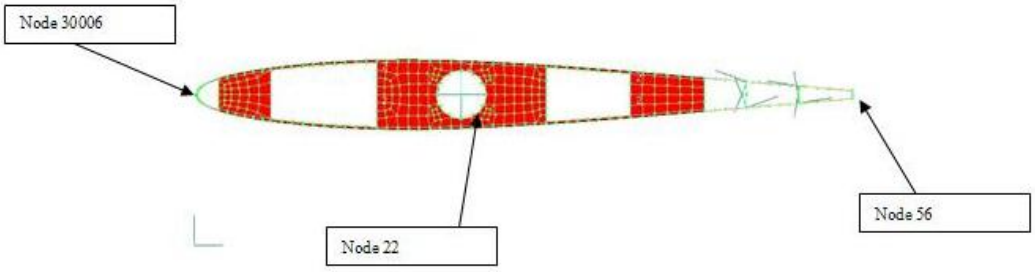

Figure 6-4 Reference nodes on top view fin.

Input data and specifications utilised for the dynamic analysis:

1) Actuation Mechanism:

Digital Servo Hitec HS-7950TH

Servo-mechanism forcing frequency: 5Hz;

2) Modal Response Analysis data:

Frequency Range of interest: 0-100 Hz;

Cut-off frequency: 100Hz;

Number of Modes for Modal Eigenvalue Analysis: 10

TSTEP function for time intervals: 800 intervals from 0.05 sec each;

Period: 4 seconds;

Structural Damping: 0.02

3) Aerodynamics data:

Gust scale factor (angle of attack): 1.0;

Dynamic pressure: $980.0 \frac{kg}{m \cdot s^2}$;

Mach: 0.0 (no compressibility effects are taken in account);

6.1.3 Modal Frequency Response Analysis

The frequency response analysis study investigates the aeroelastic response of the tail when a sudden activation of the actuation mechanism induces on the GRAF model the worst loading case scenario. The load pressure distribution is input into the FE model as a dynamic load following the amplitude factor and frequency variation of diagram, as illustrated in Figure 6-5.

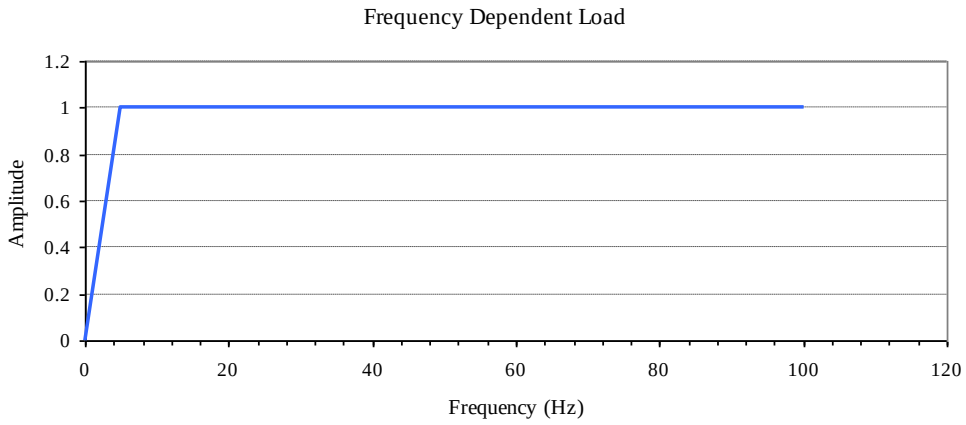

Figure 6-5 Amplitude factor for frequency dependent load.

The loading case scenario established with the aerodynamic analysis follows a frequency-varying linear ramp from 0-5Hz reaching then its maximum unit amplitude for the entire range of frequencies of interest. The analysis has run within the frequency range of 0-100Hz, with equally spaced intervals of 0.25Hz each. The graph below shows the in-frequency domain response of the three nodes selected for the output of this analysis, all located at the tip of the fin structure (i.e. nodes 30006/22/50).

The lateral displacements of the three nodes with varying frequency of dynamic load are shown in Figure 6-6.

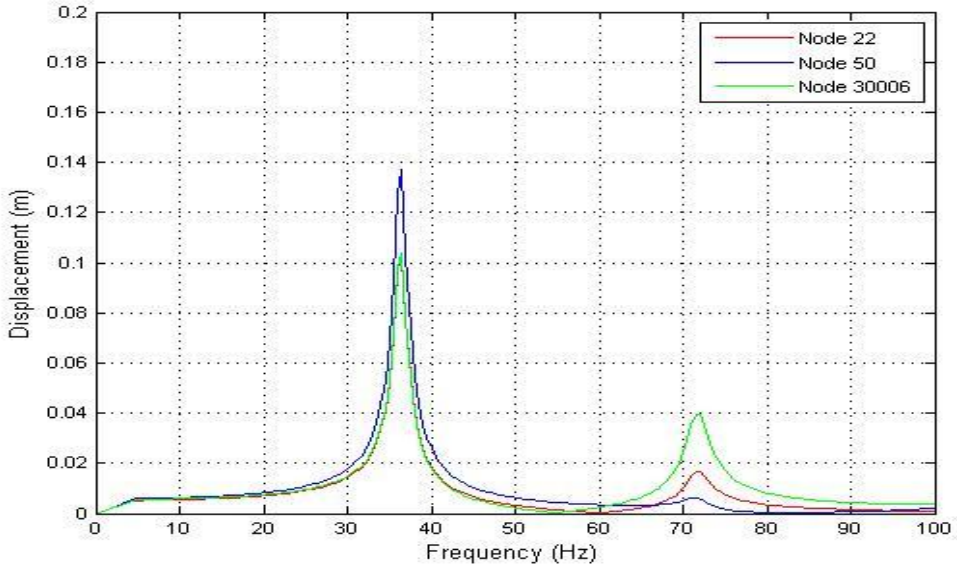

Figure 6-6 Frequency response of the MTF4 model.

All the three nodes are located on the master rib element. Node 22 also represents the centre of the primary shaft. In the range of frequency corresponding to the actuator activation there is a warning level of displacements or exciting frequencies which might induce a revision of the structural configuration of the design. The only two zones concerning high level of displacements are met approaching the first and third modes at the frequency of 37Hz and 73Hz respectively.

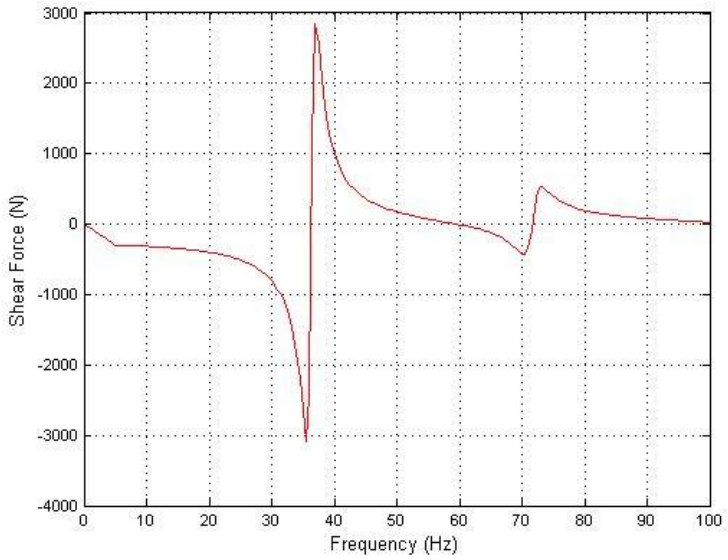

Figure 6-7 Fuselage-fin mount node shear force reaction.

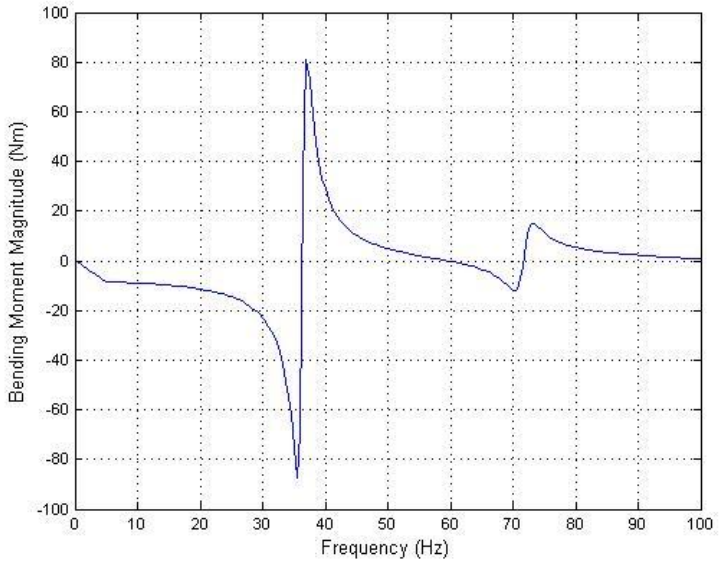

Figure 6-8 Fuselage-fin mount node bending moment reaction.

For the same analysis case, the diagrams in Figs. 6-7 and 6-8 plot the response of the shear force reaction and bending moment retrieved at the root of the primary shaft (i.e. Node 21866). The highest values of the reacting forces on the fin mount occur corresponding to the same resonance frequency shown in the displacement graph.

WP21: From the displacements and forces results it has been seen the GRAF peak response to the frequency dependent load occurs in correspondence of the I and III modes frequencies, in practice, well beyond the frequency range of the twist and camber surface activation.

6.1.4 Modal Transient Aeroelastic Response Analysis

In the modal transient response analysis, the time dependent loading actions follow the variation of the curve presented in Figure 6-9. The red line has a unit magnitude lasting 1sec and starting with a delay of 0.1sec, soon followed by a linear ramp of 0.2sec. The time delay is applied to damp out the residual oscillations from preceding cycles. It describes the same typology of worst loading case scenario presented for the frequency response case, but, this time, it simulates the activation and holding of

the fin twist and camber mechanism for 1sec. The sudden variation of the aerodynamic asset of the structure varies the surrounding external pressure and so the loads generated on the aerodynamic grid of the FE model. The consequent displacements of the whole tail and the support reaction at the fin root are recorded in the outputs file obtained from the NASTRAN Flight Loads tool, shown in Figure 6-10.

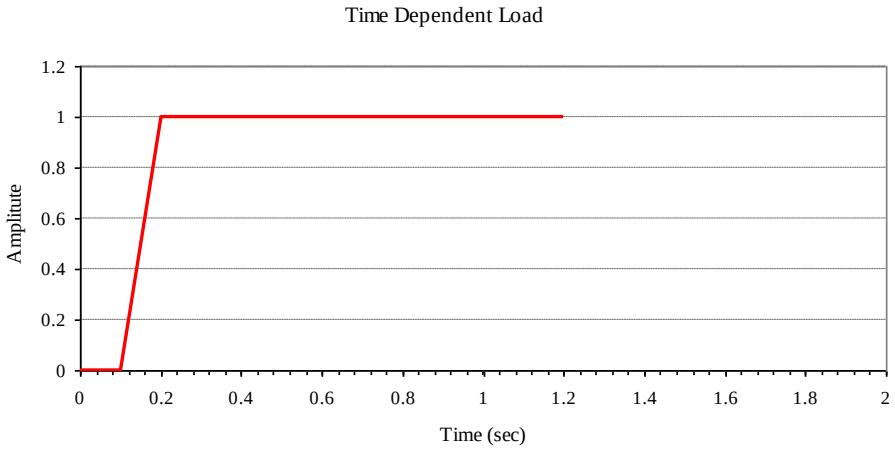

Figure 6-9 Amplitude factor for time dependent load.

The time intervals for the response solutions cover a period of 4 seconds, during which 800 intervals of 0.005sec each are taken into account. Hence, the transient response of the aeroelastic fin model due to a sudden activation of the twist and camber devices is presented in Figure 6-9. The diagram shows how, once the mechanical effect has ceased, the fin restores its original neutral position by rotating all its structural nodes back to 0° angle.

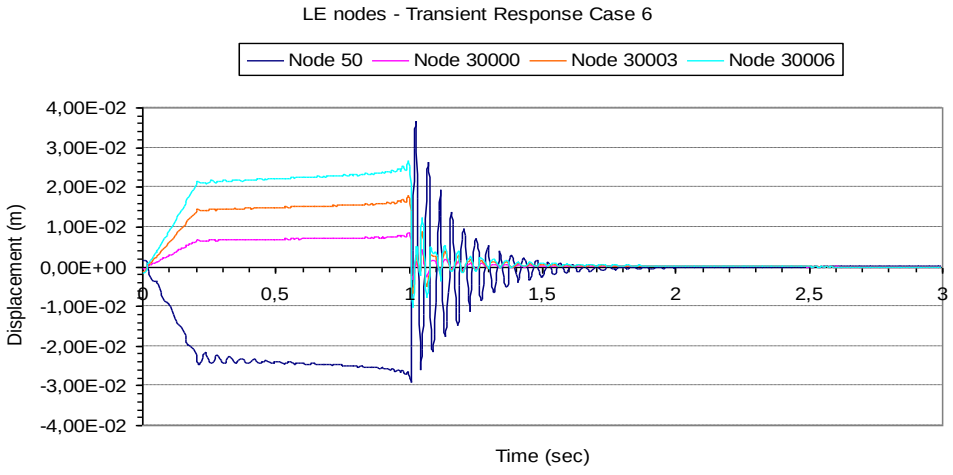

Figure 6-10 MTF4 transient response: LE reference nodes displacements.

The oscillations generated by the structure response are damped out in less than a second. Therefore, no comparison with the current Eclipse hinged rudder fin can be made, and no data about any dynamic aeroelastic analysis conducted on the original Eclipse fin configuration are included in the reference thesis. A small difference in the nodes response can be noted between the two opposite nodes of the master-rib, Node 30006 (LE) and Node 50 (TE). The oscillation of Node 50 is damping out slower than the respective node on the leading edge. The displacements, too, are generating diverse response values. The reasons for that are due to the increased flexibility needed by the TE section for cambering tasks which makes the TE panels more flexible in sudden oscillations compared to the stiffer closed box of the leading edge part. The rapid excitation of the structure generates a considerable bending moment response at the bottom of the primary shaft. Node 21866, representing the joint between the fin and the fuselage mount, shows the bending moment variation in the graph of Figure 6-11.

The bending moment result is in line with the values obtained in the aerodynamic evaluation of the static loading cases in Chapter 5.

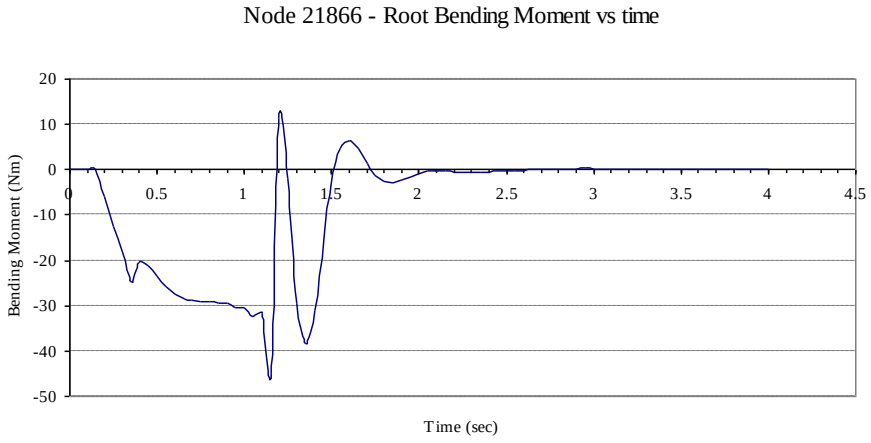

Figure 6-11 MTF4 transient response: root node bending moment.

WP22: The bending moment results of the transient case show values in line with the values obtained in Chapter 5. The aeroelastic fin can successfully recover its original position with 1.5 sec.

6.1.5 Discrete Gust Aeroelastic Response

This section presents the last paragraph of the aeroelastic response analysis, concluding the global overview of the structural design of the GRAF empennage. In particular, this part of the chapter will focus on the fin response investigation when a lateral gust disturbance of the "*1-cos*" type is suddenly met by the flying aircraft. Although, as previously said, currently there are no detailed indications and precise regulations about carrying out such tests on UAV platforms, as explained in Chapter 3, this analysis will refer to the existing issued normative for airworthiness certification such as the CS-23, under the conditions and data listed as follows:

- Derived gust velocity of 15.24m/s (peak side wind);
- Geometric wing reference chord: 1.1m;
- Penetrated distance into the gust: 13.75m;
- Aircraft flight speed 40.8m/s;
- Air density (sea level);

and by considering the gust shape expression from CS-23.333:

$$U = \frac{U_{de}}{2}\left(1 - \cos\frac{2\pi s}{25\bar{c}}\right)$$

then substituting for the value of the mean chord and derived gust velocity, it gives the discrete gust curve expressed as:

$$U = 7.62\left(1 - \cos 0.228s\right)$$

which is plotted in Figure 6-12 on the following page.

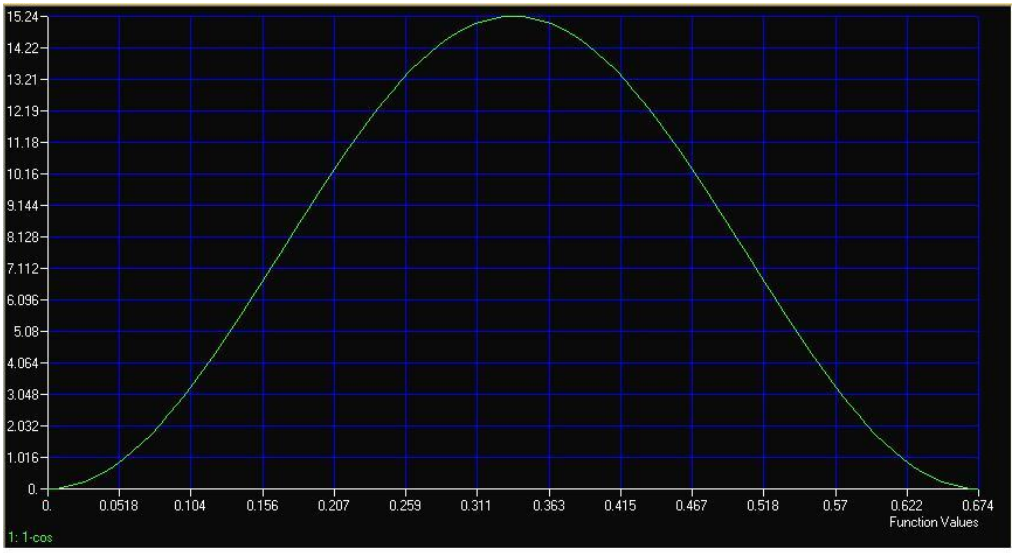

Figure 6-12 MTF4 lateral 1-cos type gust velocity distribution.

The above described gust condition induces the fin and the vehicle, flying at cruise speed, to travel through the gust disturbance for an estimated time of 0.674sec. In that period the aircraft will fly for a number of 12.5 chords into the gust before reaching its peak value. The results related to this circumstance are discussed next.

Displacements of the reference nodes and the shear force and bending moment diagrams are presented here and illustrated in Figure 6-13. The shear force and bending moment outputs of Node 21866 at the bottom end of the shaft are plotted in Figs. 6-14. The discrete gust response study has run two different cases for the restrained and unrestrained configuration. The former deploys the GRAF tail structure held in position, at zero angle of attack, by the actuation mechanism while the gust condition occurs. The latter sees the fin released by the servo mechanism and free to sense the external perturbation and warp the fin shape according to the side wind intensity.

The unexpected gust perturbation causes a rapid bending deflection in both configurations of the fin structure. Node 22, also representing the top extremity of the main shaft, indicates evident displacement on one side of the fin, moving the profiles out of the fin vertical plane of symmetry. The top graph of Figure 6-13 shows all nodes displacing on the same side of the deflection, just barely hinting a twisted shape. This is visible from the leading and trailing edge nodes of the fin

which have different values of displacements thus having an angled position with respect to the aircraft's longitudinal axis.

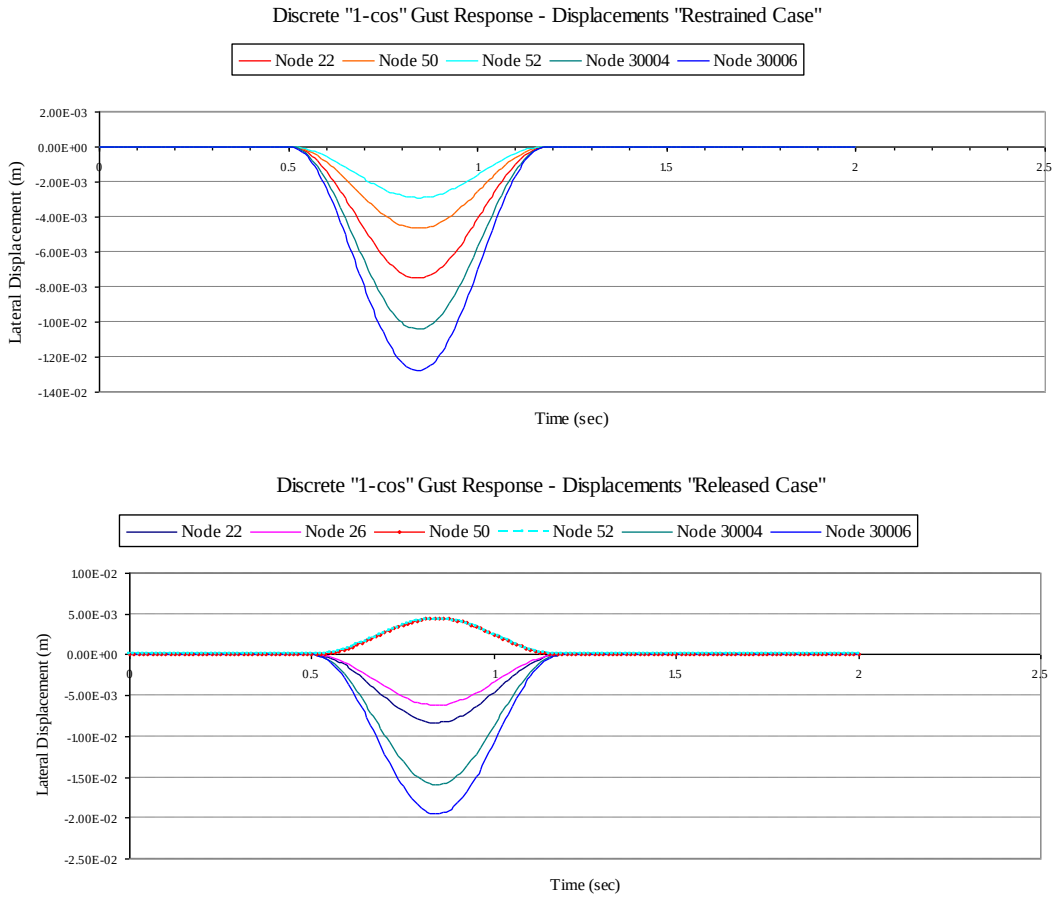

Figure 6-13 MTF4 reference nodes displacements due to gust loads for restrained (top) and free-to-twist (bottom) fin configurations.

The fin tip, in the restrained case, displaces as much as 0.0075m (Node 22) with a twist distortion of 1.41°. The twist angle is computed measuring Node 30006 (on the LE) and Node 50 (TE) and taking as offset displacement the bending deflection identical for the entire fin. The second configuration, with the fin assembly free to twist, presents different results from the preceding one. The overall lateral displacement measured on Node 22 reaches 0.008m, with an increased twist of 4.25°. This is due to the larger deformation on the nodes at the LE and TE of the fin which reach, at the tip section, 0.0192m and -0.005m of lateral displacement respectively (the negative sign indicates the node has moved onto the opposite side of the fin symmetry plane). This test has also shown that although there is a rapid and almost instantaneous excitation of the GRAF structure to such an external disturbance, the

twisting capability of the warping fin can react very responsively and effectively to the lateral gust phenomenon. The diagrams below present the forces and bending moment collected at the root of the fin-aircraft connection.

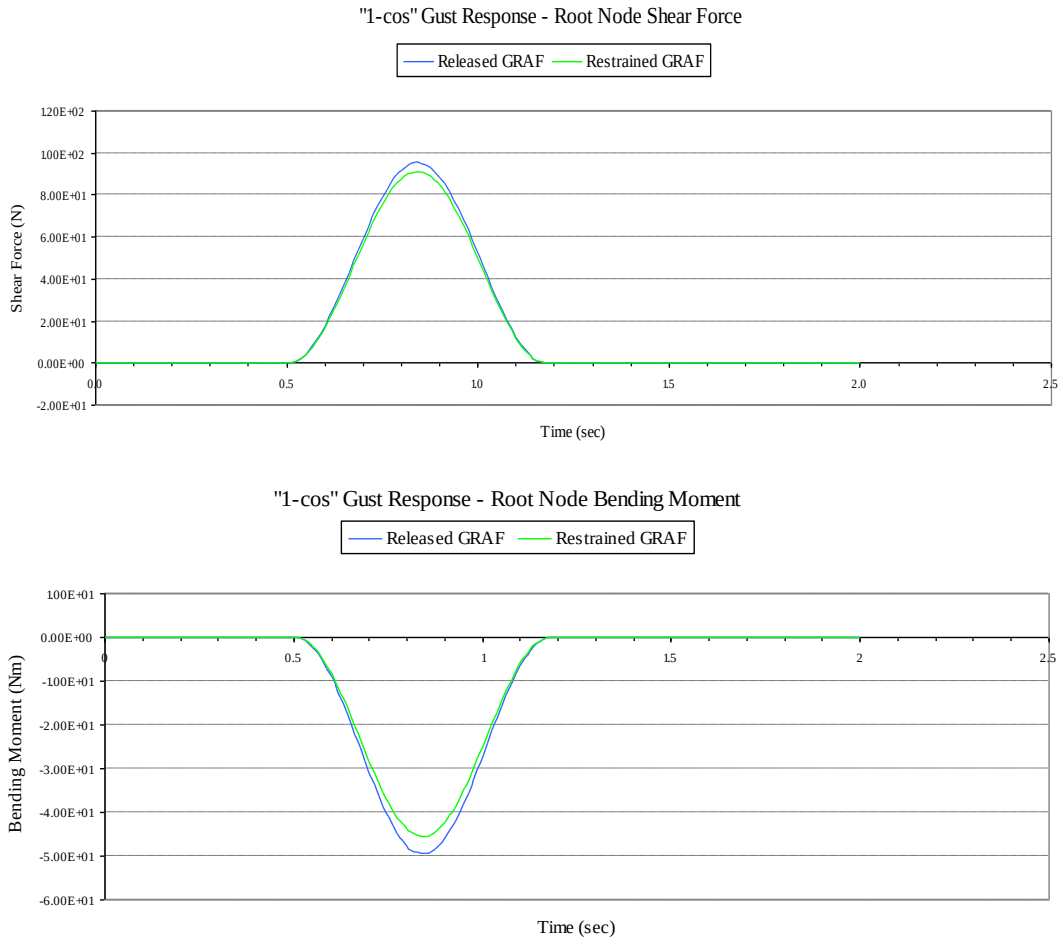

Figure 6-14 MTF4 root node shear force and bending moment due to gust loads for restrained (top) and free-to-twist (bottom) fin configurations.

In both figures, it can be seen that the “released” case shows higher values for both the force and the bending moment results. The reason for that is mainly due to the fact that although a very short time period is involved in the gust phenomenon, when the fin is free to twist, the twisting increases further a little more of the fin angle of attack, thus eventually generating a higher aerodynamic load upon it. Therefore, the forces at the root of the primary shaft have slightly augmented their effectiveness and reaction.

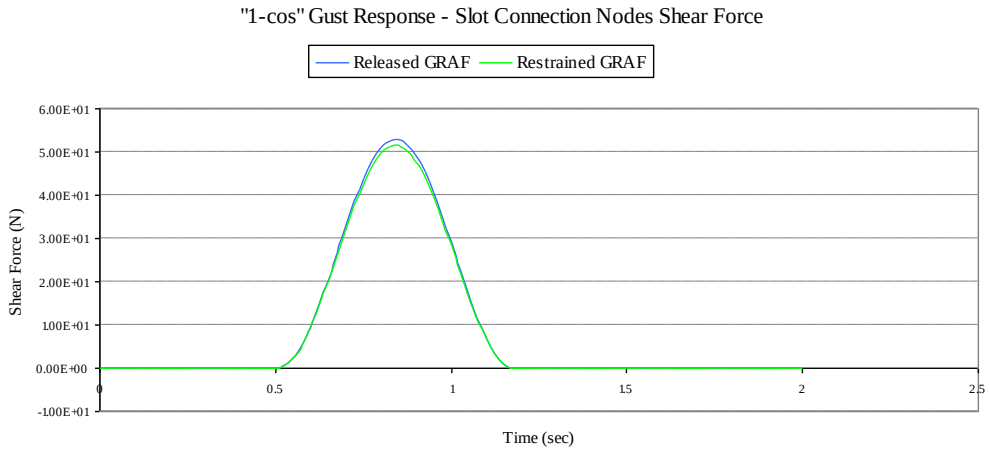

Figure 6--15 MTF4 slot-connection reference nodes shear force due to gust loads for restrained (top) and free-to-twist (bottom) fin configurations.

The value of the shear force and bending moment recorded by this analysis satisfy the structural requirements used to size the primary shaft and the design of the whole fin components.

WP23: The attention in this case is primarily focussed on the bending moment diagram the value of which is slightly greater than the static cases. However, the results of the structural static analysis of the shaft showed low level of stresses and deformation for the component. It is, therefore, assumed that even with the slight increase of the bending moment due to the impulsive gust load, the shaft structure can still cope with the solicitations due to this particular case.

6.2 *Fish-tailing* test case: yaw effectiveness

This last paragraph of the dynamic response analysis outlines the effectiveness of the MTF4 tail once applied on board the airplane, compared to the rigid current version of the Eclipse fin. The experiment analysis has been conducted by using the same FE model run for the previous cases. The FE model of the Eclipse vehicle has been included together with the fin model for the Flight Loads runs carried out with an input flight speed of 40.8m/s (cruise speed). A cyclic 1-cos side wind perturbation

has been input in the model, with a frequency of 0.25Hz, but with lower intensity than the wind speed used for the preceding gust analysis – almost reduced by 50% to simulate the most likely flight conditions. The outputs are shown in Figure 6-16.

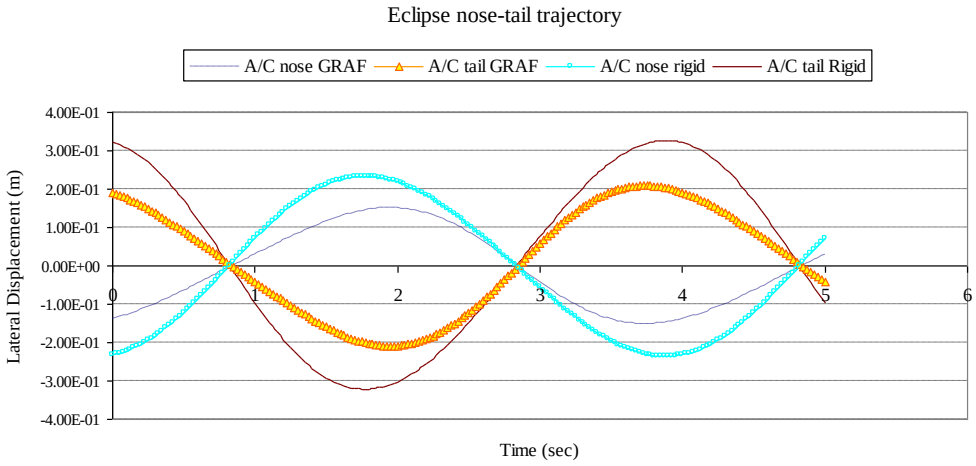

Figure 6-16 Fish-tailing results: MTF4 empennage and Eclipse UAV integration.

The curves in the "Eclipse Nose-tail" diagram show the trajectory followed by the nose and tail of the aircraft when the vehicle is hit by a side wind when flying at cruise speed. Two nodes, one on the aircraft nose and one on the tail, display the sinusoidal reaction to the external perturbation, as shown in Figure 6-16. The inner curves represent the model with the GRAF tail integrated on the vehicle. The outer curves, instead, refer to the rigid tail assembly, not provided with a twisting capability. The results show that the aircraft with the aeroelastic fin is less susceptible to lateral disturbances. The GRAF configuration displaces less than the rigid tail. It means the fin is more effective in either trying to restore the original heading of the vehicle or reducing the movements from its original course.

WP24: The side wind tends to laterally displace the aircraft identically in both cases, but its effect is felt less when the aeroelastic tail is activated. That reduces the amplitude of the oscillations and the lateral accelerations, and increases flight comfort for potential passengers.

Chapter 7 - GRAF MTF4 concept demonstrators prototyping

7.1 Introduction

This chapter is the last technical section of the thesis before concluding this work with the final comments and discussions. In particular, this Section will introduce the manufacturing process followed to build and assembly the concept demonstrators of the LSS-swivel devices and of the entire warping empennage. The first concept prototype built for this research project is the 0.08m fin section with the morphing TE part and the swivel edge closure integrated on it. The second prototype is the entire MTF4 tail built in 1:1 scale. Both prototypes have been built for concept demonstration and preliminary static displacement tests. The current stage of the research has not foreseen wind tunnel test experiments. Further aerodynamic tests will be carried out in a future research phase.
The materials used for the fabrication of the components are composite materials, in the specific, carbon and glass fibres laminates, balsa wood and low density foam.
The components built for the morphing TE concept demonstrator are:

- A rigid 0.75c airfoil section in balsa wood and glassfibre ;
- The flexible 0.25c glassfibre TE panels;
- The glassfibre swivel edge closure;
- The carbon fibre LSS components.

While the components manufactured for the other prototype regarding the whole MTF4 assembly, are:

- Four glass fibre ribs;
- Two carbon fibre ribs;

- Two glass fibre halves shell (i.e. covering skin);
- Wooden/foam fin mount.

The number of layers applied on the component manufacturing respects the real value determined in the analytical and numerical analysis of the fin structure already presented in the previous Sections.

7.2 Manufacturing and assembling of the prototypes

7.2.1 The morphing TE prototype

The TE concept demonstrator construction has started with the wooden frame chord section for the rigid part of the eight centimetres span fin strip, Figure 7-1.

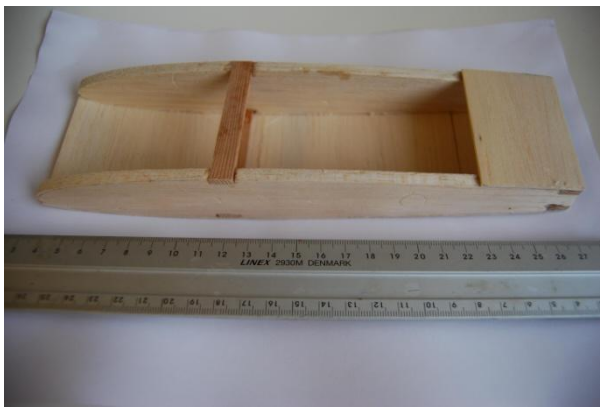

Figure 7-1 Wooden rib section

Then the swivel edge closure and the flexible three-layers glassfibre panels are built. The swivel component is manufactured as unique rigid element with and internal passing through oval hole. The one-piece edge has been later broken down in small segments to be attached on the two panels of the TE section, as shown in Figure 7-2.

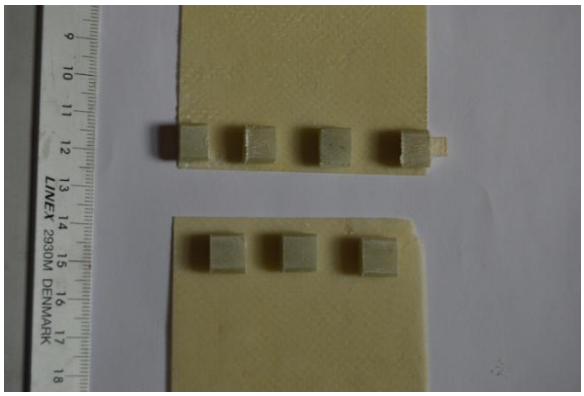

Figure 7-2 Swivel edge segments on TE panels

The hollow swivel element has been obtained by laying the layers of epoxy resin and glassfibres around a rod with an oval cross section. Once cured, the rod has been removed, thus leaving the internal hole. The figure below show the detail of a single element of the swivel device with still a section of the internal oval rod used for manufacturing, see Figure 7-3; while Figure 7-4 show the TE panels and the rigid airfoil frame prior to final assembly.

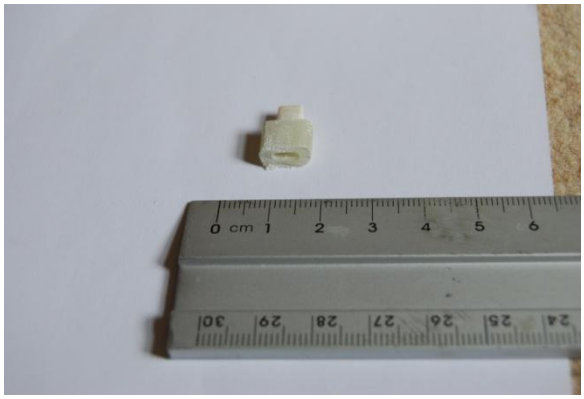

Figure 7-3 Swivel edge device single element

Figure 7-4 TE section components ready to be assembled

Two other elements are included in the final assembly of the morphing TE concept demonstrators, not shown in the previous pictures. They are the secondary carbon fibre shaft and the push-rods needed to activate the TE surfaces. The Figure 7-5 and 7-6 show the element assembled all together.

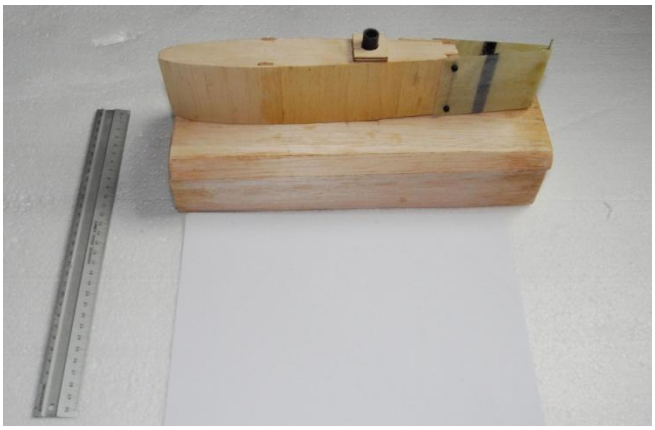

Figure 7-5 Top-left view of the TE concept demonstrator.

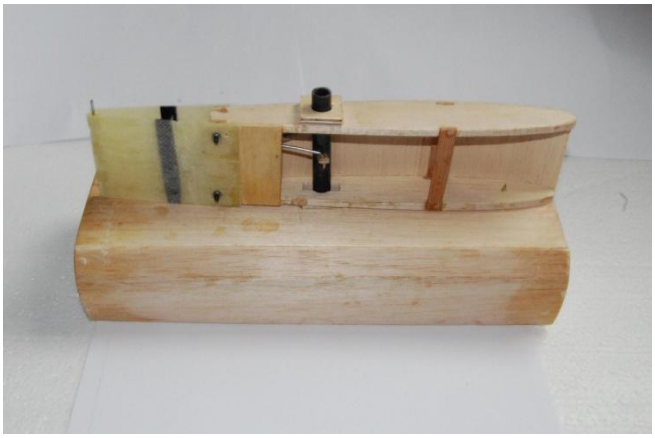

Figure 7-6 Top-right view of the TE concept demonstrator.

The last figure of this part of the chapter, Figure 7-7, shows the final assembly undergoing the deflection test with a conventional mechanical servo-actuator.

Figure 7-7 TE camber deflection

The TE concept demonstrator successfully achieved the required 24mm of deflection, even with the application of only one set of LSS stringers. It also generates a satisfactory deformed shape well resembling the one obtained with the smooth MATLAB computation.

7.2.2 The MTF4 GRAF empennage prototype

The first elements to be manufactured for the aeroelastic fin prototype have been the two halves shell of the cladding skin. The two sections solution rather than a unique shell has been primarily adopted to speed up the manufacturing process at this stage of construction. A slightly more articulated mould would have been needed to build a single shell. In this way the two halves will be sealed together at the end of the construction. The first part of the skin moulding has seen the production of the mould necessary to shape the external skin. The set of four figures shown in Figure 7-8 illustrate the initial steps followed to build the skin mould.

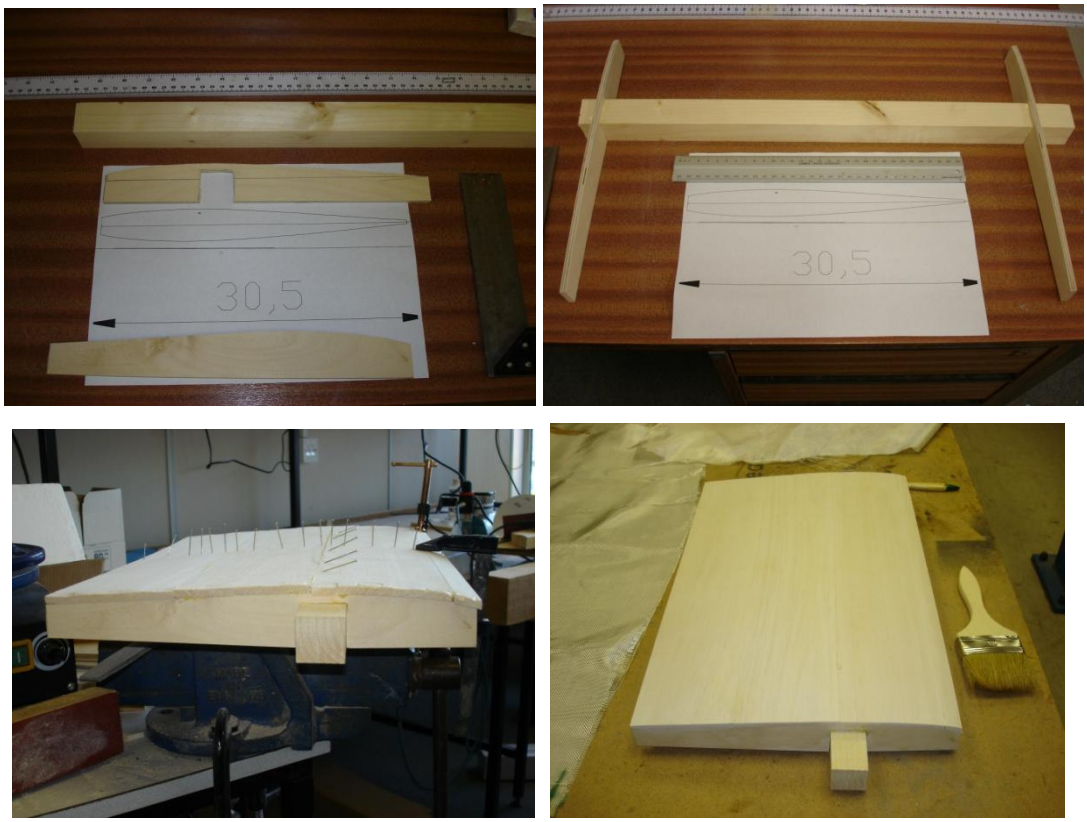

Figure 7-8 Wooden mould for skin manufacturing

As shown in the figures above a wooden jig frame shaped in the form of half RAE 101 airfoil section to work as positive mould has been constructed. For this part of the construction two key elements are identified in the process, namely the base mould and the lid. The wooden frame of Figure 7-8 is termed base mould, and made of hardwood. The function of this mould is to work as base, or technically speaking

as positive mould, to layup and shape the fibreglass layers impregnated with epoxy resin for the skin manufacturing. The skin layers once impregnated with the resin undergo hydrostatic pressure applied via an external mould, the lid, built in mat and with the same shape of the base mould in order to squeeze out the resin in excess and pre-form the profile curved shape.

Figure 7-9 Mat fibres used for lid manufacturing (left) and lid application on skin layers (right)

The Figure 7-9 shows the lid on top of the laminate and the base mould during the lamination process and the mat fibres used for the lid manufacturing. This type of material, less resilient than the glassfibres fabric, has been used because of the non-structural importance of this piece and the cheaper cost of the material. A series of sand bags are placed upon the mat lid to apply a uniform distributed pressure on the laminate.

A similar technique of positive and negative moulds has been applied for the ribs manufacturing. Although the materials selected for the ribs in the original design is carbon fibre, in the specific case of this prototype construction only two of the six ribs have been made in carbon fibre. They show the feasibility of building such an articulated rib shape with the carbon fibre. The rest of them are manufactured in glassfibre. The ribs are made by laying the composite layers inside the negative mould, Figure 7-10, on top of which it will be inserted the rib core (i.e. positive mould) in order to help the layers to perfectly adhere to the negative mould and meantime squeeze out the resin in excess. In order to ease the release operation of the manufactured product, the negative mould can be split up. During manufacturing the two sections of the negative mould are held together by a clamp or a vice.

Figure 7-10 Ribs moulding making: negative mould (left), split negative mould (middle), positive mould (right)

The Figure 7-11 shows the final product of the manufactured before refining and polishing their shapes, and after including the roller bearings, Figure 7-11 (right one).

Figure 7-11 Manufactured ribs

The figures below present the first assembly of the GRAF MTF4 fin before polishing and painting all the fin components. In particular Figure 7-12 illustrates the entire structure assembled together with only the LE section waiting to be sealed in.

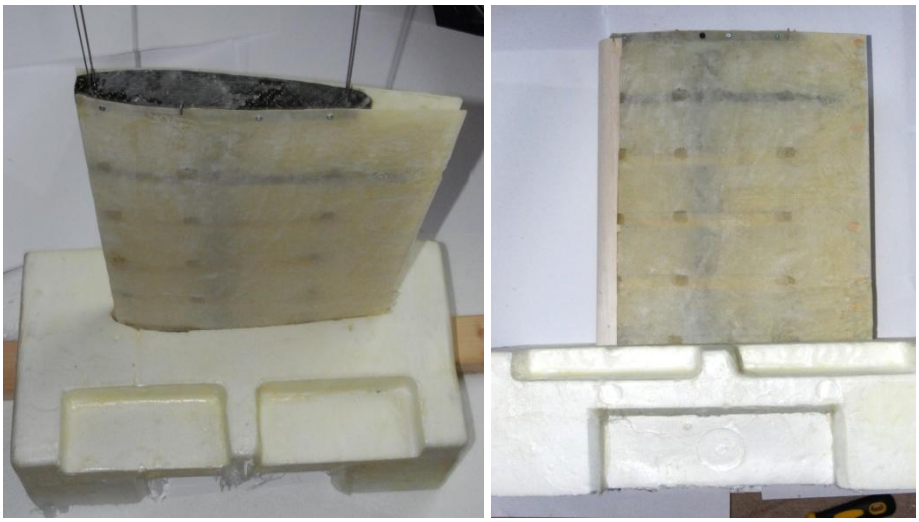

Figure 7-12 MTF4 prototype: top and side view.

The top view of Figure 7-13, instead, gives an insight of the internal arrangement of the fin structure. In the picture are visible the support brackets attached on the panel skin which will be connected to the fin ribs via piano wires slid from the top of the assembly.

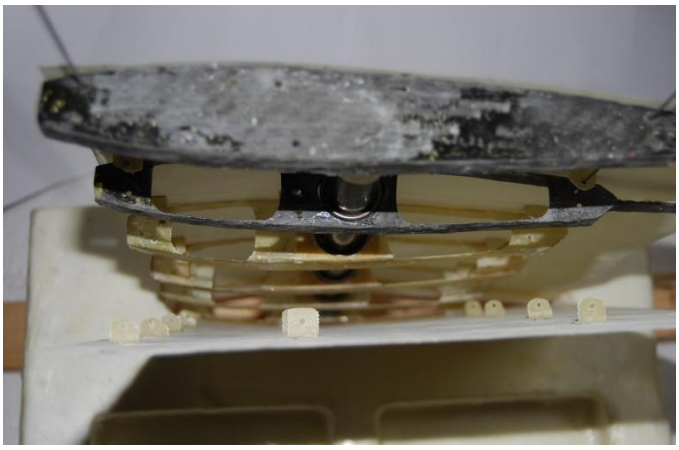

Figure 7-13 Fin internal top view

The next stage of the research will evaluate the possibility to test with wind tunnel experiments the capability of the GRAF design.

Figure 7-14 MTF4 prototype: first twist actuation.

The MTF4 model has performed a twist deformation of 18mm. The nose displacement of the master-rib has been measured by using a laser pointer. The 18mm deflection generated by applying the nominal torque of the designed actuator translates only into 8.5°. Assembly issue have reduced the twist performance of the fin. Moreover, it has been noticed the manufacturing of the external shell have

produced a skin slightly thicker than the one designed for the GRAF model. The reason of that is primarily due to the fact not all resin in excess has been squeezed out from the layer, thus making the laminate thicker and stiffer. The table below presents the GRAF components listed with their respective mass weighted during the prototype manufacturing process. The physical components' weight is compared to the FEM weight estimation extracted from the MSC/NASTRAN model of the fin.

Table 15 – FEM and Physical GRAF model comparison

Comparison FEM model and GRAF prototype

Component	Material	Physical Model Weight (kg)	FEM model Weight (kg)	Quantity
Main shaft	CFRP	0.091	0.08	x1
Secondary shaft	CFRP	0.04	0.025	x1
External skin	GFRP	0.218(with LE)	0.232 (with LE)	x1
Central Ribs	CFRP	0.02	0.016	x5
Master Rib	CFRP	0.028	0.026	x1
LSS	CFRP	0.04	0.03	x1
Swivel Edge device	GFRP	0.02	0.02	x1
Ancillaries	Steel	0.04	0.025	
Roller bearing	Steel	0.014	0.008	x4
Total Weight		0.633	0.55	

As it may be observed from the findings included in Table 15, a little difference in weight diversifies the manufactured products from the FEM model's parts, resulting in a 14% heavier prototype model. Improvements and further developments of the prototype will follow in the future research stage of this project.

WP25: The mass comparison between the prototype and the FEM model shows 0.083kg difference in the final weight of the built and numerical model. The MTF4 prototype has also shown a reduced twist angle then expected from the preliminary design performance (i.e. 15% less). The reason of that is mainly attributed to the lack of accuracy in the manufacturing and assembling processes.

Chapter 8 – Conclusions

8.1 General discussion

This work has presented the design concept and modelling of a novel vertical empennage configuration. The unconventional features applied on a vertical tail and the project preliminary requirements have imposed an unusual design philosophy for the realisation of the GRAF model. The thesis has presented and discussed the path followed to study, analyse and develop the MTF4 empennage under the various and multidisciplinary perspectives necessary to investigate and model the novel layout. The preliminary study of aerodynamic and flight performance has allowed the author to assess the functions and capability of the novel design in order to be integrated within the specific compliant design layout of the new fin structure. The final assembly enables seamless and conforming deformations. The warping and cambering capabilities allow the fin generating directional stability, and control forces to enhance the fin efficiency and flight effectiveness. The original arrangement of the internal components of the fin, in addition to a flexible cladding skin, and the introduced key novelties of the LSS device, the slot-connection and the "swivel TE closure", have made it possible for the empennage to satisfactorily accomplish and improve the side force and yawing moment generation tasks. The self-adaptive capability of the MTF4 fin, in combination with the exploitation of the aeroelastic effect have made possible both the enhancement of the fin and vehicle flight performance as well as the reduction of the actuation power consumption. Nevertheless, the light frame design has eventually produced a fin model 10% lighter than the original rigid version installed on the Eclipse vehicle. The saved weight, the lack of a rudder surface, the absence of unsealed gaps between the fin parts and the original arrangement of the internal components are the elements which can be identified as the primary novelties and differences compared to classic fin designs.

The following conclusions are drawn from the results obtained from the GRAF study, development and analysis. They are presented in the list below.

- *Aerodynamics*
  - In terms of drag force generation, the selected *smooth* variant for the TE section offers the third best drag coefficient with respect to the four profiles already investigated, it generates 15% less drag than a plain rudder (WP2);
  - The lift coefficient generated by the profile adopting the seamless *smooth* camber shape is greater than the other TE variants; it can generate 20% more lift than a plain rudder configuration (WP1-3);
  - It is believed the sealed gaps will reduce the drag generation; however, an accurate aerodynamic model for more detailed CFD simulation must be created to verify the improved efficiency. The CFD model was not part of this research project;
  - The novel GRAF tail insure more efficient aerodynamics while guaranteeing adequate control and stability performance;
  - Less drag generation enhances the flight efficiency of the entire aircraft and, above all, reduces the fuel consumption, thus augmenting endurance and range;
  - Gapless designs may favour the military application of such technologies, e.g. for stealth purposes.

- *Directional control and stability performance*
  - The flexibility of the compliant design in conjunction with the exploitation of the aeroelastic effect and the introduced technical novelties have provided the fin with the capability to generate the necessary controllability and stability in flight performance;
  - From a stability standpoint:
    - The passive self-adaptive mode of the warping fin has enhanced the effectiveness of the fin weathercock effect by

30% at cruise speed $\left(i.e.\, C_{n_\beta}\,,\, Section\ 5.4\right)$ if compared to the original Eclipse fin (WP19);

- A more effective empennage makes the entire aircraft more responsive against external disturbances such as side wind conditions or lateral gusts (WP21-23);
- As shown in the *fish-tailing* analysis case, the augmented GRAF responsiveness can reduce the lateral in-yaw oscillations with respect to a rigid fin configuration, thus increasing comfort in civil aircraft concepts (WP24);

▪ From a controllability standpoint:

- The directional control derivatives also enhance its effectiveness by 10% in the case of cross winds, due to the inherent twist capability of the MTF4 design (WP19); however, in normal operating condition without cross wind components, the MTF4 tail, by twisting only, struggles to achieve the same performance as a conventional plain deflected rudder (WP4-5);
- It has been necessary to introduce an active camber TE section to enhance the generation of side force coefficients;
- The fixed and sealed root constraint causes a limitation in twist deformation, thus reducing the effectiveness in generating adequate side forces;
- The base constraint reduces the camber of the TE section which can achieve the largest deflection only at the opposite end, on the fin tip, where it is completely free to deflect.

o *Structural concept, design & modelling*

▪ The worst loading case scenario assessed by the aerodynamic investigation has established as the worst loading condition corresponding to 10° of twist and 21° of FR TE camber (WP6);

- Based on those loads, the three layers of glass fibre fin skin, the carbon fibre primary shaft and the actuation power have been determined (WP9-16);
- The structural fin model meets the strength and stiffness requirements without any failure or critical stress levels for any part;
- The maximum fin displacement obtained with the 8.9Nm torque and the slot-connection joint is of 10°, while the camber deflection can achieve up to 21° of deformation at the fin tip. These values are sufficient to guarantee control and stability of the whole aircraft;
- Gusty and rapidly varying loads do not generate worrying values of shear force and bending moments for the fin mount and the withstanding primary shaft structure;
- The overall weight of the MTF4 structure is 0.55kg, 10% lighter than the existing Eclipse fin;
- The weight saved, besides being able to be used to carry more fuel, payload on board, might, in the specific configuration of the Eclipse vehicle, be utilised to reduce the weight of the ballast inside the fuselage. That might allow shifting the CG location and eventually vary the static margin and so the manoeuvrability of the whole aircraft;
- The structural design of the MTF4 has successfully met the structural requirements under the steady and unsteady aerodynamic analysis;
- The divergence and flutter speeds of the GRAF are above the design speed limit of the Eclipse design (WP20);
- However, higher speeds than 70m/s might result in being critical for the fin structure even with the stiffer four layers skin configuration;
- The section dedicated to the prototype construction feasibility has proven normal procedures of manufacturing processes apply to the model without any complicated moulding issue detected during construction.

- *Aeroelastic effect and actuation mechanism*
    - The design analysis has shown that the actuators' torque for both cambering and twist deformations can satisfy the final objectives of the GRAF;
    - The primary shaft actuators can provide enough torque to twist the fin, and recover its neutral position even against the continuous presence of the aeroelastic moment tending to keep twisting the shape (WP18);
    - The self-generated aeroelastic effect has proved it can autonomously induce a twist deformation on the structure during side wind circumstances and lateral gusts, thus beneficially enhancing the aircraft's directional stability;
    - Even during control authority tasks, once the twist is initiated by the mechanical actuators, the aeroelastic effect has proved to be efficient in continuing the twist and reducing the workload for the actuation systems;
    - However, due to the controlled-diverging effect of the aeroelastic deformation, the actuation power is needed to rotate the fin back to zero when the task is accomplished; the purely structural elasticity of the parts cannot guarantee the backwards rotation of the tail.

- *Outcomes from the introduced novelties*
    - **Internal compliant layout**: the smart combination of rotating ribs and the circular shaft allow more freedom to the thin skin during twist and camber actuation, successfully achieving the degrees of deformations needed for stability and control purposes;
    - **Aeroelastic effect technique**: the passive mode exploitation of aeroelastic deformations beneficially favours the enhancement of the stability performance and reduces the power consumption of the actuation system during control authority tasks;

- **L-shape stringers (LSS)**: although the current design can limit the TE camber deflection, this internally integrated mechanism can successfully transform linear forces in bending moments for the trimming and control tasks of seamless morphing surfaces;
- **Swivel edge closure**: the implementation of this device on the MTF4 empennage represents one of the two most important novelties which contributed to the goal's achievement by considerably increasing the DOFs of the TE part without leaving an open gap between the trailing edges;
- **Slot-connection**: this is the second most important novelty without which large deformations onto such a mono-coque shell structure would have not been achieved with modest actuator torque; it has increased the twist angle outputs and lowered the stress levels on the whole structure.

- *Limitations of the design*
  - No optimization study has been conducted on the structural components: that might further save weight and enhance the whole stiffness of the assembly;
  - Although the presence of the slot connection may reduce the stress level on the skin and ribs while twisting, the continuous warping deformation might induce fatigue and delamination problems on the composite parts of the structure when forced to deform either by the internal actuators or external aerodynamics;
  - The overall weight is lighter than the conventional tail, however two actuators are needed for the GRAF version compared to the one of the Eclipse;
  - Despite the gained stability performance, the control effect achieves only the minimum requirement in directional authority, therefore the overall size of the empennage can not be reduced to a smaller version at this stage of the research;

- A reduced fin dimension is hoped to further reduce the drag force generation and increase flight performance;
- GRAF manufacturing and assembling complexity must be considerably improved.

8.2 Achievements & Conclusions

The final conclusions are drawn in this paragraph. They will reflect the objectives of the project stated at the beginning of this work and further commented where the target has been achieved or missed by the GRAF design.

What has been achieved:

- A rudderless fin configuration design with a hingless control surface;
- An effective vertical tail capable of exploiting morphing and warping techniques to perform directional control and stability tasks;
- A unitised vertical tail, with the external shape designed in one-piece structure;
- A composite lightframes structural layout which has effectively reduced the overall weight of the novel fin;
- A novel fin concept capable of sensing wind direction and intensity to be beneficially exploited by the self-adaptive nature of the design, thus enhancing the directional effect during stability tasks, but not effective enough in control;
- A smart structural layout whose components and overall inherent flexibility made possible the exploitation of aeroelastic effect induced deformation to contribute in enhancing the side force generation for control and stability purposes, while reducing the power actuation needed to activate the GRAF;
- A more aerodynamically efficient design; the gapless configuration and the smooth TE camber features help reducing the drag force generation; further

aerodynamic efficiency is gained by the lighter weight design which contributes reducing the vehicle fuel consumption;

- A design that comply with all stiffness and strength criteria tested for steady and unsteady aerodynamic load cases;
- A successful combination of techniques and devices, in particular the five introduced novelties, which might be successfully used and adapted for other aerodynamic surfaces such as winglets and horizontal wings.

What has not been achieved:

- An effective directional control authority based only on warping capability; even after the integration of the TE camber device the GRAF cannot enhance in control the side force generation of the Eclipse fin-rudder configuration, but only match it.
- The reduction of the number of actuators deployed with the novel fin design; one more actuator has been need in order to help the fin combine the twist and camber shape effects;

8.3 Future developments and application of the GRAF concept

The GRAF concept design is a project which started out to evaluate whether an unusual layout and technology application might improve vertical fins and aircraft performance. This dissertation has proved how such an unconventional configuration when applied on a rudderless fin can perform equally as well as a conventional tail in control, and even better for stability tasks. However, as the reader may have already realised, such a novel concept design with the introduced novelties could be successfully applied on other typologies of aerodynamic surfaces such as wings and winglets. The GRAF systems and technology might be used on wings for passive trimming and manoeuvrability purposes, while they could work as directional stabilisers in the case of winglets application, and also, if free to twist, as gust alleviation devices, as similarly applied by Ainul *et al.* on horizontal gust alleviation devices [5]. The two most exploitable and applicable components of the whole

GRAF are the LSS actuation system and the swivel edge closure. The former can be applied to internally activate morphing surfaces either for wings or tailplanes. For instance, smart SMA wires could be attached between the LSS stringers and thermally activated to vary the camber of the profile for trimming the most efficient shape of the airfoil section. The latter can be applied to further enhance morphing capabilities of aerodynamic surfaces thus increasing the DOFs of the whole part. It is hoped, more detailed studies and development of the GRAF project will be continued in the future and next phase of this research. As, for example, it is recommended to carry out a more accurate aerodynamic investigation of the entire fin model by means of CFD tools to obtain more precise aerodynamic and flight performance results. Also an optimisation study to maximize the effectiveness of used composite materials and try where possible, with appropriate tailoring, to reduce further the weight of the GRAF structure is expected to be conducted in the next stages of the GRAF research.

References

[1] *Active Aeroelastic Aircraft Structures (3AS) programme*, available at http://cordis.europa.eu/archive/message1_en.html, (accessed December 2009).

[2] *Active Aeroelastic Wing Programme (AAW), NASA*, available at http://www.nasa.gov/centers/dryden/news/FactSheets/FS-061-DFRC.html, (accessed May 2009).

[3] *Active Aeroelastic Wing Programme (AAW), Boeing*, available at http://www.boeing.com/assocproducts/aaw/, (accessed December 2009).

[4] Addington, D. M and Schodek, D. L. (2005), *Smart materials and new technologies: for architecture and design professions*, Architectural Press, UK.

[5] Ainul. A., Cooper. J.E. and Sensburg., O. (2007), "Development of a gust alleviation device", *International Forum on Aeroelasticity and Structural Dynamics,(IFASD*), 18-20 Jun. 2007, Stockholm, Sweden.

[6] Allegri, G., Guo, S. and Trapani, M. (2007), "On the design of an aeroservoelastic fin for a flight demonstrator", *Interantional Forum on Aeroelasticity and Structural Dynamics, IFASD 2007*, Stockolm, Sweden.

[7] Ames, M. B. Jr. (1941), *Wind-tunnel investigation of control-surface characteristics III – A small aerodynamic balance of various nose shapes used with a 30-percent-chord flap on an NACA 0009 airfoil*, report L-301, Langley Memorial Aeronautical Laboratory, Washington.

[8] Amprikidis M, Cooper J.E. and Sensburg O, "Initial development of an active aeroelastic all movable vertical tail", *International Forum On Aeroelasticity And Structural Dynamics*, June 2003, Amsterdam.

[9] Amprikidis, M., Cooper, J. E. and Sensburg, O. (2004), Development of an adaptive stiffness all-moving vertical tail, *45th AIAA/ASME/ASCE/AHS/ASC Structures, Structural Dynamics & Materials Conference*,19 - 22 April 2004, Palm Springs, California, AIAA, Reston, VA.

[10] Amprikidis, M., Cooper, J. E., et al. (2005), "On the use of adaptive internal structures for wing shape control", *46th AIAA/ASME/ASCE/AHS/ASC Structures, Structural Dynamics & Materials Conference*, 18 - 21 April 2005, Austin, Texas, AIAA, Reston, Nevada.

[11] Amprikidis, M. and Cooper, J. E. (2005), "Development and evaluation of an adaptive stiffness attachment for an all-movable vertical tail", *13th AIAA/ASME/AHS Adaptive Structures Conference*, April 2005, Austin, Texas.

[12] Banerjee, J. R., Guo, S. and Howson, W. P. (1996), "Exact dynamic stiffness matrix of a bending-torsion coupled beam including warping", *Journal of Computers and Structures*, Vol. 59, No. 4, pp. 613-621, Elsevier B. V., U.S.

[13] Baker, A., Dutton, S. and Kelly, D., (2004), *Composite materials for aircraft structures (2nd ed)*, AIAA Education Series, Reston, Virginia.

[14] Barbarino, S., Pecora, R., et al. (2009), "A novel SMA-based concept for airfoil structural morphing", *Journal of Materials Engineering and Performance*, Vol. 18, No. 5-6, Springer, New York.

[15] Barrau, J. and Laroze, S. (1983), "Torsion of a composite beam", *Proceedings of the 2nd International Conference on Composite Structures*,

Composite Structures 2, I. H. Marshall. Applied Science Publishers, p. 146-154.

[16] Barré de Saint Venant,J. (1864), Résumé des lecons sur l'application de la mécanique (3rd ed.), Paris, edited by Saint Venant.

[17] Barrett, R. (1993), "Aeroservoelastic DAP missile fin development", *Journal of Smart Materials and Structures*, Vol. 2, No. 2, June 1993, p. 55-65, IOP Publishing Ltd, UK.

[18] Bartley-Cho, J. D., Wang, D. P., et al. (2004), "Development of high-rate, adaptive trailing edge control surface for the smart wing phase 2 wind tunnel model*", Journal of intelligent material systems and structures*, Vol. 15, No. 4, p. 279-291.

[19] Bauchau, O. A., Coffenberry, B. S. and Rehfield, L. W. (1987), "Composite box beam analysis: theory and experiments", *Journal of Reinforced Plastics and Composites*, Vol. 6, p. 25-35, SAGE publications.

[20] Beckwith, S. (2009), Designing with Composites: Suggested "Best Practices" Rules, *SAMPE Journal*, Vol. 45, No. 1, p.16-17.

[21] Bernhard, A. P. F. and Chopra, I. (2001), "Analysis of a bending-torsion coupled actuator for a smart rotor with active blade tips*", Smart Materials and Structures*, Vol. 10, p. 35–52, , IOP Publishing Ltd, UK.

[22] Berry, P. (1996), *"Segmented flap with variable camber for aircraft wing"*, International Patent B64C 3/48, World Intellectual Property Organization.

[23] Bicos, A. S. and Springer, G. S., "Design of a composite boxbeam", *Journal of Composite Materials*, Vol. 20, pp. 86-109, SAGE publications.

[24] Bisplinghoff, R. L., Ashley, H. and Halfman, R. L. (1996), *Aeroelasticity*, Dover Publications Inc., New York.

[25] Blondeau, J., Richeson, J. and Pines, D. J. (2003), "Design, development and testing of a morphing aspect ratio wing using an inflatable telescopic spar", *44th AIAA/ASME/ASCE/AHS Structures, Structural Dynamics, and Materials Conference*, 7-10 April 2003, Norfolk, Virginia, AIAA, Reston, Nevada.

[26] Boehm, B.,Flick, P., Sanders, B., Pettit, C., Reichenbach, E. and Zillmer, S. (2000), **"**Static aeroelastic response predictions of the active aeroelastic wing (AAW) flight research vehicle", *42nd AIAA/ASME/ASCE/AHS/ASC Structures, Structural Dynamics and Materials Conference*, Seattle, WA, April 2000, AIAA, Reston, VA.

[27] Bornengo, D., Scarpa, F. and Remillat, C. (2005), "Evaluation of hexagonal chiral structure for morphing airfoil concept", *Journal of Aerospace Engineering*, Vol. 219, No. 3, p. 185-192, Professional Engineering Publishing, London.

[28] Boresi, A. P. and Schmidt, R. J. (2003), *Advanced mechanics of materials*, John Wiley & Sons, UK.

[29] Bourdin, P., Gatto, A. and Friswell, M. I. (2006), "The Application of Variable Cant Angle Winglets for Morphing Aircraft Control", *24th Applied Aerodynamics Conference*, 5 - 8 June 2006, San Francisco, California, AIAA, Reston, Nevada.

[30] Bradbrook, K. (1999), *Contribution to the aerodynamic design for the Eclipse,* (MSc thesis), Cranfield University, Cranfield.

[31] Brenner, M. J. and Prazenica, R. J. (2003), *"Aeroservoelastic model validation and test data analysis of the F/A-18 Active Aeroelastic Wing",*

NASA report TM-2003-212021, NASA Dryden Flight Research Center Edwards, California.

[32] Brewer, J. D. and Polhamus J. F. (1948), *"Wind-tunnel investigation of the boundary layers on a NACA 0009 airfoil having 0.25- and 0.5- airfoil chord plain sealed flaps"*, report No. 1574, Langley Memorial Aeronautical Laboratory, Washington.

[33] Bruhn, E. F.(1965), *Analysis and design of flight vehicle structures*, Tri-State Offset Company, United States.

[34] Burnelli, V. J. (1930), "*Camber mechanism*", Aircraft Engineering, Patent No. 319,983, p. 50, February 1930, Emerald Group Publishing Limited, United Kingdom.

[35] Cadogan, D., Graham, W. and Smith, T. (2003), "Inflatable and rigidizable wing for unmanned aerial vehicles", *2nd AIAA "Unmanned Unlimited" Conference, Workshop, and Exhibit*, September 15-18, 2003, San Diego, CA.

[36] Cadogan, D., Scarborough, S., Gleeson, D. and Dixit, A. (2006), "Recent development and test of inflatable wings", *47th AIAA/ASME/ASCE/AHS/ASC Structures, Structural Dynamics, and Materials Conference*, Newport, Rhode Island, May 1-4, 2006, AIAA, Reston, VA.

[37] Cambridge-MIT Institute (2006), *The 'Silent' aircraft initiative,* available at http://www.silentaircraft.org/, (accessed 19th November 2009).

[38] Campanile, L. F. and Hanselka, H. (1998), "A lightweight concept for aerodynamic surfaces with variable camber", International Congress of the Aeronautical Sciences (ICAS 1998), Melbourne, Australia.

[39] Campanile, L. F. and Sachau, D. (2000), "The belt-rib concept: a structronic approach to variable camber", *Journal of Intelligent Material Systems and Structures* , Vol. 11 , No. 3, p. 215-224, Sage Publications.

[40] Campanile, L. F. and Anders, S. (2005), "Aerodynamic and aeroelastic amplification in adaptive belt-rib airfoils", Journal of Aerospace Science and Technology, Vol. 9 No. 1, pp. 55-63, Elsevier B. V., US.

[41] Campanile, L. F. and Thwapiah, G. (2009), A non-linear theory of torsional divergence, Proceedings of the Institution of Mechanical Engineers, Part C: Journal of Mechanical Engineering Science, Vol. 223, No. 11, pp. 2707-2711,

[42] Campbell, I. J., Blanks, C. F. and Leaver, D.A. (1960), *Aerodynamic characteristics of rectangular wings of small aspect ratio*, Reports and Memoranda No. 3142, Aeronautical research Council, Ministry of Aviation, London.

[43] Centolanza, M., R., Smith E. C. and Munsky, B. (2002), "Induced-shear piezoelectric actuators for rotor blade trailing edge flaps, *Smart Materials and Structures*, No. 11, p. 24-35, IOP Publishing Ltd, UK.

[44] Cero´n-Mun˜oz H. D. and Catalano, F. M. (2006), "Experimental analysis of the aerodynamic characteristics adaptive of multi-winglets", *proceedings IMechE, Journal of Aerospace Engineering*, Vol. 220, p. 209-215.

[45] Chattopadhyay, A., Seeley, C. E. and Jha, R. (1999), "Aeroelastic tailoring using piezoelectric actuation and hybrid optimization", *Journal of Smart Materials and Structures*, No. 8, p. 83-91, IOP Publishing Ltd, UK.

[46] Clarke, R., Allen, M. J., et al. (2005), "Flight test of the F/A-18 Active Aeroelastic Wing Airplane", *AIAA Atmospheric Flight Mechanics*

Conference and Exhibit, 15 - 18 August 2005, San Francisco, AIAA, Reston, VA.

[47] Cole, J. B. (1984), "*Variable camber leading edge assembly for an airfoil*", United States Patent, No. 4,475,702, 9th October 1984.

[48] Cook, M. V. (2007), *Flight Dynamics Principles (2nd ed)*, Elsevier Butterworth-Heinemann.

[49] Cooper, J.E., Amprikidis, M., Ameduri, S., Concilio, A., San Millán, J. and Castañón, M. (2005), "Adaptive stiffness system for an active all-moving vertical tail", *European Conference for Aerospace Sciences (EUCASS)*, July 2005, Moscow.

[50] Coulomb, C. A. (1784), Historie de l'academie, p. 229-269, 1787, Paris.

[51] Cumming, S. B. and Diebler, C. G. (2005), "Active aeroelastic wing aerodynamic model development and validation for a modified F/A-18A", *AIAA Atmospheric Flight Mechanics Conference*, 15-18 Aug. 2005, San Francisco, CA, United States.

[52] Diederich, F. W. and Budiansky, B. (1948), *Divergence of swept wings*, NACA Report TN-1680.

[53] Dong, Y., Boming, Z. and Jun, L. (2007), "A changeable aerofoil actuated by shape memory alloy springs", *Materials Science and Engineering*, Vol. 485, No. 1-2, June 2008, p. 243-250, Elsevier B. V., U.S.

[54] Engineering Sciences Data Unit (1948), *Effect of gap on slope of lift curve and slope of lift increment curve due to control surface deflection*, ESDU report Controls No. 01.01.04, United Kingdom.

[55] Engineering Sciences Data Unit, *Lift-curve slope for single fin and rudder body shape merging into fin*, ESDU Controls report No. 01.01.01, April 1982, United Kingdom.

[56] Engineering Sciences Data Unit, *Rudder side force, yawing moment and rolling moment control derivatives at low speeds: Yζ, Nζ and Lζ*, ESDU report No. 87008, June 1987, United Kingdom.

[57] Engineering Sciences Data Unit (1992), *Drag due to gaps round undeflected trailing-edge controls and flaps at subsonic speeds*, ESDU report No. 92039, United Kingdom.

[58] Engineering Sciences Data Unit, *Examples of excrescence drag prediction for typical wing components of a subsonic transport aircraft at the cruise condition*, ESDU No. 93032, December 1993, United Kingdom.

[59] Engineering Sciences Data Unit, *"An introduction to lateral static aeroelasticity: controllability, loads and stability"*, ESDU report No. 03011, May 2003, United Kingdom.

[60] Engineering Sciences Data Unit, *Computer program for estimation of spanwise loading of wings with camber and twist in subsonic attached flow(Lifting – surface theory) (With Appendix A: effect of plain flaps)*, ESDU 95010, March 1999, United Kingdom.

[61] Eppler, R. and Somers, D. (1980), *A computer program for the design and analysis of low-speed airfoils*, report NASA TM-80210.

[62] Eppler, R. (1963), "Praktische Berechnung laminarer und turbulenter Absauge-Grenzschichten", *Archive of Applied Mechanics*, Vol. 32, No. 4, p. 221-245.

[63] FangFang, W. and HaiFeng, L. (2009), "Influence of stiffening ribs on warping stress of the thin-walled steel box beam", *16th International Conference on Industrial Engineering and Engineering Management*, 2009. IE&EM, Bejing.

[64] Fatmi, R. E. (2007), A non-uniform warping theory for beams, p. 467-474, *Comptes Rendus Mecanique*, Vol. 335, No. 8, Elsevier B. V., US.

[65] Fielding, J. P. (1999), *Introduction to Aircraft Design*, Cambridge University Press, UK.

[66] Fielding, J.P., Macci, S.H.M., Mackinnon, A.V., and Stollery, J.L. (1992), "The aerodynamic and structural design of a variable camber wing", *18th International Congress of Aeronautical Sciences (ICAS 1982)*, Vol. 2, Beijing, AIAA, Washington, DC, p. 1098a-1098k.

[67] Fielding, J. P., Mills, A. and Smith, H. (2009), Design and manufacture of the DEMON unmanned air vehicle demonstrator vehicle, *proceedings IMechE Journal of Aerospace Engineering*, Vol. 224, No. 4, p. 365-372.

[68] FLAVIIR Programme: http://www.flaviir.com/, (accessed December 2009);

[69] Flexsys Inc. (Kota S., Hetrick J.A.), *"Adaptive compliant wing and rotor system"*, Patent No. WO 2004/108525 A1, World Intellectual Property organisation, US.

[70] Flick, P.M., Love, M.H. and Zink, P.S., "The impact of active aeroelastic wing technology on conceptual aircraft design", *Proceedings of the RTO Applied Vehicle Technology Specialists' Meeting on "Structural Aspects of Flexible Aircraft Control,"* NATO Research and Technology Agency, Ottawa, Canada, October 18-20, 1999. RTO MP-36.

[71] Fung, Y. C. (1993), *An introduction to the theory of aeroelasticity*, Dover Publications, New York.

[72] Gandhi, F. and Anusonti-Inthra, P. (2008), "Skin design studies for variable camber morphing airfoils", *Smart Materials and Structures,* Vol. 17, No. 1, p. 015025 – 015033.

[73] Gano, S. E. and Renaud, J. E. (2002), "Optimized unmanned aerial vehicle with wing morphing for extended range and endurance", *9th AIAA/ISSMO Symposium and Exhibit on Multidisciplinary Analysis and Optimization*, 4 - 6 Sep 2002 Atlanta, Georgia.

[74] Garcia, H. M., et al. (2003), "Roll control for a micro air vehicle", *AIAA Guidance, Navigation, and Control Conference and Exhibit,* 11 - 14 August 2003, Austin, Texas, AIAA, Reston, VA.

[75] Giavotto, V. (1995), *Strutture aeronautiche (Aircraft structures),* Città Studi Edizioni, Italy (in Italian).

[76] Giurgiutiu, V., Rogers, C. A., "Incrementally adjustable rotor-blade tracking tab using SMA composite", *38th AIAA/ASME/ASCE/AHS/ASC Structures, Structural Dynamics, and Materials Conference, and Adaptive Structures Forum,* April 7-10, 1997, Paper No. 97-1387, Kissimmee, FL.

[77] Gledhill, A.R. (1999), *Flight control system and simulation development for the unmanned air-vehicle Eclipse,* (MSc thesis), Cranfield University, Cranfield.

[78] Global Energy Concepts, LLC (2005), *Evaluation of aeroelastically tailored small wind turbine blades fina1 project report*, report No. DOE-00, Washington.

[79] Good M. G., *Development of a variable camber compliant aircraft tail structural optimization*, MSc Thesis, Virginia Polytechnic University (USA) , July 2003.

[80] Gosowski, B. (2006), Non-uniform torsion of stiffened open thin-walled members of steel structures, *Journal of Constructional Steel Research*, Vol. 63, No. 6, pp. 849-865, Elsevier B. V., US.

[81] Guo, S., Banerjee, J. R., Cheung, C. W. (2003), "The effect of laminate lay-up on the flutter speed of composite wings", *Proc. IMechE, Part G: J. Aerospace Engineering*, No. 217, p. 115-122.

[82] Guo, S., Chen, W. and Cui, D. (2005), *"*Optimisation of composite wing structures for maximum flutter speed", *1st AIAA Multidisciplinary Design Optimization Specialist Conference; 46th AIAA/ ASME/ASCE/AHS/ASC Structures, Structural Dynamics, and Materials Conference*; 18-21 April 2005, Austin, Texas.

[83] Guo, S. (2006), *"*Aeroelastic optimisation of a tapered composite wing structure", *5th Int. Conference on Mechanics and Materials in Design*, 24-26 July 2006, Porto.

[84] Guo, S. (2007), "Aeroelastic optimisation of an aerobatic aircraft wing structure", *Journal of Aerospace Science & Technology*, Vol. 11, No. 5, June 2007, p. 396-404, Elsevier B. V., U.S.

[85] Hannah, M. O., *Expanding Wing for Aero-plane*, U.S. Patent No. 1,773,530, Aug.19, 1930.

[86] Hart-Smith, L. J. (1992), The ten-percent rule for preliminary sizing of fibrous composite structures", *51st SAWE Annual Conference*, 18-20 May

1992, Hartford, Connecticut, published by Society of Allied Weight Engineers, Inc.

[87] Hassis, H. (1998), "A warping theory of plate deformation", *European Journal of Mechanics – A/Solids,* Vol. 17, No. 5, pp. 843-853, , Elsevier B. V., U.S.

[88] Hertz, T. J., Shirk, M. H. et al. (1981), *Aeroelastic tailoring with composites applied to forward swept wings*, Air Force Wright Aeronautical Laboratories, Report No. TR-81-3043, Ohio.

[89] Hileman, J. I., Spakovszky, Z.S., et al. (2006), "Aerodynamic and aeroacoustic three-dimensional design for a "Silent" aircraft ", *44th AIAA Aerospace Sciences Meeting and Exhibit*, 9-12 January 2006, Reno,Nevada, AIAA, Reston, VA.

[90] Hileman, J. I. and Sargeant, M. A. (2007), "Airframe design for Silent Aircraft", *45th AIAA Aerospace Sciences Meeting and Exhibit*, 8 - 11 January 2007, Reno, Nevada, AIAA, Reston, VA.

[91] Hileman, J. I., et al. (2007), "Development of approach procedures for Silent Aircraft", *45th AIAA Aerospace Sciences Meeting and Exhibit*, 8 - 11 January 2007, Reno, Nevada, AIAA, Reston, VA.

[92] Hinshaw, T. L. (2008), *Analysis and design of a morphing wing tip using multicellular flexible matrix composite adaptive skins*, Master of Science Thesis, Virginia Polytechnic Institute and State University, VA.

[93] HITEC Radio accessories http://www.hitecrcd.com, (accessed June 2010).

[94] Hoggard, H. P. Jr. and Bulloch, M. E. (1944), *Wind-tunnel investigation of control-surface characteristics XVI – Pressure Distribution over an NACA*

0009 airfoil with 0.30-airfoil-chord bevelled-trailing-edge flaps, report L-205, Langley Memorial Aeronautical Laboratory, Washington.

[95] How, J. (2003), *Lecture Notes: Aircraft Lateral Dynamics, MIT, open access notes*, available at: http://ocw.mit.edu/NR/rdonlyres/Aeronautics-and-Astronautics/16-61Aerospace-DynamicsSpring2003/B97E0200-2B1C-45A9-96AD-3CED05AE7233/0/lecture18.pdf, (accessed December 2009).

[96] Howe, D. (2004), *Aircraft loading and structural layout*, Professional Engineering Published, UK.

[97] Huff, L. (1999), *Contribution to the group design project for the Eclipse aircraft*, (MSc thesis), Cranfield University, Cranfield.

[98] Ishimitsu, K.K. (1973), *Mechanisation and Utilization of Variable Camber in Fighter and Attack Airplanes*, Report no. D180-15377-1, Office of Naval Research (code 461) Department of Navy, Washington.

[99] Jacob, J. D., Simpson, A. and Smith, S. (2005), "Design and flight testing of inflatable wings with wing warping", *SAE transactions*, Vol. 114, No. 1, p.1306-1315, Society of Automotive Engineers, New York.

[100] Jardine, A. P., Bartley-Cho, J. and Flanagan, J. (1999), "Improved design and performance of the SMA torque tube for the DARPA smart wing programme", *SPIE Conference on Industrial and Commercial Applications of Smart Structures Technologies,* March 1999, Newport Beach, California, Jack H. Jacobs, Editors, Bellingham, WA.

[101] JAVAFOIL Applet: *http://www.MH-AeroTools.del*, (accessed August 2009)

[102] Jones, R. T. and Ames, M. B. Jr. (1942), *Wind-tunnel investigation of control-surface characteristics V – The use of a bevelled trailing edge to*

reduce the hinge moment of a control surface, report L-464, Langley Memorial Aeronautical Laboratory, Washington.

[103] Katz, J. and Plotkin, A. (2001), *Low-Speed Aerodynamics (2nd ed),* Cambridge Univertisty Press, UK.

[104] Kollar, L. P. and Springer, G. S. (2003), *Mechanics of Composite Structures*, Cambridge University Press, UK.

[105] Kothera, C. S., et al. (2008), *Fluid-driven artificial muscles as mechanism for controlled actuation,* United States Patent, No. US2008/0035798 A1, Feb. 14, 2008.

[106] Krone, N. J., Jr. (1975), Divergence Elimination with Advanced Composites, *Aircraft Systems and Technology Meeting*, Los Angeles, August 1975.

[107] Lai, Y. C., Barman, C. P. L. and Onal, H. (2007), "Optimizing the aerodynamic efficiency of intermodal freight trains", *Transportation Research*, Part E, Vol. 44, pp. 820–834, Elsevier B. V., U.S.

[108] Lee, S. W. and Kim, Y. H. (1987), "A new approach to the finite element modelling of beams with warping effects*", International Journal of Numerical Methods in Engineering*, Vol. 24, p. 2327- 2341.

[109] Leifsson, L. T. and Mason, W. H., *The Blended Wing Body Aircraft,* Virginia Polytechnic Institute and State University, VA, USA (unpublished report).

[110] Leite, A., et al. (2009), "Development of morphing strategies for flight demonstrator RPV", *50th AIAA/ASME/ASCE/AHS/ASC Structures, Structural Dynamics, and Materials Conference 17th*, 4 - 7 May 2009, Palm Springs, California.

[111] Librescu, L. and Song, O. (1992), On the static aeroelastic tailoring of composite aircraft swept wings modelled as thin-walled beam structures, *Journal of Composites Engineering*, Vol. 2 No. 5-7, pp. 497-512, Pergamon Press Ltd., UK.

[112] Librescu, L. and Song, O. (2006), *Thin-walled composite beams: Theory and Application*, Springer, Netherlands.

[113] Lind, R. (2003), "Morphing for flight control of micro air vehicles", *AIAA Guidance, Navigation, and Control Conference and Exhibit,* 11 - 14 August 2003, Austin, Texas, AIAA, Reston, VA.

[114] Lizotte, A. M. and Alle, M. J. (2007), "Twist model development and results from the Active Aeroelastic Wing F/A-18 Aircraft", *International Forum on Aeroelasticity and Structural Dynamics (IFASD),* 18-20 Jun. 2007, Stockholm, Sweden.

[115] Loughlan, J. and Ata, M. (1995), "The restrained torsional response of open section carbon fibre composite beams", *Journal of Composite Structures*, Vol. 32, pp. 13-31, Elsevier B. V., U.S.

[116] Loughlan, J. and Ata, M. (1997), "The constrained torsional characteristics of some carbon fibre composite box beams", *Journal of Thin-Walled Structures,*Vol. 28, Nos. 3-4, pp. 233-252, Elsevier B. V., U.S.

[117] Loughlan, J. and Ata, M. (1997), "The behaviour of open and closed section carbon fibre composite beams subjected to constrained torsion", *Journal of Composite Structures,* Vol. 38, No. 1-4, pp631-647, Elsevier B. V., U.S.

[118] Loughlan, J. and Ata, M. (1998), “Variable twist torsion tests on carbon fibre composite beams”, *Journal of Composite Structures,* Vol. 42, pp. 307-327, Elsevier B. V., U.S.

[119] Love, M. H., Zink, P. S., et al. (2007),"Demonstration of morphing technology through ground and wind tunnel tests", *AIAA/ASME/ASCE/AHS/ASC Structures, Structural Dynamics and Materials, Conference*, Reston, VA 20191-4344, United States, 2007, pp. 337-348.

[120] Love, M. and Bohlmann, J., *Aeroelastic tailoring and integrated wing design*, General Dynamics internal report, No. 89-25167, Forth Worth, Texas.

[121] Lyon, D. G.: "Variable shaped airfoil", U.S. Patent No. 3,179,357, Apr.20, 1965.

[122] Martins, A. L., Catalano, F. M. (2003), “Drag optimization for transport aircraft Mission Adaptive Wing”, *Journal of the Brazilian Society of Mechanical Sciences and Engineering*, Vol. 25, No.1, p. 1-8.

[123] Megson, T.H.G., *Structural and stress analysis (2nd ed.)*, Elsevier Butterworth-Heinemann, Oxfod.

[124] Monner, H. P., Sachau, D. and Breitbach, E. (1999), “Design aspects of the elastic trailing edge for an adaptive wing”, *RTO AVT Specialists' Meeting on "Structural Aspects of Flexible Aircraft Control",* Ottawa, Canada, 18-20 October 1999, NATO, published in RTO MP-36.

[125] MSC.Software Corporation (2002), MSC.Nastran Version 68 – Aeroelastic Analsysi, User’s guide,MSC.Software Corporation, CA.

[126] Multhopp, H. (1955), *Methods for calculating the lift distribution of wings (subsonic lifting-surface theory),* ARC R&M No. 2884.

[127] Musat, S. D. and Epureanu, B. I. (1996), Study of warping torsion of thin-walled beams with closed cross-section using macro-elements, *Journal of Communications in Numerical Methods in Engineering*, Vol. 12, p. 873-884, John Wiley & Sons, Ltd, USA.

[128] Nagel, B., Kintscher, M. and Streit, T. (2008), "Active and passive structural measures for aeroelastic winglet design", *26th International Congress of the Aeronautical Sciences (ICAS 2008)*, 14-19 Sept 2008, Anchorage, Alaska.

[129] Neal, D. A., Good, M. G., et al. (2004), "Design and wind-tunnel analysis of a fully adaptive aircraft configuration", *45th AIAA/ASME/ASCE/AHS/ASC Structures, Structural Dynamics & Materials Conference*, 19 - 22 April 2004, Palm Springs, California, AIAA, Reston, Nevada.

[130] Neal, D. A. (2006), *Design, development, and analysis of a morphing aircraft model for wind tunnel experimentation,* (MSc Thesis), Virginia Polytechnic Institute and State University, VA.

[131] Niu, C. Y. M., (1999), *Airframe Structural Design* (2nd ed), Hong Kong Conmilit Press Ltd, Hong Kong.

[132] Papachristodoulou , A. N. and Culick , F. E. C. (2003), "Flight mechanics of the Wright aircraft 1903-1912", *41st Aerospace Sciences Meeting and Exhibit*, 6-9 January 2003, Reno, Nevada, AIAA, Reston, VA.

[133] Parker, H. F. (1920), *The Parker variable camber wing*, NACA Report No. 77, Langley Memorial Aeronautical Laboratory, Washington.

[134] Parker, H. F. (1920), *Variable Camber wings*, United States Patent, No. 4,361,299, Nov. 30, 1982.

[135] Peeters P.M., Middel J. and Hoolhorst A. (2005), *Fuel efficiency of commercial aircraft - An overview of historical and future trends*, report NLR-CR-2005-669, National Aerospace Laboratory NLR, Netherlands.

[136] Perera, M. and Guo, S. (2008), "Optimal design of an aeroelastic wing structure with seamless control surfaces", *Journal of Aerospace Engineering*, Vol. 223, No. 8, p. 1141-1151, Professional Engineering Publishing, London.

[137] Philen, M., Shan, Y., *et al.* (2006), "Variable stiffness adaptive structures utilizing hydraulically pressurized flexible matrix composites with valve control," *AIAA/ASME/ASCE/AHS/ASC Structures, Structural Dynamics and Materials Conference*, pp. 6387-6397, AIAA, Reston, VA, United States.

[138] Phillips, E. M. and Pugh, D. S., *How to get a PhD: a handbook for students and their supervisors (4th ed.)*, Open University Press, MacGrownHill, UK.

[139] Phillips W.F., *Minimizing induced drag with geometric and aerodynamic twist on a wing of arbitrary planform*, Department of Mechanical and Aerospace Engineering – Utah State University, USA (unpublished report).

[140] Phillips, W. F (2004), *Mechanics of Flight*, J. Wiley.

[141] Phillips,W. F. (2004), "Lifting-line analysis for twisted wings and washout-optimized wings", J*ournal of Aircraft*, Vol.41, No. 1, p. 128–136, AIAA, Reston, VA.

[142] Phillips, W. F., Fugal S. R. and Spall R. E. (2006), "Minimizing induced drag with wing twist, computational-fluid-dynamics validation, *Journal of Aircraft*, Vol. 43, n°2, p. 437-444, AIAA, Reston, VA.

[143] Poonsong, P. (2004), *Design and analysis of multi-section variable camber wing*, Master of Science Thesis, University of Maryland, USA.

[144] Popelka, D., Lindsay, D., et al. (1995), Results of an aeroelastic tailoring study for a composite tiltrotor wing, *AHS,* 51st *Annual Forum*, Fort Worth, Texas, 9-11 May 1995, pp. 1117-1131, US.

[145] Ramrakhyani, D. S., Lesieutre, G. A., et al. (2005), "Aircraft structural morphing using tendon-actuated compliant cellular trusses", *45th AIAA/ASME/ASCE/AHS/ASC Structures, Structural Dynamics & Materials Conference*, 19 - 22 April 2004, Palm Springs, California.

[146] Raymer, D. P. ( ), *Aircraft Design: A Conceptual Approach (4th ed.)*, AIAA Education Series.

[147] Rediniotis, O. K., *et al.* (2002), "Development of a Shape-Memory-Alloy actuated biomimetic hydrofoil", *Journal of Intelligent Material Systems and Structures*, Vol. 13, No. 1, p. 35-49, Sage Publications.

[148] Reddy, J. N., *Mechanics of laminated composite plates and shells : theory and analysis (2nd ed.)*, 2004, CRC Press, Washington D. C.

[149] Rocha, J., Moniz, P. and Suleman, A. (2007), "Aeroelastic control of a wing with active skins using piezoelectric patches", *Mechanics of Advanced Materials and Structures*, Vol. 14, p. 23–32, Taylor & Francis, London.

[150] Roskam, J.(1979), *Part I: Airplane Flight Dynamics and Automatic Flight Controls*, Roskam Aviation and Engineering Corporation, Kansas.

[151] Roskam, J.(1979), *Part II: Preliminary configuration design and integration of the propulsion system*, Roskam Aviation and Engineering Corporation, Kansas.

[152] Roskam, J.(1979), *Part IV: Layout Design and Landing Gear System*, Roskam Aviation and Engineering Corporation, Kansas.

[153] Sanders, B., Eastep, F. E. and Forster, E. (2003), Aerodynamic and aeroelastic characteristics of wings with conformal control surfaces for morphing aircraft, *Journal of Aircraft*, 2003, Vol. 40, No. 1, p. 94-99.

[154] Sanders, B., Joo, J. J. and Reich, G. W. (2005),"Conceptual skin design for morphing aircraft", 16th *International Conference on Adaptive Structures and Technologies (ICAST)*, Paris, France.

[155] Sears, R. I. (1941), *Wind-tunnel investigation of control-surface characteristics I – Effect of gap on the aerodynamic characteristics of an NACA 0009 airfoil with a 30-percent-chord plain flap*, report L-377, Langley Memorial Aeronautical Laboratory, Washington.

[156] Sears, R. I. and Liddell, R. B. (1942), *Wind-tunnel investigation of control-surface characteristics VI – A 30-percent-chord plain flap on the NACA 0015 airfoil*, report L-454, Langley Memorial Aeronautical Laboratory, Washington.

[157] Sharrock, B. (1980), *Variable Camber wings*, United States Patent, No. 4,361,299, Nov. 30, 1982.

[158] Shirk, M.H., Hertz, T.J., and Weisshaar, T.A., "Aeroelastic tailoring - Theory, practice, and promise", *Journal of Aircraft*, Vol. 23, No. 1, January 1986, p. 6-18.

[159] Simpson, J., Delgado, L. A., Nilsson, B., Vaccaio V. and Kawiecki, G. (2005), "Review of the Europe Research Project Active Aeroelastic Aircraft

Structures" (3AS), *European Conference for Aerospace Sciences (EUCASS)*, July 2005, Moscow.

[160] Sippola, M., Lindroos, T. and Brander, T. (2007), "Adaptive composite structures in shape control applications", *Journal of Structural Mechanics*, Vol. 40, No. 1, 2007, p. 65-79.

[161] Smith, M. J. , Komerath, N. et al. (2001), Performance Analysis of a Wing with Multiple winglets, *19th AIAA Applied Aerodynamics Conference*, Anaheim, CA, 11-14 June 2001, Reston, VA.

[162] Smith, J. W., Lock, W. P. and Payne, G. A. (1992), *Variable-camber systems integration and operational performance of the AFTI/F-111 Mission Adaptive Wing*, NASA Technical Memorandum 4370, Edwards, California.

[163] Song, G. and Zeng, M. (2005), "A thin-film magnetorheological fluid damper/lock", *Journal of Smart Matererials and Structures*, Vol. 14, p. 369–375, IOP Publishing Ltd, UK.

[164] Spearman, M. L. (1945), *Wind-tunnel investigation of control-surface characteristics XXIII – A 0.25-airofil-chord flap with tab having a chord twice the flap chord on an NACA 0009 airfoil*, report L-47, Langley Memorial Aeronautical Laboratory, Washington.

[165] Spearman, M. L. (1948), *Wind-tunnel investigation of an NACA 0009 airfoil with 0.25- and 0.50-airfoil-chord plain flaps tested independently and in combination,* report No.1517, Langley Memorial Aeronautical Laboratory, Washington.

[166] Statkus, F.D., *''Continuous skin, variable camber airfoil edge actuating mechanism''*, U.S. Patent No. 4,351,502, 1982.

[167] Stemple, A. D. and Lee, S. W. (1988), "Finite element model for composite beams with arbitrary cross-sectional warping", AIAA Journal, Vol. 26, p. 1512-20.

[168] Stinton, D. (1996), *The Anatomy of the Airplane*, co-published by AIAA Reston, VA, and Blackwell Science Ltd, UK.

[169] Straub, K. F. and Merkley, D. J. (1997), "Design of a smart material actuator for rotor control", *Smart Materials and Structures*, No. 6, p. 223-234, IOP Publishing Ltd, UK.

[170] Strelec, J. K. and Lagoudas, D. C. (2002), "Fabrication and Testing of a Shape Memory Alloy Actuated Reconfigurable Wing", *Proceedings Smart Structures and Materials 2002: Smart Structures and Integrated Systems*, Vol. 4701, pp.267-280, L. Porter Davis Editors, USA.

[171] Theodorsen, T. (1931*), Theory of Wing Sections of Arbitrary Shape*, NACA Report No. 411, National Advisory Committee for Aeronautics, Washington D. C.

[172] Thill, C., Etches, J., *et al.* (2008), "Morphing skins", *The Aeronautical Journal*, Vol. 112, No. 1129, p. 117-139, Royal Aeronautical Society, London.

[173] Thuwis, G. A. A., De Breuker, R., Abdalla, M. M. and Gürdal, Z. (2009), "Aeroelastic tailoring using lamination parameters - Drag reduction of a Formula One rear wing", *Journal of Structural and Multidisciplinary Optimization*, Springer Berlin / Heidelberg (published with open access at Springerlink.com).

[174] Timoshenko, S. P. and Woinowsky-Krieger, S., *Theory of plates and shells (2nd ed.)*, Mc Graw-Hill, New York.

[175] Timoshenko, S. and Goodier, J. N., *Theory of elasticity (2nd ed.)*, Mc Graw-Hill, New York.

[176] Tsai, S. W. (1987), C*omposite Design (4th ed.)*, Think Composites, Dayton-Paris-Tokyo.

[177] Tsai, S. W. (2009), *Strength and life of composites*, Composites Design Group, Stanford University, Stanford, CA.

[178] Trahair, N. S. (2003), *Non-linear elastic non-uniform torsion*, Research Report No. R828, Department of Civile Engineering, The University of Sydney.

[179] Trapani, M. and Guo, S. (2008), "Development of a Rudderless Aeroelastic Fin Technology", *26th International Congress of the Aeronautical Sciences (ICAS 2008)*, 14-19 Sept 2008, Anchorage, Alaska.

[180] Trapani, M. and Guo, S (2009), "Design and analysis of a rudderless aeroelastic fin", *proceedings IMechE, Journal of Aerospace Engineering*, Vol. 223, No. 6, p. 701-710.

[181] Ursache, N. M., Keane, A. J. and Bressloff, N. W. (2006), "On the Design of Morphing Airfoils using Spinal Structure", *47th AIAA/ASME/ASCE/AHS/ASC Structures, Structural Dynamics, and Materials Conference*, 1 - 4 May 2006, Newport, Rhode Island, AIAA, Reston, VA.

[182] Ursache, N. M., Melin, T., Iskiveren, A. T. and Friswell, M. I. (2007), "Morphing winglets for aircraft multi-phase improvement", *7th AIAA*

Aviation Technology, Integration and Operations Conference (ATIO), 18 - 20 September 2007, Belfast, Northern Ireland.

[183] Ursache, N. M., Melin, T., Iskiveren, A. T. and Friswell, M. I. (2008), "Technology integration for active poly-morphing winglets development", *ASME Conference on Smart Materials, Adaptive Structures and Intelligent Systems,* October 28-30, 2008, Ellicott City, Maryland, USA.

[184] Veers, P., Bir, G. and Lobitz, D. (1998), "Aeroelastic tailoring in wind-turbine applications", *Windpower '98, American Wind Energy Association Meeting and Exhibition,* Bakersfield, California, April 28 – May 1, 1998.

[185] Vermeeren, C. (2002), *Around Glare : a new aircraft material in context*, September 24-26, 2001, Delft University of Technology, Dordrecht, Kluwer.

[186] Vlasov, V.Z. , *Thin-Walled Elastic Bars (in Russian, 2nd ed.)*, Fizmatgiz, Moscow, 1959.

[187] Vlot, A. (2001), *Glare: History of the Development of a New Aircraft Material*, Kluwer Academic Publishers, 2001, ISBN 1-402-0124-X.

[188] Voracek, D., Pendleton, E., Reichenbach, E., Griffin, K. and Welch, L. (2003),*The Active Aeroelastic Wing phase I flight research through January 2003,* NASA report TM-2003-210741, Dryden Flight Research Center, Edwards, California.

[189] Vos, R. *et al.* (2007), "Post-buckled precompressed elements: a new class of control actuators for morphing wing UAVs", *Smart Matererials and Structures,* Vol. 16, No. 3, p. 919-926, IOP Publishing Ltd, UK.

[190] Vos, R., Gurdal, Z. and Abdalla, M. (2008), A novel mechanism for active wing warping, *49th AIAA/ASME/ASCE/AHS/ASC Structures, Structural*

Dynamics, and Materials Conference, 7 – 10 April 2008, Schaumburg, Illinois, AIAA, Reston, VA.

[191] Weisshaar, T. A. (1992), Adaptive aeroelastic composite wings-control and optimization issues, *Journal of Composites Engineering*, Vol. 2, No. 5-7, pp. 457-476, Pergamon Press Ltd., UK.

[192] Weisshaar, T. A., Nam, C., Batista-Rodriguez, A. (1998), "Aeroelastic tailoring for improved UAV performance", *39th AIAA/ASME/ASCE/AHS/ASC Structures, Structural Dynamics, and Materials Conference*, Long Beach, California, April. 20–23, 1998.

[193] Weisshaar T.A. and Duke D.K. (2006), "Induced drag reduction using aeroelastic tailoring with adaptive control surface", *Journal of Aircraft*, Vol. 43, No.1, p. 157-164, AIAA, Reston, VA.

[194] Wikipedia Encyclopedia, Langley Samuel Pierport, http://en.wikipedia.org/wiki/Samuel_Pierpont_Langley , (accessed March 2010).

[195] Wikipedia Encyclopedia, Vought F-8 Crusader, http://en.wikipedia.org/wiki/Vought_F-8_Crusader, (accessed March 2010).

[196] Wildschek, A., Havar, T. and Plotner, K. (2010), "An all-composite, all-electric, morphing trailing edge device for flight control on a blended-wing-body airliner", Proc. IMechE, *Journal of Aerospace Eengineering*, Vol. 224, No 1, p. 1-9.

[197] Wolko, H. S. and Anderson, J. D. (1987), National Air and Space Museum - *The Wright Flyer: an engineering prospective*, Smithsonian Institution Press,Washington DC.

[198] Wooldridge, E. T., *N-1M: the first Northrop flying wing*, http://www.century-of-flight.net/Aviation%20history/flying%20wings/northrop.htm, (accessed March 2010).

[199] Worden, K., Bullough, W.A. and Haywood, J. (2003), *Smart Technologies*, World Scientific Publishing, UK-USA.

[200] Wright, J. R. and Cooper, J. E. (2007), Introduction to Aircraft Aeroelasticity and Loads, Wiley Ltd, UK.

[201] Yarf-Abbasi, A., Clarke, A., Lawson, C. P. and Fielding, J. P. (2008), "Design and development of the Eclipse and Demon demonstrator UAVs", *26th International Congress of the Aeronautical Sciences (ICAS 2008)*, 14-19 Sept 2008, Anchorage, Alaska.

[202] Yerkes, N. T. and Wereley, N. M., "Pneumatic Artificial Muscle Activation for Trailing Edge Flaps", *46th AIAA Aerospace Sciences Meeting and Exhibit*, 7 - 10 January 2008, Reno, Nevada.

[203] Zenith Aircraft Co., http://www.zenithair.com/, (accessed December 2009)

Appendix A

Potential flow:

The potential flow [102] theory is the model used to describe the numerical panel method adopted in both JAVAFOIL and Flight Loads tools (this one developed in DLM or VLM):

The circulation around any curve can be defined as :

$$\Gamma = \oint \nabla\Phi \cdot d\mathbf{l} \qquad \text{(A1)}$$

And considering the Kelvin's Theorem that states the circulation o fhte same fluid elements around a closed curve is constant in time, and expressing that in the rate change of circulation in time, it yields:

$$\frac{D\Gamma}{Dt} = 0 \qquad \text{(A2)} \quad \text{then,} \quad \Gamma(t) = \Gamma(0) \qquad \text{(A3)}$$

And the by applying the Stoke's Theorem, it can be written:

$$\Gamma \equiv \oint_C \vec{q} \cdot d\vec{l} = \int_S \nabla \times \vec{q} \cdot \vec{n} dS = \int_S \zeta \cdot \vec{n} dS \quad \text{(A4)}$$

Where $\zeta = \nabla \times \vec{q}$ and $\vec{q}$ represents the flow velocity and that brings us to define that in a simply connected, bounded region there exists a scalar function whose gradient can be defined as the velocity filed $\vec{q}$ as:

$$\vec{q} = \nabla\phi \qquad \text{(A5)}$$

In Cartesian coordinates the velocity components are given by

$$u = \frac{\partial\phi}{\partial x}; \quad v = \frac{\partial\phi}{\partial y}; \quad w = \frac{\partial\phi}{\partial z} \qquad \text{(A6)}$$

Thus substituting equation (a5) in the equation of continuity for incompressible fluids, it leads to the expression of the differential equation for the velocity potential, know also as Laplace's equation:

$$\nabla^2\phi = 0 \qquad \text{(A7)}$$

To find the velocity field of the flow suitable boundary condition for the flow on the body and at infinity must be defined. The mathematical formulation that does so is expressed by the following equations system:

$$\begin{cases} \nabla^2\phi = 0 \\ \dfrac{\partial\phi}{\partial n} = \vec{n}\cdot\overrightarrow{q_B} \quad on body \\ \nabla\phi \to 0 \quad at \quad r \to \infty \end{cases} \qquad \text{(A8)}$$

It is important to note that the solution of Laplace equation can be obtained by distributing elementary solutions, as doublets and sources, on the boundaries of the problem. These particular solutions will fulfil the boundary conditions decaying at $r \to \infty$ and becoming singular entities at $r \to 0$. The proper solution for a fluid dynamic problems is in to finding the appropriate singularity elelmtn distribution to satisfy the BC. When the potential is specified on the problem boundaries then this type of approach is called Dririchlet problem and is frequently applied for numerical solutions as the panel method. Instead, when the problem is faced specifying the zero normal flow BC, then it is called Neumann problem.

The statement of the potential flow problem reduces to the following three equations:

$$\nabla^2\phi = 0 \qquad \text{(A9)} \qquad \nabla\phi\cdot\vec{n} = 0 \qquad \text{(a10)} \qquad \lim_{r\to\infty}\left(\nabla\phi - \vec{q}\right) = 0 \qquad \text{(A11)}$$

Following the *Green's identity* and distributing singularitie n the body and the wake, whose strength must be determined, is possible to write the general solution for the problem as:

$$\phi(P) = \frac{1}{2\pi}\int_{S_B}\left[\sigma\ln r - \mu\frac{\partial}{\partial n}(\ln r)\right]dS - \frac{1}{2\pi}\int_{S_W}\mu\frac{\partial}{\partial n}(\ln r)dS + \phi_\infty(P) \qquad \text{(A12)}$$

Once this singularities distribution of sources, doublets or vortexes to satisfy equation (A9) is found, then through the general expression of the potential the velocity $\vec{q}$ at each point can be known and consequently the corresponding pressure p can be computed according the steady-state Bernoulli equation:

$$p_\infty + \frac{\rho}{2}Q_\infty^2 = p + \frac{\rho}{2}q^2 \qquad \text{(A13)}$$

Where p_∞ *and* Q_∞ are the pressure and velocity of the free-stream far away from the body's boundaries.

Equation a12 can be rewritten in the airfoil's body frame and assuming that only doublet or vortexes act on the wake, as:

$$\phi^*(x,y,z) = \frac{1}{4\pi}\int_{Body+Wake} \mu \bar{n}\cdot\nabla\left(\frac{1}{r}\right)dS - \frac{1}{4\pi}\int_{Body}\sigma\left(\frac{1}{r}\right)dS + \phi_\infty \qquad \text{(A14)}$$

The BC can specify the ϕ^* on the boundary of an enclosed region (e.g. $S_{B)}$ defining so the Dirichlet problem, as $\partial\phi^*/\partial n = 0$, then the potential inside the body does not change and is:

$$\phi_i^* = const. \qquad \text{(A15)}$$

Panel Method

Let us reduce the problem to a set of linea equations by discretizing the body surface and the wake into a series of rectangular panels and considering the BC for the potential as $\phi_i^* = \phi_\infty$. Let us indicate with N the number of panels on the body and N_W the ones on the wake, rewriting at this stage the Dirichlet boundary condition fo reach of the N collocation points as:

$$\sum_{k=1}^{N}\frac{1}{4\pi}\int_{body\,panel}\mu\bar{n}\cdot\nabla\left(\frac{1}{r}\right)dS + \sum_{l=1}^{N_W}\frac{1}{4\pi}\int_{wake\,panel}\mu\bar{n}\cdot\nabla\left(\frac{1}{r}\right)dS - \sum_{k=1}^{N}\frac{1}{4\pi}\int_{body\,panel}\sigma\left(\frac{1}{r}\right)dS = 0$$

(A16)

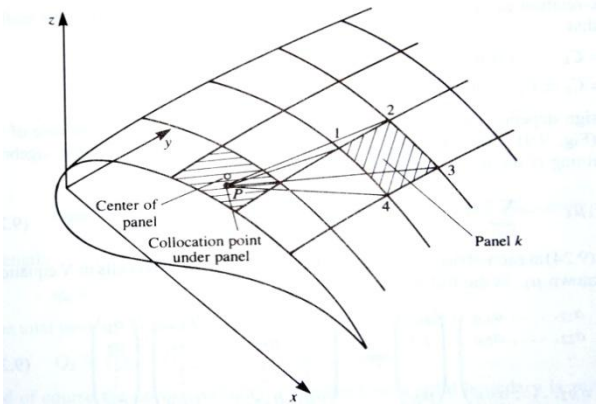

Figure A01- Aerodynamic boxes distribution for panel method theory

The summation of the influence due to all *k* body panels and *l* wake panels must be taken into account into the numerical or analytical computation, bringing at the end for each internal point P:

$$\sum_{k=1}^{N} C_k \mu_k + \sum_{l=1}^{N_w} C_l \mu_l + \sum_{k=1}^{N} B_k \sigma_k = 0 \qquad \text{(A17)}$$

From the Dirichlet condition is required also that the sources have strength equal to $\sigma = \bar{n} \cdot \bar{Q}_\infty$ that turns the source term, addressed under the B_k coefficients, in being moved on the right-hand side of the equation. In adjunct to the *Kutta condition,* that must be respected at the trailing edge of the sections, the wake doublets can now also be expressed in function of the unknown surface doublets. In compact form the system can be reduced to:

$$\sum_{k=1}^{N} A_k \mu_k = -\sum_{k=1}^{N} B_k \sigma_k \qquad \text{(A18)}$$

Or also explicitly written as N equations in N unknown μ_k, as follows:

$$\begin{pmatrix} a_{11} & a_{12} & . & . & . & a_{1N} \\ a_{21} & a_{22} & . & . & . & a_{2N} \\ : & : & & & & : \\ : & : & & & & : \\ a_{N1} & a_{N2} & . & . & . & a_{NN} \end{pmatrix} \begin{pmatrix} \mu_1 \\ \mu_2 \\ : \\ : \\ \mu_N \end{pmatrix} = - \begin{pmatrix} b_{11} & b_{12} & . & . & . & b_{1N} \\ b_{21} & b_{22} & . & . & . & b_{2N} \\ : & : & & & & : \\ : & : & & & & : \\ b_{N1} & b_{N2} & . & . & . & b_{NN} \end{pmatrix} \begin{pmatrix} \sigma_1 \\ \sigma_2 \\ : \\ : \\ \sigma_N \end{pmatrix} \qquad \text{(A19)}$$

Once the unknown singularities μ_k are obtained by solving the full matrix system, then the total velocity in the local coordinate of each panel can be written as:

$$\bar{Q}_k = \left(Q_{\infty l}, Q_{\infty m}, Q_{\infty n}\right)_k + (q_l, q_m, q_n)_k \qquad \text{(A20)}$$

The velocity field allows to compute the pressure distribution coefficient over each panel, thus writing the general vector form for the fluid dynamic load generated by every single panel *k*, as follows:

$$\Delta\overline{C_{F_k}} = -\frac{C_{p_k} \Delta S_k}{S} \cdot \bar{n}_k \qquad \text{(A21)}$$

With this last equation the short dissertation about the flow potential and the panel method technique turn to a conclusion, continuing more details about these theories and methods in the sections dedicated to the codes and computing methods used in the analysis design.

Appendix B

- COALA program results for four layers laminate:

LAMINATE CONSTITUTIVE EQUATION FOR THE ANALYSED CONFIGURATION

"A"/"a"-MATRIX			"B"/"b"-MATRIX			"D"/"d"-MATRIX		
.1262E+05	.4424E+04	-.4333E-05	.6538E+03	-.3815E-05	.1090E+03	.2958E+03	.5937E+02	.2461E-07
.4424E+04	.1262E+05	.4676E-04	-.3815E-05	-.6538E+03	.1090E+03	.5937E+02	.2958E+03	.1887E-05
-.4333E-05	.4676E-04	.4100E+04	.1090E+03	.1090E+03	.7629E-05	-.1343E-06	.1729E-05	.5260E+02
.1055E-03	-.3787E-04	.7131E-05	-.2276E-03	-.4064E-04	-.1401E-03	.4056E-02	-.6912E-03	.3874E-03
-.3787E-04	.1055E-03	-.7131E-05	.4064E-04	.2276E-03	-.1401E-03	-.6912E-03	.4056E-02	-.3874E-03
.7131E-05	-.7131E-05	.2487E-03	-.8943E-04	-.8943E-04	-.3327E-10	.3874E-03	-.3874E-03	.1959E-01

LAMINATE MEMBRANE EQUIVALENT ENGINEERING ELASTIC CONSTANTS

Ex	Ey	mx	my	NUxy	NUyx	Gxy
.18959E+05	.18959E+05	-.67601E-01	.67601E-01	.35897E+00	.35897E+00	.80425E+04

LAMINATE BENDING EQUIVALENT ENGINEERING ELASTIC CONSTANTS

Ex	Ey	mx	my	NUxy	NUyx	Gxy
.23671E+05	.23671E+05	-.95521E-01	.95521E-01	.17043E+00	.17043E+00	.49002E+04

- COALA program results for three layers laminate:

LAMINATE CONSTITUTIVE EQUATION FOR THE ANALYSED CONFIGURATION

"A"/"a"-MATRIX			"B"/"b"-MATRIX			"D"/"d"-MATRIX		
.9993E+04	.2793E+04	.8718E+03	.3492E+03	-.1312E+03	-.1090E+03	.1389E+03	.3820E+02	.1476E+02
.2793E+04	.9993E+04	.8718E+03	-.1312E+03	-.8672E+02	-.1090E+03	.3820E+02	.8439E+02	.1476E+02
.8718E+03	.8718E+03	.2550E+04	-.1090E+03	-.1090E+03	-.1312E+03	.1476E+02	.1476E+02	.3535E+02
.1389E-03	-.3727E-04	-.2825E-04	-.5283E-03	.3294E-03	.2915E-03	.1043E-01	-.4591E-02	-.2613E-02
-.3727E-04	.1152E-03	-.1434E-04	.1964E-03	-.7053E-04	.1344E-03	-.4591E-02	.1514E-01	-.2794E-02
-.2825E-04	-.1434E-04	.5062E-03	.2287E-03	.2185E-03	.1561E-02	-.2613E-02	-.2794E-02	.3766E-01

LAMINATE MEMBRANE EQUIVALENT ENGINEERING ELASTIC CONSTANTS

Ex	Ey	mx	my	NUxy	NUyx	Gxy
.19196E+05	.23153E+05	.20335E+00	.12451E+00	.26828E+00	.32358E+00	.52679E+04

LAMINATE BENDING EQUIVALENT ENGINEERING ELASTIC CONSTANTS

Ex	Ey	mx	my	NUxy	NUyx	Gxy
.21808E+05	.15032E+05	.25047E+00	.18457E+00	.43997E+00	.30326E+00	.60430E+04

- Gust Load Case requirements from EASE Certification Specifications for Normal, Utility, Aerobatic, and Commuter Category Aeroplanes CS-23

(3) For each required altitude and weight, for any practicable distribution of disposable load within the operating limitations specified in CS 23.1583 to 23.1589.

(c) When significant the effects of compressibility must be taken into account.

CS 23.331 Symmetrical flight conditions

(a) The appropriate balancing horizontal tail load must be accounted for in a rational or conservative manner when determining the wing loads and linear inertia loads corresponding to any of the symmetrical flight conditions specified in CS 23.331 to 23.341.

(b) The incremental horizontal tail loads due to manoeuvring and gusts must be reacted by the angular inertia of the aeroplane in a rational or conservative manner.

(c) Mutual influence of the aerodynamic surfaces must be taken into account when determining flight loads.

CS 23.333 Flight envelope

(a) *General.* Compliance with the strength requirements of this subpart must be shown at any combination of airspeed and load factor on and within the boundaries of a flight envelope (similar to the one in sub-paragraph (d)) that represents the envelope of the flight loading conditions specified by the manoeuvring and gust criteria of sub-paragraphs (b) and (c) respectively.

(b) *Manoeuvring envelope.* Except where limited by maximum (static) lift coefficients, the aeroplane is assumed to be subjected to symmetrical manoeuvres resulting in the following limit load factors:

(1) The positive manoeuvring load factor specified in CS 23.337 at speeds up to V_D;

(2) The negative manoeuvring load factor specified in CS 23.337 at V_C; and

(3) Factors varying linearly with speed from the specified value at V_C to 0·0 at V_D for the normal and commuter category, and -1·0 at V_D for the aerobatic and utility categories.

(c) *Gust envelope*

(1) The aeroplane is assumed to be subjected to symmetrical vertical gusts in level flight. The resulting limit load factors must correspond to the conditions determined as follows:

(i) Positive (up) and negative (down) gusts of 50 fps at V_C must be considered at altitudes between sea level and 6096 m (20 000 ft). The gust velocity may be reduced linearly from 50 fps at 6096 m (20 000 ft) to 25 fps at 15240 m (50 000 ft); and

(ii) Positive and negative gusts of 25 fps at V_D must be considered at altitudes between sea level and 6096 m (20 000 ft). The gust velocity may be reduced linearly from 25 fps at 6096 m (20 000 ft) to 12·5 fps at 15240 m (50 000 ft).

(iii) In addition, for commuter category aeroplanes, positive (up) and negative (down) rough air gusts of 66 fps at V_B must be considered at altitudes between sea level and 6096 m (20 000 ft). The gust velocity may be reduced linearly from 66 fps at 6096 m (20 000 ft) to 38 fps at 15240 m (50 000 ft).

(2) The following assumptions must be made:

(i) The shape of the gust is –

$$U = \frac{U_{de}}{2}\left(1-\cos\frac{2\pi s}{25\bar{C}}\right)$$

where –

s = Distance penetrated into gust (ft.);

$\bar{C}$ = Mean geometric chord of wing (ft.); and

U_{de} = Derived gust velocity referred to in sub-paragraph (1) linearly with speed between V_C and V_D.

(ii) Gust load factors vary linearly with speed between V_C and V_D.